UNIVERSIDAD COMPLUTENSE DE MADRID

FACULTAD DE CIENCIAS FÍSICAS

TESIS DOCTORAL

El Jet del Atlántico Norte desde una Perspectiva Multiparamétrica

The North Atlantic Eddy-Driven Jet revisited from a Multiparametric Perspective

MEMORIA PARA OPTAR AL GRADO DE DOCTORA

PRESENTADA POR

Marina García Burgos

DIRIGIDA POR

Blanca Ayarzagüena Porras

Ricardo Francisco García Herrera

UNIVERSIDAD COMPLUTENSE DE MADRID
FACULTAD DE CIENCIAS FÍSICAS

TESIS DOCTORAL

El Jet del Atlántico Norte desde una Perspectiva Multiparamétrica

The North Atlantic Eddy-Driven Jet revisited from a Multiparametric Perspective

PROGRAMA DE DOCTORADO EN FÍSICA

MEMORIA PARA OPTAR AL GRADO DE DOCTORA

Presentada por
Marina García Burgos

Directores

Blanca Ayarzagüena Porras
Ricardo Francisco García Herrera

Madrid, 2024

Agradecimientos

La última noche de Ramadán, mi amigo Mahmoud nos invitó a cenar en los tejados de Madrid. Como único requisito de asistencia, compartir con el resto de invitados nuestro propio significado de 'pertenecer' (los que me conozcáis sabréis la pereza que me dio). Hacia el final de la noche, nuestra amiga Sandra bellamente nos contó que pertenecemos a todos los instantes vividos, a los lugares, olores, sensaciones y personas a las que el destino nos ha ligado. A través de ellos, la vida me enseñó que esta tesis es el resultado de cada experiencia vivida durante estos últimos cuatro largos años, durante esta pequeña parcela de la existencia.

De esta manera, agradezco la perfecta conjunción de mi escritorio con el sol del sur. Agradezco por mis compañeros de despacho y de viaje, por su firme apoyo y complicidad. Agradezco la risa de Blanca en el pasillo indicándome que ya son las 10 y que puedo ir a buscarla. Agradezco que la mejor climatización de la Facultad sea la del despacho 220, modulo central, cuarta planta. En general, agradezco a la cuarta planta, a sus gentes, a los numerosos portales que recorren su pasillo, invitándote a asomarte a profundos abismos de galaxias, terremotos y calentamientos súbitos, al despacho de Elvira Zurita, al juego de puertas que colocan la de mi directora justo delante de la mía. Agradezco la diversión de dar clase en LCC, Física de la Atmósfera o en los múltiples laboratorios, y el tedio de la corrección. A Meteolab y sus talleres, a la Semana de la Ciencia. Agradezco las emocionantes charlas a las que esta experiencia me ha permitido asistir. Siempre recordaré cómo, mientras un quasi-premio nobel nos hablaba sobre el cambio climático que acabó con los dinosaurios, Jose y yo estábamos embelesados y Vero y Sol tenían cosas más importantes que hacer. Agradezco la puntería de haber caído en el grupo STREAM, lleno de personas a las que admiro.

Agradezco a la Facultad por haberme visto crecer, una parte de mí siempre vivirá entre sus muros, sus imponentes torres y sus parques. Agradezco a la joven que hace doce años, llena de ilusión y hambre de física, recorrió por primera vez el camino verde, azul y gris y cruzó su umbral, ritual que estaría destinada a repetir incontables veces. Agradezco por mis siempre amigos hechos en sus aulas, por su constante compañía y amor, por hacerme

reír, por satisfacer esa parte tan importante de mi ser, por levantar y aguantar mi ánimo. Agradezco los infinitos cuidados de mi madre, la capacidad de mi padre de recibirme siempre contento. A Carlos en su totalidad, por ser primer testigo y sostén de toda mi variabilidad. Agradezco por todos los oídos que han escuchado a mi boca decir que no puede más, también por las miradas que han respondido con alegría cuando expreso que he aprendido algo nuevo. Recientemente a Juan por volverme a emocionar después de mucho. También, profundamente a mi cuerpo, especialmente a mis tripas que sin duda se han llevado la peor parte, pero también a mis piernas por quedarse sentadas cuando solo querían correr.

Con especial cariño agradezco a mi queridísimo Víctor por hablarme de huracanes, reventones cálidos y turismo de extremos mucho antes de que estuviese preparada para comprender. A Belén, por su pasión, interés y entusiasmo, que fueron una luminosa guía en un momento de gran confusión. A Tim (o señor Woollings como me gusta llamarle) por mostrarme que no pasa nada cuando las cosas no siguen el curso que deseamos, por hacerlo todo fácil y cercano. A David, por su rigor, atención al detalle y buen humor. Nada de lo que he hecho sería igual sin tu mano. Recuerdo las primeras palabras de reconocimiento que me dijeron por haber mejorado, fueron tuyas. A Ricardo, al que he pasado de temer a admirar. Gracias por encarnar el rol de decir siempre las cosas como son, con las palabras adecuadas. Finalmente, a Blanca, por confiar en mi versión polluela, por llevarme de la mano durante el primer año y por no abandonarme los demás. Por ser paciente con los errores, por celebrar los aciertos, por calmar mis bucles (aunque no lo sepas). Por querer siempre lo mejor para mí y esforzarte en que así sea. Por las innumerables horas que me has dedicado y por tener siempre hueco disponible para esta tesis.

A todos los hilos que tejen mis días, gracias.

*Este trabajo ha sido financiado por la ayuda para la formación de personal investigador (*PRE2019-090618*) otorgada por el Ministerio de Ciencia e Innovación.*

Contents

Acronyms

AA	Arctic Amplification
AICc	Akaike's information criterion correction
AMOC	Atlantic Meridional Overturning Circulation
AUC-ROC	Area Under the Receiver Operating Characteristic Curve
AWB	Anticyclonic Wave Breaking
CEU	Central Europe
CMIP6	Coupled Model Intercomparison Project Phase 6
CWB	Cyclonic Wave Breaking
DJF	December-January-February
EDJ	Eddy-Driven Jet
EEU	Eastern Europe
EGR	Eady Growth Rate
EKE	Eddy Kinetic Energy
ENSO	El Niño-Southern Oscillation
EOF	Empirical Orthogonal Function
ERA5	Fifth generation ECMWF Interim reanalysis
Grad200	Meridional temperature Gradient at 200 hPa
Grad850	Meridional temperature Gradient at 850 hPa
JAS	July-August-September
JF	January-February
MCA	Maximum Covariance Analysis
MLR	Multiple Linear Regression
NAH	North Atlantic Horseshoe
NAO	North Atlantic Oscillation
NATL	North Atlantic
NCAR	National Center for Atmospheric Research
NCEP	National Centers for Environmental Prediction
ND	November-December

NDJF	November-December-January-February
NPO	North Pacific Oscillation
PNA	Pacific North American Pattern
R^2	Coefficient of determination
RWB	Rossby Wave Breaking
SCA	Scandinavia
SLP	Sea level pressure
SNOW	North American Snow Cover
SPV	Stratospheric Polar Vortex
SST	Sea surface temperature
TA	Tropical Amplification
TDJ	Thermal-Driven Jet
TN	Daily minimum temperature at 2m
TNH	Tropical Northern Hemisphere
TX	Daily maximum temperature at 2m
WH	Warming Hole
WMED	Western Mediterranean
Z500	Geopotential height at 500 hPa

Resumen

Introducción

El Eddy-Driven Jet (EDJ) es una potente corriente del oeste que regula el tiempo en latitudes medias, influyendo también en la ocurrencia de extremos (Barry & Chorley, 2009). En el Atlántico Norte, el principal modo de variabilidad del EDJ es un desplazamiento meridional (Athanasiadis et al., 2010; Eichelberger & Hartmann, 2007). Sin embargo, recientemente, se ha visto que las migraciones latitudinales del EDJ no pueden explicar toda su variabilidad (Frame et al., 2013; Madonna et al., 2019) y que se requiere de otras características para comprender su comportamiento completamente. Algunos autores han propuesto métricas para medir otros aspectos relevantes del EDJ, como la inclinación o extensión longitudinal (Messori & Caballero, 2015). No obstante, éstos han sido presentados e investigados de forma aislada.

Dada la importancia del EDJ y sus impactos, es importante conocer los posibles forzadores de su variabilidad. No obstante, la mayoría de los estudios se centran en explicar la variabilidad latitudinal e ignoran la influencia en otros aspectos del EDJ (Gastineau et al., 2016; Ronalds & Barnes, 2019). En la misma línea, los impactos en superficie relacionados con el EDJ se estudian atendiendo a sus características individuales, sin tener en cuenta la estructura completa (Mahlstein et al., 2012; Röthlisberger et al., 2016). Respecto a las proyecciones de cambio climático, a pesar de los estudios dedicados a su análisis, existen aún grandes incertidumbres en cuanto a los cambios que sufrirá el EDJ del Atlántico Norte en invierno (Barnes & Polvani, 2015; Peings et al., 2018).

Objetivos

El objetivo principal de esta tesis doctoral es proporcionar un estudio exhaustivo sobre la variabilidad climática del EDJ de Atlántico Norte en invierno desde una perspectiva multiparamétrica en la que se consideran diversas características del EDJ. Para ello, se abordarán los siguientes temas:

1. Caracterización de los estados recurrentes del EDJ y evaluación de las transiciones preferidas entre ellos.
2. Evaluación de la relación entre las estructuras del EDJ y la ocurrencia de eventos extremos de temperatura en diferentes regiones de Europa.

3. Identificación de los principales factores que fuerzan la variabilidad de los parámetros del EDJ y evaluación de los mecanismos implicados.
4. Cuantificación de los cambios futuros de los parámetros del EDJ, así como una evaluación de sus incertidumbres asociadas, relacionándolas con las de otros fenómenos climáticos.

Datos y métodos

En esta tesis doctoral, hemos desarrollado una nueva metodología para caracterizar el EDJ desde una perspectiva multiparamétrica, ampliando el enfoque tradicional presentado por Woollings et al. (2010). El método proporciona un conjunto de diez parámetros, cada uno de los cuales cuantifica un aspecto específico de la estructura de la EDJ. Estos parámetros son la intensidad, la anchura, la posición latitudinal y longitudinal, los flancos latitudinales, las elongaciones longitudinales, la inclinación y la desviación. La metodología también proporciona una detección 2D del EDJ que identifica su estructura espacial. Los cálculos están basados en el viento zonal de niveles bajos en el Atlántico Norte. Los reanálisis NCEP-NCAR y ERA5 se utilizan para investigar el clima actual y las salidas de los modelos del CMIP6 para las proyecciones futuras.

Resultados

1. Se identifican cuatro estados recurrentes del EDJ: norte (N4), central (C4), desplazado hacia el sur e inclinado (St4) y desplazado hacia el sur y partido (Sp4). Aunque existe cierta correspondencia entre los regímenes multiparamétricos y sus homólogos latitudinales, la correspondencia no es perfecta ya que un mismo estado latitudinal puede pertenecer a distintos regímenes multiparamétricos según el estado del resto de parámetros. Además, St4 y Sp4 son indistinguibles desde una perspectiva latitudinal, ya que ambos pertenecen al estado sur. Los regímenes presentan una migración hacia el polo (Sp4-St4-C4-N4). Sin embargo, la transición abrupta del EDJ desde latitudes norte hacia el sur observada en la literatura no parece tan clara cuando se consideran los regímenes inclinado y partido.

2. Cuatro regiones se conforman considerando las diferentes estructuras del EDJ que desencadenan eventos extremos de temperatura sobre Europa: Escandinavia,

Europa central y oriental y Mediterráneo occidental. Dichas estructuras del EDJ no sólo difieren en los parámetros latitudinales, sino que requieren de otros para su obtención. En todos los casos, la acción conjunta de los parámetros detectados para cada región capta mejor la ocurrencia de eventos extremos que considerando únicamente la latitud. La intensidad del EDJ es una característica importante en casi todas las regiones. Del mismo modo, la inclinación del EDJ es el principal parámetro en algunas de ellas. En comparación, la latitud pierde importancia.

3. Se han detectado siete forzadores de gran escala que influyen en la variabilidad interanual del EDJ: el patrón Pacífico-Norteamérica, el patrón Tropical-Hemisferio Norte y la oscilación del Pacífico Norte, los cuales están relacionados con El Niño-Oscilación del Sur, el vórtice polar estratosférico, la circulación meridional de retorno del Atlántico, la herradura del Atlántico Norte y la cubierta de nieve de Norteamérica. La perspectiva multiparamétrica desvela una jerarquía entre los forzadores, con papeles principales y secundarios, siendo el vórtice polar el de mayor influencia. La variabilidad latitudinal es la mejor explicada por estos forzadores. La influencia de cada forzador sobre el EDJ está mediada por patrones únicos de forzamiento de eddies y de ruptura de ondas.

4. Bajo condiciones de cambio climático, el ambiguo desplazamiento latitudinal del EDJ durante el invierno no se detecta cuando se analizan por separado el principio y el final del invierno. Por el contrario, los modelos coinciden en un desplazamiento hacia el polo a principios de invierno seguido de una tendencia hacia el ecuador a finales de invierno. Este desplazamiento intraestacional está relacionado con los cambios futuros del gradiente meridional de temperatura de la alta troposfera y el 'agujero de calentamiento' de la temperatura de la superficie del mar del Atlántico Norte a principios de invierno, y del vórtice polar estratosférico a finales de invierno. Además, se constata que los sesgos de los modelos en la latitud del EDJ también influyen en las proyecciones latitudinales. Aparte, tampoco se detecta el conocido 'estrechamiento' del EDJ, lo que indica que podría ser un artefacto derivado de la mezcla de diferentes respuestas intraestacionales del EDJ.

Summary

Introduction

The Eddy-Driven Jet (EDJ) is a powerful westerly current that strongly regulates the weather in midlatitudes, influencing also the extreme events occurrence (Barry & Chorley, 2009). In the North Atlantic sector, the greatest mode of the EDJ variability is a meridional shift (Athanasiadis et al., 2010; Eichelberger & Hartmann, 2007). In recent years, several studies point out that the EDJ latitudinal migrations cannot account for all the EDJ variability (Frame et al., 2013; Madonna et al., 2019) and the definition of other features are required to fully understand its behaviour. Some authors have proposed some metrics to measure relevant aspects of the EDJ (Messori & Caballero, 2015). However, they were presented and investigated in isolation.

Given the importance of the EDJ and its associated impacts, the study of its potential drivers becomes important. However, most of the studies are still centred at the latitudinal perspective, missing the potential influence on other EDJ aspects (Gastineau et al., 2016; Ronalds & Barnes, 2019). Similarly, the surface impacts related to EDJ are studied focusing on EDJ single features, without attending to the whole structure (Mahlstein et al., 2012; Röthlisberger et al., 2016; Trigo et al., 2004). Concerning the EDJ projections under climate change conditions, despite the studies dedicated to its analysis, there are still major uncertainties regarding the changes the North Atlantic EDJ will undergo in winter (Barnes & Polvani, 2015; Peings et al., 2018).

Objectives

The principal objective of this PhD thesis is to provide a comprehensive study about the North Atlantic EDJ wintertime climatic variability from a multiparametric perspective, where several characteristics of the EDJ are considered. To do so, the following subtopics will be addressed:

1. Characterization of the EDJ recurrent states and evaluation of the preferred transitions among them.
2. Assessment of the relationship between the EDJ structures and the occurrence of temperature extreme events over different regions of Europe.

3. Identification of the main drivers leading the EDJ parameters variability and evaluation of the involved mechanisms.
4. Quantification of the EDJ parameters future changes and evaluation of their associated uncertainties, relating them to those of other climatic phenomena.

Data and Methods

In this PhD thesis, we have developed a new methodology to characterize the EDJ from a multiparametric perspective, by extending the traditional approach presented by Woollings et al. (2010). The method provides a suite of ten parameters, each of them quantifying a specific aspect of the EDJ structure. These parameters are intensity, sharpness, latitudinal y longitudinal position, latitudinal flanks, longitudinal elongations, tilt and departure. The methodology also provides a 2D detection of the EDJ, which identifies the explicit spatial structures. The computation is based on the low-level zonal wind in the North Atlantic sector. The NCEP-NCAR and ERA5 reanalyses are used for investigating the current climate and CMIP6 model outputs for future projections.

Results

1. The multiparametric perspective enables the identification of four recurrent states of the EDJ: northern (N4), central (C4), southward-shifted and tilted (St4) and southernmost-shifted and split-like (Sp4). Although some correspondence exists between the multiparametric regimes and their latitudinal counterparts, it is not perfect since the same latitudinal state can belong to different multiparametric regimes depending on the rest of the EDJ parameters. Also, St4 and Sp4 are indistinguishable from a latitudinal perspective since both fall in the southern peak. The regimes present a poleward migration (Sp4-St4-C4-N4) but, the abrupt transition from northern to southern latitudes established in the literature does not appear so clear when tilted and split patterns are considered.

2. Four regions are shaped based on the different EDJ structures triggering temperature extreme events over Europe: Scandinavia, Central and Eastern Europe and western Mediterranean. These structures not only differ in the EDJ latitudinal parameters, but require from others for their obtention. The joint action of the

detected EDJ parameters captures better the extreme events occurrence than considering only latitudinal parameters. The EDJ intensity is important characteristic in almost all regions. Similarly, the EDJ tilt is the leading parameter in some of them. In comparison, the EDJ latitude becomes less important.

3. Seven large-scale drivers are detected to influence the EDJ interannual variability: Pacific-North American pattern, Tropical-Northern Hemisphere pattern and North Pacific Oscillation, which are related to El Niño-Southern Oscillation, Stratospheric Polar Vortex, Atlantic Meridional Overturning Circulation, North Atlantic Horseshoe and North America snow cover. The multiparametric perspective unravels a hierarchy of drivers, with major and minor roles, with the polar vortex being the most influential. Latitudinal variability is best explained by these drivers. Each driver influence on the EDJ is mediated by unique eddy forcing and wave breaking patterns.

4. Under climate change conditions, the no clear latitudinal shift of the wintertime EDJ is no longer detected when analysing early and late winter separately. On the contrary, models agree on a poleward shift in early winter followed by an equatorward tendency in late winter. This intraseasonal shift is related to the future changes of the upper tropospheric temperature meridional gradient and the sea surface temperature warming hole of the North Atlantic in early winter, and the stratospheric polar vortex in late winter. Moreover, model biases in the EDJ latitude are found to also influence the latitudinal projections. Finally, the well-established EDJ squeezing is not detected, indicating it could be an artefact from mixing different intraseasonal EDJ responses.

I. Motivation

The jet streams are powerful currents that flow in the atmosphere of different planets, being key elements of the atmospheric general circulation and important regulators of weather and climate. The jet streams are narrow large-scale meandering flows that reach high intensities, with strong horizontal and vertical shears. On Earth, there are two main jets per hemisphere, located at the tropopause and blowing west to east. Although they circumnavigate the planet, they are not continuous along the entire pathway, but present discontinuities. The jet streams longitudinal chunks cover long distances, typically varying from 1000 to 5000 km. Instead, their width encompasses only a few hundred of km, and their vertical thickness solely 5-10 km.

At midlatitudes, the Eddy-Driven Jet (EDJ) is the most important element controlling weather variations. Although its core is located uplift, the EDJ influences directly the variability at ground-level in a number of ways (Ma et al., 2020). For instance, the EDJ location strongly determines the day-to-day near-surface temperature. Similarly, the trajectories of the storms are deflected by the EDJ, controlling which regions become wet or dry. Even more, if the EDJ persists over one location for several days it can lead to the generation of an extreme event such as heat waves or droughts. Due to its intimate relation with these important processes for human societies, understanding the EDJ variability becomes a priority.

Traditionally, the EDJ variability has been reduced to the latitudinal one, encompassing poleward and equatorward migrations. Although the meridional shift collects most of the EDJ variability (Athanasiadis et al., 2010; Eichelberger & Hartmann, 2007), it is unable to account for all. The EDJ latitude also struggles in identifying complex EDJ structures (Madonna et al., 2017; Woollings et al., 2010). As such, several recent studies show that the EDJ also present pulsing intensity variations (Barnes & Hartmann, 2011), zonal elongations and changes in the tilt (Messori & Caballero, 2015). This PhD thesis aims to present a comprehensive study of the EDJ variability over the North Atlantic (NATL) sector from a novel multiparametric perspective. The method provides a suite of ten daily parameters, each of them representing a specific characteristic, and a 2D EDJ detection

that represents the explicit spatial structure of the EDJ. Along the PhD thesis, we use this multiparametric approach to obtain new results on some well-established topics around the EDJ, such as the drivers of its interannual variability or the future projections, as well as others not so extensively investigated, like the EDJ impacts on the extreme temperature field.

II. State of the Art

II.1 General Atmospheric Circulation: Atmospheric cells and jets.

The general circulation of the atmosphere is driven by two intrinsic physical characteristics of the Earth system. One is the Earth's spherical shape, which leads to an uneven incoming solar radiation between the equator and the poles. This uneven forcing at the top of the atmosphere varies throughout the year, due to the angle of the Earth's rotation axis with respect to the ecliptic plane and the translation movement around the Sun. The second fact is that the Earth is rotating. The intrinsic acceleration of the rotating reference system produces deviations in the trajectories of the fluid parcels that travel in the atmosphere (Barry & Chorley, 2009). The effect of this inertial force is quantified by the Coriolis parameter (Equation II.1), proportional to the Earth's rotation rate and dependent on the fluid parcel latitude.

$$f = 2\Omega \, sin\varphi \qquad (\text{II}.1)$$

where Ω is the Earth's angular velocity and φ is the latitude.

The annual mean conditions of the incoming shortwave radiation with latitude can be observed in Figure II.1. The orange line shows an unequal amount of incoming solar radiation between the equator and the poles. In the same figure, the outgoing longwave radiation emitted by the atmosphere is also plotted. The mean conditions over low latitudes present more incoming than outgoing radiation, indicating a net warming of the tropics. Contrary, polar regions emit back to space more radiation than that received from the Sun, indicating a large cooling and a negative net heat balance. This asymmetry implies a meridional heat transport from the equator to the poles carried out by the atmosphere and the oceans (Barry & Chorley, 2009). Both circulations act to attenuate the strong meridional temperature gradient imposed by the incoming solar radiation.

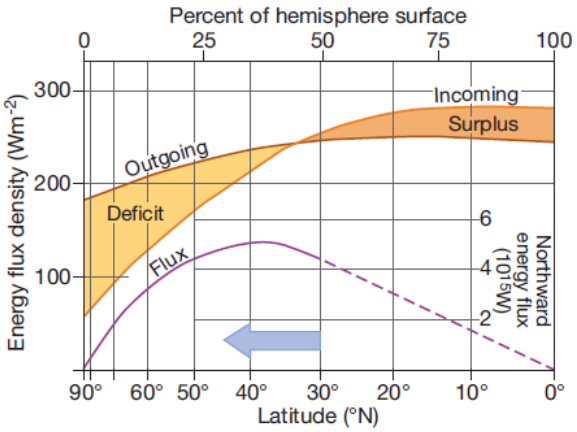

Figure II.1 Meridional balance at the top of the atmosphere between incoming solar radiation and outgoing radiation from the surface and the atmosphere. Surplus and deficit areas are maintained in balance through the poleward energy transport carried out by the atmosphere and oceans. Taken from Barry & Chorley (2009).

Following the hydrostatic balance, the warming of the tropical regions leads to an expansion of the air columns. The consequent meridional pressure gradient established with respect to the pole, together with the Earth's rotation, lead to a mean meridional circulation organised in three independent cells (Figure II.2a) separated by two upper-level westerly jets in each hemisphere (Figure II.2a and b; Stull, 2015). Hadley and Polar cells

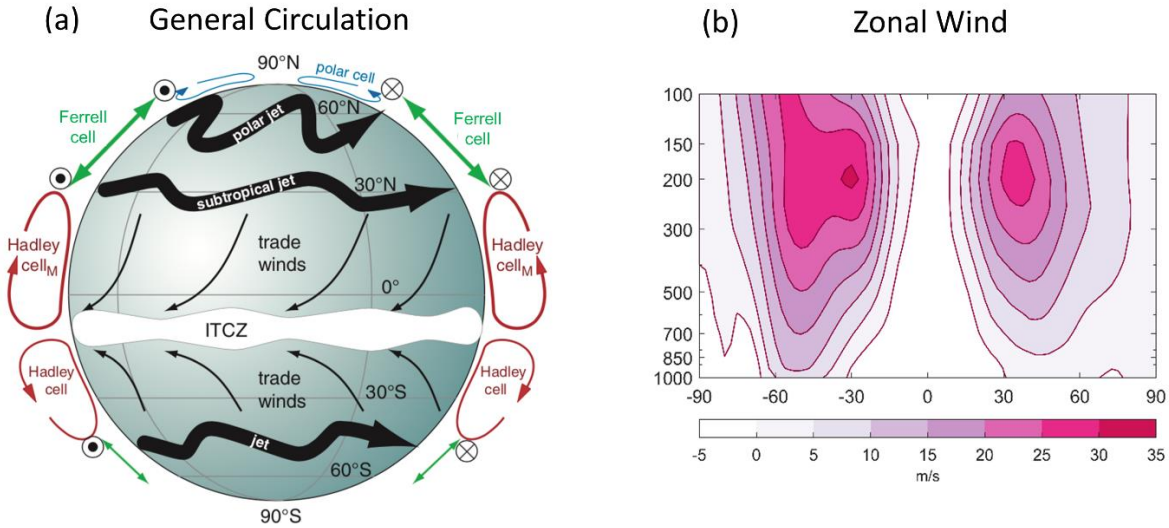

Figure II.2 (a) Three-cell (colours) and upper-level jets (black ribbons) atmospheric circulation model during boreal winter. Modified from Stull (2015). (b) Zonal wind zonal mean [ms^{-1}] annual climatology (1979-2009, ERA5).

transport heat poleward, so-called thermally direct, and slow down the Earth's rotation by friction with the surface. Contrary, Ferrell cell is thermally indirect and accelerates the Earth's surface, such that the angular momentum is conserved after considering the three cells contribution. In the atmosphere, the net angular momentum transport is always towards midlatitudes and the net heat transport towards high latitudes, after considering the effect of the eddies (Hartmann, 2007).

Two upper-level westerly jets govern the atmospheric circulation. At subtropical latitudes, the Thermal-Driven Jet (TDJ) constitutes the border between the Hadley and Ferrell cells. The current, also called subtropical jet, is driven by the local vorticity balance (Held & Hou, 1980; Hoskins et al., 1983). As the air parcels move poleward, their distance to the Earth's rotation axis decreases. Following the angular momentum conservation, the zonal wind must increase. Consequently, the poleward flow is strongly deflected eastward at the upper branch of the Hadley cell generating a shallow westerly jet with high vertical shear (easterly winds at the surface) (Holton, 2004; Li & Wettstein, 2012). The TDJ is very steady with almost no meanders. The fastest winds locate at 12 km of altitude and present intensity variations along the longitudinal circle, from 45 to 80 ms^{-1} from the Atlantic to the Pacific Ocean (Stull, 2015). Differently, between the Ferrell and Polar cells (Figure II.2a), a deep barotropic westerly jet (westerly across the entire troposphere) oscillates at extratropical latitudes, between 30°-60°. The momentum forcing produced by midlatitudes transient eddies lead to the generation of the extremely variable EDJ, characterized by large meanders expanding extensively in latitude. The winds core places around 9 km and varies from 25 to 100 ms^{-1}. The processes leading the jets, i.e. angular momentum transport and baroclinic eddies, operate and interact continuously, making sometimes difficult to relate a particular jet to a specific driving process (Lee & Kim, 2003; Walker & Schneider, 2006). The shape and size of the continents and oceanic basins establish particular conditions that lead to different configurations of the wind.

In the NATL, the combination of the poleward location of the strongest baroclinicity region together with weak Atlantic Hadley cell result in a well separated EDJ and TDJ in winter, presenting a double zonal wind maximum at upper levels (Son & Lee, 2005). Contrary, in the North Pacific, the powerful Pacific Hadley cell is able to locate the upper-level zonal wind maximum further poleward such that the Pacific TDJ and EDJ appear

merged (Lee & Kim, 2003). Because the EDJ is the central topic of this PhD thesis, a more detailed description of the Ferrell cell and EDJ generation is provided next.

- Ferrell Cell

At midlatitudes, the Coriolis force is able to balance the pressure gradient force generated between subtropical and subpolar regions. The latter, known as Geostrophic balance, together with the strong meridional temperature gradients established by the cells atmospheric configuration, result in a westerly flow that travels parallel to the isobars and presents a vertical shear that follows the expression below:

$$\frac{\partial \overline{V}_g}{\partial \ln p} = \frac{R}{fp} \hat{k} \times \nabla_p T \qquad \text{(II. 2)}$$

where f is the Coriolis parameter, R is the gas constant, p is the pressure, $\overline{V}_g$ is the horizonal geostrophic wind and ∇T is the temperature gradient. The Equation II.2 is the thermal wind equation, in reference to the vertical shear of the horizontal wind (Stull, 2015). In the Northern Hemisphere, the temperature decreases poleward and hence, the geostrophic wind decreases with pressure. Since pressure decreases with height, the geostrophic wind becomes increasingly eastward (or westerly) with height.

As mentioned above, the geostrophic balance is generally satisfied in extratropical latitudes (Barry & Chorley, 2009). In the case any forcing disrupts the midlatitudes geostrophic balance, ageostrophic circulations are generated in order to re-establish the equilibrium (Martin, 2006). From a zonal mean perspective, these ageostrophic circulations or transient eddies generate the thermally indirect meridional circulation known as Ferrell cell. Although the Ferrell's mean meridional circulation transports heat from high to low latitudes at upper-levels of the troposphere, the net heat transport remains poleward, due to the dominance of the poleward heat transport carried out by the transient eddies (boreal winter heat fluxes are shown in Figure II.3b; Eady, 1949). Transient eddies are disturbances that grow using the potential energy stored in the atmosphere, specifically in the mean flow baroclinicity (Hartmann, 2007). Consequently, the baroclinic eddy activity becomes strongest during wintertime, when the meridional temperature gradient is maximised.

In addition to transporting heat poleward, the transient eddies accelerate the mean flow in extratropical latitudes (Held & Hou, 1980; Hoskins et al., 1983; Panetta, 1993). This acceleration is produced by the intense eddy momentum convergence that occurs in the upper troposphere (boreal winter momentum fluxes are shown in Figure II.3a). The momentum convergence reinforces the midlatitudes geostrophic westerlies leading to the generation of the Eddy-Driven Jet (EDJ; Limpasuvan & Hartmann, 2000; Holton, 2004; Li & Wettstein, 2012).

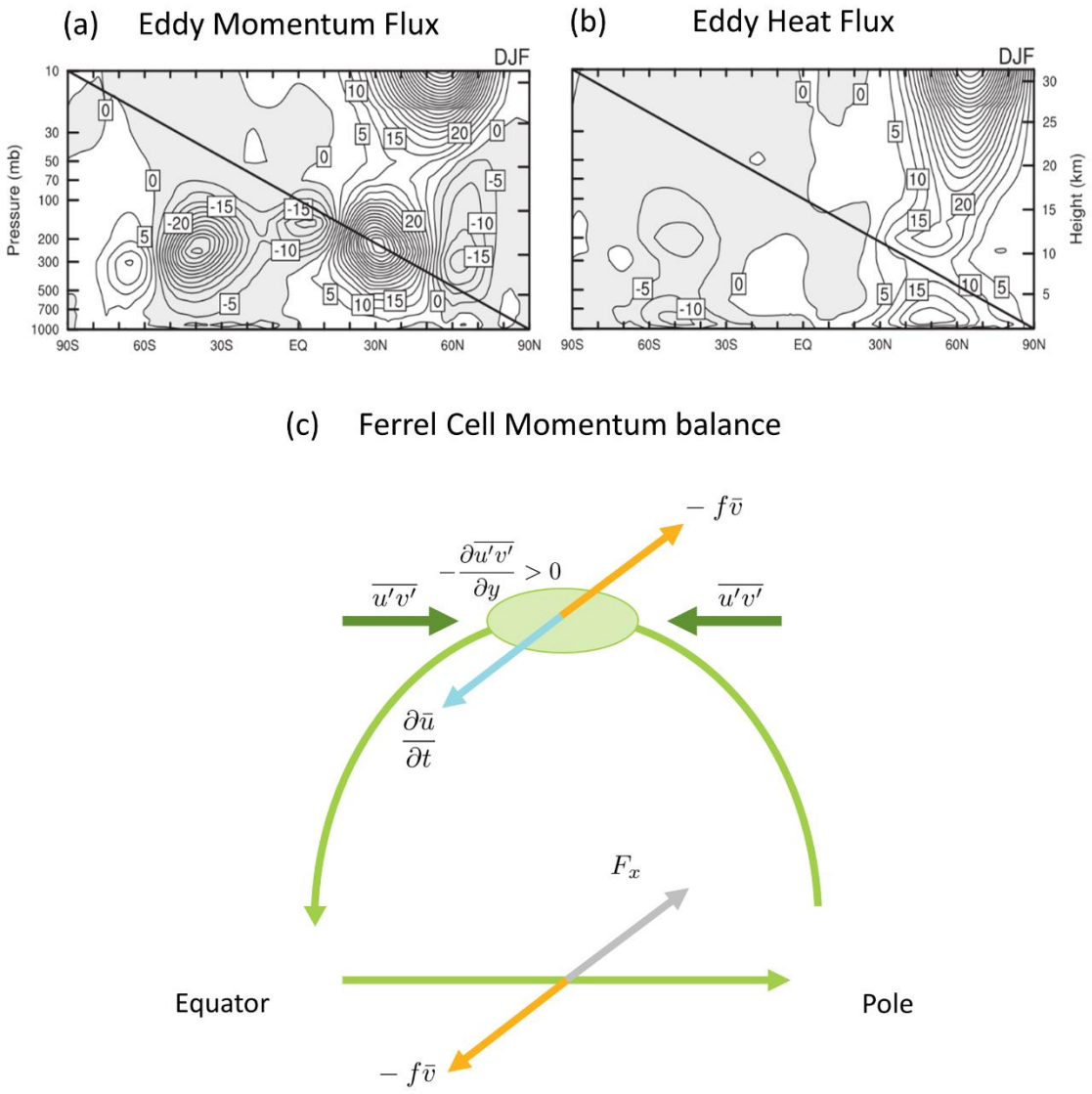

Figure II.3 (a) Average distribution of the eddy momentum flux and (b) of the eddy heat flux during boreal winter. Taken from Hartmann (2007). (c) Schematic of the momentum balance in Ferrell cell. The convergence of eddy momentum flux at upper levels (dark green arrows) accelerates the EDJ (blue arrow) and forces the Ferrell cell (light green arrows). At upper levels, the EDJ is balanced with Coriolis (orange arrow) and, at the surface, Coriolis is balanced with friction (grey arrow).

According to the zonal momentum equation (Equation II.3), the convergence of momentum ($-\frac{\partial \overline{u'v'}}{\partial y} > 0$) not only accelerates the westerlies ($\frac{\partial \bar{u}}{\partial t}$) but also forces the Ferrell cell ($-f\bar{v}$). At the upper branch of the meridional circulation, Coriolis force opposes the direct effect of the transient eddies, decelerating the upper-level zonal wind and decreasing the vertical shear (Figure II.3c). Similarly, following the thermodynamic equation (Equation II.4), the convergence of eddy heat flux at high latitudes ($-\frac{\partial \overline{v'\theta'}}{\partial y}$; Figure II.3b) also forces the Ferrell cell ($-\bar{\omega}\Theta_p$) by adiabatic cooling. The latter opposes the direct impact of the eddies and reinforces the meridional temperature gradient. The connection between the temperature and wind is possible due to the thermal wind relation (Equation II.2). In the lower branch of the Ferrell cell, Coriolis force accelerates the westerlies against the friction force (F_x) that acts to decelerate it (Figure II.3c; Hartmann, 2007). Thus, the Ferrell cell transports the momentum deposited at upper levels downward to the surface, where it is dissipated by friction (Hartmann, 2007).

$$\frac{\partial \bar{u}}{\partial t} - f\bar{v} \sim -\frac{\partial \overline{u'v'}}{\partial y} \quad \text{(II. 3)}$$

$$\frac{\partial \bar{\theta}}{\partial t} - \bar{\omega}\Theta_p \sim -\frac{\partial \overline{v'\theta'}}{\partial y} \quad \text{(II. 4)}$$

where $\bar{}$ denotes zonal mean, $'$ the deviation from zonal mean, u, v, ω are the zonal, meridional and vertical components of the wind, θ is the potential temperature, $u'v'$ and $v'\theta'$ are the eddy momentum and heat flux and Θ_p is the reference stability profile.

- Midlatitudes Baroclinicity

Although the Northern Hemisphere extratropical latitudes present the strongest meridional temperature gradients of the Earth, by the encounter of warm air from Hadley cell and cold air from polar radiative cooling, they are not zonally symmetric. On the contrary, the baroclinicity depends on the longitude. Figure II.4a shows that the western borders of North Pacific and North Atlantic (NATL) Ocean basins are the regions with the strongest air surface temperature gradients of the Northern Hemisphere. There are two sources for the generation of this specific configuration. First, the eastern flanks of

planetary stationary troughs establish a strong meridional temperature gradient over the eastern coast of the continents (contours in Figure II.4b). These anomalies in the zonal flow are generated downstream of major mountain ranges, such as the Rocky Mountains, due to the conservation of absolute vorticity (Hoskins & Karoly, 1981; Vallis & Gerber, 2008; Brayshaw et al., 2009). Besides, the oceans also contribute to the baroclinicity generation at the west of the basins (shading in Figure II.4b; Nakamura et al., 2008; Wilson et al., 2009; Sampe et al., 2010). In particular, the great heat capacity of the oceans together with the

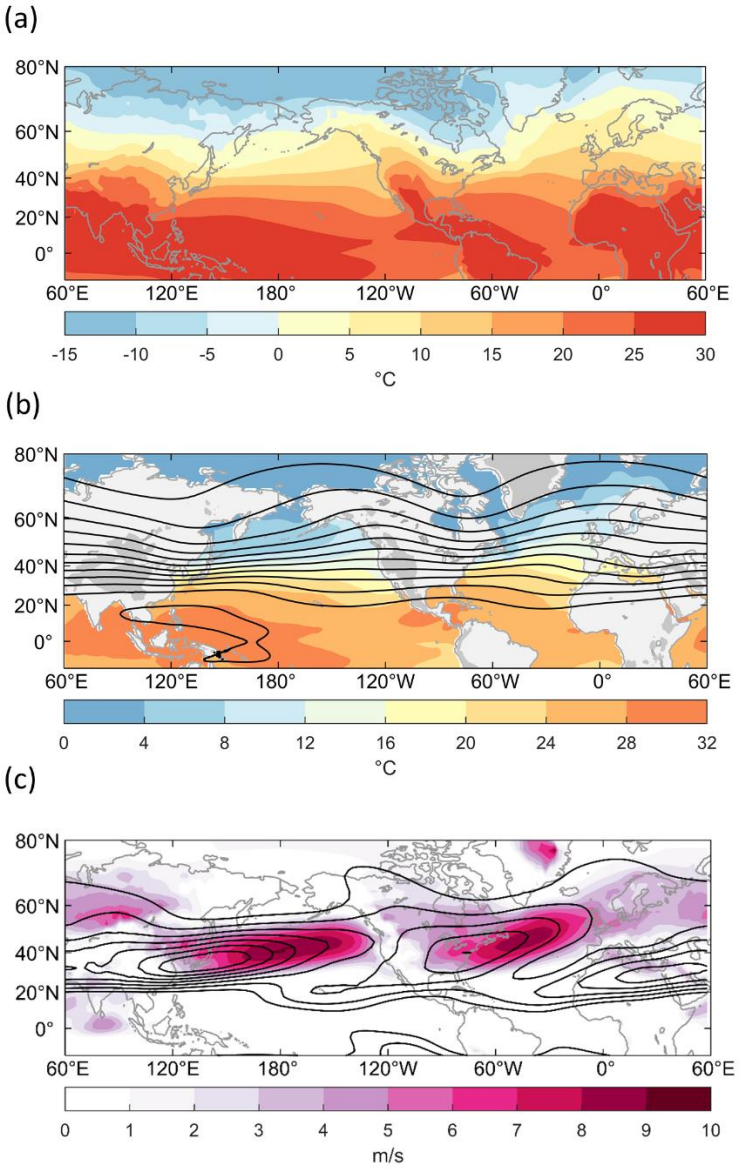

Figure II.4 Annual climatology of (a) temperature [°C] at 1000 hPa (shading), (b) sea surface temperature [°C] (shading) and geopotential at 200 hPa [m^2s^{-2}] (contours, drawn every 1000 m^2s^{-2} from 11000 m^2s^{-2} to 22000 m^2s^{-2}) and (c) zonal wind [ms^{-1}] at 850 hPa (shading) and 200 hPa (contours, drawn every 5 ms^{-1} from 10 ms^{-1} to 45 ms^{-1}) (1979-2009, ERA5). Dark grey over the continents in (b) denote regions with altitude higher than 1500 m over sea level.

strong temperature advection carried by confluent subtropical and subpolar ocean currents establishes an oceanic front that restores the baroclinicity of the overlying atmosphere (Nakamura et al., 2004; 2008; Sampe et al., 2010). The strongest midlatitude winds overlap the sharp baroclinic regions (Figure II.4c; Brayshaw et al., 2009, 2011).

- Transient Eddies

The low-level temperature and humidity gradients (Figure II.4a; Chang, 2001; Hoskins & Valdes, 1990) together with the upper-level strong winds (Figure II.4c) establish the proper atmospheric conditions for the generation of eddies and the EDJ (Robinson, 2000). Warm and expanded air columns are very close to cold and contracted ones. Locally, at each latitude, the columns are in stable equilibrium, as dense air is located at the surface and becomes lighter with height. However, latitudinally, the proximity of air columns with different temperatures leads to an unstable equilibrium. Denser air parcels are located at higher altitudes than lighter parcels and hence, the potential energy can be reduced by reorganizing the air parcels adiabatically (Marshall & Plumb, 2007). Under this atmospheric scenario, eddies can grow extracting potential energy from the mean flow (P_Z), through baroclinic instability processes (Holton, 2004). Baroclinic instabilities and related mechanisms predominantly take place in the troposphere, because the stratosphere is characterized by a strong stratification that hinders vertical movements (Marshall & Plumb, 2007). By reducing the meridional temperature gradient, the poleward eddy heat flux leads to the conversion of P_Z into potential energy available for the eddies (P_E). Also, the rising of the near-surface warm and light air and sinking of the cold and dense air of upper levels, imply the loss of P_E and gain of kinetic energy of the eddies (K_E), process known as baroclinic conversion. At upper levels, where the eddies propagate meridionally out of the generation region (Robinson, 2000), a strong momentum transport from subtropics to midlatitudes leads to the EDJ formation (Equation II.3; Hartmann, 2007). The transformation process from K_E into kinetic energy for the mean flow (K_Z) is so-called barotropic decay. The cycle ends with the generation of the Ferrell cell, which transforms K_Z into P_Z by transporting heat from cold to warm latitudes at upper levels. This closed energy cycle describes the eddy-mean flow interaction of extratropical regions (Lorenz, 1955) and is summarized in the schematic of Figure II.5.

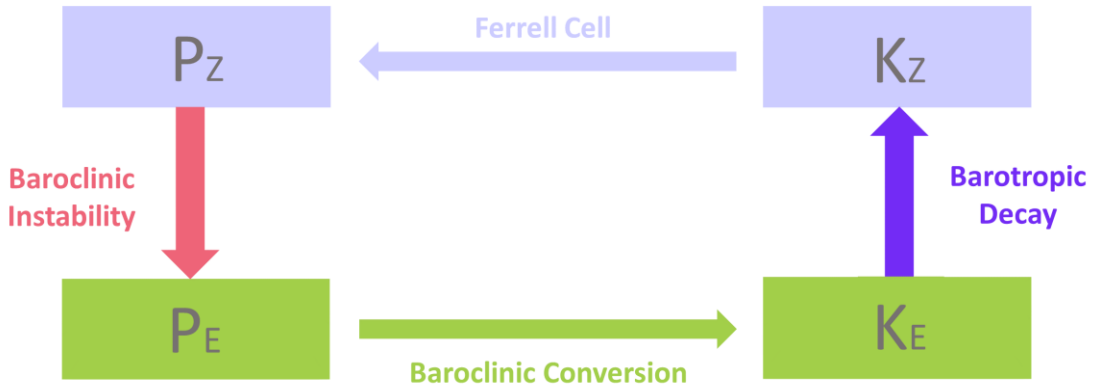

Figure II.5 Lorenz energy cycle.

As Lorenz's cycle exhibits, the transient eddies interact with the mean flow during their life-cycle, which may affect the extratropical circulation during 1-2 weeks (Feldstein, 2000; Rivière & Orlanski, 2007). Particularly, the barotropic decay stage strongly influences the EDJ variability, affecting its position and intensity through momentum transport (Robinson, 2006). At upper levels, when eddies have grown and present a great amplitude, the momentum fluxes start to dominate over heat fluxes (Simmons & Hoskins, 1978) producing Rossby wave breaking (RWB; McIntyre & Palmer, 1983), which leads to important modifications in the EDJ structure. The RWB type depends on the transient eddies lifecycle, which can be of two types (LC1 and LC2) (Figure II.6; Thorncroft et al., 1993) depending on the intrinsic structural characteristics of the eddies and the mean flow in which they develop (Drouard et al., 2013; 2015).

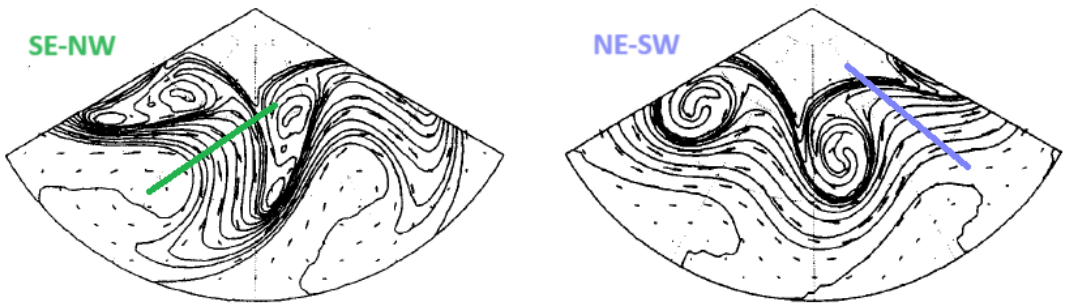

Figure II.6 Structure of the two non-linear baroclinic wave decay at upper levels. Contours of potential vorticity at the dynamical tropopause for LC1 (left) and LC2 (right). The contours are drawn every 5 K from 290 K to 350 K. The represented area spans from 20°-90°N. Taken from Throncroft et al. (1993).

LC1 lifecycles are associated with SW-NE tilting of the phase lines and anticyclonically deformed contours (Figure II.6a). The breaking of LC1 occurs equatorward of the jet core region, being influenced by the anticyclonic shear of the EDJ. This life cycle ends with an anticyclonic wave breaking (AWB), which subtracts momentum from the tropics toward midlatitudes, shifting the EDJ poleward (Lee & Feldstein, 1996; Orlanski, 2003; Thorcroft et al., 1993). Differently, LC2 evolve under the cyclonic shear of the EDJ and are characterized by cyclonic tilting along the NW-SE direction (Figure II.6b). During LC2 breaking or cyclonic wave breaking (CWB), momentum from polar regions is extracted towards midlatitudes shifting the EDJ equatorward. Both lifecycles and associated RWB strongly differ on their impact on the large-scale flow, playing an important role in the extratropical variability. The average effect of transient eddies maintains the EDJ location and variations in the eddies forcing lead to meridional shifts (Lorenz & Hartmann, 2003; Vallis & Gerber 2008).

II.2 The North Atlantic Eddy-Driven Jet

Hereafter, we focus on the NATL EDJ. A detailed description about the NATL EDJ mean state and variability is provided below. Also, different aspects related to both the near-surface impacts and the drivers of its variability at interannual scales are discussed. Lastly, the principal insights on the expected future changes of the NATL EDJ under climate change are revised.

II.2.1 Main Characteristics of the EDJ

- Mean State and Variability

The NATL EDJ is fuelled by the growth and decay of baroclinic eddies, and shaped by the NATL specific configuration. The basin orographic and oceanic forcing inserts a zonal asymmetry in the flow, by weakening the eastward acceleration on the EDJ. This eddy forcing causes the EDJ and storm track to tilt and shift poleward in the NATL, in comparison to other basins (Figure II.4c, Wilson et al., 2009). The NATL EDJ winds are stronger during

winter than in the other seasons, presenting an average value of 5 ms^{-1} at the surface and a maximum of 40 ms^{-1} at a height of 12 km (Hurrell & Deser, 2010). At 850 hPa (the EDJ reference level used in this PhD thesis), the average value is 14 ms^{-1} for winter and 10 ms^{-1} for summer (Woollings et al., 2010). During the latter season, the flow is weaker due to the more uniform distribution of incoming radiation and the predominance of the Azores high over all the NATL. Overall, the variability during summer is only half as large as that of wintertime (Hurrell & Deser, 2010; Wallace et al., 1993)

The winter NATL EDJ locates over 46°N and presents a small seasonal cycle of 4°, being further north in summer than in winter (Woollings et al., 2010). Since the NATL EDJ becomes the strongest and most variable on winter, in the following we focus only on this season. Also, for simplicity, the NATL EDJ is referred solely as EDJ hereafter. During the cold season, the daily latitude shows a trimodal behaviour with three well separated maxima (Figure II.7a). The cross section of the zonal wind over the NATL sector shows that northern and central EDJs are clearly separated from the TDJ (Figure II.7b-c). Only in the southern location there is not a clear separation between them (Figure II.7d). The EDJ deep barotropic structure enables the lower troposphere wind latitude to become representative of the location of the EDJ. The latitudinal positions are related to the frequency and location of the wave breaking. Southern EDJs present high occurrence of wave breaking at the south of Greenland (Figure II.8a). This wave breaking occurs in the cyclonic shear region of the EDJ leading to a CWB and equatorward shift of the EDJ. The lower AWB frequency over Europe allows the equatorward EDJ shift throughout the sector. The opposite conditions lead to northern EDJs (Figure II.8c). Reduced RWB in the cyclonic shear at the western NATL, together with enhanced over the anticyclonic shear over Europe, shift the EDJ poleward. During central EDJs, there is lower occurrence of RWB compared to northern and southern EDJs (Figure II.8b). This establishes the central EDJs as the unperturbed state.

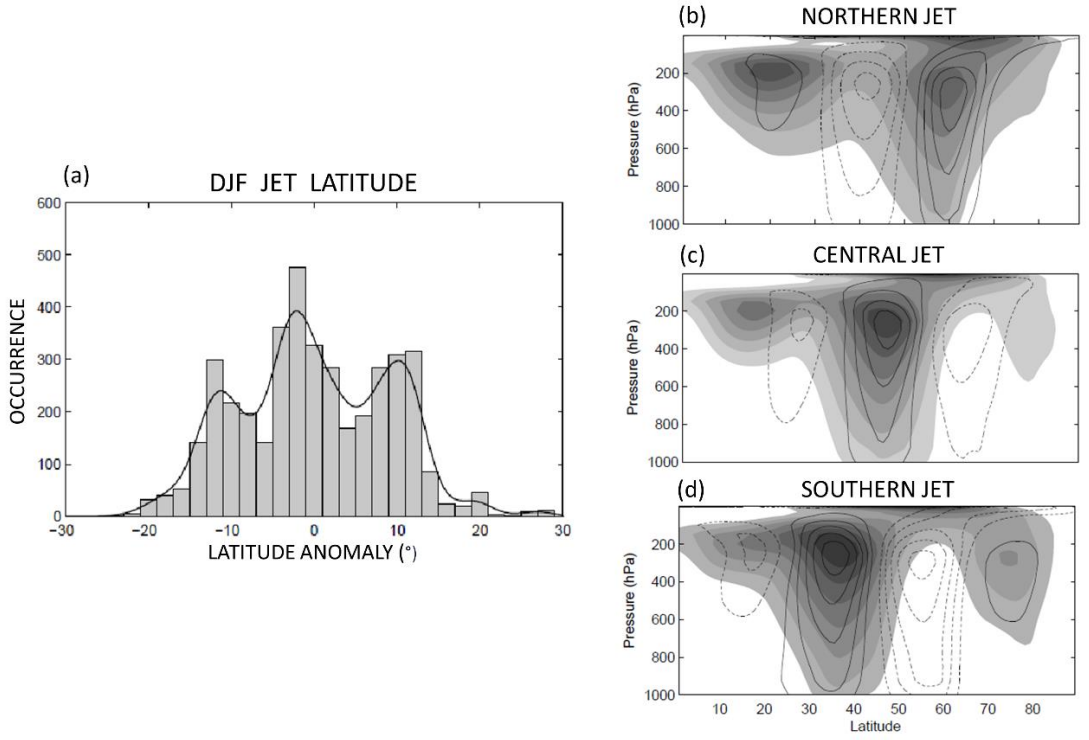

Figure II.7 (a) Probability distribution function of the daily wintertime EDJ latitude anomalies in ERA-40. (b-d) Composites of the zonal wind averaged over [60°W-0°] for the three locations of the EDJ depicted in (a): (b) northern, (c) central and (d) southern jet. Shading shows the full field starting at 5 ms^{-1} and drawn every 5 ms^{-1}. Contours show anomalies from the DJF climatology every 3 ms^{-1}. Positive anomalies are drawn in solid contours and negative in dashed contours. Taken from Woollings et al. (2010).

The North Atlantic Oscillation (NAO, Wallace & Gutzler, 1981), which is the most important mode of the NATL variability (Visbeck et al., 2001), summarizes the variability of the three latitudinal states. The synoptic eddies distribute mass between the subtropical Azores high and the subpolar Iceland low. The variability of this pressure gradient is measured by the NAO, comprising the meridional excursions of the EDJ core (Wittman et al., 2005). Positive phases of the NAO capture intensified and poleward shifted EDJs (reinforced climatological conditions). On the contrary, negative NAO phases capture weakened and equatorward shifted EDJs (disturbed climatological conditions) (Benedict et al., 2004; Franzke et al., 2004; Riviere & Orlanski, 2007). More precisely, the three latitudinal positions (Figure II.7b-d) and associated structures can be described by combinations of the NAO and East Atlantic (EA) patterns (dominant modes of NATL sea level pressure (SLP) variability) (Madonna et al., 2017; Mellado-Cano et al., 2019; Woollings et al., 2010; Woollings & Blackburn, 2012).

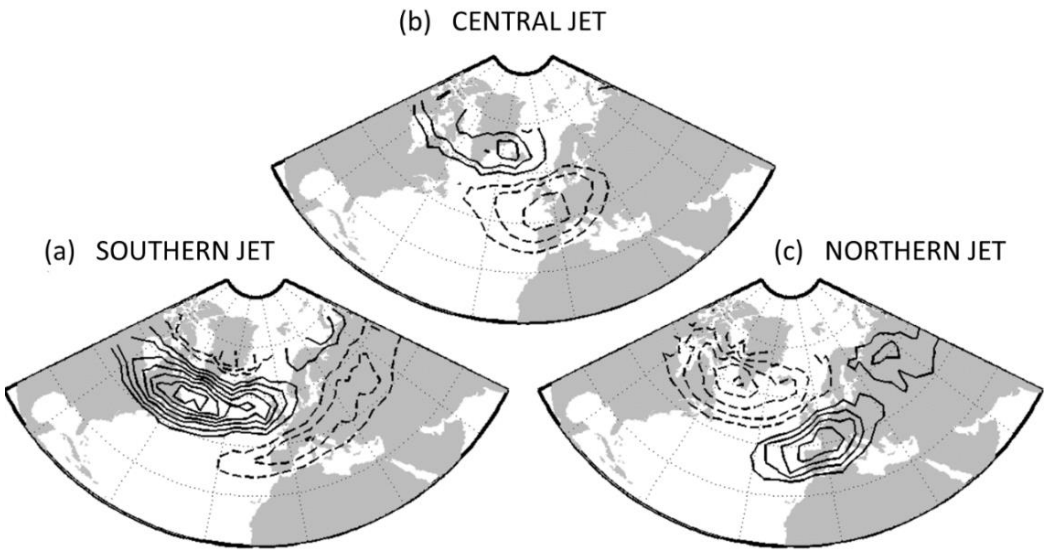

Figure II.8 Composites of wave breaking occurrence for the days corresponding to the three jet locations: (a) southern, (b) central and (c) northern jet. Wave breaking anomalies from the DJF climatological mean are contoured every 0.05 day^{-1}. Positive anomalies are represented by solid contours and negative ones by dashed contours. Taken from Woollings et al. (2010).

- Classical characterization and Limitations

The classical characterization of the NATL winter EDJ follows the three preferred latitudinal positions identified by Woollings et al., (2010), corresponding to the south (S), central (C) and northern (N) states (Figure II.7b-d). This perspective has been widely utilised since, as shown, the meridional shift is the leading pattern of the NATL wind variability and explains most of it (Eichelberger & Hartmann, 2007; Athanasiadis et al., 2010).

In recent years, several studies have revealed that latitude alone cannot fully account for the EDJ variability and structure. In addition to the latitudinal variations, the EDJ also experiences pulsing variations that become more prominent under poleward migrations (Barnes & Hartmann 2011) and in the presence of a strong TDJ (Eichelberg & Hartmann 2007). Further, the EDJ can present states with zonal elongations and changes in the tilt (Messori & Caballero, 2015). Merged patterns of S EDJs with the TDJ have also been reported. They are driven by the suppressed transient eddy activity due to the strong zonal flow, resulting in a shift in the balance between the thermal and eddy processes (Madonna et al., 2019). The EDJ latitude is not able either to describe alone the large-scale circulation in the NATL sector. In fact, the main variability modes of the NATL weather and climate are

a combination of at least changes in the latitude, speed and width of the EDJ (Monahan & Fyfe, 2006). The dominant weather regimes of the NATL are not well captured by the three latitudinal regimes either. Particularly, the European blocking is not detected since the EDJ latitude struggles to identify complex configurations of the flow (Woollings et al., 2010; Madonna et al., 2017). Blockings are defined as anomalous high-pressure systems that expand across the troposphere and persist for several days (Barriopedro et al., 2010; Woollings et al., 2018). Highly disrupted EDJs, such as strongly tilted or split EDJs, are particularly challenging since the latitude is poorly constrained in these configurations and so, its predictability of the EDJ decreases (Frame et al., 2013).

As shown, the structure of the EDJ is complex and can be challenging to be described by using a single latitudinal index. Wider approaches, like feature-based (Koch et al., 2006; Limbach et al., 2012; Strong & Davis, 2008; Woollings et al., 2018) or spatially-resolved zonal wind fields (Dorrington & Strommen, 2020; Frame et al., 2011; Hannachi et al., 2012; Madonna et al. 2017) provide a more complete picture of the EDJ structure but they often lack an explicit measure of its attributes. Single metrics accounting for other relevant aspects of the EDJ, such as the tilt (Woollings & Balkburn 2012; Messori & Caballero 2015) or waviness of the midlatitude circulation (Cattiaux et al., 2016; Chen et al., 2016; Di Capua & Coumou, 2016) have been proposed, however, in isolation. Ideally, the proper representation of the EDJ structure would be addressed by a combination of EDJ features.

II.2.2 EDJ impacts in Current Climate

One of the most relevant aspects to focus on when studying a certain phenomenon of the climate system is the potential impacts it may have on surface weather and climate, due to the important consequences for the human communities. This topic becomes especially relevant for the NATL EDJ since, as previously mentioned, is the main regulator of weather and climate in the NATL-European sector (Ma et al., 2020). Concretely, the EDJ climatology and variability strongly determine fundamental variables like near-surface air temperature or precipitation, including their extreme events.

- Surface Temperature

As pointed above, the EDJ appears as a strong physical barrier in the NATL. The associated winds act as a wall across the troposphere that separates subtropical warm air masses towards the equator from polar cold air masses located poleward. This relation imposes the surface air temperature climatology being shaped by the EDJ mean state. Figure II.4a shows that the strongest temperature gradients spatially coincide with the path followed by the zonal wind maximum across the basin (contours in Figure II.4c). Also, both fields present the characteristic SE-NW tilting of the EDJ. This intimate relation implies that departures of the EDJ from its climatological state are followed by similar variations in the temperature field.

The impact of the EDJ variability on the surface temperature has been traditionally studied in terms of large-scale atmospheric anomalies (Hurrell, 1995, 1996; Hurrell & Van Loon, 1997; Osborn et al., 1999). During periods of reinforced climatological conditions (NAO+), characterized by the intensification of the Azores high and Iceland low pressure systems (Figure II.9a), the meridional SLP gradient reinforces and hence, there is a strengthening and poleward shift of the EDJ (Figure II.9b; Ambaum et al., 2001). The anomalous intense westerlies carry out an increased advection of moist and warm oceanic air masses towards the northeast of the NATL sector, leading to warmer conditions over Scandinavia and occidental northern Russia. At the same time, the enhanced northerly winds over Newfoundland and Greenland result in strong advections of polar air masses, leading to colder conditions over the western region of the basin (Figure II.9c; Pinto & Raible, 2012). Contrary, during periods characterized by anticyclonic circulations located at high latitudes over the NATL (NAO-; Figure II.9d; Buehler et al., 2011; Sillmann et al., 2011), the EDJ weakens and displaces equatorward (Figure II.9e), following the weakened meridional SLP gradient. These conditions favour horizontal advection of cold air over northern Europe and warm advection from the ocean over the western NATL (Figure II.9f).

The EDJ variability also drives the extreme events of temperature over different regions of Europe. Similarly, the occurrence of temperature extremes in Europe has typically been understood in terms of large-scale circulation anomalies. For instance, winter cold spells occur downstream of the anticyclonic circulation anomalies, in the southern and eastern parts of a blocking high (Sousa et al., 2018, 2021). As for warm events, a reinforcement of

the climatological westerlies bring extra warm and moist air from the ocean toward the continent (Andrade et al., 2012; Trigo et al., 2004). Winter warm events have received less attention than cold spells, even when they will become more frequent due to climate change (Seneviratne et al., 2021). Since the EDJ leads the large-scale circulation, some studies have also investigated the dependence of the temperature extremes occurrence on the NATL EDJ structure. As mentioned, blocking systems over the NATL may imply an equatorward or poleward displacement of the westerlies, resulting in different patterns of extreme temperature (Kautz et al., 2022). As representative cases, both winters of 2010 and 2012 experienced extremely cold temperatures under very different EDJ

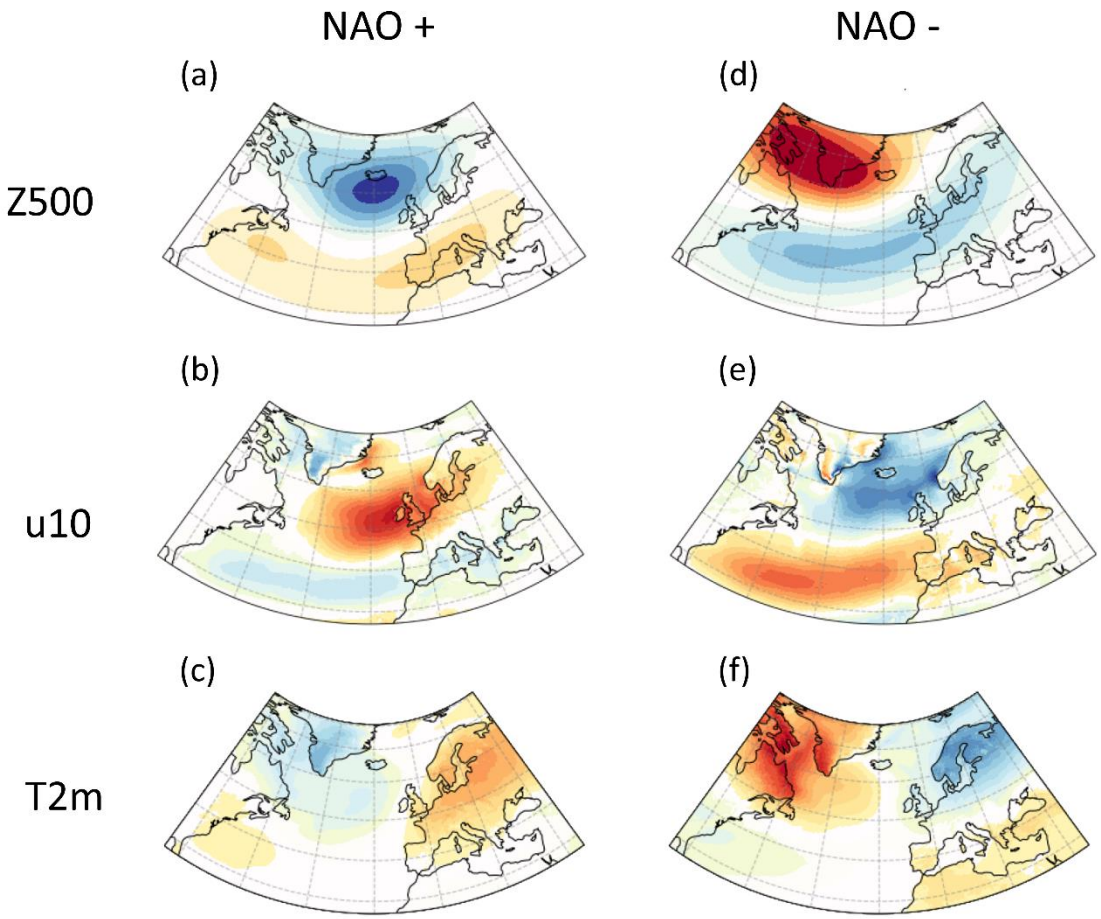

Figure II.9 NAO variability impact on (a, d) geopotential height at 500 hPa ([m], shading is drawn every 50 m from -175 m to 175 m), (b, e) wind speed at 10 m ([ms^{-1}], shading is drawn every 0.25 ms^{-1} from -3 ms^{-1} to 3 ms^{-1}) and (c, f) temperature at 2 m ([K], shading is drawn every 0.5 K from -7 K to 7 K). Left column shows the impacts associated with positive NAO (NAO+) conditions and right column with negative NAO (NAO-) conditions. Figure based on NDJFM, 1979-2001. Modified from Tedesco et al. (2023).

configurations (Santos et al., 2013). The former was characterized by an equatorward shifted EDJ accompanied by a generalized cooling over northern Europe, whereas the latter featured a northerly EDJ and cold temperatures in southern and Eastern Europe. This illustrates a diversity of EDJ configurations associated with extreme events. As EDJ characteristics determine the type of extreme and region affected, this calls for a comprehensive assessment of the specific features of the EDJ that are relevant for the occurrence of regional extremes.

The analysis of the EDJ and its influence on extremes has been typically assessed by considering a single EDJ characteristic individually (i.e. disregarding other aspects of the EDJ structure). Consequently, EDJ impacts on extreme temperature remain poorly characterized, essentially limited to those caused by the sole effect of a single EDJ feature. For instance, Trigo et al. (2004) found that when the EDJ intensity is strong, maximum and minimum temperatures are higher than average over southern and Central Europe and lower than average over Scandinavia. The opposite occurs during blocking situations, which are associated with weakened midlatitude westerlies and shifted EDJs. Differently, Mahlstein et al. (2012) focused on the EDJ latitude and found that the odds of extreme events over Europe are significantly modulated by the EDJ position of the day and some days before the occurrence of the temperature extreme (Figure II.10). More specifically, the probability of experiencing a cold event in central and northern Europe increases when the EDJ is southward displaced, whereas it decreases if it is at central or northern latitudes. Besides intensity and latitude, other EDJ parameters have also been linked to extreme temperatures. For example, Röthlisberger et al. (2016) reported an increased occurrence of cold extremes over western Europe and the Mediterranean Sea for wavy EDJs. The perspective followed by these studies simplifies the assessment of the EDJ influence on temperature extreme events and helps to understand the associated processes. However, due to its complex nature and high variability, the EDJ can rarely be described in terms of a single parameter. Therefore, these single-parameter approaches ignore the combined effects of different relevant features (e.g., latitude, intensity, tilt, etc.), limiting the understanding of impact on the extremes.

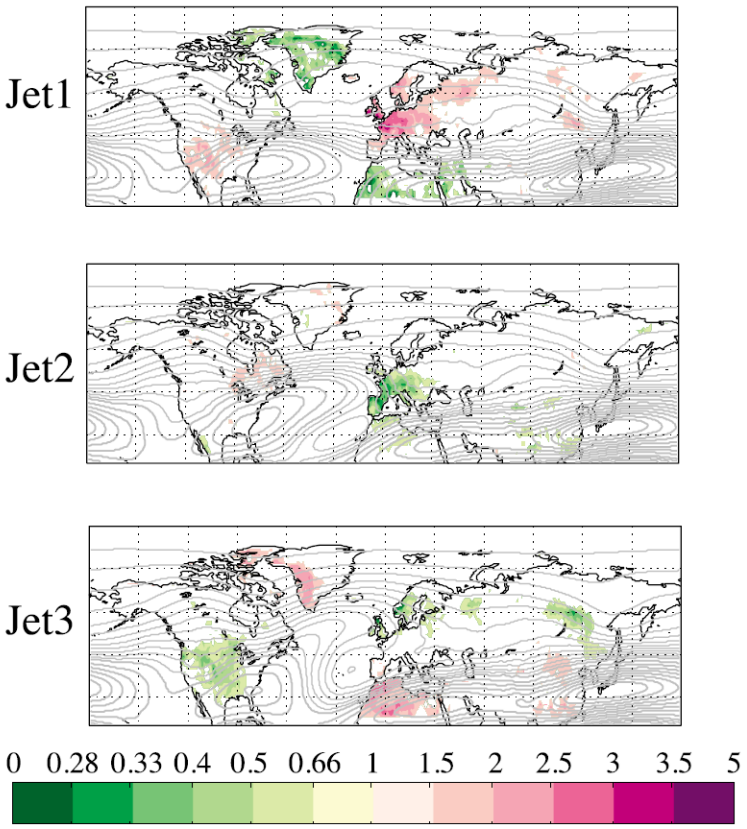

Figure II.10 Areas with statistically significant changes in the odds of cold extremes in DJF for simultaneous southern (Jet1), central (Jet2) and northern (Jet3) EDJs (shaded) (5% quantile). The green colours indicate a reduction and purple colours indicate an increase of the odds of cold extremes. The grey contours show the zonal wind at 200 hPa (drawn every 2 ms^{-1}). Taken from Mahlstein et al. (2012).

- Precipitation

The wintertime precipitation climatology is also dependent on the EDJ structure due to the consequent changes in the advection and convergence of moisture (Hurrell 1995; Osborn et al., 1999). The main responsible of the generation of midlatitudes precipitation are baroclinic waves. As pointed above, they are generated in the western oceanic basins of midlatitudes where the gradients of temperature and moisture become strongest. During their evolution, the disturbances cross the NATL basin following a preferred trajectory, known as storm track (Hurrell & von Loon, 1997), which is influenced by the low-level baroclinicity (Hoskins & Valdes, 1990; Held, 1993; Brayshaw et al., 2009). Figure II.11a shows that the winter storm track climatology follows a similar SW-NE tilted trajectory, but remaining at the poleward flank of the EDJ. This configuration results from the transient eddies crossing the EDJ regions with the strongest divergence and uplift of air masses, needed for their intensification.

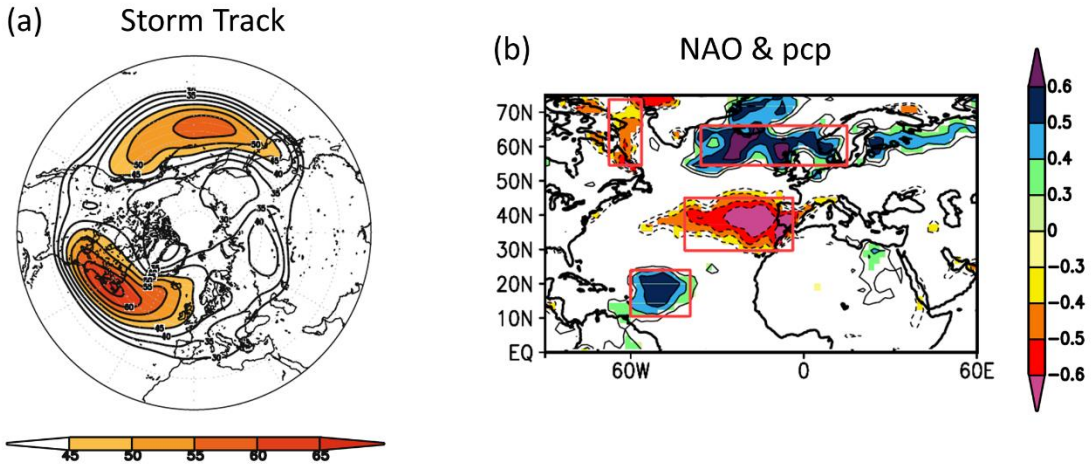

Figure II.11 (a) Climatological winter 500 hPa storm track ([gpm], contours drawn each 5 gpm). Taken from Pinto et al. (2010). (b) Correlation of precipitation and NAO index during winter. The contours start at 0.3 and are drawn every 0.1. Positive correlations are drawn in solid contours and negative in dashed contours. Significant values at 95% confidence level are shaded. Modified from Mariotti & Arkin (2006).

Changes in the EDJ are accompanied by important shifts in the storm track and impact on the regional precipitation over Europe. Similar to the surface temperature, during periods of intense accelerations of the EDJ, the storm track is intensified and deflected poleward (Rogers, 1997; Trigo, 2006). Consequently, the maximum of moisture transports towards the northeast, establishing wetter conditions over Scandinavia and northern Europe and drier over central and southern Europe (Figure II.11b, Hurrell & von Loon, 1997). Conditions are reversed under periods of weak and equatorward shifted EDJs.

II.2.3 Drivers of the EDJ

A great fraction of the NATL EDJ variability is driven by high frequency and chaotic dynamical processes of the atmosphere (internal or unforced variability; Lorenz, 1963). However, remote external mechanisms can also imprint lower-frequency variability on the NATL EDJ, forcing a more predictable signal against the complex unpredictable background (Madden, 1976). This interrelation between climate anomalies over vast distances is known as teleconnection. Teleconnection pattens consist of recurrent and persistent large-scale

circulation anomalies that explain a substantial part of the atmospheric and oceanic evolution (Barnston & Livezey, 1987; Marshall et al., 2001; Wallace & Gutzler, 1981). The teleconnections belong to the natural variability of the system, and can be both internally generated or externally activated by certain phenomena, which are known as drivers. Below, we introduce the most relevant drivers and associated teleconnections of the literature detected to influence wintertime interannual variability of the EDJ.

- Remote Drivers and associated Teleconnections

I. El Niño-Southern Oscillation

El Niño-Southern Oscillation (ENSO) is the primary mode of interannual climate variability (Trenberth, 1997), consisting in an ocean-atmosphere coupled phenomenon in the equatorial Pacific Ocean (Bjerknes, 1969). Under climatological conditions, the strong tropical trade winds push the warm shallow water westwards, leading to the Warm Pool in the west of the basin and upwelling of cold water in the east. This configuration establishes zonal gradients of sea surface temperature (SST) and SLP between the western and eastern Pacific, which in turn allows to maintain the easterly winds. Departures from this climatological state may lead to an SST warming over the eastern and central Pacific, known as El Niño, when the upwelling is reduced due to the weakening of the trade winds. Reversed conditions, characterized by an enhancement of the trade winds and the upwelling, lead to a strong cooling of the SST (La Niña). The fluctuation between warm and cold phases ranges from 3 to 7 years, with the SST anomalies peaking on the boreal winter (Rasmusson & Carpenter, 1982).

The zonal migration of the SST maximum shifts the regions of deep convection, where great amount of energy is released toward the atmosphere. As a consequence, the global circulation is modified. The main impacts of ENSO occur around the Pacific but remote regions, such as the NATL-European sector, can also be affected (Brönnimann, 2007). Overall, there are three main dynamical mechanisms connecting ENSO and the NATL EDJ. In the troposphere, the deep convection over the tropics leads to the generation of two upper-level anticyclonic circulations at both sides of the equator (Gill, 1980; Matsuno, 1966). These anomalies produce extratropical propagation of Rossby waves by the

modification of the planetary vorticity of the flow. Consequently, anomalous development and propagation of synoptic eddies embedded in the westerly flow may be enhanced, and therefore, influence the NATL (Drouard et al., 2013; 2015; García-Serrano et al., 2011; Li & Lau, 2012; Raible et al., 2004).

Extratropical waves are characterized by alternating quasi-stationary high and low circulations and travel poleward from the tropics following an eastward arched trajectory (Hoskins & Karoly, 1981). Depending on ENSO morphology and location, different planetary waves can be activated. One of them is the Pacific-North American Pattern (PNA), which presents four action centres connecting the North Pacific and the western NATL. During the positive phase, the Aleutian low is deepened and the westerly flow is extended over the eastern Pacific and western North America. Contrary, the Pacific EDJ remains contracted at the western of the basin during the negative PNA phase, due to the disruption of the flow led by the high pressures over Aleutian Islands (Pinto et al., 2011). Although at interseasonal and interannual scales it is mainly driven by ENSO (Franzke et al., 2011; Mo & Livezey, 1986), this teleconnection can be also triggered by internal variability processes (Johnson & Feldstein, 2010). Another teleconnection pattern that modulates the Northern Hemisphere variability is the Tropical Northern Hemisphere (TNH; Mo & Livezey, 1986; Trenberth et al., 1998). Contrary to PNA, this teleconnection can be only activated by ENSO and is related to the interannual and longer variabilities. The wave train presents similar characteristics to PNA, with four centres of action, but slightly eastward shifted (Barnston & Livezey, 1987), in such a way that both teleconnections are out of phase (Soulard et al., 2019). Previous studies have proposed that ENSO events with the SST anomalies shifted to the east of the basin are related to TNH, while those presenting the anomalies at the centre and east of the Pacific are associated with PNA, depending on the location of the Rossby wave source and the mean flow configuration (Yu et al., 2015).

Although not driven by the equatorial SSTs, the North Pacific Oscillation (NPO, Walker & Bliss, 1932) can also influence the downstream climate variability by modulating the impact of ENSO in Northern Hemisphere midlatitudes. Depending on the NPO phase, the atmospheric response to ENSO can be enhanced or suppressed generating different impact patterns that reach the extratropics (Gershunov & Barnett, 1998; Pierce, 2002; Yu & Sun, 2020). During El Niño events, the Aleutian low deepening is enhanced by a positive NPO

phase, leading to a reinforcement of a PNA-like signal. Contrary, a negative NPO phase offsets the deepening, leading to a different pattern into the extratropics (Gershunov & Barnett, 1998; Pierce, 2002). Conjunctly, the three teleconnections, PNA, TNH and NPO, explain around one third of the variance of the Northern Hemisphere wintertime flow (Mo & Livezey, 1986).

The deep convection also activates the atmospheric bridges connecting the tropical oceanic basins zonally by perturbing the Walker cells. The equatorial inter-basin link leads to the further activation of the Atlantic Hadley cell which impact on the NATL circulation (Wang et al., 2004). The ENSO signal also modulates the wave activity into the stratosphere producing wind anomalies (Manzini, 2006), which then propagate downward reaching the troposphere and impacting on the NATL region (Baldwin & Dunkerton, 2001; Domeisen et al., 2019; Polvani et al., 2017). Independently from the mechanism, the ENSO impact over the NATL circulation is common for late winter. In general, the canonical signal of El Niño episodes encompasses disrupted EDJs, characterized by an equatorward shifting (Figure II.12a). Contrary, La Niña events are related to poleward shifted EDJs (Pozo-Vázquez et al., 2005; Zhang et al., 2015). Although this impact on the NATL EDJ is robust in models and consistent with observations (Cagnazzo & Manzini, 2009), multiple studies argue that the teleconnection is non-stationary (Ivasić et al., 2021; Jimenez-Esteve & Domeisen, 2020; López-Parages et al., 2015; Rodríguez-Fonseca et al., 2016).

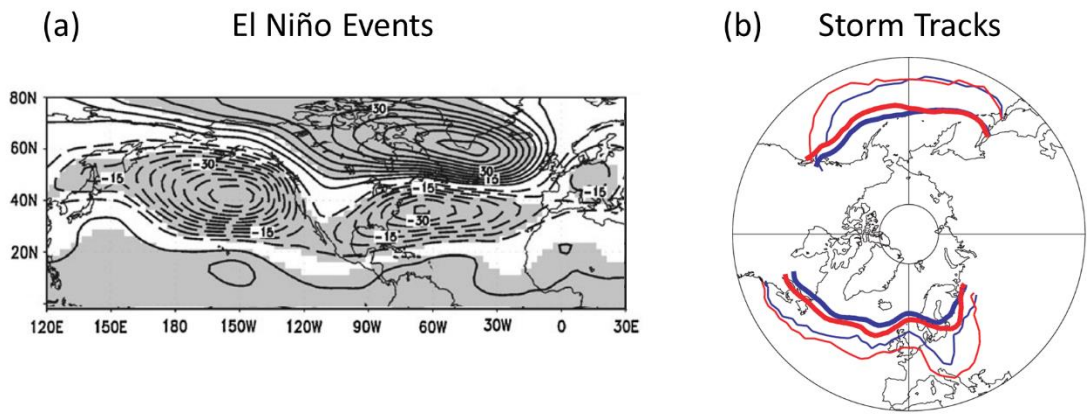

Figure II.12 Main impacts regarding the ENSO tropospheric pathway and the PVS variability. (a) Regression map of geopotential height at 500 hPa onto ENSO ([m], solid contours represent positive values and dashed contours negative). Statistically significant regions at 98% confidence level are shaded. (b) Composite of storm tracks latitudes in the Atlantic and Pacific Oceans during weak (thick read line) and strong (thick blue line) vortex conditions. Thin lines indicate the lowest latitude at which a cyclone is expected. Taken from García-Serrano et al. (2011) and Baldwin & Dunkerton (2001), respectively.

II. The Stratospheric Polar Vortex

The wintertime polar stratospheric circulation is dominated by intense westerlies that encircle the North Pole. This circulation, known as stratospheric polar vortex (SPV), is established due to the strong negative meridional temperature gradient between midlatitudes and the winter pole as there is no solar heating at high latitudes in that season (Waugh & Polvani, 2010). The vortex starts to develop in autumn and is maintained until the following spring, when the sunlight comes back to the pole and the characteristic easterly mean flow of summer is established. The intensity of the polar vortex presents a high variability, from very strong to disrupted westerlies. The Sudden Stratospheric Warmings (SSW) are the major events of the vortex variability. They are depicted by large decelerations of the winds led by a sustained dissipation of planetary wave activity propagating from the troposphere. When waves break in the high-latitude stratosphere, they transfer easterly momentum to the mean flow (Baldwin et al., 2021). The transferred momentum results in the vortex deceleration but also poleward flow and downwelling over the Arctic that leads to a rapid adiabatic warming over the pole (Baldwin et al. 2021). Consequently, the meridional temperature gradient is reduced and the zonal flow, following the geostrophic balance, may be reversed. There are many phenomena that may modulate the stratospheric wave activity such as ENSO, solar activity or equatorial stratospheric circulation.

The vortex variability often propagates downward reaching the troposphere, where the anomalies can remain up to 60 days (Baldwin & Dunkerton, 2001). In particular, an SSW is typically followed by anomalously weak westerlies in the extratropical troposphere, and the opposite for extreme strong vortex events (Figure II.12b). The signature appears as a meridional shift of the EDJ in the NATL, with poleward shift under strengthened vortex conditions and equatorward shifted for a weakened vortex (Kodera et al., 1996; Maycock et al., 2020). Although the signal is well reported, the underlying downward mechanisms are only partly understood (Gerber et al., 2012).

III. Arctic Amplification

In recent decades, the Arctic near-surface temperature has warmed more than twice than the global averaged temperature (Holland & Bitz, 2003; Screen & Simmonds, 2010). This phenomenon, Arctic Amplification (AA), presents its maximum during autumn over the Arctic Ocean (Cohen et al., 2018) and is driven by multiple and complex mechanisms such as sea ice loss, cryospheric and cloud feedbacks and modifications in the oceanic and atmospheric heat transport (Cohen et al., 2020; Taylor et al., 2022). Several studies have focused on the potential impact the AA may have on the midlatitude circulation and weather extremes. The increment of heat release into the atmosphere and consequent reduction of the meridional temperature gradient can induce an EDJ response characterized by a weakening and equatorward shift (Francis & Vavrus, 2012; Ronalds & Barnes, 2019; Vihma, 2014). In addition, these studies suggest that the EDJ may become wavier, but others do not support this relation (Barnes, 2013; Hassanzadeh et al., 2014; Screen & Simmonds, 2013). In reality, the AA influence on midlatitudes is a subject of active debate (Screen, 2017; 2018).

Also, recent research indicates that regional Arctic warming and sea ice melting can induce regional responses in the weather of midlatitudes. Particularly, temperatures at eastern North America and northern Europe are influenced by sea ice and temperature anomalies around Greenland (Cohen et al., 2020; Vihma et al., 2020). However, there is a lack of consensus between observational and modelling analysis on the response to pan-Arctic warming and sea ice anomalies. Observational studies noted some simultaneity between winter AA and extreme cooling over midlatitudes in recent decades. However, modelling experiments and recent observational studies do not find that signal and attribute the observed cooling to internal variability (Blackport et al., 2019; Blackport & Screen, 2020; Cohen et al., 2023).

IV. Northern Hemisphere Snow Cover

Regional wintertime climate variability can also respond to the hemispheric land surface state, concretely, to the snow cover, which acts as a low-level thermal forcing. The main snow cover land masses of the Northern Hemisphere are the North America and Eurasia ones. Both regions present important impacts on local and remote climates, especially,

during the spring snow melt and autumn snow fall (Brown et al., 2010). Anomalous snow cover can modify the albedo and hence, unbalance the surface heat and moisture equilibrium leading to potential impacts on atmospheric circulation.

During the last decades efforts have been primary focused on studying the autumn snow cover over Eurasia, Siberia and Tibetan Plateau, since diverse impacts have been reported all over the hemisphere (Chen et al., 2020, 2021; Gong et al., 2002, 2003; Mote & Kutney, 2012). A particularly robust impact has been detected for an increment of autumn snow cover on the negative phase of the wintertime NAO (Lin & Wu, 2011; S. Liu et al., 2022; Qian et al., 2019). The increased snow cover can excite anomalous upward-propagating planetary wave activity from the surface into the stratosphere, leading to a weakening of the polar vortex and the subsequent disruption of the NATL EDJ. Although the North American snow cover has received less attention, the persistence of the winter snow cover over the high and extensive Rocky Mountains has been detected to influence local and remote climate too (Dickson & Namias, 1979; Walland & Simmonds, 1996). Increased North American snow cover during wintertime may enhance and shift eastward the low-level stationary wave patterns, leading to a southward shift of the maximum temperature gradient region and the storm track. The consequent modification of the transient eddy activity may lead in turn to a weakening, equatorward shift and downstream development of the EDJ by eddy-mean flow interaction (Li et al., 2020; Sobolowski et al., 2007, 2010). Further, model experiments report a simultaneous negative NAO pattern impact under a forcing comprising the whole northern hemisphere winter snow cover (Cohen & Entekhabi, 2001; Gastineau et al., 2023; Vavrus, 2007).

- Atlantic Drivers and associated Teleconnections

V. Atlantic Meridional Overturning Circulation

The NATL Ocean circulation consists of a complex set of currents driven by the density differences of the water parcels. The transport of warm and salty water northward along the Atlantic Ocean surface, and returning of very dense low temperature and saline water southward over the seabed, is summarized as the Atlantic Meridional Overturning Circulation (AMOC, Foukal & Chafik, 2022). At polar latitudes, over the deep-water

formation regions, the water sinks from the ocean surface into the deep ocean due to the strong density change, establishing the movement of the circulation. The AMOC variability consists of an enhancement or weakening of the current such that, during the positive phase, the increased poleward heat transport produces a warming over the subpolar region, near Terranova (Figure II.13a). These changes at the oceanic surface modify the overlying atmospheric baroclinicity (Sampe et al., 2010) leading to adjustments of the mean flow and the storm track mean state and variability (Brayshaw et al., 2009; 2011; Wilson et al., 2009).

There is evidence that the AMOC can impact on the NATL atmospheric circulation from monthly to decadal timescales. Several climate model studies show that the AMOC intensification and the associated subpolar SST warming during winter lead to a weakening of the EDJ, generally captured by a negative NAO (Figure II.13a, Gastineau et al., 2013, 2016; Gastineau & Frankignoul, 2012). The atmospheric response may result from the decrease of the lower tropospheric baroclinicity over the principal region of transient eddy generation (Gastineau & Frankignoul, 2012), leading to a weakening of the meridional eddy heat flux and a weakening of the storm track activity downstream (Gervais et al., 2019).

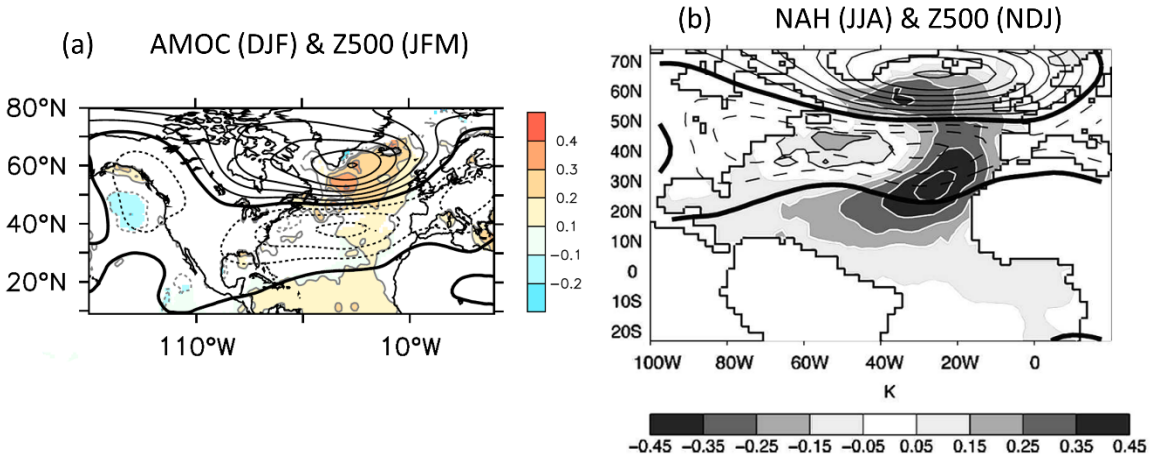

Figure II.13 North Atlantic drivers impact on NATL circulation. (a) Patterns of the first mode of maximum covariance analysis between DJF SST ([K], shading and gray contours) and JFM Z500 ([m], contours drawn every 4 m with positive values in solid lines and negative in dashed). Modified from Gastineau & Frankignoul (2015). (b) Patterns of the first mode of maximum covariance analysis between NDJ Z500 ([m], contours drawn every 5 m with positive values in solid lines and negative in dashed) and JJA SST ([K], positive values are indicated with white contours and negative with black). Taken from Frankignoul & Kestenare (2005).

VI. North Atlantic Horseshoe

In addition to the response to near-simultaneous SST forcing, the NATL atmospheric circulation may also be affected by highly lagged oceanic signals. Observations show that the late summer NATL SST Horseshoe (NAH) has significant influence on the wintertime extratropical circulation (Czaja & Frankignoul, 1999; 2002; Gastineau et al., 2012; 2013; Saunders & Qian, 2002; Wen et al., 2005). The NAH is the main oceanic variability mode of summer and fall seasons (Czaja & Frankignoul, 2002; Wen et al., 2005) characterized by a warming in the subpolar and eastern tropical NATL SST during its positive phase (Figure II.13b). Although it becomes most energetic during the warm season, the atmosphere is not affected possibly due to the state of the background mean flow. However, as the SST anomalies persists until early winter, the atmospheric conditions during fall and early winter allow the upward release of the oceanic turbulent heat flux and hence, weaken and shift the EDJ equatorward (Czaja & Frankignoul, 1999, 2002; Wen et al., 2005). There is evidence that the NAH persistent SST anomalies can also impact on the winter circulation by the alteration of the western lower-tropospheric baroclinicity. The modification of the stationary and transient eddies generation can induce a barotropic response on the EDJ by eddy-mean flow interactions (Cassou et al., 2004; Deser et al., 2007; Nie et al., 2019; Peng et al., 2003).

II.2.4 EDJ Projections

The EDJ response to an atmospheric increase of GHG concentrations has been a topic of interest since the first phases of the Coupled Models Intercomparison Project (CMIP, Eyring et al., 2016). A robust consensus has been found across models and generations on the poleward shift of the EDJ when considering annual and zonal averages (Barnes & Polvani, 2013; Hay et al., 2022; Oudar et al., 2020; Peings et al., 2018; Shaw, 2019). However, the picture changes for the winter season and the NATL sector. The NATL EDJ response to climate change presents a seasonal cycle characterized by a poleward shift from spring to autumn, peaking in summer, but without a clear latitudinal displacement in winter (black boxplot in Figure II.14b; Barnes & Polvani, 2015; Oudar et al., 2020) Climate

change projections of the EDJ latitude in winter present a strong inter-model spread, spanning from poleward to equatorward responses. This behaviour has sometimes been interpreted from the multimodel mean perspective as an increasing presence of the EDJ on its central latitude in the future (Dorrington et al., 2022; Harvey et al., 2023; Peings et al., 2018).

In addition to the latitudinal position, the spatial structure of the EDJ changes in the future, showing a squeezing and strengthening of the jet core region with a reduction of the zonal wind on the poleward and equatorward flanks (Figure II.14d; Peings et al., 2018; Oudar et al., 2020; Oudar et al., 2020b; Harvey et al., 2023). However, there is no consensus either on this reinforcement of the EDJ, as some studies find it insignificant or do not detect

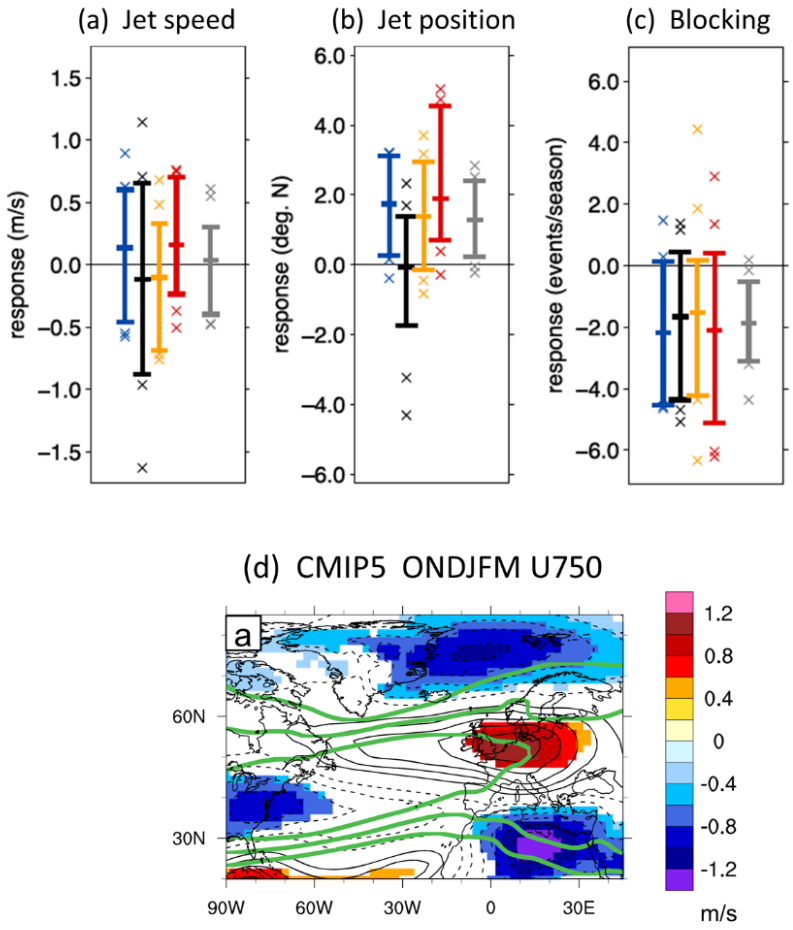

Figure II.14 Long term seasonal changes in the NATL sector of (a) jet speed, (b) jet position and (c) blocking frequency (OND (blue), JFM (black), AMJ (yellow), JAS (red), Annual (grey). Modified from Barnes & Polvani (2015). (d) CMIP5 multimodel mean of future minus present 750 hPa zonal wind ([ms^{-1}], positive changes are shown in solid contours and negative in dashed). Shading indicates areas with significant changes at 95% confidence level. Present-day climatology is drawn in green contours ([ms^{-1}], contour interval of 3 ms^{-1}). Taken from Peings et al. (2018).

it (Figure II.14a and d; Barnes & Polvani, 2013; Barnes & Polvani, 2015; Dorrington et al., 2022). Apart from the changes in the typically studied EDJ features (latitude and intensity), variations in other aspects have also been detected. An eastward elongation over Europe (Harvey et al., 2020; 2023; Ulbrich et al., 2009) and increased zonalization (Dorrington et al., 2022; Peings et al., 2017) have been reported since early CMIP phases. Generally, these changes have been inferred from the analysis of EDJ-related variables such as the zonal wind (Harvey et al., 2020) or European blocking frequency (Figure II.14c; Barnes & Polvani, 2015; Schiemann et al., 2020). Moreover, although a few studies have also analysed these features from the multimodel perspective, little attention has been paid to the inter-model spread.

The uncertainties of the EDJ climatological response to climate change are determined by multiple factors such as changes in large-scale phenomena, since different drivers can lead to different responses of the EDJ mean state. A well-known example is the 'tug-of-war' between the strong upper tropospheric tropical warming (or Tropical Amplification, TA) and the rapid near-surface AA. Both phenomena imply changes in the air temperature distribution, leading to a strengthening of the upper tropospheric negative meridional temperature gradient and a weakening of the lower one, respectively. Consequently, the TA and AA can potentially shift the EDJ poleward and equatorward, respectively (Barnes & Simpson, 2017; Butler et al., 2010; Deser et al., 2015; Oudar et al., 2017). There is high confidence that both regions warm at faster rates than the global mean under GHG increases. As TA and AA act simultaneously, the combined effect can result in poleward or equatorward EDJ migrations, depending on which one dominates in each model. In turn, these migrations can lead to further changes in the meridional gradients (Woollings et al., 2023). Something similar happens for the projected changes in SST. There is a large agreement across the model projections on a global heterogeneous warming of the oceans, particularly more pronounced in the tropics and Northern Hemisphere (Xie, 2020). However, this generalized warming presents a striking anomaly in the NATL ocean. Projections of the NATL subpolar gyre region indicate a lack of warming or even a cooling, a feature known as the NATL Warming Hole (WH). The NATL WH modifies the western oceanic baroclinicity, which can affect the storm track and the EDJ latitude and intensity through thermal wind responses (Bellomo et al., 2021; Gervais et al., 2019). An EDJ

eastward extension has also been linked to the baroclinicity strengthening (Ulbrich et al., 2009; Harvey et al., 2015; Woollings et al., 2012). Although the NATL WH is a robust aspect of climate change, the magnitude of the change presents a high spread across models, which propagates to the EDJ response (Woollings et al., 2012).

The uncertainties of the EDJ projections further increase when not only the magnitude but also the sign of the driver's response to climate change is uncertain. For instance, the stratospheric polar vortex is projected to reinforce or weaken under increasing GHG concentrations depending on the model (Manzini et al., 2018; Zappa & Shepherd, 2017). Non-stationary responses of the drivers through the winter would further increase the uncertainty of EDJ projections by inducing seasonally-varying responses. For the tropical Pacific SSTs, it is well established that the teleconnections linking the Pacific and Atlantic basins are different in early and late winter, yielding intraseasonal influences on the EDJ (Abid et al., 2021; Ayarzagüena et al., 2018; Herceg-Bulić et al., 2023; Sung et al., 2013). Little attention has been given to study intraseasonal effects of other drivers on the NATL circulation (Cassou, 2008). Finally, the presence of model biases is an additional source of uncertainty. For example, models often present systematic biases in the representation of the EDJ latitudinal position, which tends to be equatorward shifted compared to observations (Barnes & Polvani, 2013; Bracegirdle et al., 2022). This may potentially contribute to the spread in the projections of the NATL circulation (Oudar et al., 2020).

III. Scientific Questions

The aim of this PhD thesis is to improve the understanding of the present and future climate variability of the North Atlantic EDJ, particularly for the winter.

To achieve this goal, a new multiparametric methodology is developed for capturing different aspects of the EDJ variability and complex structures that are overlooked under the traditional approaches based on single parameters or 2D fields. Under this new perspective, different topics that have not been extensively investigated yet or that do not show a consensus among previous studies are analysed in detail.

Concerning present, the specific questions to be addressed are:

a) Is the multiparametric perspective able to provide a better description of the EDJ recurrent states than the previous descriptions? Can we better understand the transitions from one recurrent state to another?

b) What is the relation between the EDJ parameters and the temperature extreme events? Is the relationship between the EDJ and the extremes better understood with the multiparametric perspective than with the traditional one?

c) What are the main EDJ drivers? How much variability of the EDJ parameters are they able to explain? What are the mechanisms followed by the drivers to impact on the EDJ?

Concerning future, the specific questions to be addressed are:

d) How will climate change affect the mean state of the EDJ? Given that models present high uncertainties in the EDJ projections, can our multiparametric perspective help to understand these uncertainties?

The above questions are addressed in the following Chapters. Chapter V introduces in detail the new EDJ parameters framework. Likewise, the relationship between the variety of EDJ structures and the specific combination of parameters is presented. By using the EDJ parameters, Chapter VI explores the recurrent states of the EDJ as well as their persistence and potential transitions (Barriopedro et al., 2023). In Chapter VII, the occurrence of temperature extreme events over different regions of Europe is explained in terms on EDJ structures, linking univocally specific EDJ parameter sets to specific extremes and regions (García-Burgos et al., 2023). Chapter VIII dissects the interannual variability forced by some drivers. Specific analyses are undertaken for explaining the interannual variability of each EDJ parameter as well as the associated mechanisms. In Chapter IX, the future projections and uncertainties of the EDJ parameters mean state are quantified. The EDJ latitudinal behaviour is carefully examined, relating its future uncertainties to those of different drivers (García-Burgos et al., 2024). Finally, Chapter X summarizes the main conclusions of the thesis and provides some insights for future work.

IV. Data and Methodology

IV.1 Data

To address the goals described in the previous section, two types of data have been utilised: reanalysis data and model simulation output. The main characteristics of both datasets are described in this section.

IV.1.1 Meteorological Reanalyses

We have used two reanalysis products for atmospheric variables: National Centers for Environmental Prediction / National Center for Atmospheric Research (NCEP/NCAR) reanalysis (Kalnay et al., 1996) and ERA5 (Hersbach et al., 2020) provided by the European Centre for Medium-Range Weather Forecasts. Whereas the former has been employed in the first analyses of this thesis (Chapters V, VI, VII), the latter has been used in the most recent ones (Chapter VIII and IX), and also to verify and give robustness to the results computed with the NECP/NCAR reanalysis (Chapter V and VII).

We have used daily fields of horizonal wind components between 1000 and 200 hPa, vertical wind component between 1000 and 850 hPa, air temperature between 1000 and 200 hPa, 2m minimum (TN) and maximum (TX) temperature, 500 hPa geopotential height (Z500), cloud cover, and total radiative budget from the NCEP/NCAR reanalysis with 2.5° × 2.5° horizontal resolution. We have also utilized monthly fields of air temperature at 850 and 100 hPa, geopotential height at 500 and 200 hPa and turbulent flux.

Daily data of zonal and meridional wind, air temperature and geopotential height at different levels between 1000 and 150 hPa have been retrieved from ERA5 reanalysis at 0.75° x 0.75° horizontal resolution. Daily averages of any variable have been calculated by averaging four analysis values at 00:00, 06:00, 12:00 and 18:00 for each day. TN and TX have been computed as the minimum and maximum, respectively, from the hourly temperature data at the surface for each day. In addition, other single level variables such

as surface sensible and latent turbulent fluxes and potential temperature at the dynamical tropopause (2 Potential Vorticity Units; 2PVU) have been also used. We have also utilized monthly fields of air temperature at 850 and 100 hPa.

Regarding the SSTs, the monthly values were obtained from the Hadley Centre Sea Ice and Sea Surface Temperature dataset provided by the UK Met Office (HadISST; Rayner et al., 2003). HadISST1 construction is based on the interpolation of the Met Office Marine Data Bank (MBD) observations. The field is completed with the historical observations of the International Comprehensive Ocean-Atmosphere Data Set (ICODAS; Woodruff et al., 2011) in those grid points were MBD is not available. Finally, monthly timeseries of the North America [130°-70°W, 40°-70°N] snow cover extension during wintertime (DJF) is obtained from Rutgers University (Robinson et al., 1993).

IV.1.2 CMIP6 simulations output

Chapter IX investigates the future mean changes in NATL EDJ forced by anthropogenic climate change. Its future evolution is assessed by comparing the EDJ in simulations of present and future climate. The simulation outputs are provided by the 6th phase of the Coupled Model Intercomparison Project (CMIP6; Eyring et al., 2016). The objective of CMIP is to better understand the climate change as a consequence of natural variability or in response to changes in the radiative forcing. Consequently, it has become the central element of international assessment of climate change. To do so, CMIP project uses a multimodel context, comparing several state-of-the-art models by performing common experiments to all of them. These models are coupled models, characterized by a coupling between their atmospheric models and a dynamic ocean, a simple land surface and thermodynamic sea ice (Meehl et al., 1997).

In order to participate in the CMIP6 project, each model must simulate a handful of baseline experiments. These experiments allow to establish the model particularities such as its ability to simulate the current climate and the variability at different timescales or how they respond to climate change. Among all of the baseline experiment, we use the historical one, which simulates the climate from 1850 until present (2014), to characterize the EDJ in the present climate. Historical simulations are forced by evolving externally imposed forcing such as solar variability, volcanic aerosols or changes in atmospheric

composition caused by human activities, namely GHGs and aerosols. These forcings are based on the observations.

Apart from the core experiments, a range of CMIP6-Endorsed projects are organized to reach the CMIP6 goals. One of these projects is the ScenarioMIP which aims to investigative the impact of plausible future scenarios on physical and human systems, and on mitigation and adaptation options (Eyring et al., 2016). Similarly, it aims to assist the quantification of the projection uncertainties basing on model ensembles. To do so, ScenarioMIP establishes a set of future-long term experiments, each of them generated by a specific compatible combination of the representative concentration pathways (RCPs) and the shared socioeconomic pathways (SSPs; Figure IV.1). The former describe the pathways leading to radiative forcing levels at the top of the atmosphere of 8.5, 7.0, 4.5, 2.6 and 1.9 W/m^2 by the end of the century (IPCC, Lee et al., 2021). The latter are designed to span a relevant range of uncertainty in societal futures depending on demographic, economic, technological, social or environmental factors (O'Neill et al., 2017).

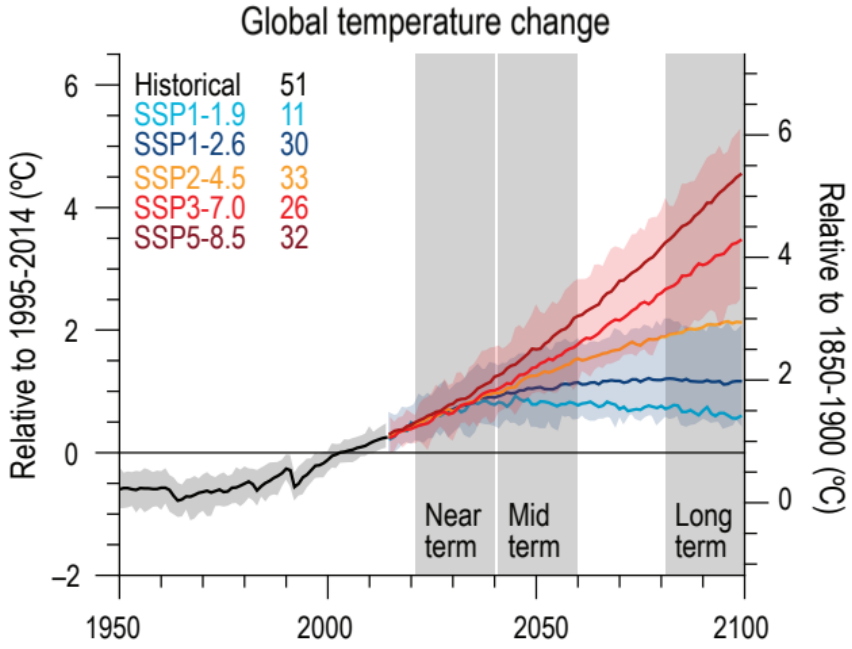

Figure IV.1 Indicator of global climate change from CMIP6 historical and scenario simulations. Global surface air temperature changes relative to the 1995-2014 average (left axis) and relative to the 1850-1900 average. averages over the CMIP6 simulations, the shadings around the SSP1-2.6 and SSP3-7.0 curves show 5-95% ranges, and the numbers near the top show the number of model simulations used. Taken and modified from IPCC (Lee et al., 2021) Chapter IV.

Since we are interested in detecting the signal of anthropogenic climate change emerging against the background of natural variability, we considered the SSP5-8.5 scenario to characterize the future climate EDJ (O'Neill et al., 2016). The SSP5-8.5 scenario represents a fossil-fuelled developed future characterized by high challenges in mitigation and low in adaptation. The latter is the consequence of developing low vulnerable societies with strong investment in technologic, energetic, economic and societal development, based on a strong reliance and dependence on CO_2 emissions (Riahi et al., 2017). Although this scenario is highly unlikely, due to its driving specific circumstances, it presents the strongest and most identifiable climate change signal among the different scenario experiments (IPCC, Lee et al., 2021).

Table IV.1 CMIP6 models included in this thesis.

Model Version	Ensemble Member	Atmospheric Model Resolution (Lon, Lat, Levels)	Top Level	Reference
BCC-CSM2-MR	r1i1p1f1	1.125° x 1.125 L46	1.46 hPa	Wu et al. (2019)
CAMS-CSM1-0	r2i1p1f1	1.125° x 1.125 L31	10 hPa	Rong et al. (2018)
CanESM5	r1i1p2f1	T63L49	1 hPa	Swart et al. (2019a)
CESM2	r1i1p1f1	1° × 1° L32	40 km	Danabasoglu et al. (2020)
CESM2-WACCM	r1i1p1f1	1° × 1° L70	150 km	Danabasoglu et al. (2020)
CMCC-CM2-SR5	r1i1p1f1	1.25° x 0.9° L30	~2 hPa	Cherchi et al. (2019)
CMCC -ESM2	r1i1p1f1	1.25° x 0.9° L30	~2 hPa	Cherchi et al. (2019)
CNRM-CM6-1	r1i1p1f2	T127 91L	78.4 km	Voldoire et al. (2019)
CNRM-ESM2-1	r1i1p1f2	T127 91L	78.4 km	Séférian et al. 2019)
EC-Earth3	r1i1p1f1	TL255 L91	0.01 hPa	Döscher et al. (2022)
EC-Earth3-Veg	r1i1p1f1	TL255 L91	0.01 hPa	Döscher et al. (2021)
FGOALS-g3	r1i1p1f1	2° x 2° L26	2.19 hPa	Boucher et al. (2020)
HadGEM3-GC31-LL	r1i1p1f3	N96 L85	85 km	Ridley et al. (2018)
INM-CM4-8	r1i1p1f1	2° x 1.5° L21	0.01 sigma	Volodin et al. (2019)
INM-CM5-0	r1i1p1f1	2° x 1.5° L73	0.2 hPa	Volodin et al. (2019)
IPSL-CM6A-LR	r1i1p1f1	N96 L79	80 km	Boucher et al. (2020)
MIROC6	r1i1p1f1	T85 L81	0.004 hPa	Tatebe et al. (2019)
MIROC-ES2L	r1i1p1f2	T42 L40	3 hPa	Hajima et al. (2020)
MPI-ESM1-2-HR	r1i1p1f1	T127 L95	0.01 hPa	Müller et al. (2018)
TaiESM1	r1i1p1f1	1.25° x 0.9° L30	~2 hPa	Lee & Liang (2020)
UKESM1-0-LL	r1i1p1f2	N96 L85	85 km	Tang et al. (2019)

The EDJ changes are assessed for a multimodel CMIP6 ensemble composed of 21 models (Table IV.1). For each individual member, the EDJ changes are obtained from the comparison between the climate at the end of 21st century, defined as the 2069-2099

mean of the SSP5-8.5 scenario simulations, and the one of the historical period, defined as the 1979-2009 mean in the historical simulations.

The meteorological variables used for the computation of the EDJ parameters and 2D frequency field include the daily 850 hPa zonal wind. For the evaluation of the changes in air temperature and zonal wind at 1000-1 hPa and sea surface temperature, we use monthly means. All simulated data have been linearly interpolated to a common regular grid with 2.5° × 2.5° horizontal resolution before performing any additional computations.

IV.2 Methodology

The methodological techniques followed to obtain the main results of the PhD thesis are explained below. The most important method developed in this PhD thesis is the novel algorithm for computing the main EDJ features. Due to its relevance for this work, it is described in detail in Chapter V.

IV.2.1 Dynamic Tools

The analysis of the mechanisms by which the large-scale drivers impact on the EDJ constitute an essential part of the Chapter VIII. In this section, the dynamic tools are introduced focusing on the two analysed topics: the wave activity propagation and the baroclinicity.

a. Wave Activity Propagation

The EDJ variability is intimately related to the wave activity since the eddies and the mean flow are continuously interacting. For instance, the EDJ acts as a waveguide for the propagation of the eddies (Branstator, 2002; Wirth et al., 2018). Here, we focus on the study of the wave activity propagation of transient eddies in extratropical latitudes. To investigate the propagation in the horizontal plane, we choose the three-dimensional **E**-vector tool.

- Transient Wave Activity

Some authors (Hoskins et al., 1983; Trenberth, 1986) developed expressions for studying the three-dimensional propagation of the transient eddies, defined as a departure

of the time mean. Previous studies (Hoskins et al., 1983), define the low-frequency (background, †) and transient eddy (′) components of the fields applying respectively, a 10-day low-pass and a 2-6 days band-pass filter, respectively. Here, we use the expression obtained by Trenberth (1986) to characterize the transient eddies, namely, the **E**-vector. Equation IV.2.2 shows the expression of the horizontal components of the **E**-vector:

$$\boldsymbol{E} = \left(\frac{1}{2}(v'^2 - u'^2)\,, -u'v'\right) \qquad \text{(IV. 2.2)}$$

Eddy components are obtained using a 2-6 day Butterworth filter (Butterworth, 1930).

E-vector provides information on the wave propagation with its arrows pointing approximately in the direction of the propagation of wave energy relative to the time-mean flow. In Figure IV.2, the eastward pointing arrows located in middle-latitudes indicate eastward propagating wave activity. Further, as baroclinic waves transport momentum in the opposite direction of wave propagation (Equation IV.2.2; Hoskins et al., 1983), the convergence and divergence of **E**-vector inform on the wave forcing on the mean flow. An important convergence of momentum results around the jet stream region in the NATL, with arrows deflecting equatorward between 25° and 45°N, and poleward above 60° (Figure IV.2). At these latitudes the eddies move outside the region of generation, especially towards the subtropics, where dissipate. On the contrary, polar and subtropical regions present **E**-vector convergence which implies a divergence of momentum and a deceleration of the westerly mean flow by the interaction with the eddies. The **E**-vector climatology reflects how the eddies transport momentum from the Hadley and Polar cells towards the Ferrell cell, by removing momentum from the subtropical jet specifically and depositing it into the extratropical jet (Hartmann, 2007).

Although the acceleration of the mean flow induced by the transient eddies could be evaluated by the divergence, these interactions will be quantified by means of the barotropic generation rate **G** (Equation IV.2.3, Mak & Cai, 1989). The scalar product of the horizontal transient eddies (**E**-vector) and the deformation of the background flow due to stretching or shearing (**G**) gives a measure of the feedback. The dissipation of the eddies in midlatitudes is represented by the negative values of **G** (Figure IV.2).

$$\boldsymbol{G} = \boldsymbol{E} \cdot \boldsymbol{D}; \boldsymbol{D} = \left(\frac{\partial u^{\dagger}}{\partial x} - \frac{\partial v^{\dagger}}{\partial y}, \frac{\partial u^{\dagger}}{\partial y} + \frac{\partial v^{\dagger}}{\partial x} \right) \quad \text{(IV. 2.3)}$$

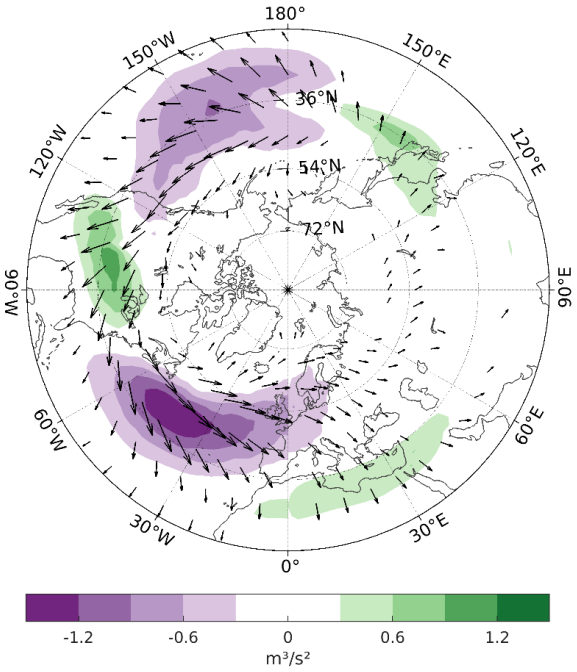

Figure IV.2 Climatology of **E**-vector (arrows, [m^2s^{-2}]) and **G** (shading, [10^{-3} m^3s^{-2}]) at 300 hPa for the winter season (DJF, 1948-2022). Dataset: ERA5.

The **E**-vector also provide indications about the eddies structure. By analyzing the zonal and meridional components, the tilt of the eddies and the orientation of propagation can be inferred, respectively. The **E**-vectors pointing equatorward indicate southwest-northeast elongated eddies and poleward momentum flux propagation. Similarly, the **E**-vectors pointing poleward indicate northwest-southeast elongated eddies and equatorward momentum flux propagation. Lastly, eastward and westward oriented **E**-vectors indicate the meridional and zonal direction of elongation, respectively (Hoskins et al., 1983; Rivière et al., 2003). High-pass transient eddies are mostly meridionally elongated. Low-pass transient eddies are predominately zonally elongated.

Depending on the way the transient eddies break, they deposit their momentum differently and hence, impact on the EDJ. To analyse the large-scale circulation conditions in the upper troposphere, we compute a daily two-dimensional Rossby Wave Breaking (RWB) index based on the potential temperature at the dynamical tropopause (2PVU). The

RWB index is two-fold. Firstly, the B index informs on the instantaneous large-scale RWB occurrence by identifying regions with reversals of the meridional gradient of θ. This is achieved by computing the average θ values to the north and south of each grid point and computing the difference between them (Equations IV.2.4 and IV.2.5). The result is a binary field with 1s at those grid points where there is RWB occurrence and with 0s where there is absence. To only capture large-scale reversals, a criterion of 14.625° of latitude ($\frac{\Delta\varphi}{2}$) both to the north and south is imposed to the RWB scale (Masato et al., 2013).

$$\overline{\theta_l^n} = \frac{2}{\Delta\varphi}\int_{\varphi_0}^{\varphi_0+\frac{\Delta\varphi}{2}} \theta_i d\varphi \quad , \quad \overline{\theta_l^s} = \frac{2}{\Delta\varphi}\int_{\varphi_0-\frac{\Delta\varphi}{2}}^{\varphi_0} \theta_i d\varphi \qquad \text{(IV. 2.4)}$$

$$B_i = \overline{\theta_l^n} - \overline{\theta_l^s} \qquad \text{(IV. 2.5)}$$

Once B is computed, the classification into AWB and CWB is provided by the DB index (Equation IV.2.6). For those locations with RWB detection, the DB index computes the difference of θ between eastward and westward grid points. Positive and negative DB values over and under a threshold identify AWB and CWB, respectively, which tend to occur to the southern and poleward flanks of the EDJ due to the wind shear (contours in Figure IV.3). More details on the RWB index are presented in Masato et al. (2013).

$$DB = \overline{\theta_{l-1}} - \overline{\theta_{l+1}} \quad , \quad \overline{\theta_l} = \frac{\overline{\theta_l^n} + \overline{\theta_l^s}}{2} \qquad \text{(IV. 2.6)}$$

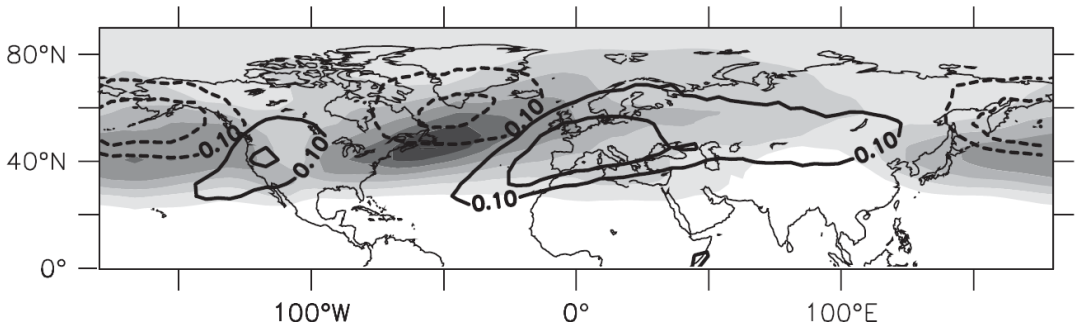

Figure IV.3 Climatology of AWB (solid contour, [%]) and CWB (dashed contours, [%]) frequency for DJF. The contours start at 10% and drawn every 5%. Frequency is based on PV contour overturnings at averaged at averaged 300, 315, 330 and 350 K. Climatology of high-frequency Eddy Kinetic Energy (shading, [m^2s^{-2}]), at 500 hPa for DJF. The shadings are coloured every 15 m^2s^{-2} from 15 m^2s^{-2} to 90 m^2s^{-2}. Modified from Swinbank et al., (2016).

b. Baroclinicity

➢ Eady Growth Rate

The main source of transient eddies is the baroclinic instability. Therefore, Eady Growth Rate (EGR) EGR is used for identifying the regions with the strongest baroclinic wave generation and activity and therefore, for measuring the synoptic activity. Overall, the areas of intense baroclinicity in the NATL tend to spatially coincide with the position of the EDJ core.

This tool assesses the baroclinic instability through a measure of static stability and the vertical wind shear between two given levels in the troposphere (Hoskins & Hodges, 2002; Hoskins & Valdes, 1990). The EGR is given by the Equation IV.2.7:

$$EGR = 0.31 \frac{f}{N} \left| \frac{\partial \boldsymbol{u}'}{\partial z} \right| \qquad \text{(IV. 2.7)}$$

where N is the Brunt-Väisälä frequency, $\boldsymbol{u}$ is the horizontal wind vector and z the vertical coordinate.

➢ Eddy Kinetic Energy

To quantify the energy involved in transient eddy processes, including eddy generation, propagation and other processes, the local budget of eddy kinetic energy (EKE) is evaluated for high-frequency eddies. The EKE measures the exchange of energy between the mean flow and the transient eddies (Vallis, 2006). More specifically, it measures the baroclinic conversion of energy at mid-lower troposphere, from atmospheric potential energy into kinetic energy for the transient eddies (shading in Figure IV.3).

$$\text{EKE} = \frac{1}{2}(u'^2 + v'^2) \qquad \text{(IV. 2.8)}$$

IV.2.2 Statistical Analysis

Throughout this PhD thesis several types of common statistical analyses have been used. They will be described in more detail in the corresponding Chapter. The most utilized computations are correlation analyses and multiple linear regressions for both continuous

and binary variables, each of them computed with a stepwise forward and backward regression and a logistic regression, respectively (Chapter VII, VIII and IX; Wilks, 2011). In relation to the latter, we computed the Area Under the Receiver Operating Characteristic Curve (AUC-ROC) to assess the performance of the logistics regression models (Wilks, 2011). During Chapter VI and VIII we also used some discriminant analysis techniques, such as k-means clustering (Wilks, 2011), Empirical Orthogonal Function (EOF, Lorenz, 1956) Maximum Covariance Analysis (MCA, Bretherton et al., 1992). The statistical significance of the results was assessed by applying a Monte-Carlo test with 1000 random permutations. The signals were considered significant at the 95% confidence level.

V. EDJ New Characterization

One of the main novelties of this work is the characterization of the EDJ as a collection of several time-varying parameters that together explain important aspects of its variability, such as the different EDJ recurrent states and transitions, and allow for a better understanding of the EDJ impacts. In this Chapter, a description of the definition and behaviour of these parameters is presented. More details can also be seen in Barriopedro et al. (2023). Figures taken from this publication are indicated by †.

As described in Chapter II, several features of the NATL EDJ have been studied in the literature. The traditional metrics, such as the latitude or the intensity, are widely used and present well-established definitions. These features, whose definitions were proposed by Woollings et al. (2010), have been the most studied ones and for the longest time since they capture a great percentage of the EDJ variability. More recently, other NATL EDJ features such as the longitude or tilt have also been revealed as important aspects of the variability (e.g., Messori & Caballero, 2015). However, these characteristics do not present as much consensus in their definition as the classical ones, being different depending on the study. In addition, and more importantly, the NATL EDJ characteristics are usually studied in isolation without considering the potential influence of other aspects that may be acting simultaneously.

Motivated by this context, we have developed an algorithm that captures the principal aspects of the NATL EDJ. We aim to identify the different NATL EDJ features that best capture its variability, and to provide robust definitions to systematize their use.

V.1 Definition of EDJ Parameters

Our approach is an extension of the traditional methodology presented by Woollings et al. (2010) for the characterization of the NATL EDJ latitude and speed. To only detect the EDJ and not the TDJ, the methodology is applied to low tropospheric pressure levels, namely, between 925 and 700 hPa. The zonal wind field is vertically averaged and subsequently 10 days low-pass filtered to remove high-frequency fluctuations. To further

minimize the local influences, such as the coastlines or the orography, the computation of the parameters is based on zonal means of zonal wind over longitudinal sectors of 60° width. These zonal means are computed centred at each longitude of the spatial domain [90°W-30°E; 15-75°N] and labelled as $u(\lambda, \varphi)$, where λ is the central longitude and φ the corresponding latitude. Taking all this into account we have identified 10 parameters can be separated in two categories: basic, related to wind speed and latitudinal aspects of the EDJ, and additional, related to the EDJ shape and configuration. The detail parameters description is supported by Figure V.1 as an illustrative example.

In the central NATL sector [60°W-0°; 15°-75°N], a special zonal mean is computed with 30°W as central longitude (λ_c). The obtained meridional profile is labelled as $u(\lambda_c, \varphi)$. The basic parameters are derived considering only this meridional profile and are defined as follows:

- *Latitudinal position (Lat)* and *intensity (Int)* are equal to Woollings et al. (2010). *Lat* is the latitude φ_m of the maximum of $u(\lambda_c, \varphi)$ (horizontal solid line in the upper right panel of Figure V.1) and *Int* is the zonal wind value at that latitude, i.e. $u(\lambda_c, \varphi_m)$. Note that *Lat* is a single value, so in the presence of split or multiple jets, only the strongest wind peak is selected.
- *Sharpness (Sh)* is computed as the difference between *Int* and the meridional mean of $u(\lambda_c, \varphi)$ meridional profile (vertical solid line in the upper right panel of Figure V.1).
- *Poleward (Latn) and equatorward (Lats) flanks* are defined at both sides of *Lat* where $u(\lambda_c, \varphi)$ has decreased the half of *Sh* (dashed horizontal lines in the upper right panel of Figure V.1). *Latn* and *Lats* values are restricted to the NATL sector latitudes, but only exceptionally reach these boundaries at 15° and 75° N.

The rest of the parameters need the additional 60° width sectoral means $u(\lambda, \varphi)$ computed from the [90°W-30°E°; 15°-75°N] spatial domain and are defined as follows:

- *Tilt (Til)* is the slope derived from the linear regression applied to the corresponding tracked latitudes of longitudinal sectors (blue line in Figure V.1). The wind maxima of the NATL meridional profiles are detected by computing *Lat*. The procedure starts at λ_c and continues to the east and west so that the contiguous sector new latitude cannot differ by more than $\pm 2\Delta$, being Δ the

spatial resolution. The obtained latitudes φ_λ (yellow filled circles in Figure V.1) have associated maxima wind speed $Int_\lambda = u(\lambda, \varphi_\lambda)$ (bottom panel in Figure V.1). The fitted latitudes are labelled as ${\varphi^*}_\lambda$ and provide the tilt, which is measured in °N/60° longitude.

- *Central longitude (Lon)* is the average of the NATL longitudes, weighted by the square of their corresponding Int_λ (vertical solid line in the bottom panel of Figure V.1). Note that *Lon* is not defined to coincide with the longitude of the maxima Int_λ. Instead, it is restricted to the NATL sector where *Lat* is obtained, and informs if this latitudinal peak is longitudinally shifted with respect to λ_c.
- *Westward (Lonw) and eastward (Lone) extensions* consider the absolute longitudinal gradient of Int_λ. Starting with an interval defined by *Lon* and its adjacent longitude with higher Int_λ, new longitudes to east and west are incorporated to the interval. The procedure finishes when half of the contours of Int_λ over the NATL are contained in [*Lonw*, *Lone*]. If one extension reaches the border of the domain before the condition is satisfied, the algorithm continues computing the opposite extension. These parameters (vertical dashed lines in the bottom panel of Figure V.1) indicate regions with high zonal gradients of zonal wind, if present, and inform on the EDJ extensions and contractions and hence, its zonal asymmetries.
- *Departure (Dep)* gives a measure of the latitudinal spread of the wind maxima across the NATL, i.e. how well the EDJ is arranged as a single continuous structure. To do so, the latitudinal positions of the EDJ have been computed for all the longitudinal sectors and labelled as Lat_λ. Well-defined single EDJ will present Lat_λ (empty red circles in Figure V.1) coincident with φ_λ (the tracked latitudes of the longitudinal wind maxima, yellow filled circles in Figure V.1). *Dep* is derived from the root mean square error (RMSE) of Lat_λ with respect to ${\varphi^*}_\lambda$. This definition minimizes any influence of *Til*. Note that complex configurations, such as split EDJs, will present large *Dep* values but this does not imply large values of *Til*, and vice versa. This parameter should not be confused with other diagnostics related to the waviness of the mean flow, since a wavy pattern can occur within a well-defined single EDJ with low values of *Dep.*

All the EDJ information provided by these metrics is collected in snake-like plots (bottom right panel of the Figure V.1) which are constructed with a dot and a line. The location of the dot informs on the EDJ location (*Lat* and *Lon*) and the size on the EDJ intensity (*Int*), being proportional to it. The line length and thickness report the longitudinal elongation (from *Lonw* to *Lone* boundaries) and the latitudinal width (depicted as the difference between *Latn* and *Lats* flanks). The line orientation follows the EDJ tilt (*Til*) and the waviness is proportional to the spread of latitudinal wind maxima across the region (*Dep*).

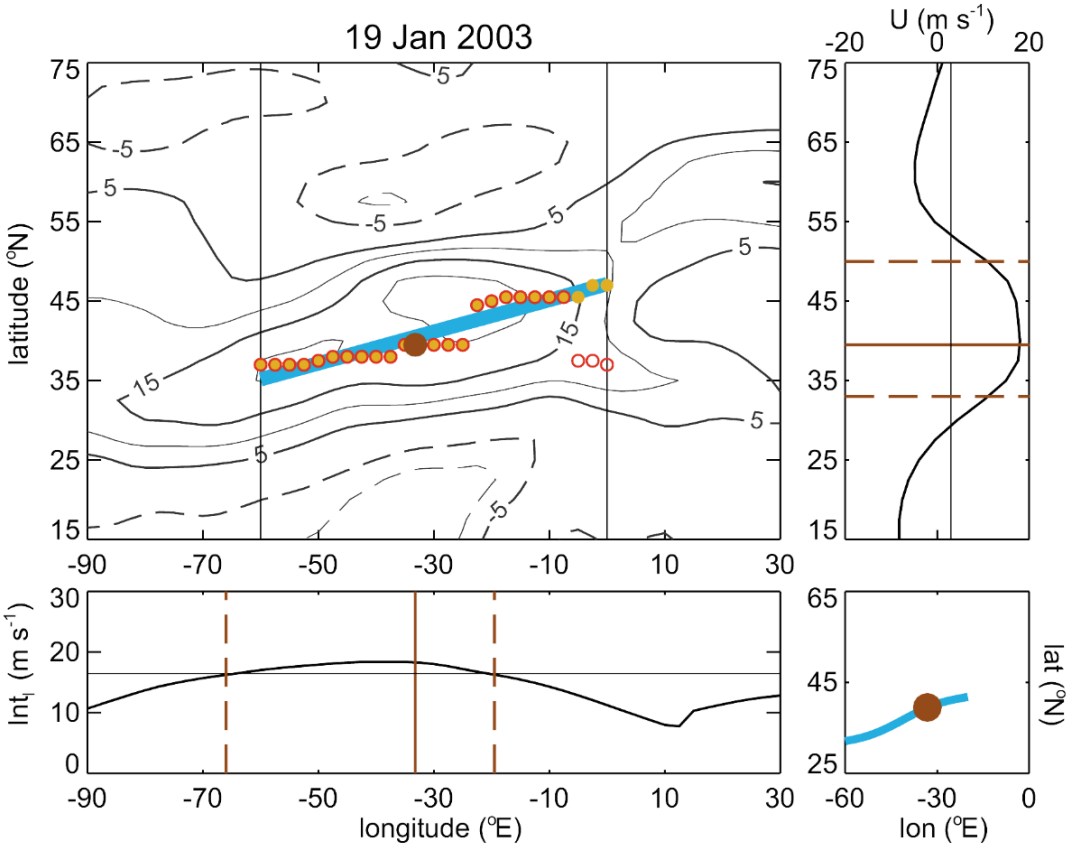

Figure V.1 Example of the diagnosis of EDJ parameters for 19 January 2003. Main plot: 2D low-pass filtered zonal wind at 925-700 hPa (contours in ms^{-1}). Vertical lines identify the NATL sector [60°W-0°]. The brown filled circle shows the position (*Lat* and *Lon*) of the NATL EDJ. Circles filled in yellow indicate the tracked latitudes of the NATL EDJ (φ_λ in the text) for running sectors of the NATL, and the slope of the fitted blue line is the tilt (*Til*). Empty red circles denote the latitude of maximum zonal wind (Lat_λ in the text) for the same sectors, whose spread measures the complexity of the EDJ (*Dep*). Right upper panel plot: meridional profile of zonal wind for the NATL sector, with the vertical line denoting the mean. The horizontal solid line corresponds to the latitude (*Lat*) and dashed lines identify to the northern and southern flanks (*Latn* and *Lats*) of the EDJ. The zonal wind value at *Lat* is the EDJ intensity (*Int*), and the height of this peak defines the sharpness (*Sh*). Bottom left panel plot: zonal wind at the tracked latitudes of the NATL EDJ (Int_λ in the text). The vertical line identifies the longitude (*Lon*) and dashed lines indicate the western and eastern edges (*Lonw and Lone*) of the EDJ. Bottom right panel: snake-like plot of the EDJ parameters. †

Finally, the EDJ parameters are accompanied by a 2D daily representation of the EDJ occurrence (Figure V.2). This field is built from the computation of the EDJ latitudinal extensions (*Latn* and *Lats*) in all the sectors of the considered domain. Thus, the latitudinal edges ($Latn_\lambda$and $Lats_\lambda$) of the zonally varying wind peaks (Lat_λ) account for the EDJ structure and horizontal variations. The method provides a binary field (0/1) of the EDJ for each day, being 1s the grid-points belonging to the EDJ core at each longitude. This 2D field will be extensively employed along this thesis for the computation of the EDJ frequencies of occurrence on a specific period. To sum up, the method provides single parameters and frequency maps for a comprehensive characterization of the EDJ.

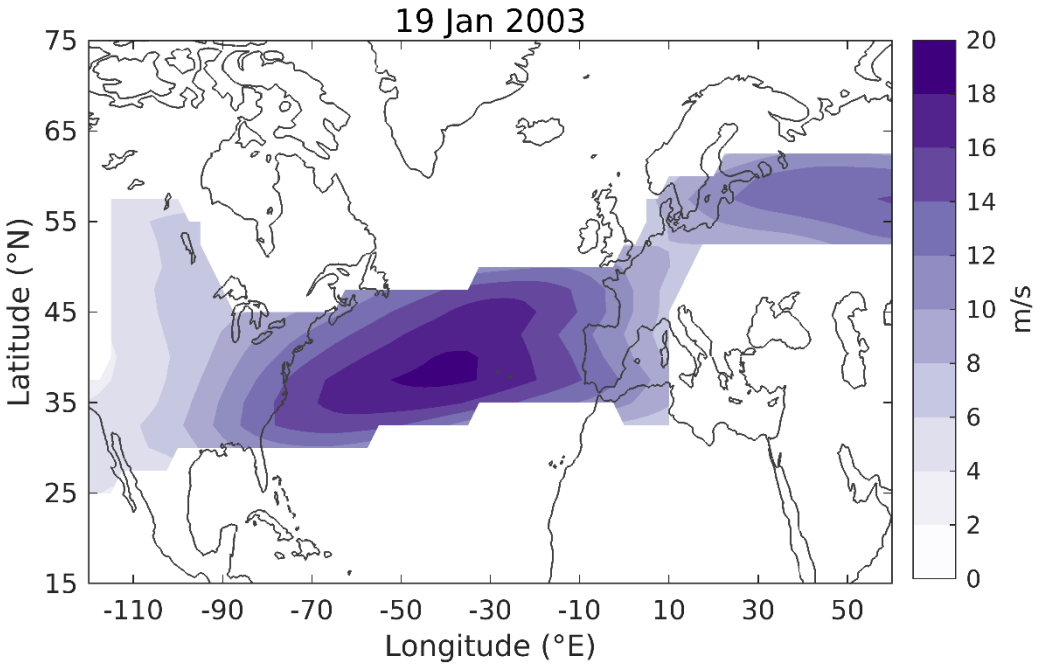

Figure V.2 Example of the 2D occurrence field of EDJ for 19 January 2003. Grid-points of the NATL sector [120°W-60°E, 15°-75°N] belonging to the EDJ are labeled with 1s and displayed with the zonal wind value at that grid-point (shading, [ms^{-1}]). The rest, that do not belong to the EDJ, are labeled by 0s.

For CGMs, the computation of the EDJ parameters and 2D frequency field include only the daily 850 hPa zonal wind, due to the absence of the other two levels in most of the models. Nevertheless, the use of a single level for the EDJ computation do not present major differences from the three averaged levels.

V.2 Climatology of EDJ Parameters

To obtain a deep understanding of the EDJ parameters and become familiar with them, their frequencies (Figure V.3) are described in this section. To do so, we use daily data from NCEP/NCAR reanalysis for the winters (DJF) of the 1948 to 2020 period. Starting with *Int* and *Sh* parameters (red and blue in Figure V.3a, respectively), their distributions show a Gaussian-like behaviour in agreement with previous studies (e.g., Woollings et al. 2010; Dorrington & Strommen, 2020). Both curves are shifted by 5 ms^{-1} approximately, which is the wintertime climatological value of the zonal wind in the NATL area over [15°-75°N]. Interestingly, the mean value of both parameters is slightly underpopulated as compared to a perfect Gaussian distribution, and visually suggests some tendency for a double peaked behaviour. Continuing with the EDJ *Lat* (red line in Figure V.3b), the trimodality is well captured presenting the three preferred locations at the south (S), centre (C) and north (N) of the NATL. These peaks are not present in the poleward and equatorward flanks of the EDJ (yellow and blue lines), arguably due to the presence of the wind speed in the definition of these parameters, which can obscure the trimodality (Strommen 2020). *Latn* distribution is strongly asymmetric, showing a pronounced peak in the north (~60°N) and a modest one in central latitudes (~50°N), corresponding to the poleward flanks of N and C EDJS. Whereas the northern peak of *Latn* is more frequent than the one of *Lat*, the opposite is obtained for the central peak, indicating that C EDJs set their poleward boundaries at very high latitudes. Lastly, no southern peak is drawn in *Latn*, pointing that S EDJs can expand their poleward boundaries over a wide range of midlatitudes, including the typical of C EDJs. *Lats* distribution also behaves asymmetrically but differently to *Latn*. It is skewed toward high values and does not present obvious peaks. Instead, there is a wide maximum spanning from ~30°-45°N, embedding the equatorward boundaries of S and C EDJs, whereas the southern boundary of N EDJs dilutes on midlatitudes. There is a sharp decrease of *Lats* at subtropical latitudes that suggests a constrained S EDJs southern flank, the latter may be caused by the subtropical easterlies. A similar behaviour is obtained for the poleward flank of the N EDJs at high latitudes. This way, N and S EDJs present their outer boundaries constrained by the easterlies, whereas C EDJs do not.

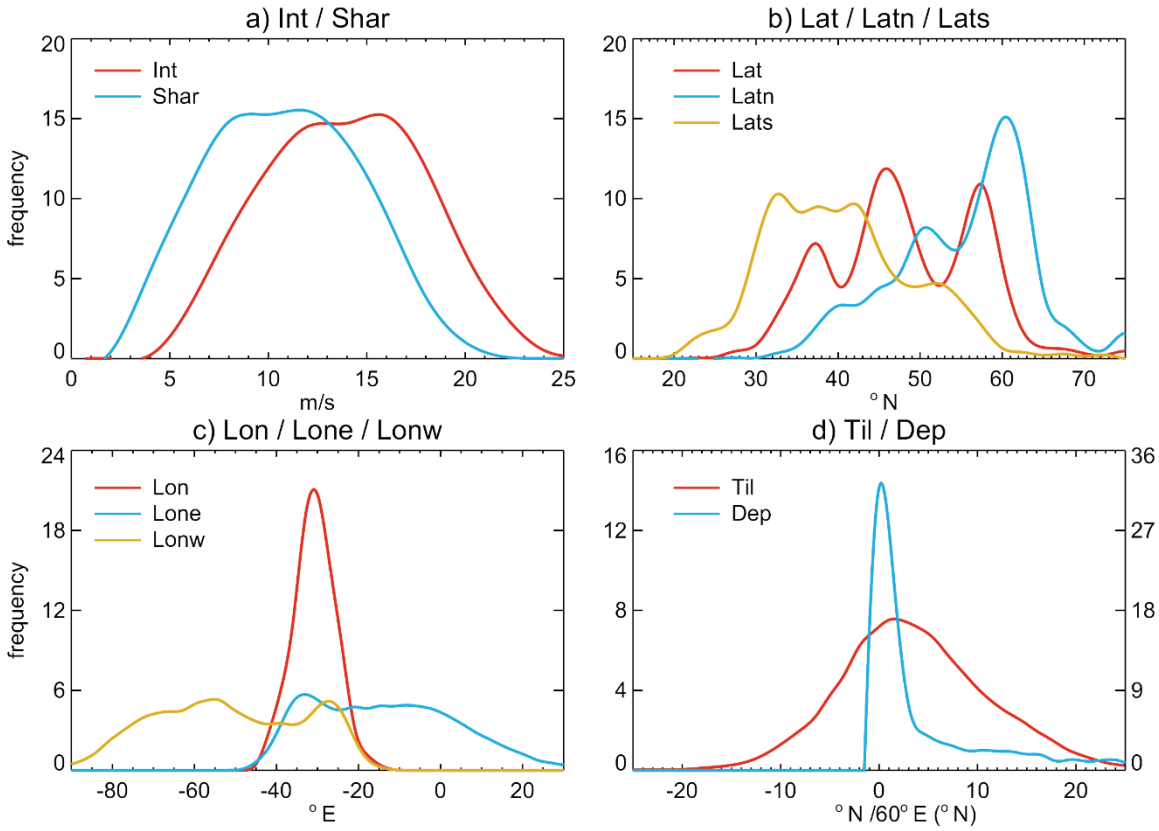

Figure V.3 Climatological mean frequency distributions of the winter EDJ parameters for the 1948-2020 period: (a) intensity and sharpness; (b) latitude and poleward and equatorward flanks; (c) longitude and eastward and westward extensions; (d) tilt and departure. For each plot, the PDFs are computed using bins of 2 ms^{-1}, 2.5°N, 3°E and 1.5°N, and fitted with a polynomial spline. The frequency of the *Dep* parameter is shown with respect to the right y-axis scale in (d). †

The EDJ *Lon* (red line in Figure V.3c) is also Gaussian-like distributed, with the frequency maxima at the middle of the NATL. Differently, the western and eastern extensions (yellow and blue lines in Figure V.3, respectively) show almost flat behaviour, with the zonal extensions being detected two thirds of the days over the NATL and decreasing rapidly over continental regions. Both *Lonw* and *Lone* display a modest peak near the tail of *Lon* distribution. The eastern peak of *Lonw* denotes the most eastward elongated EDJs towards Europe, while the western peak of *Lone* refers to the contracted EDJs over the western NATL (Figure V.3c). The latter agrees with the zonal wind composites for the upper and lower *Lon* terciles (Figure V.4a). The behaviour of the EDJ *Til* (red line in Figure V.3d) is near-Gaussian and presents the frequency maxima at low values (zonal EDJs). There is a skewness toward positive values (SW-NE orientation). EDJ configurations with negative tilts

(NW-SE) occur also quite frequently, being identified both as N and S EDJs with zonal boundaries towards western and eastern regions, respectively (blue histogram in Figure V.4b). On the contrary, configurations with very high positive tilts are related to C EDJs, but also, although less frequent, to N EDJs (red histogram in Figure V.4b). Therefore, the EDJ orientation is not fully determined by its latitudinal regimes. The distribution of the *Dep* shows a very sharp peak (blue line in Figure V.3d). Around half of the days, the EDJ presents very low values (<2°). This indicates that for many cases the EDJ is well-defined as a single continuous structure in the NATL. During the days with low *Dep* values, the EDJ is strongly zonal with intense zonal winds over the central NATL and weak over the south east. By contrast, in days with high spread of latitudinal peaks, the EDJ is split in two branches at the northeast and southwest of the NATL (Figure V.4c). Although C EDJs are not very frequent with high *Dep* values, there is not a clear relation between this parameter and the EDJ latitude.

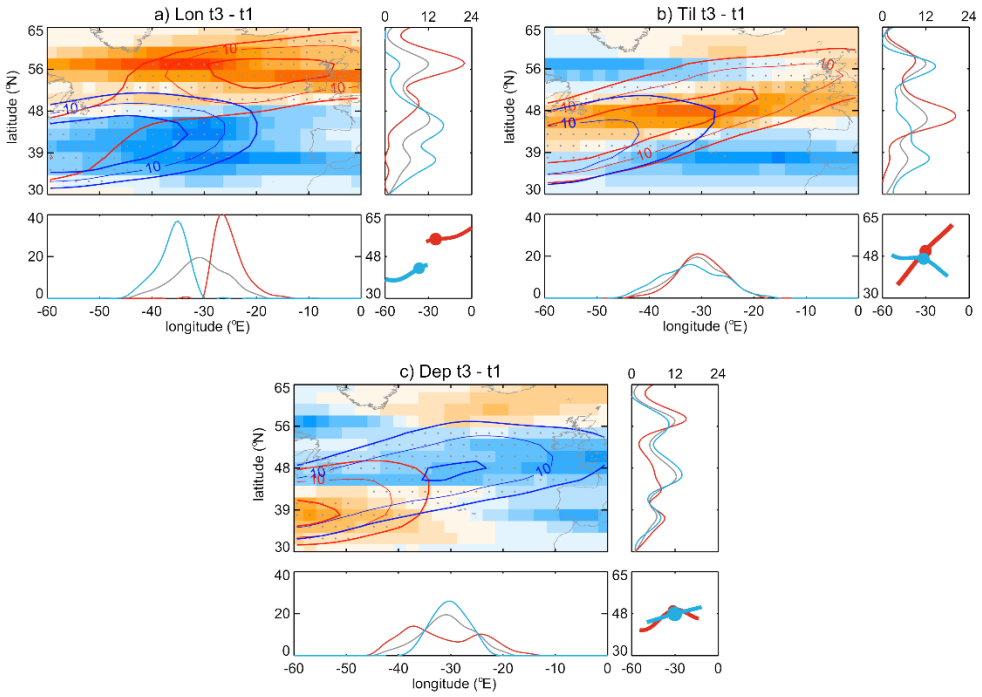

Figure V.4 Difference of EDJ frequency (shading; in percentage of days) for winter days with high (upper tercile) minus low (lower tercile) values in the NATL EDJ: (a) longitude; (b) tilt; (c) departure. The frequency is computed in percentage with respect to the total number of days of each category. Red and blue shading show positive and negative frequency anomalies with contour interval of 10%. Red and blue lines show the composited zonal wind at 925-700 hPa (ms^{-1}) for the upper and lower tercile, respectively. Grey dots indicate significant differences at p<0.01. The bottom and top right insets show the frequency distribution of the EDJ longitude and latitude, respectively, for the climatology (grey) and the upper (red) and lower (blue) tercile categories. The PDFs are shown in percentage with respect to the total number of days in each category. The bottom right inset shows the composited EDJ parameters for the upper (red) and lower (blue) tercile category. †

V.3 Relating EDJ Structures and Parameters

This suite of ten parameters allows the identification of a wide variety of EDJ structures. Actually, a simple combination of a few parameters in different states is able to reproduce the daily variability of the EDJ patterns. Figure V.5 shows composites of the low-level zonal wind (contours) and 2D EDJ (shaded) of the most common combinations of different pairs of parameters. The pairs are formed by *Lat* combined with *Int* (first row), *Til* (second row), and *Dep* (third row). To obtain the preferred combinations for each couple, we compute the probabilities of occurrence of all the possible combinations, based on the terciles of both parameters. Out of the nine, only the three most frequent are selected for each pair. To do so, the number of days for each tercile-based combination is counted. Only those combinations that display frequencies above the expected probability of occurrence for independent samples of the same size (~11%) are shown in Figure V.5. Thus, a first approximation to the most preferred combinations of parameters is provided.

For the three pairs of parameters, the EDJ structures are very different depending on the terciles combination. The most populated regions of the *Int* and *Lat* space show the C EDJs tend to be stronger (Figure V.5.a) than the ones located near the N and S peaks (Figure V.5b and c). Weak EDJs present further differences among them, since the poleward EDJ is also positively tilted (Figure V.5b), whereas the equatorward jet is negatively tilted (Figure V.5c). This behaviour is also observed for the longitudes, for which S EDJs are confined in the western NATL and N EDJs elongate eastward. Consequently, weak EDJs present more variability than the strong ones.

The *Til-Lat* space also shows a non-linear behaviour (Figure V.5 second row). The EDJs tend to be negatively tilted when they locate southward (Figure V.5e) and northward (Figure V.5.f), whereas they show positive tilts when stay at the central latitude (Figure V.5d). The least frequent combination out of the three is the one for the N EDJs. This is in agreement with the large diversity of N EDJ tilts and the non-systematic increase of poleward locations as the tilt increases (Figure V.3b).

The relation between *Dep* and *Lat* is similar to the one of the other pairs, highly non-linear. Due to the highly skewed *Dep* distribution (Figure V.3d), its terciles are biased towards low values, defining groups with extreme low values (<1), low (~1-3) and the rest

(moderate-to-high). Considering the latter, the most popular combinations are the C EDJs with low zonal asymmetries in the latitudinal position (Figure V.5h) and the N EDJs with high zonal asymmetries (Figure V.5i). Perhaps strikingly, the most frequent structure corresponds to C EDJs with high *Dep* (Figure V.5g). Despite being embedded in the C regime these EDJs present large departures in the latitudinal position, being shifted to southern latitudes and the western NATL. This behaviour is contrary to C EDJs accompanied by strong winds or moderate *Dep* for which a canonical structure is detected (Figure V.5h). The latter indicates that zonal variations in the latitudinal position can increase rapidly as the EDJ moves apart from the undisturbed central peak.

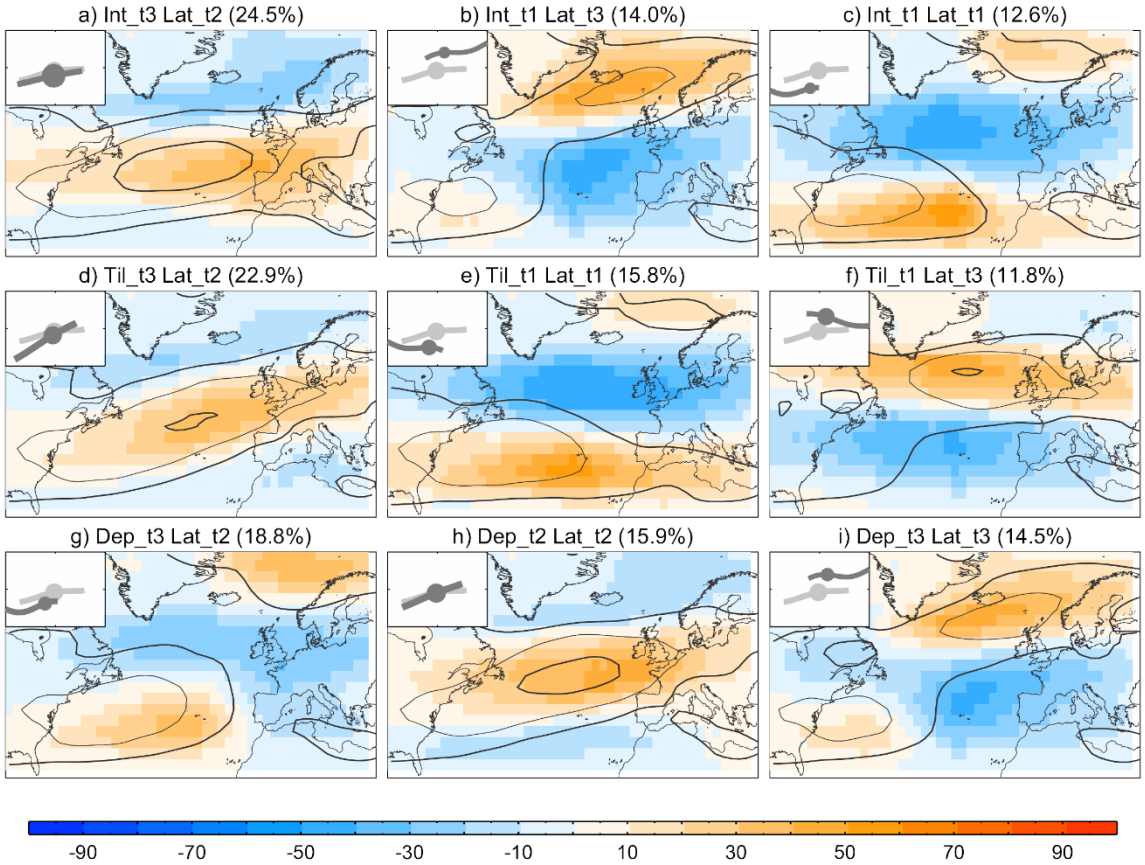

Figure V.5 Composites of zonal wind at 925-700 hPa (contours [ms^{-1}], contour interval of 5 ms^{-1} starting at 5 ms^{-1}) and EDJ frequency anomalies (shading, in percentage of days) for the preferred combinations of EDJ parameters' pairs: (a-c) latitude and intensity; (d-f) latitude and tilt; (g-i) latitude and departure. The top left inset of each panel shows snake-plots of the mean EDJ configuration for the composite (dark grey) and the climatology (light grey). The selection is based on the relative frequency of days in each tercile (t1-lower tercile; t2-middle tercile; t3-upper tercile) of the EDJ parameters. For the same pair of EDJ parameters (row panels), the most populated ninths are sorted by frequency (from left to right, in decreasing order) and identified in the title of the panels. †

Considering the nine most frequent structures as a whole, it can be observed that instead of being very different among them, similar structures are obtained from the combination of different parameters. For instance, the shape of the intense C EDJs resembles to that of positively tilted (Figure V.5.a) and zonal symmetric C EDJs (Figure V.5.d). Similarly, the weak S EDJs (Figure V.5.c) look like the negatively tilted S EDJs (Figure V.5.e), and the strong N EDJs (Figure V.5.b) like the ones with high zonal asymmetries (Figure V.5.i). Thus, in general, the EDJ tends to present some specific recurrent structures arisen from a combination of several parameters.

It should be noted that a single parameter is unable to fully characterize the EDJ structure. Instead, considering several parameters becomes necessary. As shown in this Chapter, two EDJ configurations can be very different despite sharing a parameter in the same state. Thus, the EDJ patterns can strongly vary when changing the behaviour of a single characteristic. The most surprising case is when both patterns share the latitudinal state, since this parameter has been used typically to determine the state of the EDJ. Figures V.5h and g show how C EDJs can involve two almost opposite structures i.e. zonally symmetric and very zonally asymmetric. The low *Dep* C EDJ is also strong and eastward displaced whereas the high *Dep* C EDJ is weak and westward displace. A similar picture is obtained when attending to other parameters. A weak EDJ can be north and eastward displaced (Figure V.5b), but also south and westward (Figure V.5c). Consequently, a combination of parameters is required to ensure the representation of the complex EDJ structure.

V.4 Remarks

In this Chapter, a novel multiparametric perspective for describing the NATL EDJ has been introduced. Ten daily parameters characterize the regional low-tropospheric zonal wind maxima. This approach has been constructed as a natural extension of the classical NATL EDJ latitudinal regimes (Woollings et al., 2010), by gathering additional features. The suite is formed by the intensity, the sharpness, the latitudinal and longitudinal positions, including both poleward and equatorward flanks, and eastward and westward zonal

extensions, the tilting and the departure. In addition, a 2D field of the NATL EDJ occurrence, based on the latitudinal parameters, identifies the EDJ structure and its spatial variations.

The multiparametric perspective is able to dissect the NATL EDJ structures beyond the traditional latitudinal description. Concretely, the EDJ structures can be summarised in a manageable number of relevant aspects, allowing to address complex and unusual EDJ configurations.

The methodology enables the direct application to any reanalysis dataset or model simulations since it avoids the use of subjective choices such as thresholds or anomalies. Also, although the relatively large number of parameters and the complexity of working with them altogether can be a limitation of this approach, the parameters can be used alone or combined depending on the specific EDJ aspect one is interested in. In the end, the proposed metrics are useful when a daily time series of a specific EDJ feature is desired.

VI. EDJ Regimes and Transitions

In the previous Chapter, we have detected that EDJs at the same latitudinal tercile, namely, N, C or S EDJs, may present different shapes depending on the state of the rest of the EDJ parameters. The latter implies a variety of structures beyond the three typical latitudinal states reflected in the EDJ trimodality, that has been the usual way of characterizing the EDJ regimes. In this Chapter we focus on the detection, if any, of the multiparametric structures that are frequently visited by the EDJ in the NCEP/NCAR reanalysis during the 1948 to 2020 period. We aim to unravel the meaningful number of recurrent structures that are able to isolate certain aspects of the EDJ variability, such as the three traditional latitudinal regimes of the EDJ, or more complex 2D configurations like the zonal wind spatial patterns reported by Madonna et al. (2017). Although the EDJ trimodality seems to indicate that three is the natural number of recurrent states, this number might be different. Moreover, we aim to study the preferred transitions between the recurrent states. More details can be found in Barriopedro et al. (2023).

VI.1 Recurrent Configurations of the EDJ

We start investigating the two-dimensional EDJ recurrent configurations. This topic has previously been addressed by other authors (Dorrington & Strommen, 2020; Frame et al., 2011; Hannachi et al., 2012; Madonna et al., 2017). The EDJ structures have been typically obtained from the zonal wind field or sophisticated feature-based approaches. Although these approaches provide a picture of the EDJ configurations more complete than when considering only a latitudinal index, they fail in providing a specific measurement of the different attributes that depict the configuration. To ensure a proper representation of the EDJ configurations, a combination of parameters should be considered.

Based on the latter, we make use of the k-means clustering to dissect the multi-faceted nature of the EDJ and consider the diversity of recurrent patterns. In particular, we apply it to the daily winter EDJ parameters. For this analysis the sample is required to be divided in a predefined number of clusters (k) that refer to different multiparametric states (Wilks,

2011). The k-mean clustering technique assigns each day to one of the clusters according to a metric distance, being the sum of squared Euclidean distance to the clusters' centroids in this case, so that the intra-cluster variance is minimized and the inter-cluster variance maximized. To ensure equal weights on the Euclidean norm, the winter series of the EDJ parameters have been normalized and expressed as standardized anomalies. This method is applied with 100 iterations to allow centroids to evolve enough from the random initial seeds. As some days are not expected to be similar to any cluster, the analysis was repeated disregarding points with the largest distances (above the 90^{th} percentile) but no significant differences were found.

In first place, we analyse the results obtained when only three clusters (k=3) are requested (Figure VI.1a-c). As expected, the three clusters largely capture the three preferred latitudinal positions of the EDJ, since it is the most distinguishable aspect. These patterns will be referred as C3, N3 and S3 clusters. In addition to the clusters, the latitudinal shift can be observed in the histograms of the *Lat*, computed for the days belonging to each multiparametric cluster (green lines in the right panels of Figure VI.1). We also compute the latitudinal regimes to analyse how well the latitudinal shift of the three clusters represents the trimodality. Latitudinal regimes are computed clustering only *Lat* instead of the ten parameters (N, S and C clusters of the second column of Figure VI.2).

Figure VI.2 allows a comparison between the multiparametric clusters (first column) and the latitudinal regimes (second column). The daily EDJ structures identified as a certain latitudinal regime (e.g., N) that are classified in its multiparametric counterpart (e.g., N3) are displayed in the third column. The rest (e.g., N days classified as C3 and S3) are shown the fourth column. Although there is a big correspondence between the multiparametric clusters and the latitudinal regimes, the correspondence is not perfect. Around two thirds of the days of the latitudinal regimes are classified in their multiparametric counterparts (percentages of third column in Figure VI.2). However, the remaining days, the latitudinal regimes present EDJs with parameters more similar to other clusters (fourth column in Figure VI.2). For instance, C EDJs missing in C3 cluster present relatively weak and westward shifted EDJs, which are the main characteristics of S3. Therefore, a measurable influence of the other EDJ parameters exists. The multiparametric space enables the detection of EDJ structures considering more signatures than the latitudinal one. Now, from this multiparametric space, C3 EDJs are stronger than N3 and S3, which in turn show different

longitudinal position (eastward and westward, respectively), tilt (low for S3) and degree of complexity (high for S3) (contours in Figure VI.1a-c).

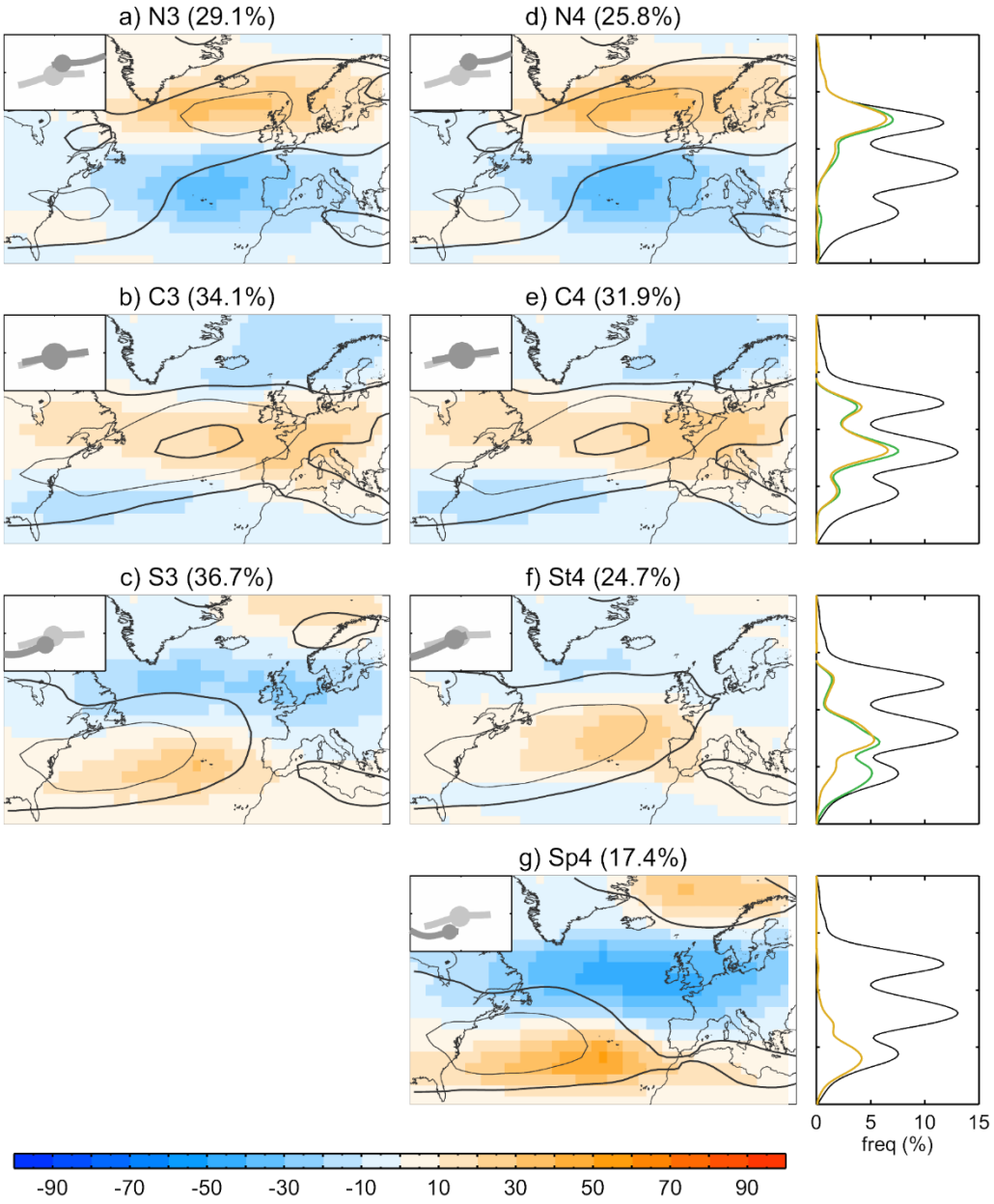

Figure VI.1 Composites of zonal wind at 925-700 hPa (contours, in ms^{-1}, contour interval of 5 ms^{-1} starting at 5 ms^{-1}) and EDJ frequency anomalies (shading, in percentage of days) for days assigned to each cluster of the NATL EDJ parameters. Results are shown for: (a-c) three clusters (N3, C3 and S3); (d-g) four clusters (N4, C4, St4 and Sp4). The relative frequency of winter days in each cluster is shown in the title. The top left inset of each panel shows snake-plots of the mean EDJ configuration for each cluster (dark grey) and the climatology (light grey). Right plots show the frequency distribution of NATL EDJ latitude for the k=3 (green) and k=4 (yellow) clusters displayed in the same row (in percentage with respect to the total number of winter days). Black line is the climatology. †

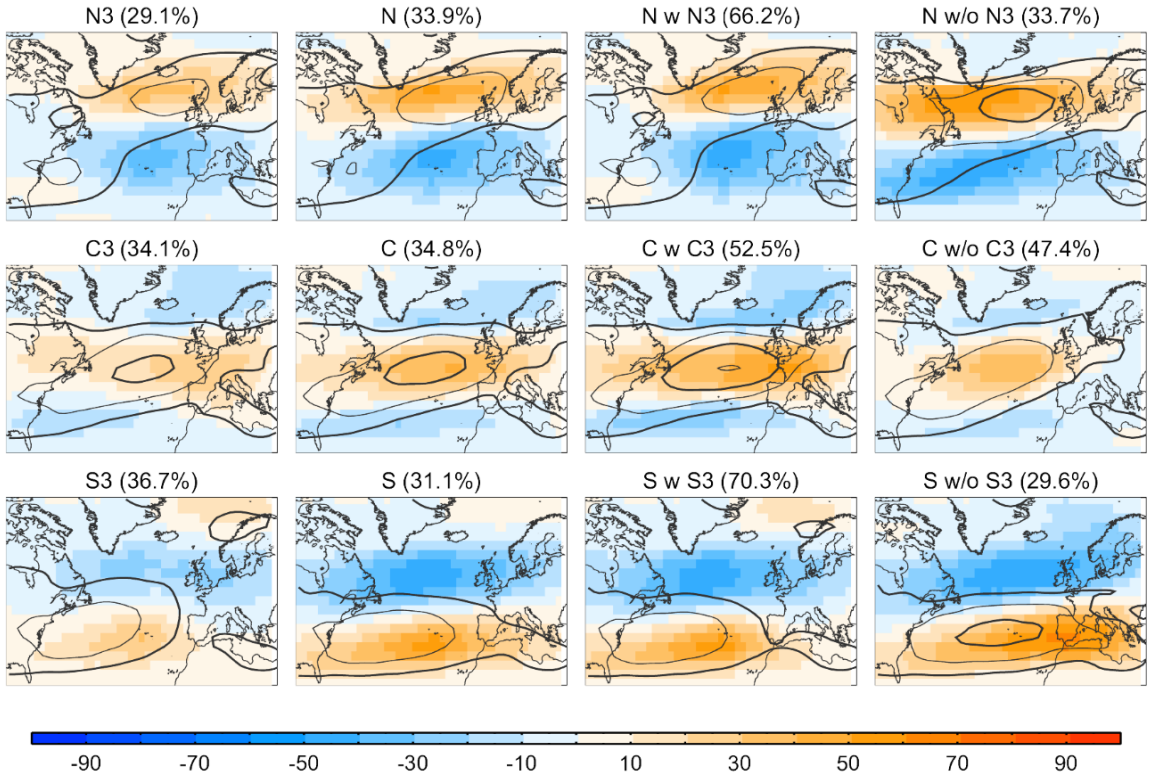

Figure VI.2 Comparison of the three clusters obtained with all parameters and latitude only: Composites of zonal wind at 925-700 hPa (contours [ms^{-1}], contour interval of 5 ms^{-1} starting at 5 ms^{-1}) and EDJ frequency (shading, in percentage of days) for days assigned to each cluster computed with all the NATL EDJ parameters (first column) and only with *Lat* (second column). Third and fourth columns are the latitudinal EDJs included and not included respectively in its multiparametric counterpart. Clusters correspond to (first row) northern, (second row) central and (third row) southern EDJs.

Although the clusters have detected the meridional shift of the EDJ, the southern peak is not well isolated (Figure VI.1c). This challenge was also faced by previous studies based on clustering (Hannachi et al., 2012; Madonna et al., 2017; Dorrington & Strommen, 2020). Consequently, the multiparametric states analysis has been extended to k=4 clusters. Now, the three well-separated latitudinal positions of the EDJ and a split-like pattern are retrieved (Figure VI.1d-g). The first two of them present almost the same features of N3 and C3 clusters, and will be labelled as N4 and C4. They still concentrate the northern and central peaks and their individual characteristics: weak and eastward shifted for N4 and strong and normal tilts for C4. The other two clusters (Figure VI.1f and g) arise mainly from S3 cluster, which concentrates EDJs with latitudes at the southern flank of the central peak and the southernmost locations. The first new cluster (Figure VI.1f) collects the EDJs shifted southward with large tilts (St4). This cluster identifies the C EDJs with similar features to S EDJs, namely, weak intensity and western located. The second new cluster resembles the

mixed pattern found in Madonna et al. (2017), and will be labelled as split cluster (Sp4). Its main feature is that it captures the flow split in two branches (Figure VI.1g). This implies that a fraction of S EDJs, particularly those most shifted to the south, are related to split patterns with southern branches that can extend zonally and merge with the subtropical jet (Madonna et al., 2017). Although St4 and Sp4 share the southern latitude, they differ in the intensity, longitudinal elongations and zonal asymmetries. Previous studies also needed four clusters to isolate the southern peak (Madonna et al., 2017) and five to separate the tilted and split patterns (Dorrington & Strommen, 2020). Thus, the four multiparametric clusters seem a good approximation to describe the preferred EDJ states without losing the latitudinal perspective.

An important remark should be mentioned before continuing. Similar recurrent structures are obtained when, instead of clustering the ten EDJ parameters, different combinations of parameters are selected, even when the selection is reduced to a few. Although the specific shape of the structure depends on the chosen combinations of parameters, the same four multiparametric recurrent structures are obtained (Figure AVI.1). However, the latter does not occur when a single parameter is considered. The multiparametric structures are not reproduced when clustering a parameter alone, even for *Lat*, confirming the added value of the other parameters (sixth column in Figure AVI.1).

VI.2 Transitions between EDJ events

Once the recurrent EDJ configurations have been scrutinized, the persistence and the potential transitions among the four structures are explored in this section. Studying these aspects of the EDJ variability becomes interesting since it may provide some predictability on extratropical synoptic conditions and hence, on midlatitude weather forecast.

The events corresponding to each cluster k_i are identified. Events are defined as one or more consecutive days that are classified in that cluster. To investigate the persistence of the events of each cluster, the frequency distribution of k_i events with a period equal or longer than d days is assessed. Transitions of the k_i events are explored using lags, with lag 0 indicating the first day of the event. For every lag, the fraction of k_i events that transition to a new cluster k_j is counted. When the lag is large enough, all events will have

occupied other states, and the cumulative frequency of k_j gives a measure of the preferred transition.

The distributions of event duration for each cluster and the cumulative frequency in the new states for lags up to 20 days are shown in Figure VI.3. Regarding the persistence, C4 events present the largest values (Figure VI.3b, 6.2 days). Agreeing with previous studies (Barnes et al., 2010; Hannachi et al. 2012), N4s have shorter durations (Figure VI.3a, 4.7 days). However, they are not the least persistent, since Sp4 and St4 present similar and even lower mean durations (Figure VI.3c and d, smaller than 4.5 days). Moving to the transitions, the events with the highest frequencies at each cluster confirm the established poleward migration of the EDJ (Franzke et al., 2011) from Sp4 to St4 (~69%, Figure VI.3d), St4 to C4 (~43%; Figure VI.3c) and C4 to N4 (~48%; Figure VI.3b), although C4 events also have a high probability to transition to equatorward states (St4). Focusing on N4 migrations, they are more likely to occur towards St4 events (35%), however this frequency is comparable to that towards C4 events. Although with slightly less probability, N4 events also migrate to the southernmost latitudinal peak (Sp4). Thus, when four EDJ patterns are considered, the established abrupt transition from northern to southern EDJs (Franzke et al., 2011; Hannachi et al. 2012) is not observed. Contrary, N4 EDJs are more likely to go back to C4 or experience moderate latitudinal shifts to St4 states.

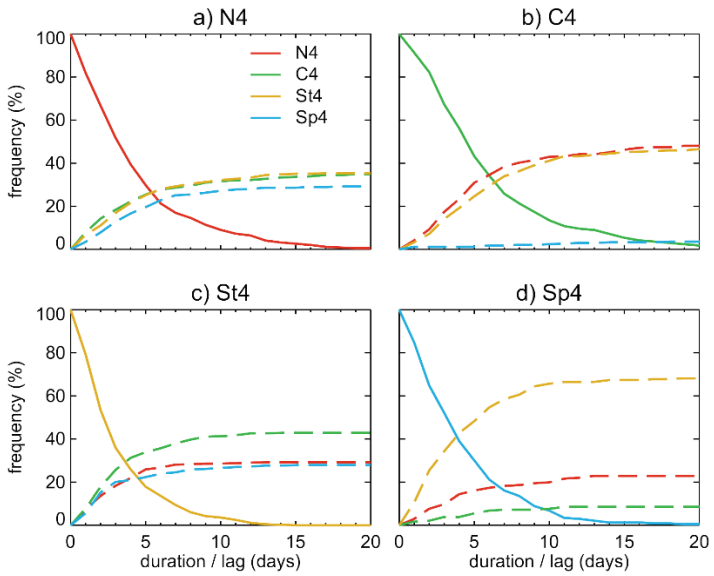

Figure VI.3 Frequency distribution with the number of EDJ events (solid lines) and cumulative transitions (dashed lines) as a function of the duration. Results are shown for the events defined from: (a-d) four (N4, C4, St4 and Sp4 events) multiparametric clusters of the NATL EDJ. Frequencies are expressed in percentage of the total number of events in each cluster. †

This is supported by the probabilities obtained from the transition matrix of Markovian process that defines the daily probability of moving from one cluster to another (Frame et al., 2011):

$$P_{ij} = P\left(x_t \in k_j \mid x_{t-1} \in k_i\right) = \frac{P\left(x_t \in k_j\, , x_{t-1} \in k_i\right)}{P\left(x_{t-1} \in k_i\right)} \qquad \text{(VI. 1)}$$

where P_{ij} represents the probability of transitioning from k_i to k_j at any lag x_t. Considering only transitions to other clusters by neglecting the days the cluster stays in the same state (null diagonal terms; Franzke et al., 2011), the transition matrix behaves:

$$P = \begin{pmatrix} 0.00 & 0.28 & 0.03 & 0.30 \\ 0.69 & 0.00 & 0.48 & 0.35 \\ 0.09 & 0.42 & 0.00 & 0.35 \\ 0.22 & 0.29 & 0.49 & 0.00 \end{pmatrix} =$$

$$= \begin{pmatrix} & \mathrm{St4} \to \mathrm{Sp4} & C4 \to Sp4 & \mathrm{N4} \to \mathrm{Sp4} \\ \mathbf{Sp4 \to St4} & & \mathbf{C4 \to St4} & \mathrm{N4} \to \mathrm{St4} \\ Sp4 \to C4 & \mathbf{St4 \to C4} & & \mathrm{N4} \to \mathrm{C4} \\ Sp4 \to N4 & \mathrm{St4} \to \mathrm{N4} & \mathbf{C4 \to N4} & \end{pmatrix} \qquad \text{(VII. 2)}$$

The most likely and unlikely transitions are indicated in bold and italics, respectively, in the case the probability of that transition is significantly ($p<0.05$) different from the one expected from equally likely transitions (binomial test). The poleward migration is detected again since Sp4 events strongly prefer evolving in St4, which in turn are more likely to transition poleward (C4) than returning equatorward (Sp4). Indeed, the short persistence of Sp4 and St4 clusters and the high probability of evolving one into the another explain why they appear merged under the same cluster when k=3. These clusters could be viewed as the phases that link the N4 and C4 EDJs, since when considered together, the preferred loop S-C-N-S through the three latitudinal regimes is recovered (Franzke et al., 2011). However, the multiparametric face of the EDJ reveals that the EDJ states evolve more likely toward their closest latitudinal states.

A deeper understanding of the EDJ transitions can be reached when analyzing the composites of the EDJ parameters during a transition between two states with at least four

days of duration, namely, periods of four or more consecutive days in the regime k_i followed by at least four consecutive days in the new cluster k_j (Figure VI.4). The selected transitions display the poleward migration (Sp4-St4-C4-N4). Lagged composites of the corresponding EDJ parameters have been computed, ordering them so that lag 0 coincides with the beginning of the new event. Overall, transitions between near latitudinal states are associated with small tendencies in the EDJ parameters. For instance, St4-C4 and C4-N4 transitions present increasing tendencies of *Lat* and *Lon*, indicating an eastward shift of the EDJs as they move poleward (Figure VI.4b and c). Moreover, EDJs increase their intensity and zonal symmetries and reduce their tilts when they evolve from St4 to C4 states. The opposite occurs for the subsequent poleward shift, from C4 to N4. Despite involving similar changes in latitude, Sp4-St4 transition presents larger tendencies than the other transitions involved in the poleward migration (St4-C4 and C4-N4), such as pronounced increases in *Til* and decreased *Dep* (Figure VI.4a).

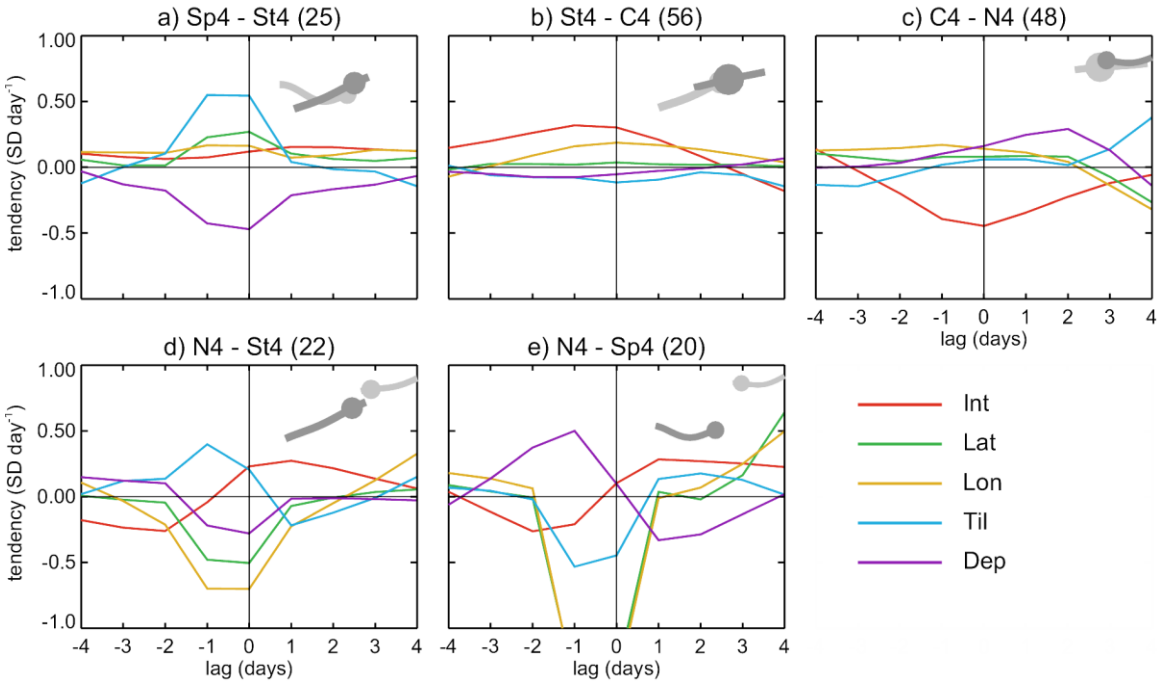

Figure VI.4 Composite tendency of EDJ parameters ([SD day^{-1}]) during the preferred transitions of EDJ events, as defined from the four multiparametric clusters of the NATL EDJ: (a) Sp4 to St4; (b) St4 to C4; (c) C4 to N4; (d) N4 to St4; (e) N4 to Sp4 transitions. Lag 0 corresponds to the first day of the transitioned event. Only events of at least four days are considered. The number of transitions considered for the composites are shown in brackets in the title. Snake-plots in the top right of each panel show the composited EDJ structure before (lag -3, light grey) and after (lag 3, dark grey) the transition. †

The differences between Sp4 and St4 are highlighted when comparing the transitions from N4 EDJs to these recurrent states. During N4-Sp4 transitions, *Dep* increases and *Til* decreases, indicating a split of tilted N4 EDJs into two branches (Figure VI.4e). The large drop in *Lat* reveals the dominance of the southern branch after the transition. Thus, the characteristic features of the Sp4 regime appear, namely, weak intensity, small or negative tilts and strong confinement in the western NATL. Differently, N4-St4 presents opposite tendencies to those of N4-Sp4, with smaller changes in *Dep* and *Til*, and no split (Figure VI.4d). During this transition, the entrance region of the tilted EDJ intensifies as the exit region weakens, so that the EDJ contracts to the southwest (large drop in *Lat* and *Lon*) and ends up as a St4 EDJ with reminiscent signatures of the original tilted configuration. Therefore, the intensification of winds at the entrance region of highly-tilted EDJs can be viewed as an abrupt equatorward transition from the latitudinal regime perspective.

VI.3 Remarks

This Chapter shows the multiparametric perspective of the EDJ has been proven to add value in comparison to the traditional perspectives based on the EDJ latitude, intensity, or other single-parameter metrics.

The joint use of the parameters provides a synthetized view of the EDJ recurrent configurations and transitions. The same latitudinal regime can present substantial differences from its canonical structure and present a complex pattern that the latitudinal parameters is not able to identify. Hence, more than one parameter is required to fully capture the 2D EDJ structure and variability. The analysis of the multiparametric space provides preferred EDJ patterns that agree with previous studies of the Euro-Atlantic flow regimes (Cassou et al., 2004). However, they provide a more satisfactory description of the EDJ patterns. These recurrent states are the northern, the central, the southward and tilted pattern and the southernmost and split configuration of the EDJ. The two latter regimes are indistinguishable from a latitudinal perspective since both fall in the southern peak. This could explain the high persistence of the southern regime found in several studies (Franzke et al., 2011; Hannachi et al., 2012). The regimes present a poleward migration

(Sp4-St4-C4-N4 evolution) accompanied by an eastward progression, followed by a weakening and increasing asymmetry as the EDJ approaches the northern state. The transition from northern to southern latitudes detected in previous studies does not appear so clear when tilted and split patterns are considered.

VII. EDJ configurations related to winter European temperature extremes

Chapter VI has given evidence that the multiparametric approach provides a better dissection of the EDJ winter variability and 2D structures than the single-parametric ones. Based on these results and considering that our new EDJ characterization allows us to synthetize complex EDJ structures into a combination of parameters, in this Chapter we study the EDJ variability during European winter temperature extreme events.

As described in the Chapter III, the EDJ is intimately related to the surface temperature since the EDJ acts as a barrier between cold polar and subtropical air masses. Although some studies have scrutinized the influence of a single EDJ feature on the surface temperature, the characterization of the EDJ impacts cannot be achieved from a single parameter (e.g., Mahlstein et al., 2012). In this context, we explore the ability of the multiparametric approach to capture the EDJ structures, if any, that lead to temperature extreme events in different regions of Europe with NCEP/NCAR reanalysis/observation daily data for the 1948-2022 period. Further, we quantify the ability of the EDJ parameters in capturing the occurrence of these events by using logistic regression models, and we compare it to the ability of the single *Lat* and *Lat-Int* together. Finally, we also show interest in the mechanisms leading to the occurrence of the extremes, which are evaluated using the tendency equation of the temperature. The results of this Chapter can be found in García-Burgos et al. (2023). Figures taken from the latter publication are indicated by ††.

VII.1 Regionalization of European temperature extreme events

As mentioned in Chapter II.2.2, the EDJ influence on the surface temperature is not spatially homogeneous over Europe (Barriopedro et al., 2023; Mahlstein et al., 2012; Röthlisberger et al., 2016; Trigo et al., 2004). Thus, in this first section of Chapter VII we

focus on the identification of the regions where the EDJ impacts similarly on the occurrence of temperature extreme events.

To obtain the regions, two types of extreme temperature events are considered: cold spells and warm events. They are computed from the detrended TN and TX, respectively. Warm events are defined locally as periods of at least five consecutive days with TX above the daily 95th percentile of the 1981–2010 period. For cold events, we simply change the criterion to TN below the 5th percentile. For each day of the year, these percentiles are determined by considering a 5-day window centred on the day of interest, following the Expert Team on Climate Change Detection and Indices (ETCCDI; Zhang et al., 2011). Similar results are obtained for other extreme definitions that, for instance, involve changes in the percentile threshold or the persistence of extreme TN/TX values. Following the definition of extreme events, extreme event fields composed of 0s and 1s are constructed. For each day, those points where there is an extreme event are labelled as 1, and as 0 where there is not.

Once the extremes field is constructed, two maps of extreme events frequency are computed for each EDJ parameter for the days the EDJ parameter falls within its lower and upper tercile categories. For instance, the lower (upper) tercile map of the *Til* parameter shows the impact of a negative (positive) tilt in cold spell frequency. Finally, we compute the difference between the upper and lower tercile frequency maps of each EDJ parameter (Figure VII.1).

As the results of the regionalization are very similar for cold and warm events, only those obtained for the former are showed in Figure VII.1. The probability maps for warm events are included in Figure AVII.1. Similarly, we do not present the results for the 10 EDJ parameters in the main text, since not all parameters are independent and some of them yield maps with high resemblance (these maps can be found in Figure AVII.2). Accordingly, we only show maps of the EDJ *Int* (representative of wind speed, including *Sh*), *Lat* (representative of *Latn* and *Lats*), *Lon* (also representative of *Lone* and *Lonw*), *Til* and *Dep*. The joint inspection of Figure VII.1a-e allows identifying four main regions, with their borders drawn where the impact changes sign or loses its intensity. The northern region, covering the Scandinavian (SCA) countries, is mainly affected by *Lat* (Figure VII.1b) and displays a distinctive behaviour in some parameters, with opposite signals to those found

in other European regions. For example, the *Dep* pattern is characterized by a dipole with a change in sign south of SCA (Figure VII.1e). Overall, the response of cold spells

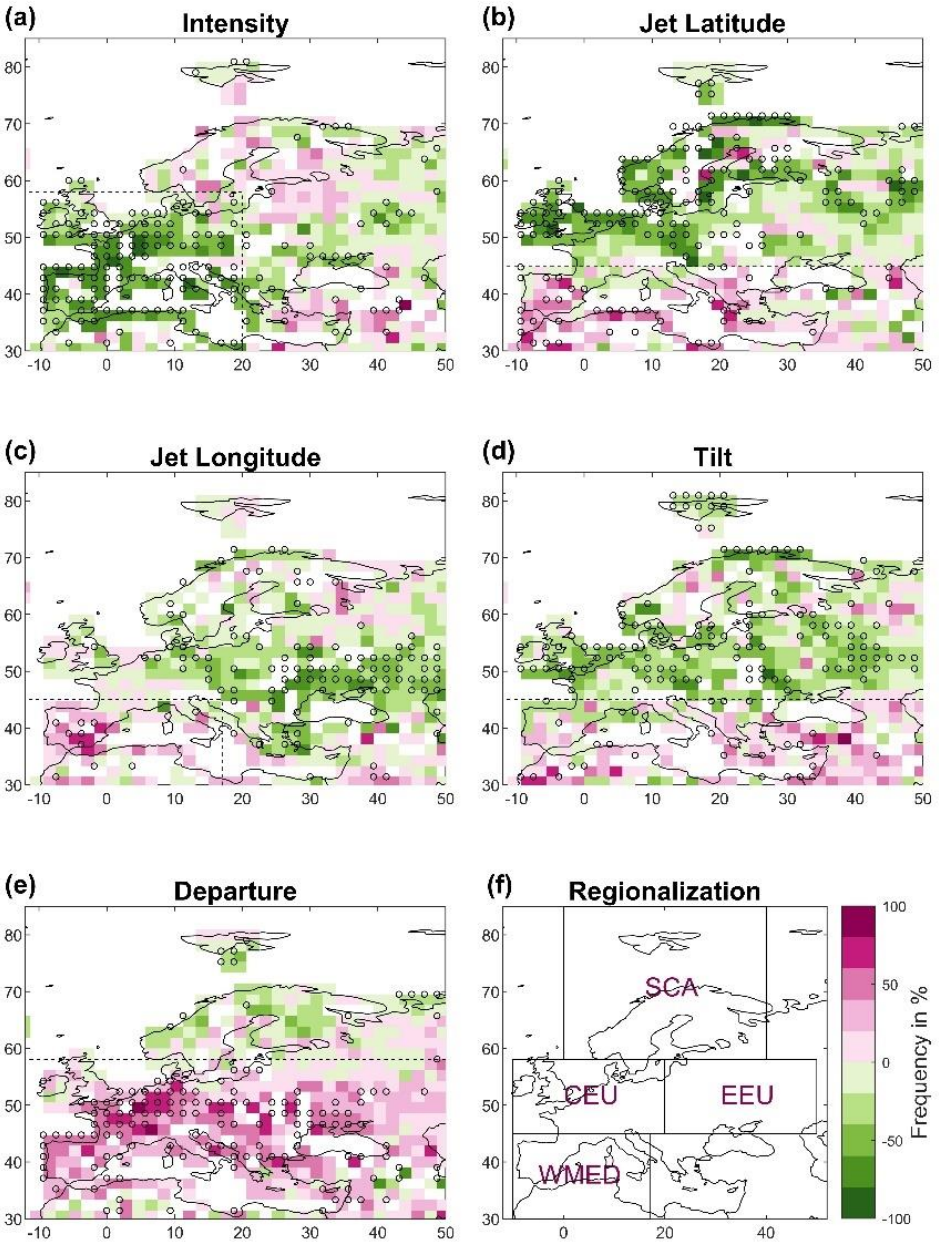

Figure VII.1 Impact of Eddy-Driven Jet (EDJ) parameters on cold spell frequency: (a-e) Difference of cold spell frequency ([frequency in %]) for winter days with EDJ parameters in the upper minus lower tercile: (a) intensity, (b) latitude, (c) longitude, (d) tilt, and (e) departure. Only grid points that are statistically significant at the 95% confidence level in both the upper and lower tercile maps are labeled as significant (o). Borders are drawn where the impact changes in sign or remarkably weakens (dashed lines). (f) European regionalization based on the impacts of the EDJ parameters shown in (a-e). ††

equatorward of SCA to the EDJ parameters is not spatially homogeneous either. The central latitudes (45°-58°N) are split into western-Central Europe (CEU) and Eastern Europe (EEU) due the stronger effect of *Int* (Figure VII.1a) in CEU than in EEU. The southern flanks of these regions are also bounded by the signals of *Til* and *Lat* parameters (Figure VII.1b and d), which present a dipole pattern with one of the antinodes over Mediterranean regions. Lastly, the impact of *Lon* allows us to divide the southern latitudes (30°-45°N) in western and eastern regions (Figure VII.1c). However, only the Western Mediterranean (WMED) region is considered since the influence of the EDJ is weak in the eastern Mediterranean (Figure VII.1 and AVII.3). Figure VII.1f summarizes the four regions that have been identified from the EDJ impacts on extreme temperature events. They are broadly consistent with the four regions used by the IPCC Sixth Assessment Report (Iturbide et al., 2020). As the regionalization determines completely the following procedures, we repeated this analysis with ERA5 reanalysis to verify the consistency between databases and did not find relevant differences (Figure AVII.4).

These four homogeneous regions in terms of the EDJ influences on extreme temperatures are employed to define warm (cold) extreme events at regional scales. This is done by averaging TX (TN) over all grid points embedded in each region. Like the local definition, regional warm events occur when the regional mean TX exceeds the 95^{th} daily percentile of the climatological distribution during at least five consecutive days. The same procedure is followed for colds spells but using TN and imposing that the regional mean TN drops below the 5^{th} percentile.

VII.2 Synoptic patterns and associated Mechanisms

Once the regions are well delimited, we explore the synoptic patterns and the leading thermodynamic mechanisms associated with warm and cold spells. Respect to the latter, we use the temperature tendency equation (Holton & Hakim, 2012) to evaluate the contribution of key processes responsible for the temperature anomaly during the extreme events. There are several ways to compute the temperature tendency, but we consider the approximation to three terms: the horizontal advection (Equation VII.1) and adiabatic

warming (Equation VII.2) that are both computed at the 1000-850 hPa pressure levels, whereas the diabatic term (collecting radiative processes and heat fluxes) is estimated as a residual of the equation (Equation VII.3)

$$\left(\frac{\Delta T}{\Delta t}\right)_h (\lambda, \phi, t) = -\vec{v} \cdot \nabla_p T \quad \text{(VII. 1)}$$

$$\left(\frac{\Delta T}{\Delta t}\right)_v (\lambda, \phi, t) = -\omega \frac{T}{\theta}\frac{\partial \theta}{\partial p} \quad \text{(VII. 2)}$$

$$\left(\frac{\Delta T}{\Delta t}\right)_d (\lambda, \phi, t) = \frac{\Delta T}{\Delta t} - \left(\frac{\Delta T}{\Delta t}\right)_h - \left(\frac{\Delta T}{\Delta t}\right)_v \quad \text{(VII. 3)}$$

where T is the air temperature, $\vec{v}$ the horizontal wind, ω the vertical velocity, and θ the potential temperature. λ, ϕ and t represent longitude, latitude and time, respectively. The different terms have been detrended in the same way as the temperature fields. For each grid point and day, we calculate the daily anomalies of these terms, identifying the leading process (i.e. the term with the largest contribution to the temperature tendency anomaly).

Figure VII.2 displays the composite maps of anomalous geopotential height at 500 hPa (Z500, in contour) for regional cold and warm extreme events, together with the statistically significant TN and TX anomalies, respectively. In general, regional cold spells occur under an anomalous anticyclonic circulation, typically located to the north or northwest of the affected region (Figure VII.2a-d). In fact, the location of the positive Z500 anomaly determines the region where the extreme event will occur. The effect of the high-pressure system on the occurrence of extreme temperature events is two-fold. On one hand, it prevents westerlies from bringing warm and moist air masses to the region (e.g., Liu, 1994; Nakamura & Huang, 2018). On the other hand, the anticyclonic circulation leads to an anomalous (geostrophic) wind from the Arctic or continental regions into warmer latitudes (e.g., Walsh et al., 2001). An assessment of the leading mechanism triggering regional cold spells confirms that, among the different contributions (i.e. horizontal advection (o), adiabatic warming (.), and diabatic processes (x) in Figure VII.2), cold spells are dominated by horizontal advection in all regions. Although the cooling is further exacerbated by other processes (e.g., reduced cloudiness and enhanced longwave radiation over WMED, Figure VII.3), they are of secondary importance compared to the

horizontal advection. In the case of cold spells over SCA, cold temperatures are restricted to the area northwards of 50°N (Figure VII.2a). In contrast, when a cold spell occurs in CEU,

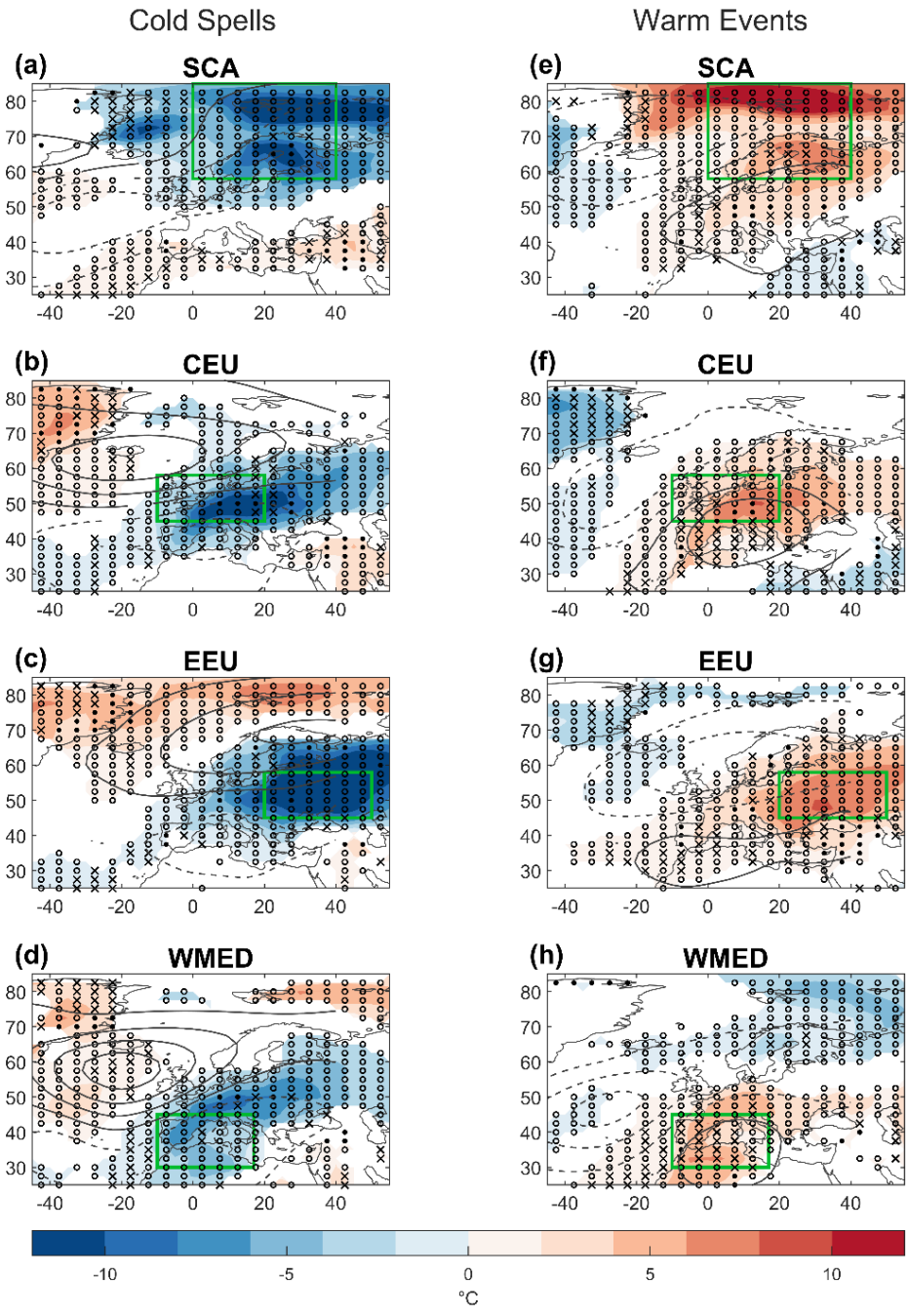

Figure VII.2 Atmospheric patterns associated with regional cold (left) and warm (right) extreme events. Colour shadings depict anomalies in TN (left) and TX (right) ([°C]). Solid (dashed) contours represent positive (negative) Z500 anomalies ([m]), with contour interval starting at 25 m and drawn every 50 m. We only show statistically significant anomalies at the 95% confidence level for both variables. The statistically significance has been computed by applying a Monte Carlo test with 1000 random permutations. Symbols denote the term with the largest contribution to the temperature changes at each grid point: horizontal advection (○), adiabatic warming (●), and diabatic processes (x). The green box indicates the region of extreme event occurrence. ††

EEU, or WMED, other large areas of Europe can also experience cold temperatures, but extreme values are confined to the specific region of study (Figure VII.2b-d). It should be noted that for specific cases, the large-scale circulation anomalies may result in simultaneous cold extreme events over nearby regions. However, the main conclusions do not change when concurrent events are excluded from the analysis (Figure AVII.5 and Figure AVII.6).

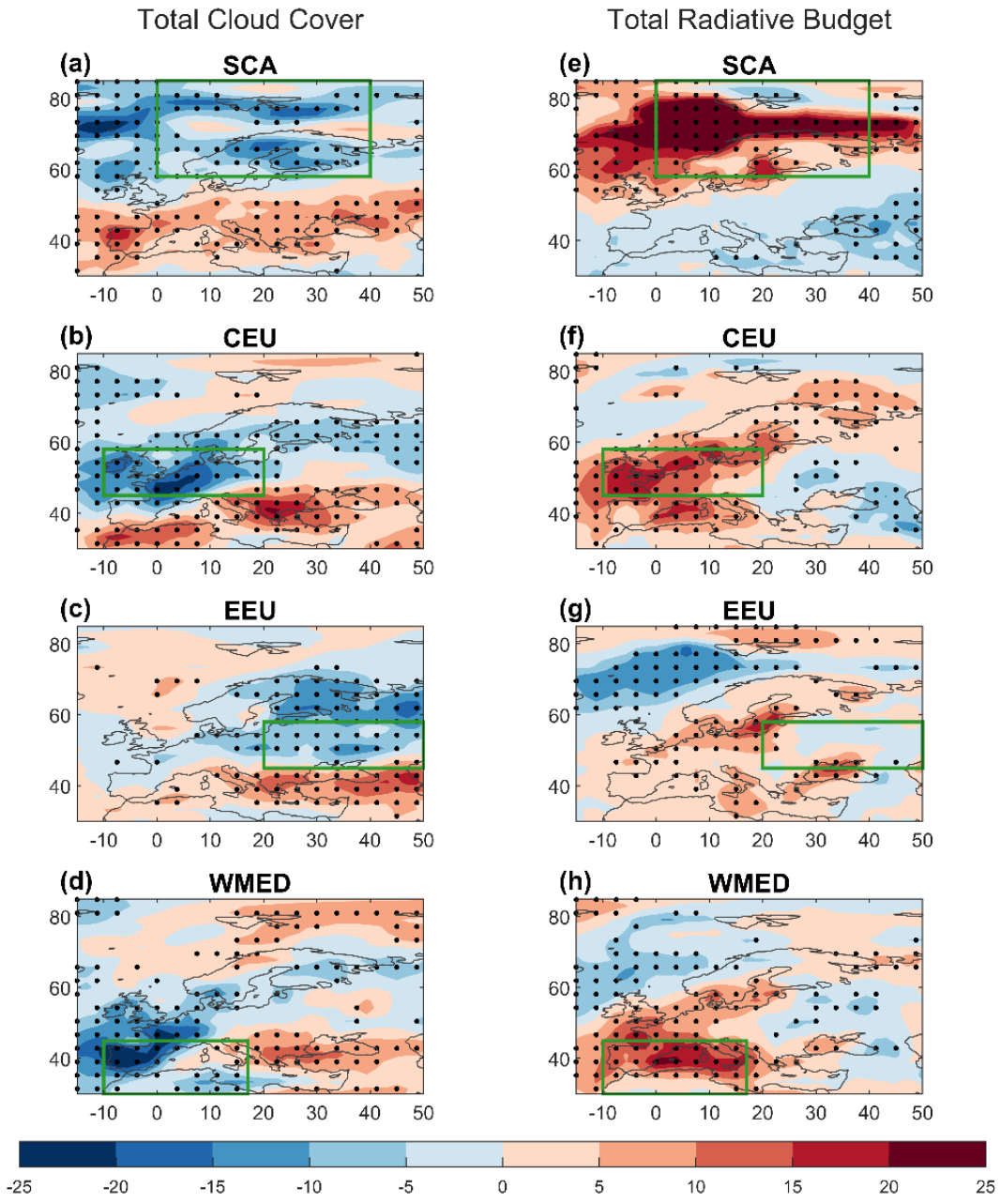

Figure VII.3 Composites of total cloud cover (a-d) and total radiative budget (e-h) anomalies for regional cold spells. Colour shadings depict the anomalies of total cloud cover (a-d; [%]) and upward radiation fluxes (e-h; [Wm^{-2}]). Statistically significant anomalies at 95% confidence level are indicated with the stippling. ††

In the case of regional warm extreme events, the associated circulation pattern consists of a meridional Z500 dipole, with varying location and orientation depending on the considered region. The dipole configuration is associated with a strengthened meridional Z500 gradient and enhanced westerlies from the NATL, bringing warm and moist air masses to the different regions. The thermodynamic equation confirms that the anomalous horizontal advection is the dominant term contributing to warm extreme events in the three northern regions.

In contrast, the diabatic term is the most important term in WMED, even in the presence of warm advection. Composite maps of cloudiness indicate significant positive anomalies over the region during WMED warm events (Figure VII.4d). Clouds do not allow longwave radiation to escape to the space, but they absorb it and reemit it to the surface, reducing the net longwave cooling at the surface (Figure VII.4h). The enhanced downward longwave radiation leads to a surface warming and explains the dominance of the diabatic term. Clouds are also associated with reduced shortwave radiation at the surface, but this effect is negligeable in comparison with that on the longwave radiation (Figure AVII.7). These results agree with Sousa et al. (2018) who analysed the radiative effects of winter blocking and subtropical ridges in Europe.

Near-surface temperature anomalies during warm events also present a large extension, but their absolute value is smaller than during cold spells for all regions, except for SCA. This asymmetry between warm and cold events is also observed in the horizontal advection term (Table VII.1). For regions with high temperature asymmetries (i.e. CEU, EEU, and WMED), absolute anomalies in horizontal advection are also greater for cold spells than for warm events. The asymmetry in the horizontal advection can be explained by the different dominant component (zonal advection for warm extremes and meridional advection for cold extremes) and more pronounced meridional thermal contrasts. Conversely, in SCA, the horizontal advection anomalies are of similar magnitude during cold and warm extremes, as it is also the case of temperature (Figure VII.2a and e). Asymmetries in other processes such as the radiative fluxes associated with cloud cover could also contribute to the asymmetric temperature responses, particularly in WMED, where the diabatic term acquires major relevance (cf. Figure VII.3h and VII.4h). In this sense, it is worth recalling that cold and warm events are assessed using TN and TX, respectively, and previous studies have reported a larger response of TN to cloud-mediated effects than that

of TX during both strong zonal flow and European blocking (Trigo et al., 2004). The enhanced westerlies during warm events are associated with increased cloud cover over large parts of the continent (Figure VII.4a-d), which dampens the warming of daytime TX due to reduced incoming radiation. Conversely, during cold spells, dry cold air masses favour clear skies, which enhance the nighttime longwave radiative cooling at the surface (Figure VII.3).

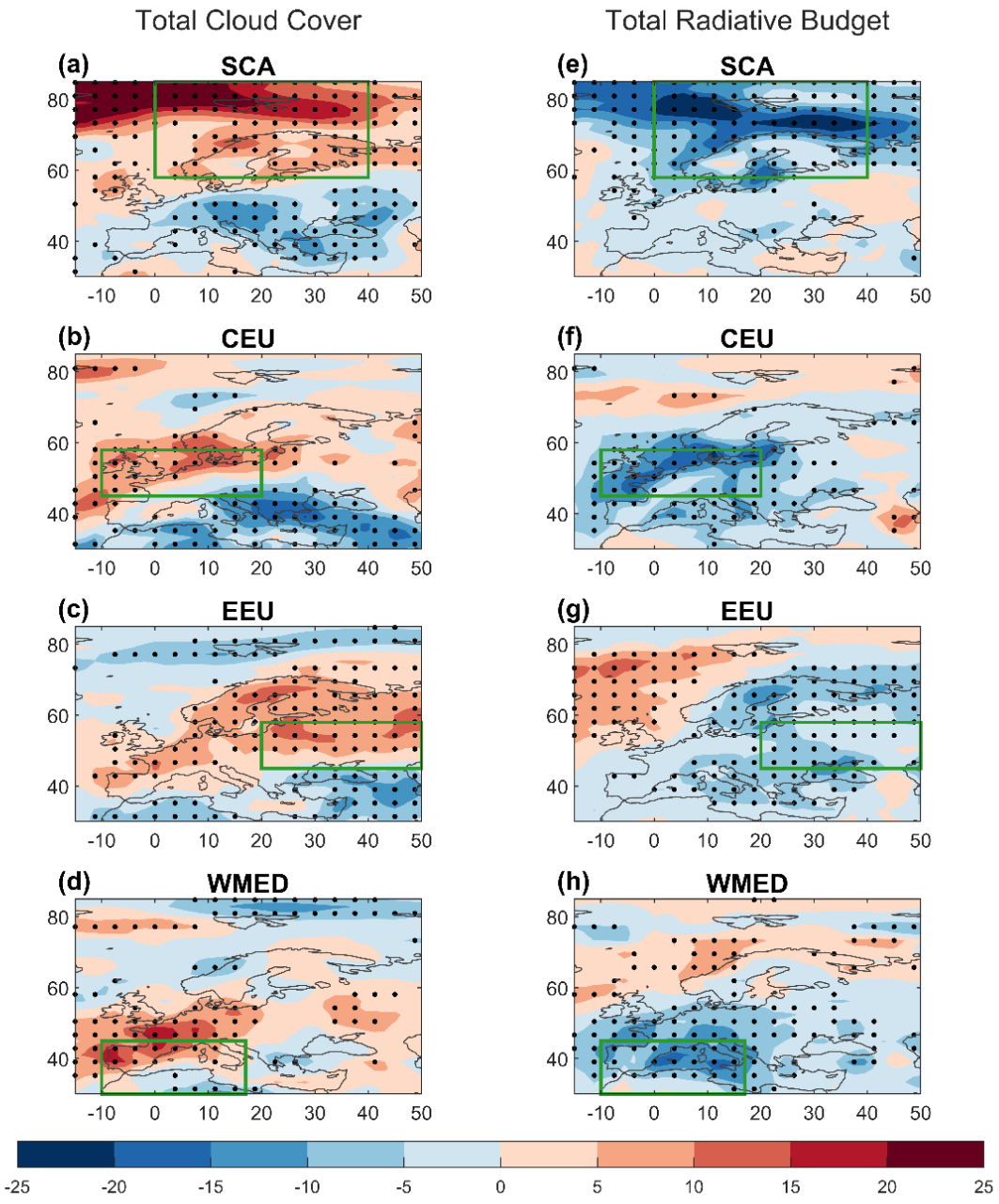

Figure VII.4 As Figure VII.3 but for warm events. ††

Table VII.1 Composited values of the regional mean horizontal advection anomaly ([°C day^{-1}]) during the occurrence of cold (first row) and warm (second row) events for the different regions (columns). Bold indicates statistical significance at the 95% confidence level after a 1000-trial Monte Carlo test.

	SCA	CEU	EEU	WMED
COLD	**-2.42**	**-2.46**	**-1.85**	**-2.16**
WARM	**2.67**	**1.24**	**1.16**	**1.09**

In addition to the magnitude of the TX and TN anomalies, the spatial patterns of warming and cooling associated with warm and cold spells are also asymmetrical, although in both cases the dominant mechanism is the horizontal advection (except for WMED). This asymmetry can be partially explained by similar asymmetries in the large-scale atmospheric patterns. For instance, the Z500 patterns associated with cold and warm extremes in SCA are not symmetrically opposite, being the cold one placed further west than the warm one (cf. Figure VII.2a and e). In this configuration, cold air masses cannot reach CEU, because their southward paths are partially blocked by the poleward flow induced by the anomalous NATL cyclonic centre. Conversely, during warm events, the corresponding high-pressure system is centred over Europe, allowing warm advection toward CEU through its northern branch. Something similar happens in CEU and WMED. In CEU, the anomalous flow associated with the temperature pattern is mostly zonal for cold spells (Figure VII.2b), but it shows an arched shape during warm events (Figure VII.2f), following the northern branch of the anticyclone. In WMED, cold event anomalies extend up to higher latitudes (~65°N) than warm event anomalies do (~50°N), because the Atlantic blocking associated with cold spells is placed further poleward than the low-pressure anomaly related to warm events (cf. Figure VII.2d and h).

VII.3 EDJ Structures

In this section, we describe the EDJ configurations associated with regional extreme events. The EDJ is represented in Figure VII.5 as the local frequency of occurrence in percentage with respect to the total number of winter days with regional extreme events (shading). We also show the corresponding frequency anomaly (in contours), as compared to the climatological mean winter frequency of EDJ occurrence.

Overall, there is a suppression of the EDJ over the region where cold extremes occur. However, the EDJ structures are very different across regions. Cold spells in SCA (Figure VII.5a) display the most distinctive pattern, characterized by an EDJ suppression at high latitudes and a southward shift. The former agrees with the anomalous easterly winds over the region (Figure VII.2a), whereas the latter is supported by the enhanced westerlies induced by the southern flank of the NATL low pressure (Figure VII.2a, ~35°N). This results in a single zonal EDJ structure at low latitudes (Figure VII.5a). When cold spells occur in CEU, the EDJ is also southward displaced, but at more equatorial latitudes than during SCA cold events (Figure VII.5b). It also displays a negative (NW-SE) tilt.

The high-pressure centred over Iceland (Figure VII.2b) denotes a negative phase of the NAO, which has been related to Greenland blocking and EDJs at southern locations (e.g., Woollings et al., 2010). At the same time, the anomalous westerlies in the equatorward flank of the Iberian low-pressure anomaly reinforce the eastward elongation of the EDJ. Although the southward shift is the most characteristic signature of the EDJ structure for cold spells in CEU, the relative frequencies of occurrence of southern EDJs are lower than for SCA because the EDJ is also detected at very high latitudes, resulting in a split-like structure. This split-like EDJ pattern is also detected during cold spells in EEU, but with the negative EDJ anomalies displaced toward the continent (Figure VII.5c). A similar eastward shift is also evident in the Z500 pattern, which is centred over Europe (Figure VII.2c). The associated anomalous easterlies at midlatitudes tend to confine the NATL EDJ to the western Atlantic. However, enhanced westerlies in the poleward and equatorward flanks of the European Z500 dipole result in a split-like EDJ structure over Europe, with northern and southern branches at extreme latitudes of the continent. Similar to CEU, the southern branch is more pronounced than the northern one, and displays a pronounced negative tilt. Finally, cold spells in WMED are associated with a poleward shifted EDJ (Figure VII.5d). The large negative frequency anomaly over the eastern NATL indicates a weakening of the midlatitude westerlies, and hence a reduced frequency of undisturbed (central) EDJs. This is consistent with the strong anticyclonic circulation anomaly over the NATL (Figure VII.2d), which also pushes the EDJ poleward by accelerating the westerlies in its northern flank. As a result, the zonal wind intensifies at high latitudes and downstream, favouring a northern and eastward displaced EDJ.

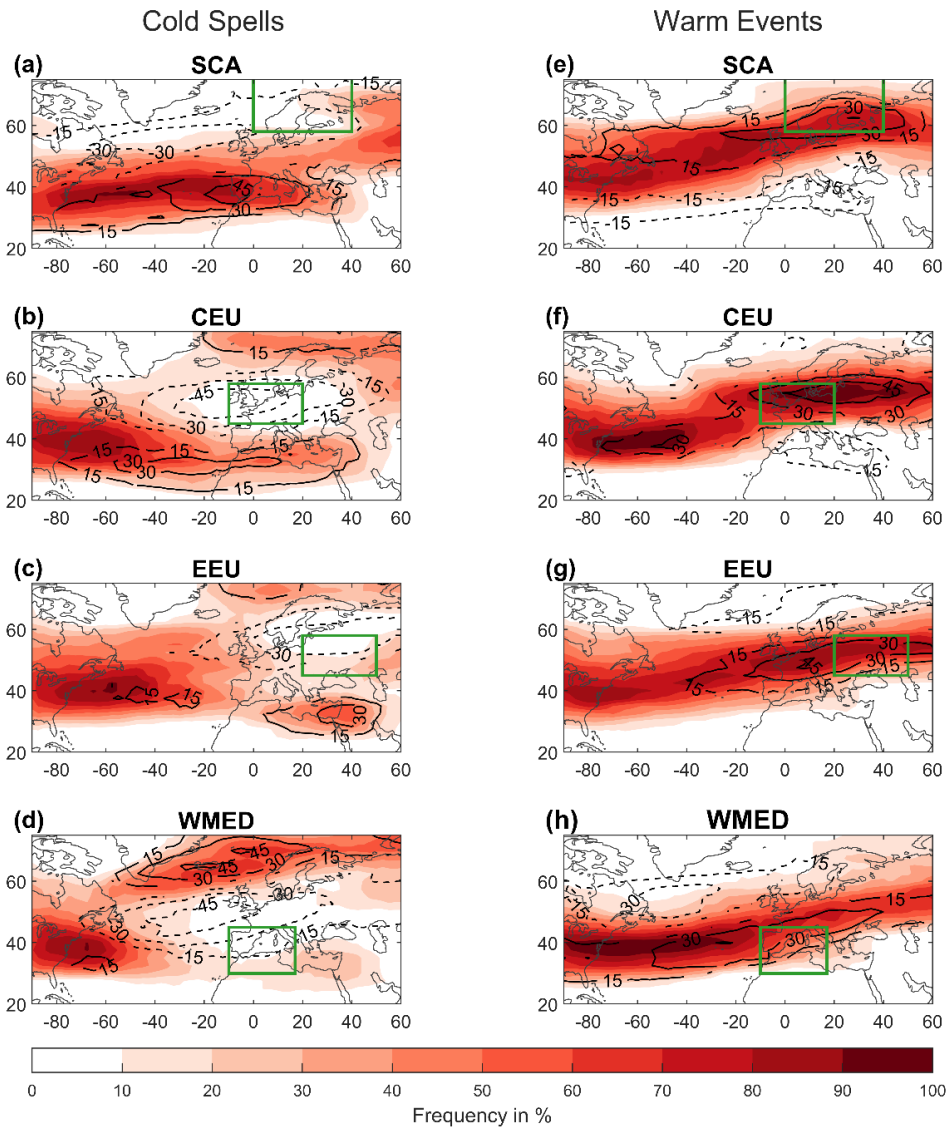

Figure VII.5 Eddy-Driven Jet (EDJ) structures associated with cold (left) and warm (right) regional extreme events over different European regions: (a, e) SCA; (b, f), CEU; (c, g), EEU; (d, h) WMED. Shading denotes the frequency of EDJ occurrence during regional extreme events (in percentage of days with respect to the number of days with a temperature extreme in this region). Contours show the corresponding frequency anomaly with respect to the climatological mean winter frequency. The contours are drawn every 15%. Only significant anomalies at the 95% confidence level (after a 1000-trial Monte Carlo test) are shown. The green box indicates the region of extreme event occurrence. ††

Before moving to the analysis of warm extremes, we address in more detail the split-like configurations associated with cold spells, which are particularly evident during CEU and EEU cold spells (Figure VII.5b and c). We ask whether the northern and southern branches of the EDJ are simultaneously present during these regional cold spells or if they result from mixing events with single EDJ structures at either poleward or southward latitudes. The latter would imply that cold spells in the aforementioned regions can occur

indistinctly with northern or southern EDJs. In fact, a more detailed analysis confirms this second hypothesis. The reason for the undefined location of the EDJ is found in the cold events that affect several regions simultaneously. The EDJ is more often detected at southern locations when CEU extreme events occur only in that region (Figure VII.6a). However, during simultaneous regional events, the EDJ can be found at northern or southern latitudes (Figure VII.6b), depending on the considered regions. For instance, poleward shifted EDJs tend to be common when cold spells occur simultaneously in CEU and EEU. The separation of EDJ structures is even clearer for cold spells in EEU: the EDJ is southward displaced for EEU-only events, but more often located at northern latitudes during concurrent cold spells (Figures VII.6c and d). The latitudinal position of the EDJ is thus case-dependent, which limits the role of the *Lat* as a relevant predictor of regional cold extremes, as described in the following section.

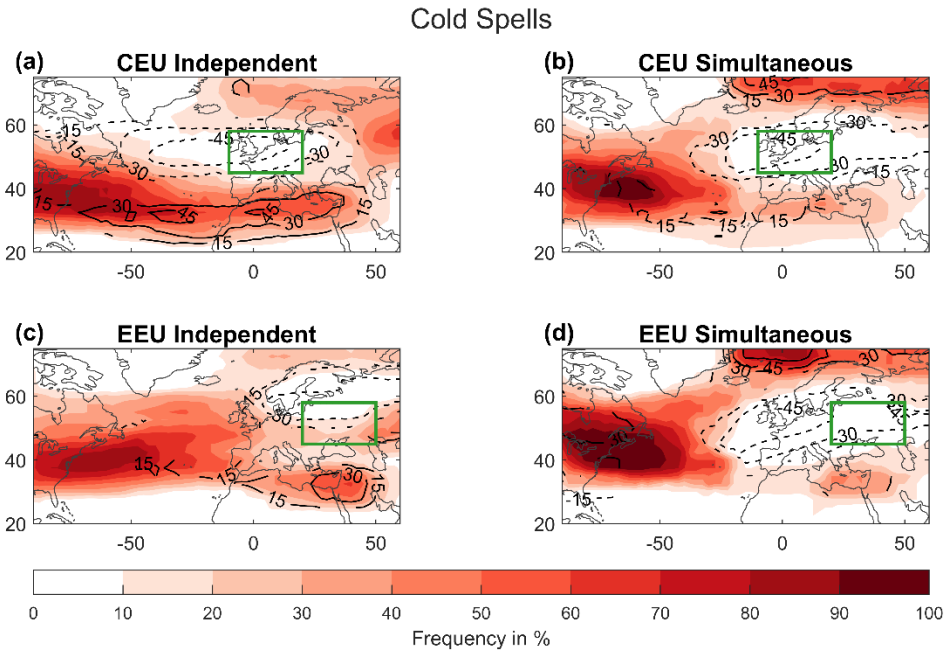

Figure VII.6 EDJ configurations associated with cold spells in CEU and EEU: independently (a, c) and simultaneously (b, d) to other regions, respectively. Shading denotes the frequency of EDJ occurrence during regional extreme events (in percentage of days with respect to the total number of winter days with regional extremes). Contours show the corresponding frequency anomaly with respect to the climatological mean winter frequency. The contours are drawn every 15%. Only significant anomalies at the 95% confidence level (after a 1000-trial Monte Carlo test) are shown. The green box indicates the region of extreme event occurrence. ††

Figure VII.5e-h displays the EDJ structures for warm events in the four regions of study. In this case, the EDJ is frequently found upstream and over the region of warm extreme occurrence, indicating a strengthening of the zonal wind and enhanced warm advection from the NATL toward the considered region (Figure VII.2e-h). Unlike cold spells, the EDJ patterns of warm events denote similar structures for all regions (typically, strong and tilted EDJs). Despite the resemblance of EDJ configurations in Figure VII.5e-h, there are some distinguishable features depending on the location of the warm event. The most remarkable difference is the latitudinal shift of the EDJ that can even be of opposite direction if the event happens in the WMED or in SCA (equatorward versus poleward shift, respectively; Figure VII.5e and h). Moreover, the EDJ is clearly displaced to eastern longitudes and shows small anomalies over the NATL during EEU events (Figure VII.5g). This is consistent with a zonal elongation of the Z500 anomalies toward the continent (Figure VII.2g), which allows the EDJ to extend farther east. Differently, CEU warm events are associated with marked zonal asymmetries in the EDJ (Figure VII.5f).

VII.4 Statistical modelling of extreme events as a function of the EDJ parameters

The previous sections provide a qualitative description of the EDJ configurations associated with the occurrence of regional temperature extremes over Europe together with the understanding of the involved processes. Now, we show that the 2D EDJ structures can be summarized by a number of parameters, which allow us to quantify the influence of the EDJ on regional extreme events and identify critical EDJ aspects for their occurrence.

The relationship is modelled with a logistic regression (Wilks, 2011) of the probability of occurrence of regional extremes onto category-based time series of the EDJ parameters (Equations VII.4 and VII.5). The model is fitted for each region separately to estimate how the EDJ parameters increase or decrease the probability of experiencing an extreme event.

$$logit\left(p(d)\right) = log\left(\frac{P(d)}{\left(1 - P(d)\right)}\right) \qquad \text{(VII. 4)}$$

$$logit\big(p(d)\big) = b_0 + \sum_{i=1}^{n} b_i \cdot JetParam_i(d) \qquad \text{(VII. 5)}$$

In Equation VII.4, $P(d)$ is the probability of occurrence of a temperature extreme on a given day and $p(d) = P(d)/(1 - P(d))$ corresponds to the odds of extremes, defined as the ratio of the probability that they will occur over the probability that they will not occur. The odds of extremes are modelled in Equation VII.5 assuming a linear relationship with the predictors (EDJ parameters). This is the so-called logit transformation, where the coefficients (b_i) are estimated using the maximum likelihood method (Wilks, 2011). In Equation VII.5, $JetParam_i(d)$ are binary sequences indicating whether the EDJ parameters are in a certain state or not on the day the extreme is detected. As EDJ parameters are continuous variables, each of them is converted to three different binary time series, one per tercile category. For a given day, these series indicate if the parameter is in that tercile (one) or not (zero). The regressions are estimated for all possible parameter combinations. The best combination of predictors for each region and type of extreme is selected based on both the coefficient of determination R^2, and the values of the exponential of the regression coefficients (e^{b_i}). These indicate the increase (if above 1) or decrease (if below 1) of the odds of observing a temperature extreme given that the EDJ parameters were in a particular state on that day. Therefore, the best combination is the one with the largest values of e^{b_i}, that is the regression model with the multiparametric EDJ states that increase the most the probability of triggering an extreme.

Another consideration is the selection of the appropriate number of predictors (n) for each regression model. The appropriate number is $n = 3$. To conclude this, we firstly test the regressions for all possible combinations of $n + 1$ predictors, starting with $n = 1$. Thus, we test whether the regression with $n = 2$ predictors is better than the $n = 1$, if so, we move on to test the regression with $n = 3$ predictors and so on. The choice of the best number of predictors relies on the fulfilment of two criteria. First, the fit based on $n + 1$ predictors must be significantly better than the n predictors fit. This comparison is made through the statistical coefficient Likelihood Ratio Test (LRT) at the 95% level (Wilks, 2011). The second criterion concerns the added value of the $n + 1$ predictor. This extra predictor is not included in the model when its e^b value is close to 1 or when the combined effects

of the $n + 1$ predictors do not substantially increase the odds of the extreme, as compared to the n predictors. By applying both criteria (Table AVII.1), we found that three is the number of predictors that best represents the relation between the EDJ parameters and extremes for all the regions, except for cold events in WMED, where we only need two.

Table VII.2 shows the 3-parameter combination that best explains the occurrence of extremes for each region (rows) and type of event (columns). The abbreviated names of the EDJ parameters are accompanied by a numeric suffix that informs about the tercile category that is linked to the extreme occurrence. For example, cold spells in SCA are related to EDJs with the northern border equatorward displaced, i.e. the *Latn* parameter is in the first tercile ($Latn_1$). For each parameter, the value in parenthesis indicates the number of times the odds of the extremes increase (e^{b_i}) when that parameter is in the corresponding tercile. Based on this metric, the EDJ parameters are ordered according to their importance in generating the extreme, being on the left the most important one. The corresponding Area Under Curve (AUC) values, which provide information on the ability of the models to distinguish between days with and without extremes, are shown in Table VII.2. The Receiver Operating Characteristics (ROC; Wilks, 2011) is a probabilistic curve that informs about how much the model is capable of distinguishing between classes (i.e. having or not having an extreme). It is constructed from the true and false positives predicted by the regression model when different cut-offs are considered to classify the model prediction into one class or another. The AUC is the area under the ROC curve and quantifies the degree of separability of the regression model: the higher the AUC, the better the model is at distinguishing between days with and without extremes. The maximum value that can be reached is 1, meaning that the regression perfectly distinguishes between classes. A value of 0.5 means that there is no discrimination between classes and the prediction is random.

For cold spells, we find that all regression models behave well and similarly across regions, with AUC values around 0.80. All five categories of EDJ parameters mentioned in section VII.1 (intensity, latitudinal and longitudinal aspects, tilt, and departure) are often necessary to distinguish where the event occurs, but their optimal combinations are very different depending on the considered region. A weak EDJ (Int_1) is the most important feature for cold spells in CEU and WMED. In both cases, the odds of cold spells at least

double when this EDJ condition is present. This is consistent with the generalized EDJ suppression reported in the previous section.

Table VII.2 Best performing EDJ models for the odds of regional extremes. For each region (rows) and type of extreme (columns), four columns are provided with the three EDJ parameters that most increase the odds of that regional extreme (ordered, from left to right, according to their importance), and the performance of the logistic regression model, defined as AUC. The suffix that completes the name of the EDJ parameter indicates its tercile (i.e. Int_3 = strong, Int_1 = weak EDJ). The number in parenthesis shows the times the odds of the extremes increase ($\exp(b_i)$) when the parameter is in the indicated tercile.

	Cold spells			AUC	Warm events			AUC
SCA	$Latn_1$ (10.0)	Dep_2 (3.1)	Int_3 (2.2)	0.81	Til_3 (2.5)	Int_3 (2.3)	Dep_3 (1.7)	0.64
CEU	Int_1 (4.7)	$Latn_1$ (3.9)	Til_1 (2.3)	0.82	Til_3 (5.7)	Lat_1 (3.2)	Int_3 (2.0)	0.72
EEU	Lon_1 (2.3)	Sh_1 (1.9)	Til_1 (1.9)	0.70	Sh_3 (2.6)	$Tilt_3$ (2.4)	Lon_3 (1.6)	0.66
WMED	Int_1 (7.6)	Lon_3 (3.5)	-	0.80	Lat_1 (10.1)	Til_3 (3.7)	Int_3 (1.9)	0.80

Despite this agreement, the rest of the parameters are different. In the case of CEU, cold spells are favoured by southward constrained EDJs ($Latn_1$), as much as by weak EDJs (see also Figure VII.5b). For WMED, the odds of cold spells increase if, apart from being weak, the EDJ is also westward displaced. In EEU, the extremes are enhanced when the EDJs are wide (Sh_1), which are usually also weak. However, zonal asymmetries, i.e. a negative tilt (Til_1) and westward displacement (Lon_1), are important EDJ parameters for cold spell occurrence, as described in the previous section (Figure VII.5c). Contrary to the rest of regions, the most favourable EDJ configuration for cold spells in SCA requires a strong EDJ (Int_3). Although this may sound counterintuitive to the idea of a local suppression of the EDJ, we note that this condition comes with a southward shifted EDJ ($Latn_1$). These two conditions imply a strong EDJ at southern latitudes, which is also associated with zonal wind weakening over SCA (see also Figure VII.5a). Hence, all parameters must be considered together when interpreting the optimal EDJ configuration.

We also note that, contrary to the traditional view, latitudinal parameters are not the leading aspects of the EDJ for cold spells, and they do not appear in two out of the four regions considered. This result should not be overstated, though, since other EDJ

parameters, or combinations thereof, can implicitly include information on the EDJ latitudinal position (see more details in Barriopedro et al. (2023)). For example, a northward EDJ is usually displaced to the east, and hence the preference for Lon_3 EDJ states during WMED cold spells is also informing on the EDJ latitude. Nevertheless, it is important to note that latitudinal parameters are not selected as the leading EDJ aspects of cold spells. This agrees well with the fact that latitude is not a discriminant parameter for the region of occurrence of cold spells, particularly in regions experiencing concurrent cold spells. As described in the previous section, apparent split-like EDJ patterns during CEU and EEU cold spells result from averaging concurrent and single cold spells, which present EDJs at very different latitudinal positions. Therefore, in regions with a relatively high frequency of concurrent cold spells (e.g., EEU), latitudinal parameters are not expected to add much skill to the model performance. When explicitly included (e.g., CEU), the model captures the main pattern that leads to (single) cold extremes, but it would fail during concurrent cold spells associated with other latitudinal positions of the EDJ. In summary, these results are consistent with the 2D EDJ configurations described in the previous section (Figures VII.5a–d), but they allow a quantitative assessment and identification of the most salient EDJ aspects related to regional cold spells.

For warm events, all regional models display similar AUC coefficients of around 0.70 (Table VII.2), which is slightly worse than those for cold spells. The differences in model performance to opposite temperature extremes may suggest type-dependent influences of the EDJ or missed EDJ attributes in our set of parameters. The case of SCA is noteworthy, since it shows by far the largest change in AUC, with one of the best performing models for cold spells but the worst one for warm events. However, in this case, the flawed representation of SCA warm events is aggravated by an inhomogeneous distribution of cases across the analysed period, which hampers the fit of the model (Figure AVII.8). Unlike cold spells, the optimal combinations of EDJ parameters are not so different across regions (Table VII.2), confirming that regional warm events occur under similar EDJ structures (Figures VII.5e-h). Warm events in the four regions are associated with a positive tilt of the EDJ (Til_3). In addition, in three out of four regions, a strong (Int_3) and, in two out of four, a southward shifted (Lat_1) EDJ is a favourable condition for the occurrence of warm events. For regions sharing the same EDJ parameters, the model is not expected to differentiate where the extreme event may take place. However, additional relevant information can be

gleaned from the relative importance of the selected EDJ parameters. A good example is found in CEU and WMED. Both regions show exactly the same parameters but ordered differently, i.e. their relative importance in the generation of the event is different. If the EDJ is southward displaced, it is several times more likely to report a warm extreme in WMED than in CEU (10.1 versus 3.2), whereas if the positive tilt is the most remarkable feature of the EDJ, warm events will have higher chances to occur in CEU than in WMED (cf. Figs VII.5f and h). In the rest of the regions, there are other discriminant EDJ parameters such as *Lon* (in EEU) and *Dep* (in SCA). These results confirm the importance of accounting for additional EDJ parameters, other than the latitude and intensity.

When cold and warm events are considered together, the *Til* parameter shows a great influence in generating temperature extremes, since it is selected in six out of eight regional events (in as many models as *Int*). This result agrees with the key role of the horizontal advection in triggering temperature extremes. The *Til* informs on the EDJ orientation and so, the direction that the cold and warm air masses will follow when advected by the EDJ. A positive (SW-NE) *Til* implies that the EDJ brings warm air masses from lower to higher latitudes, increasing the probabilities of experiencing warm extremes by advection. Similarly, NW-SE tilts are commonly present during cold spells. Interestingly, the *Int* is not the leading parameter in most regional models, particularly those for warm events, which may be counterintuitive with the key role of horizontal advection in temperature extremes. This is arguably because a relatively strong zonal wind, characteristic of warm events, is already implicit in the detection of the EDJ, which searches for zonal wind maxima. Furthermore, extreme events (in particular cold spells) are also strongly mediated by the meridional component of the wind, which is not accounted for by *Int*.

To further stress the added value of our EDJ parameters with respect to the traditional ones (*Lat* and *Int*), in Figure VII.7, we compared the total increase in the odds of regional events predicted by the combinations presented in Table VII.2 with that obtained when either only *Lat* or *Lat* and *Int* together are considered. In all cases, the maximum increase in the odds of regional extremes is obtained for our models of Table VII.2. Although the regions attaining the highest odds (dark purple boxes) include both latitudinal and intensity parameters in their models (SCA and CEU for cold spells and CEU and WMED for warm events), the consideration of an additional EDJ aspect yields an abrupt increase in the probability of occurrence. The improvement is particularly notorious in CEU and WMED,

where the *Til* brings at least a fivefold increase in the odds of warm events as compared to the *Lat-Int* model.

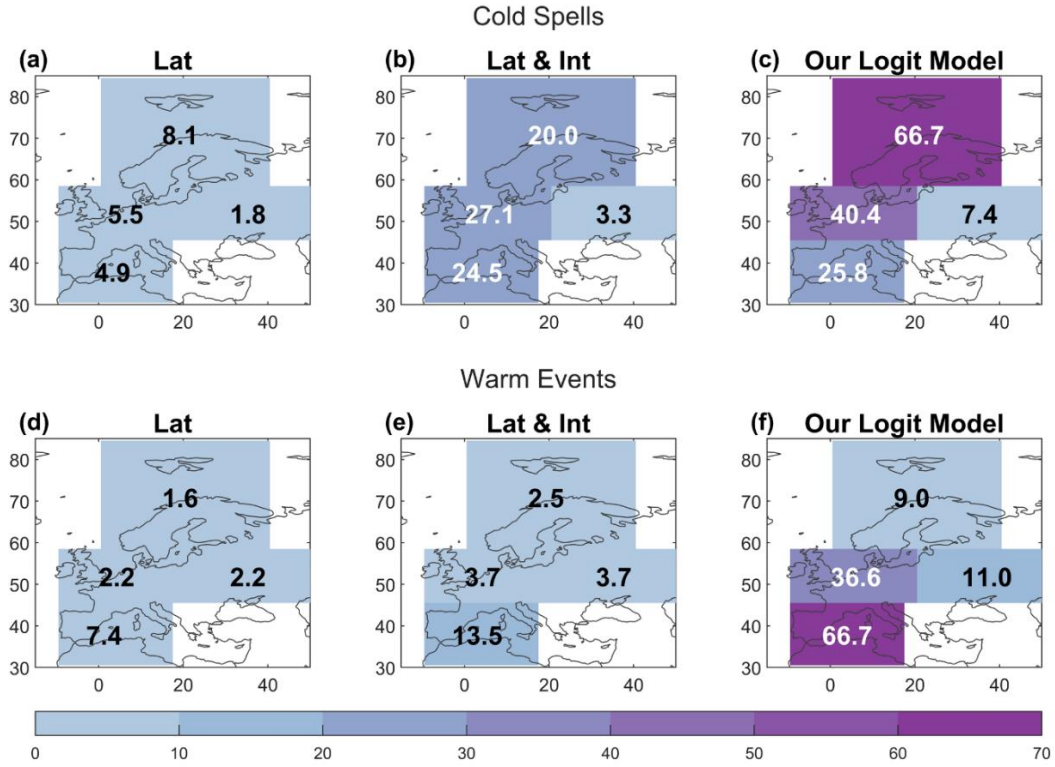

Figure VII.7 Increase in the odds of regional cold spells (a-c) and warm events (d-f) for the four regions under the joint action of different selections of Eddy-Driven Jet (EDJ) parameters: *Lat*-only (a, d); *Lat* and *Int* (b, e); the combination of EDJ parameters of Table VII.2 (c, f). ††

This change is much higher than the doubling odds after including *Int* to the *Lat*-only model. As for cold spells in SCA and CEU, the probabilities increase by at least 1.5 times with respect to the *Lat-Int* model when zonal asymmetries (either *Dep* or *Til*) are also accounted for.

For the other regional events, our best model does not even include the two basic aspects of the EDJ captured by *Lat* and *Int*, meaning that other EDJ parameters are more informative. Accordingly, the predictive skill of the corresponding *Lat-Int* models is worse than for the regional events described above (exception made for WMED cold spells). In these cases, the increase in the odds of extreme events predicted by our model at least doubles that of the *Lat-Int* model, which is higher than the gain brought by the *Lat-Int* model over the *Lat* model alone. The only exception is WMED cold spells, for which our model is only slightly better than the Lat-Int model. This behaviour was expected since for

this case, our logit model only selects two parameters, *Int* and *Lon*, and the latter is related to *Lat*. Therefore, its performance is similar to that of the *Lat-Int* model.

VII.5 Remarks

In this Chapter, we have studied the occurrence of wintertime 2m temperature extremes over different European regions, and their relationships with the NATL EDJ. We show that the multiparametric description of the EDJ helps to explain the occurrence of winter cold and warm events on regional scales. In particular, we find that EDJ effects on the occurrence of temperature extremes in different regions should be explained in terms of a complex EDJ configuration that can only be described by the combination of different EDJ parameters. This implies that assessments based on a single EDJ feature are oversimplified, particularly if the extreme requires specific EDJ configurations that affect several parameters of its structure.

We have identified four European regions with measurable effects of at least one EDJ parameter on extreme temperature events: SCA, CEU, EEU, and WMED. The occurrence of cold spells is associated with high-pressure systems advecting polar air masses to the area of interest. Warm events are related to enhanced westerlies by a low-high anomalous dipole over the NATL, which reinforces the horizontal advection of warm oceanic air masses. Although advection is the major contributor to the temperature anomaly for both types of extremes, diabatic processes play an important role in some regions (e.g., warm events in WMED). These findings are consistent with previous studies that described the impacts of blockings and/or strong zonal flow on extreme temperatures (e.g., Kautz et al., 2022 and references herein; Buehler et al., 2011; Trigo et al., 2004).

From the EDJ perspective, the spatial signatures of the EDJ patterns are also associated with regional extreme events. Overall, cold spells occur under a localized weakening of the westerlies over the region of extreme occurrence, which implies different rearrangements of the EDJ depending on the considered region. EDJ structures are more similar during regional warm events, which are in all cases associated with intensified and tilted EDJs, albeit with appreciable differences across regions. Therefore, cold and warm extreme events are associated with distinctive multiparametric states of the EDJ.

By employing statistical logit regression models, we have identified the EDJ parameters and states (tercile categories) that are more relevant for each type of extreme event and region. In all cases, we found that a limited number of EDJ parameters are required to achieve reasonable model performances. For almost all regions and types of events, the joint action of the selected EDJ parameters increases the odds of the extremes several times more than models based on the latitudinal and intensity parameters.

It is noteworthy that the EDJ intensity is a critical aspect for the occurrence of temperature extremes, being in agreement with the dominant role of horizontal advection in generating these events. Comparatively, the latitude is less often included. This is likely because the latitudinal position of the EDJ can often be inferred from other EDJ parameters (e.g., longitude), but also because some regional extremes can occur under northward and southward shifted EDJs. Finally, other EDJ parameters that have often been overlooked play an important role in the occurrence of extreme events. In particular, the tilt is included in more than half of the regional models, being selected as the leading EDJ parameter in some of them. Changes in the tilt tercile category imply substantial (at least twofold) variations in the odds of extreme occurrence, which are comparable to those deduced from the latitude or intensity of the EDJ.

Our results agree with previous studies that analysed the influence of specific NATL weather systems (e.g., Buehler et al., 2011; Trigo et al., 2004) or EDJ parameters (e.g., Mahlstein et al., 2012; Röthlisberger et al., 2016) on temperature extremes. An important asset and novelty of our approach is the decomposition of the 2D EDJ into a reduced multiparametric space, which allows us to describe complex EDJ configurations as a combination of interpretable EDJ parameters, and uncover the key aspects of the EDJ that are more relevant for the occurrence of extremes on regional scales. The method can be applied at different spatial scales, and to different types of extreme. Herein, it has enabled to extend the traditional analysis of winter cold spells to warm events, which have been much less studied in the literature. Finally, the multiparametric perspective considers several aspects of the EDJ simultaneously by means of different parameters. This represents a step forward with respect to the usual approach based only on one EDJ feature (e.g., Mahlstein et al., 2012; Röthlisberger et al., 2016), as it can account for more complex configurations. Very recently, and following the same rationale, Galfi & Messori (2023) have used three EDJ parameters (intensity, latitude, and zonality) to analyse the

relationship between persistent anomalies of the NATL EDJ and long-lasting precipitation and temperature extremes. They highlight that the zonality of the EDJ (a metric related to our *Dep* and *Til* parameters) affects the occurrence of temperature extreme events, as much as latitude and intensity. Our findings confirm these results, and expand them by considering additional EDJ parameters, different regions and specific modeling of single and combined EDJ influences on the odds of extremes.

VIII. EDJ Drivers and Mechanisms

The great influence of the specific configurations and parameters of the EDJ on the European surface temperature has already been proven in the previous Chapter. Considering the latter, exploring the diverse factors that affect the EDJ parameters becomes of interest. Although seasonal and interannual variability of the EDJ are usually related to internal variability (Lorenz, 1963), it can be also potentially forced by some remote drivers (Hall et al., 2015; 2017; Scaife et al., 2014). Bearing the latter in mind, in this Chapter we study the EDJ drivers in winter with a special focus on the mechanisms they follow to impact and modulate the EDJ.

The study of the EDJ drivers has become a topic of interest in recent years since a good understanding of their effects on EDJ allows improving the seasonal and interannual predictions. Thus, the detection of drivers that impact on these time scales becomes a central and meaningful aspect. In general, most attention has been focused on finding the EDJ drivers for winter (Hall et al., 2015) since, as already mentioned, this season presents the greatest variability. Several phenomena of the climate system have already been identified to impact on the EDJ. However, the study of their influence has been focused on the latitudinal framework, particularly, on the NAO. In addition, the drivers' effect on the EDJ has been studied separately, so the combined picture remains unknown. Here, we aim to quantify the drivers' impacts to ultimately identify the most relevant driver for the different EDJ parameters. By using ERA5 reanalysis/observations during the 1948-2022 period, we focus on quantifying the variance for each parameter that the drivers are able to explain. Further, we aim to detect the associated mechanisms, as well as, the differences that lead to the diverse impacts on the EDJ parameters.

VIII.1 Identification of the EDJ Drivers

From the set of potential large-scale drivers presented in the section II.2.3, we define below only those found to significantly impact on the EDJ. To characterize them, in some cases, the corresponding variable is simply averaged over a certain box in order to capture

the variability. However, due to the complexity of the climate system, sometimes isolating a specific climate process turns difficult and statistical discriminant techniques are required to define the process and capture its variability properly. For those cases, we use the *Empirical Orthogonal Function* (EOF) and *Maximum Covariance Analysis* (MCA, section IV.2) to define them. The EOF identifies the modes in which the climate variability of a field is organized, looking for patterns that explain the maximum amount of variance. EOF analysis is based on the covariance matrix obtained from a single spatiotemporal anomalies field. In a similar way, the MCA identifies the coupled modes of variability between two different variables, based on the 'cross' covariance matrix obtained from two distinct anomalies fields. Both methods provide the spatial structures and the time evolution series (so-called principal components in EOF and expansion coefficient in MCA) of the modes in which a single or a couple of fields vary.

- Definitions of the Drivers

All driver's indices consist of a 75-years monthly standardized time-series during wintertime (December-to-February; DJF), except for the North Atlantic Horseshoe which is defined for late summer (July-to-September; JAS). To visualize the drivers, their corresponding patterns are provided in Figure AVIII.1. Next, we provide their definitions and summarize their effects on the NATL circulation described in the literature:

- El Niño-Southern Oscillation (ENSO):
    - Pacific North America (PNA): Z500 expansion coefficient of the 1st mode of the MCA between the monthly North Pacific [150°E-60°W; 10°-80°N] Z500 anomalies and the equatorial Pacific [160°E-80°W; 5°S-5°N] SST anomalies. During El Niño events, positive PNA phase induces a negative NAO, characterized by a weakened and equatorward shifted EDJ (Pinto et al., 2010).
    - Tropical Northern Hemisphere (TNH): Z500 expansion coefficient of the 2nd mode of the previously described MCA. Negative TNH phase is related to a negative NAO, under El Niño conditions (Zou et al., 2014).

- North Pacific Oscillation - El Niño Southern Oscillation (NPO-ENSO): The SLP pattern difference between El Niño-Low NPO months minus La Niña-High NPO months is computed. NPO is defined as the 2nd principal component the monthly North Pacific [150°E-60°W; 10°-80°N] SLP anomalies. ENSO as the 1st principal component of the Equatorial Pacific [150°E-90°W; 5°S-5°N] SST anomalies. El Niño-Low NPO months are detected when ENSO and NPO indices are over and below 0.5 and -0.5 std, respectively. The opposite applies for La Niña-High NPO months. The NPO-ENSO driver is obtained by multiplying the SLP difference pattern and the SLP DJF anomalies field. The NPO phase modulates the entrance of ENSO signal in the NATL sector, potentially influencing the EDJ latitude (Pierce, 2002).

- Stratospheric Polar Vortex (SPV): Average of T100 anomalies northern to 65°N. The index has been multiplied by -1 so that positive values represent a stratospheric vortex stronger than usual. A disrupted vortex favours a weakening of the NATL tropospheric extratropical circulation (Baldwin & Dunkerton, 2001).

- Atlantic Meridional Overturning Circulation (AMOC): To capture temperature variations in the NATL subpolar gyre region, the difference of the averaged SST anomalies over the Northern Hemisphere and the Subpolar Gyre region [40°-30°W; 50°-55°N] is computed (Rahmstorf et al., 2015). An enhancement of the AMOC circulation (positive phase) leads to a warming and a reduction of the baroclinicity over Newfoundland and hence, a weakening of the EDJ and storm track (Woollings et al., 2012).

- North Atlantic Horseshoe (NAH): Z500 expansion coefficient of the 1st mode of the MCA between monthly DJF North Atlantic [100°W-20°E; 20°-80°N] Z500 anomalies and the JAS [100°W-20°E; 0°-65°N] SST anomalies. The summer season warming in the subpolar and eastern tropical NATL SST (positive phase) effectively induces a negative winter NAO (Czaja & Frankignoul, 2002).

- North America Snow Cover (SNOW): Timeseries of the North America snow cover extension. Data is only available since 1966, so the time series 1948-1965 interval is filled with missing values. The EDJ shifts southward under an increment of the North America snow cover, which is indicated by positive values of the index (Cohen & Entekhabi, 2001).

VIII.2 Impacts of the Drivers on the EDJ

We hypothesize that the wintertime EDJ variability can be partly understood as a linear combination of the impacts of different drivers. To verify this, we perform a multiple linear regression (MLR) between each of the EDJ parameters, as the predictand variable, and the EDJ drivers, as the predictor variables (Equation VIII.1). Thus, we can find the phenomena that influence every feature of the EDJ, as well as their relative importance. The process is repeated considering the 2D EDJ occurrence field as the predictand variable, (Equation VIII.2) to relate the EDJ structures and parameters:

$$Param = a + \sum_{i=1}^{N} b_i Driver_i + res \qquad \text{(VIII. 1)}$$

$$Freq_x = a_x + \sum_{i=1}^{N} b_{x,i} Driver_i + res_x \qquad \text{(VIII. 2)}$$

where the variables $Param$ and $Freq$ are the wintertime EDJ parameters and the 2D EDJ frequency, respectively. The coefficient a provides the expected response in the EDJ for no changes in the drivers, b_i gives the EDJ response to anomalies in the remote driver $Driver_i$, and res represents residual variations not captured by the linear regression. The suffix x represents the grid-point in the longitude-latitude plane.

The potential multicollinearity among the drivers is dealt by using a stepwise regression with forward selection and backward elimination, instead of a regular MLR. The reason is that the stepwise regression is specifically constructed for selecting a few variables that provide the best fit of the data while minimizing the overfitting of the model. To do so, the

method performs a subset of multiple regressions for selecting the best variables to include in the final model, instead of a single one. The method starts with an empty model and every time step the variables are introduced or removed based on their contribution to the total fit of the model. These contributions are evaluated with the p-value. Also, since potential overfitting can lead to unnecessary complex models, we also compute the Akaike's information criterion correction (AICc, Cavanaugh & Neath, 2019) which indicates the balance between the fitness of the model and its complexity. AICc favours the model that best explains the data with a minimum of predictors, i.e. the simplest model. We verify the model selected by the stepwise regression is also the one with the lowest AICc, among all the possible regression models constructed with our sample of predictors (Figure AVIII.2).

The drivers' impact on the main EDJ parameters is summarized in Figure VIII.1. Colours represent the magnitude of the regression coefficients with blue colours for negative values, and orange/yellow colours for positive ones. The predictors selected by the stepwise MLR are indicated with a cross. Similarly, the related impacts on the 2D EDJ structure are present in Figure VIII.2. The latitudinal parameters are the most influenced EDJ features by the drivers, presenting around a 30% of explained variance. The drivers are

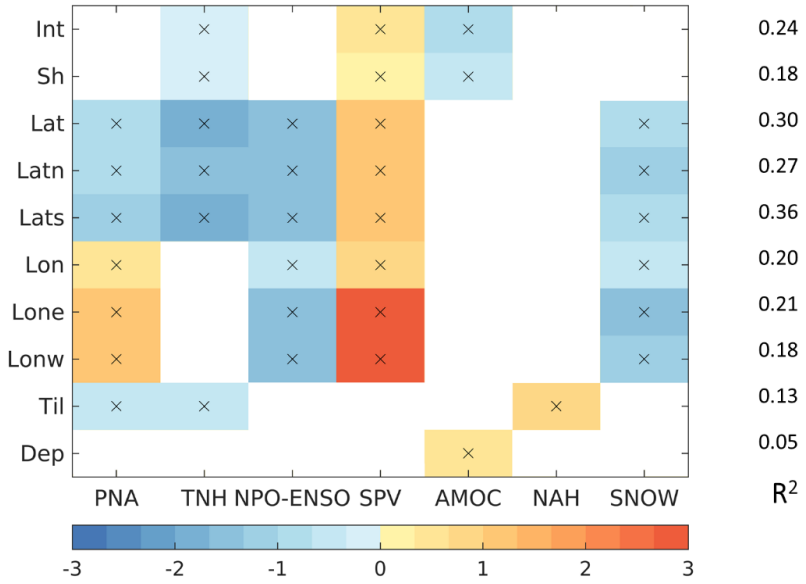

Figure VIII.1 Regression coefficients (*Int*, *Sh* [ms^{-1}]; *Lat*, *Latn*, *Lats* [°N]; *Lon*, *Lone*, *Lonw* [°E]; *Til*, *Dep* [°N/60°]) for the predictors of EDJ parameters. White cells indicate the predictor was not selected by the MLR model. The R^2 coefficient indicates the variance explained by the predictors found to be significant in the MLR model for each EDJ parameter.

PNA, TNH, NPO-ENSO, SPV and SNOW. Although ENSO related drivers agree on shifting the EDJ equatorward (Figure VIII.2a-c), they present differences when influencing the tilt, wind-speed and longitudinal related parameters (Figure VIII.1). The second most influenced parameters are the longitudinal ones which show the largest regression coefficients. The large SPV influence on *Lone* and *Lonw* is observed in Figure VIII.2d, where the great elongation of the EDJ crosses the whole of Europe. Further, the SPV appears as the most important driver, having an impact in almost all features. Although subtle, the AMOC is the only driver influencing *Dep*. The latter gives the AMOC impact pattern a characteristic shape, showing a double jet over [60°W-0°] (Figure VIII.2e).

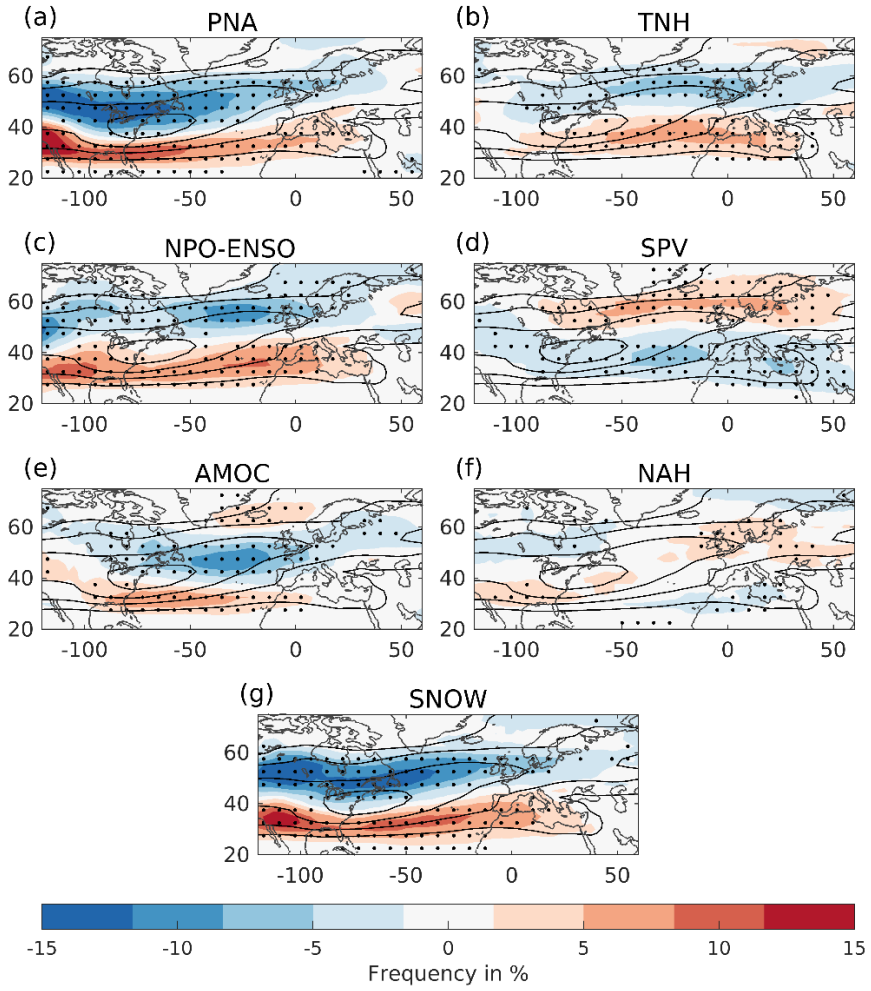

Figure VIII.2 2D EDJ frequency response under the influence of the EDJ drivers. Forced response in the EDJ frequency [%] associated with +1 sigma departure of the following EDJ drivers: (a) PNA, (b) TNH, (c) NPO-ENSO, (d) SPV, (e) AMOC, (f) NAH and (g) SNOW. Black contours show the 2D frequency climatology of the 1948-2022 period (starting at 10% and drawn every 30%). Stippling indicates significance at the 95% confidence level (i.e. local regression coefficients of the corresponding driver that are significantly different from zero).

A more detailed discussion about the detected relation between the drivers and the EDJ parameters is presented below. Also, we move on to explore the mechanisms that lead to these specific impacts on the EDJ. To do so, in the following section we analyse the state of some dynamical fields when the different drivers are active.

VIII.3 Mechanisms

Considering that the NATL baroclinicity, specially over the western entrance region, strongly influences the EDJ variability, we have computed the modulation of the latter by the drivers. Figure VIII.3 shows the regression maps of EGR at 500 hPa (shaded) together with the 2D frequency field (contours) onto the drivers' timeseries. The common behaviour among the large-scale drivers is that all of them present a statistically significant impact on the western NATL baroclinicity.

There is a high correspondence between the shift in the baroclinicity and the shift of the EDJ core region (green contours in Figure VIII.3). This behaviour is driven by the thermal-wind relation, which increases the vertical shear of the wind over regions with enhanced temperature gradient (Equation II.2). Therefore, in most of the cases, the patterns of the anomalous baroclinicity reflect the modified EDJ characteristics by the drivers (Figure VIII.2). ENSO related drivers, SPV and SNOW present a meridional dipole over the NATL basin, reflecting their impact on the EDJ latitudinal parameters. Similarly, the extension of each dipole provides a hint on the impact on the EDJ longitudes. For instance, the positive frequency anomaly in SNOW extends much more westward than the negative anomaly at higher latitudes (green contours in Figure VIII.3g), implying an EDJ westward elongated during increased snow cover episodes (Figure VIII.1; Figure VIII.2g). The same applies to PNA and NPO-ENSO during El Niño phases (Figure VIII.3a and c). Moreover, strong baroclinic anomalies over the EDJ frequency climatological maximum between [60°-0°W] reflect the impact on *Int* and *Sh*. This condition is satisfied by TNH, SPV and AMOC (Figure VIII.3b, d and e) which are the drivers that impact on the wind speed related parameters (Figure VIII.1; Figure VIII.2b, d and e). The split of the EDJ under the influence of an acceleration of the AMOC (positive phase) (Figure VIII.2e) is also clearly observed in the

anomalous baroclinic pattern, where the EGR is enhanced over Greenland and the subtropical NATL but reduced in the middle of the basin (green contours in Figure VIII.3e).

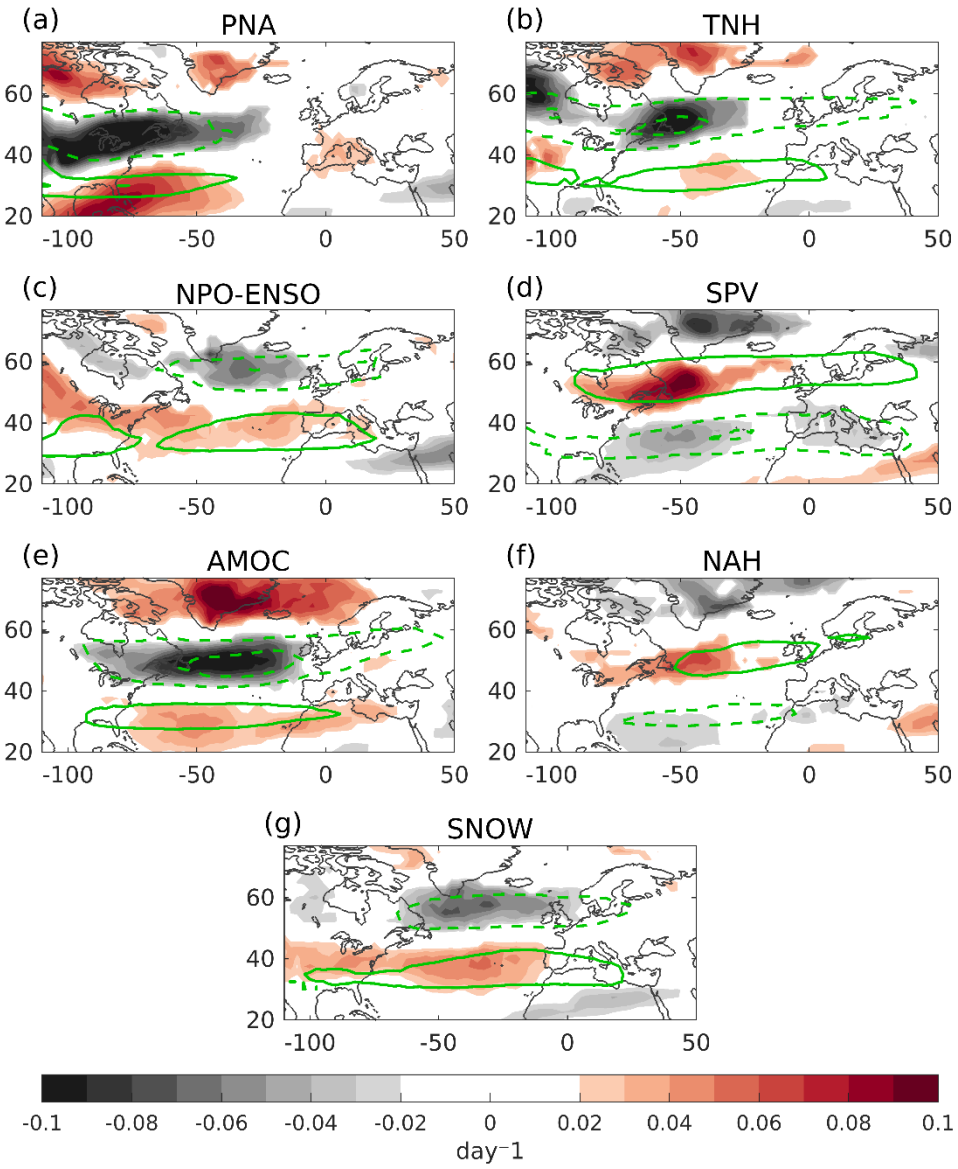

Figure VIII.3 Baroclinicity modification associated with the EDJ drivers. Regression maps of monthly wintertime fields of dynamical diagnostics onto the following EDJ drivers: (a) PNA, (b) TNH, (c) NPO-ENSO, (d) SPV, (e) AMOC, (f) NAH and (g) SNOW. Dynamical diagnostics include the Eady Growth Rate at 500 hPa (EGR, shading, [day^{-1}]) and 2D EDJ occurrence field (green contours, [%]). Green contours start at 5% and are drawn every 5%. Only statistically significant coefficients ($p<0.05$) are displayed.

Although many of the impacts on the EDJ parameters and 2D structure are consistent with the direct effect that the drivers produce on the baroclinicity, there are some impacts that cannot be explained by this mechanism, such as the enhancement of the EDJ

frequency in the jet exit region under the strong SPV and positive NAH influence (solid contours over Europe in Figure VIII.3d and f and positive significant frequencies in Figure VIII.2d and f). To provide a satisfactory response to this question, we inspect further dynamical diagnostics.

- Transient Pathway

The previous description about the impact of particular drivers on the EDJ features follows the geostrophic framework, where the modification of the baroclinicity induces anomalous winds that can enhance or disturb the climatological EDJ. However, the anomalous baroclinicity can further impact on the EDJ by another mechanism, namely, the generation of transient eddies. The NATL baroclinicity is intimately related to the EDJ since it establishes the conditions for the generation of transient eddies, which are the key elements that determine the EDJ variability. For this reason, in the following section we study the change in the available turbulent kinetic energy (EKE) induced by the drivers. This EKE will be used by the eddies to grow. Moreover, we analyse the propagation of the transient eddies and how they finally interact with the mean flow.

The shifts in the baroclinicity modify the regions where the baroclinic instabilities take place and hence, the regions with available EKE for the eddies (Vallis, 2006). The latter is observed in Figure VIII.4, where the regions with enhanced EKE are similar and downstream of those with enhanced baroclinicity (Figure VIII.3). The downstream displacement of EKE with respect to the baroclinicity appears because of the characteristic lifecycle of the transient eddies. The eddies amplify through the storm track and decay downstream (Hoskins & Hodges, 2002), when they interact with the mean flow (Thorncroft et al., 1993). The propagation of the anomalous transient eddies is also displayed, through the **E**-vectors, together with the zonal wind to observe the result of their impact. In most of the cases, the transient signal reinforces the geostrophic one. An illustrative example of the latter is the case of the AMOC influence. During warm SST conditions in the subpolar gyre region, the suppression of the baroclinicity in the western NATL ocean around 50°N (Figure VIII.3e) places a negative EKE region just downstream, in the eastern NATL ocean around 50°N (Figure VIII.4e). Considering that transient eddies act to re-establish normal baroclinicity conditions (Martin, 2006), the anomalous triggered eddies travel towards negative EKE

regions, converging around 50°N (Figure VIII.4e). Note that the meridional component of **E**-vectors is equal but negatively signed to the eddy momentum flux (Equation IV.2.4), so pole and equatorward pointing arrows imply an equator and poleward momentum transport respectively, and hence, a similar shift of the EDJ. The convergence of eddies implies a divergence of momentum, decelerating the zonal wind over 50°N and

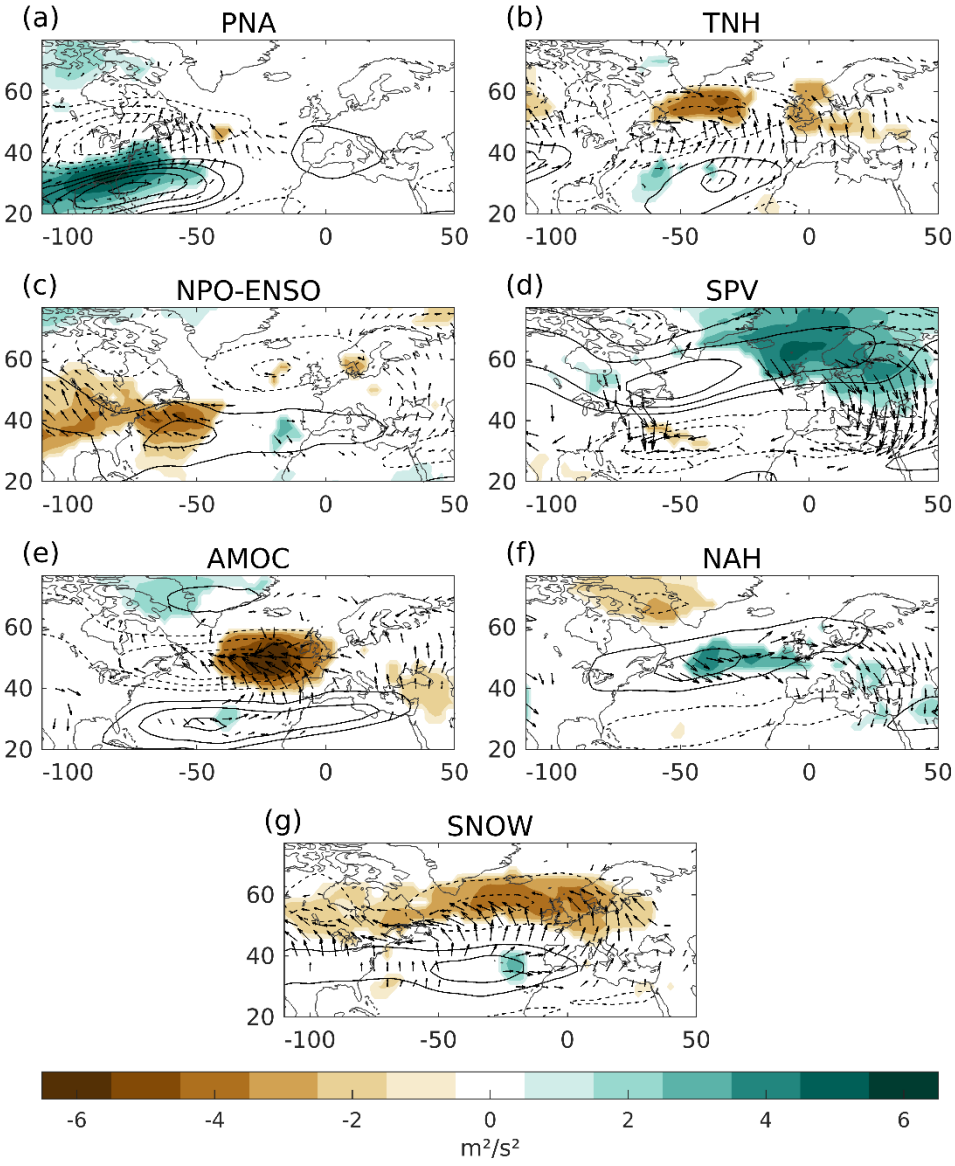

Figure VIII.4 Transient eddies associated to the EDJ drivers. Regression maps of monthly wintertime fields of dynamical diagnostics onto the indices of the following EDJ drivers: (a) PNA, (b) TNH, (c) NPO-ENSO, (d) SPV, (e) AMOC, (f) NAH and (g) SNOW. Dynamical diagnostics include EKE averaged between 1000-200 hPa (EKE, shading, [m^2s^{-2}]), wind at 200 hPa (contours, [ms^{-1}]) and **E**-vectors at 300 hPa (arrows, [m^2s^{-2}]). Only statistically significant coefficients ($p<0.05$) are displayed.

accelerating it pole and equatorward (contours in Figure VIII.4e). The latter results in a two-jet structure which affects the *Dep* and *Int* EDJ features.

Although the impact on *Int* and *Dep* is already understood, we provide the barotropic generation rate (**G**) and the cyclonic (CWB) and anticyclonic (AWB) RWB in Figure VIII.5 to better capture the interaction between the transient eddies and the zonal flow. The convergence of eddies is able to weaken the EDJ because they extract kinetic energy from downstream and decelerate the flow upstream (zonally-oriented dipole of **G** in Figure VIII.5e). The latter is consistent with the enhanced CWB activity on the western NATL, which grows at expenses of the mean flow and hence, weakens it (Trenberth et al., 1986). The presence of AWB at the same latitude of CWB modulates the impact on the zonal asymmetries. The combined action of both WB types supplies pole and equatorward momentum flux of the breaking latitude, respectively, leading to the impact on the *Dep* parameter.

Now, under the transient eddies' framework, the increment of the EDJ frequency in the EDJ exit region under the SPV and NAH positive phase influence (solid contours over Europe in Figure VIII.3d and f) can be explained. In both cases, the increment of the baroclinicity in the western NATL releases positive EKE downstream (Figure VIII.4d and f). By using the available energy, eddies can grow and travel eastward through the EDJ, interacting with it at the exit region, during the end of the eddies' life cycle. In the case of a strong SPV, the **E**-vectors deflect equatorward over Europe and diverge over the eastern NATL leading to a poleward convergence of momentum (Figure VIII.4d). Thus, the acceleration of the zonal wind over this region elongates the EDJ poleward and eastward in agreement with, the impact of these drivers on *Lat* and *Lon* related parameters in Figure VIII.1. The latter is consistent with the high frequency of AWB over central and eastern North Atlantic (Figure VIII.5d) that transport momentum poleward. The poleward migration of the EDJ is also consistent with the limited occurrence of CWB in the poleward side by the constraining effect of the latitudes on the propagating eddies (Barnes et al., 2010). This pattern of WB can be explained by the zonal dipole of **G**. Transient eddies extract kinetic energy upstream, leaving less energy for CWB, and deposit it downstream, providing more energy for AWB. Further, **G** dipole is also able to explain the impact on *Int* since accelerates the EDJ downstream. Moving to NAH, the eddies also travel equatorward over Europe under the

influence of this driver (Figure VIII.4f) shifting the EDJ poleward. In this case, the progressive eastward increment of the **E**-vectors meridional component, indicates a progressive poleward displacement of the EDJ along the NATL and hence, an impact on the *Til* parameter. The latter is consistent with an acceleration of the mean flow over Europe (purple shading in Figure VIII.5f), accompanied by an enhanced AWB frequency.

The same process applies for the other drivers. During El Niño phase, PNA and NPO-ENSO present strong anomalies of EKE and **E**-vectors over the western NATL and North America. Considering that these anomalies occur downstream of the baroclinic anomalies, the latter ones must locate upstream, in the North Pacific (Figure AVIII.3). Starting with the PNA, the equatorward shift of the baroclinicity over the subtropical North Pacific (Figure AVIII.3a) releases a large positive EKE anomaly over the region that travels downstream up to the subtropical NATL entrance region. The transient eddies triggered in the North Pacific basin travel eastward and shift poleward when they reach the western NATL (Figure AVIII.4a, Li & Lau, 2012; Drouard et al., 2015; Jimenez-Esteve & Domeisen, 2018). The equatorward momentum flux associated with the eddies is consistent with the enhanced CWB over Terranova and the suppressed AWB over Europe (Figure VIII.5a). Further impacts on *Til* are also associated with the suppressed AWB and so, the EDJ in its exit region is less northward shifted than normal. The NPO-ENSO modulation of the EDJ presents a comparable situation but with opposite sign. The modification of the baroclinicity upstream, over the North Pacific, generates an anomalous negative EKE region that propagates downstream, over North America and the western NATL. Therefore, anomalous poleward **E**-vectors are generated and the EDJ is shifted equatorward in the NATL entrance. In this case, as the total available EKE is lower than for the PNA case, the zonal wind is weaker over this region (contours in Figure VIII.4a and c). The transient wave activity is consistent with these impacts in *Lat* and *Lon* (Figure VIII.5c). Enhanced western CWB activity and suppressed eastern AWB, which indicate a southward shift of the EDJ, also lead to an EDJ confinement at the western NATL. These similar WB patterns associated with both parameters explain why poleward EDJs also tend to extend further downstream.

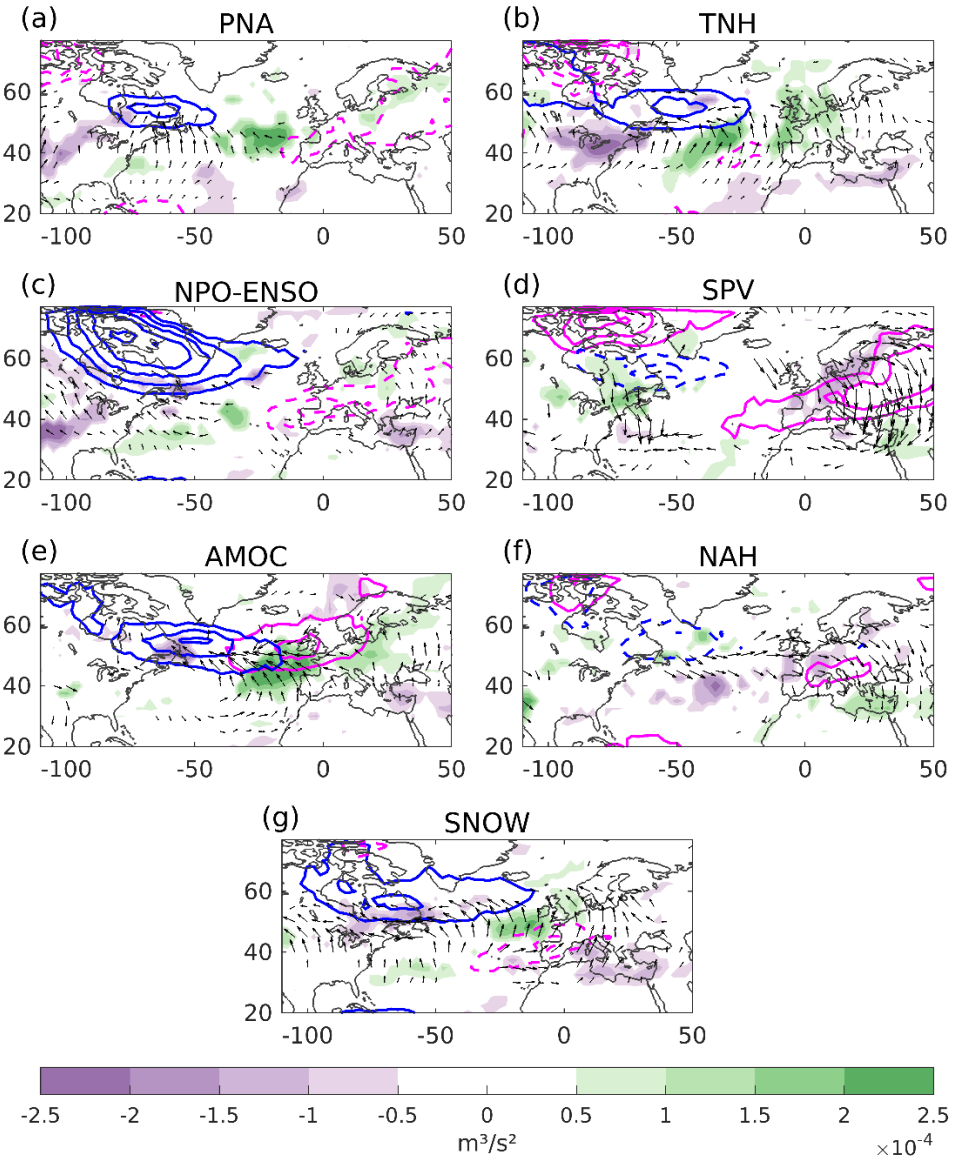

Figure VIII.5 Interaction between the transient eddies and the mean flow associated to the EDJ drivers. Regression maps of the monthly wintertime fields of dynamical diagnostics onto the indices of the following EDJ drivers: (a) PNA, (b) TNH, (c) NPO-ENSO, (d) SPV, (e) AMOC, (f) NAH and (g) SNOW. Dynamical diagnostics include the barotropic generation rate at 300 hPa (**G**, shading, [m^3s^{-2}]), wave breaking frequency at 2PVU (contours, with AWB in pink and CWB in blue, [frequency]) and **E**-vectors at 300 hPa (arrows, [m^2s^{-2}]). For a given type of wave breaking, we only show the signed correlations with the highest absolute coefficient. Solid and dashed contours denote positive and negative correlations. Only statistically significant coefficients ($p<0.05$) are displayed.

The TNH shows a different behaviour for El Niño phase since the transient eddies source is not upstream (Figure AVIII.4b). On the contrary, they are generated more locally (Figure VIII.4b). The negative baroclinicity anomaly over Terranova is related to the lower than

normal EKE over the NATL and central Europe, leading to the poleward pointing arrows across the whole NATL and European sector. The impact on *Lat* by the transient wave activity is similar to that found for PNA but stronger. The zonal dipole of G indicates both a large weakening of the EDJ and CWB frequency that shifts the EDJ southward (Figure VIII.5b). Finally, SNOW presents a similar behaviour to the TNH over the NATL, but it is stronger and originates over North America. The modification of the baroclinicity due to the presence of snow cover generates poleward transient eddies that break cyclonically and hence, transport momentum equatorward (Figure VIII.4g and 5g). The latter, leading to less AWB over Europe, also explain the westward elongation of the EDJ under increased snow cover extension conditions.

- Stationary Pathway

After analyzing the eddy-mean flow interaction related to the drivers, we explore how the signal travels in first place from the drivers' remote location to the NATL sector. To this end, Figure VIII.6 presents the regression maps of the stream function (shaded) onto the drivers' indices. The three ENSO related drivers are associated with strong stationary eddies in the stream function (Figure VIII.6a-c). The well-defined arched wave patterns, with alternating high and low circulations, arise from the equatorial Pacific, travel towards and through extratropical latitudes and reach the NATL. The different teleconnections reach the NATL with a specific pattern that shape the different impact on baroclinicity (Figure VIII.3). For instance, PNA wave imposes a latitudinal dipole pattern in the western NATL (Figure VIII.6a). This composition of pressure systems suppresses the baroclinicity around 50°N and enhance it over 30°N (Figure VIII.3a). Both TNH and NPO-ENSO also reach the NATL with a dipole pattern, but with some differences. While the TNH influence is only confined in the NATL basin (Figure VIII.6b), the NPO-ENSO effects span more longitudinally towards the continents (Figure VIII.6c). However, despite the difference between both patterns, they account for the equatorward shift of the baroclinicity during their positive phases (Figure VIII.3b-c), suppressing it around 55°N and reinforcing it at 30°N. The quasi-stationary wave structures can be enhanced and maintained by the interaction of the downstream propagating and locally generated baroclinic waves with the EDJ (Cassou & Terray, 2000; Pozo-Vázquez et al., 2005; Graf & Zanchettin, 2012).

The rest of the drivers do not show wave patterns but, meridional dipoles over the NATL (Figure VIII.6d-g). These stream function patterns lead to the anomalous enhancement or suppression of the baroclinicity over the western of the basin around 50°N (Figure VIII.3d-g). The four structures are consistent with previous studies about the drivers' impact on the NAO (Kidston et al., 2015; Gastineau et al., 2016; Czaja & Frankignoul, 2002; Cohen & Entekhabi, 2001).

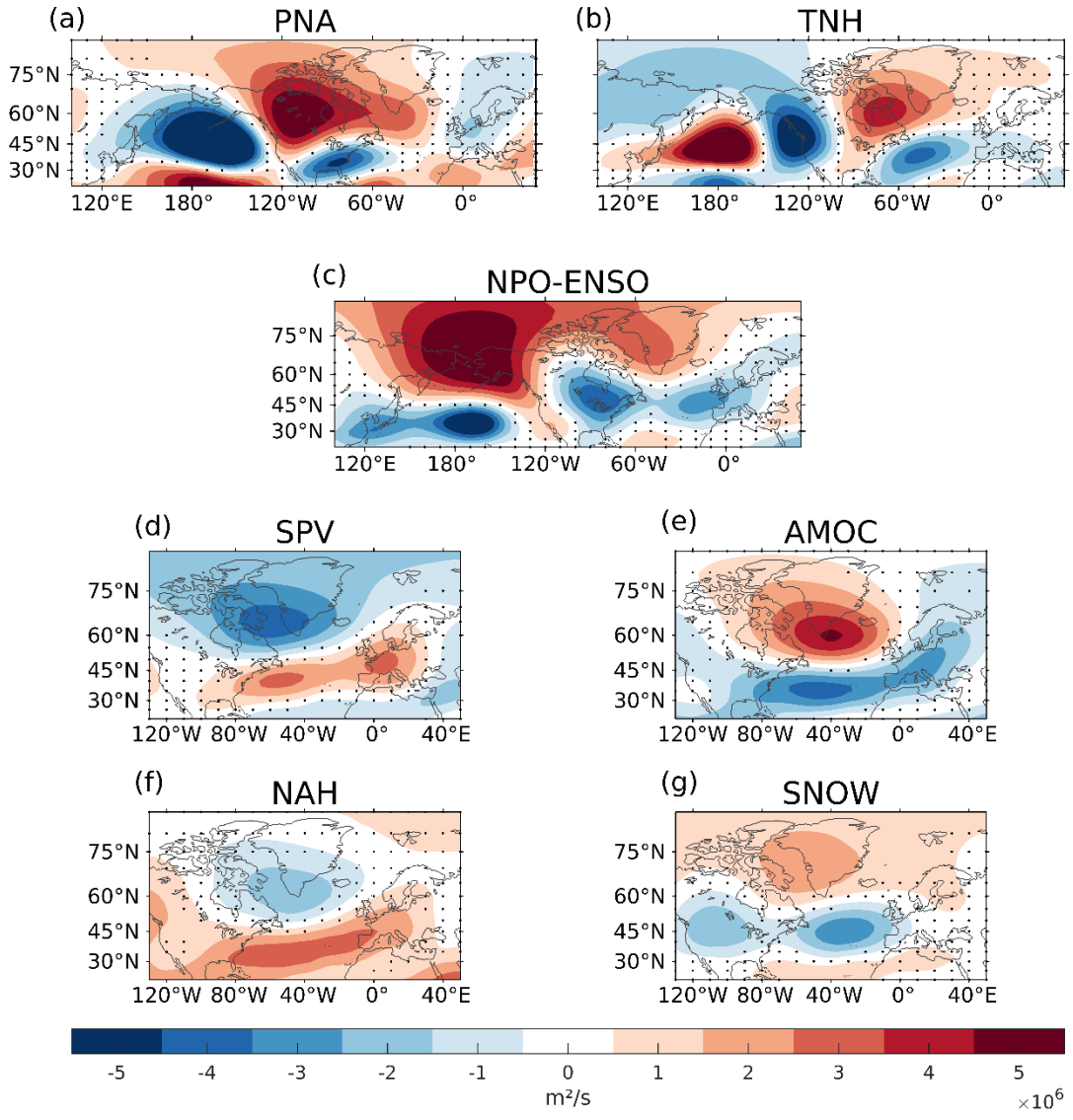

Figure VIII.6 Stream function and stationary eddies associated with the EDJ drivers. Regression maps of the monthly wintertime fields of dynamical diagnostics onto the indices of the following EDJ drivers: (a) PNA, (b) TNH, (c) NPO-ENSO, (d) SPV, (e) AMOC, (f) NAH and (g) SNOW. Dynamical diagnostics include the stream function (shading, [m^2s^{-1}]) at 200 hPa. Non statistically significant coefficients ($p<0.05$) are indicated with black dots.

➢ How does NAH modify the baroclinicity?

Lastly, we explore the origin of the baroclinicity anomalies associated with NAH in more detail (Figure VIII.6f), since it is the only driver with an EDJ response lagged in time with respect to its signal. This may provide some predictability. Considering that the previous late summer presents the NAH pattern that most impact on the wintertime EDJ, we compute the regression maps of the SST (first column Figure VIII.7) and EKE together with **E**-vectors (third column Figure VIII.7) from JAS to DJF onto the JAS NAH index to observe the oceanic and atmospheric evolution. In addition, to capture the interaction and exchange of energy between the ocean and the atmosphere, we also compute the turbulent flux regression maps (second column Figure VIII.7). Same as with the other drivers, the following mechanistic description is associated with a positive index of NAH, i.e. anomalous warming in NATL SSTs.

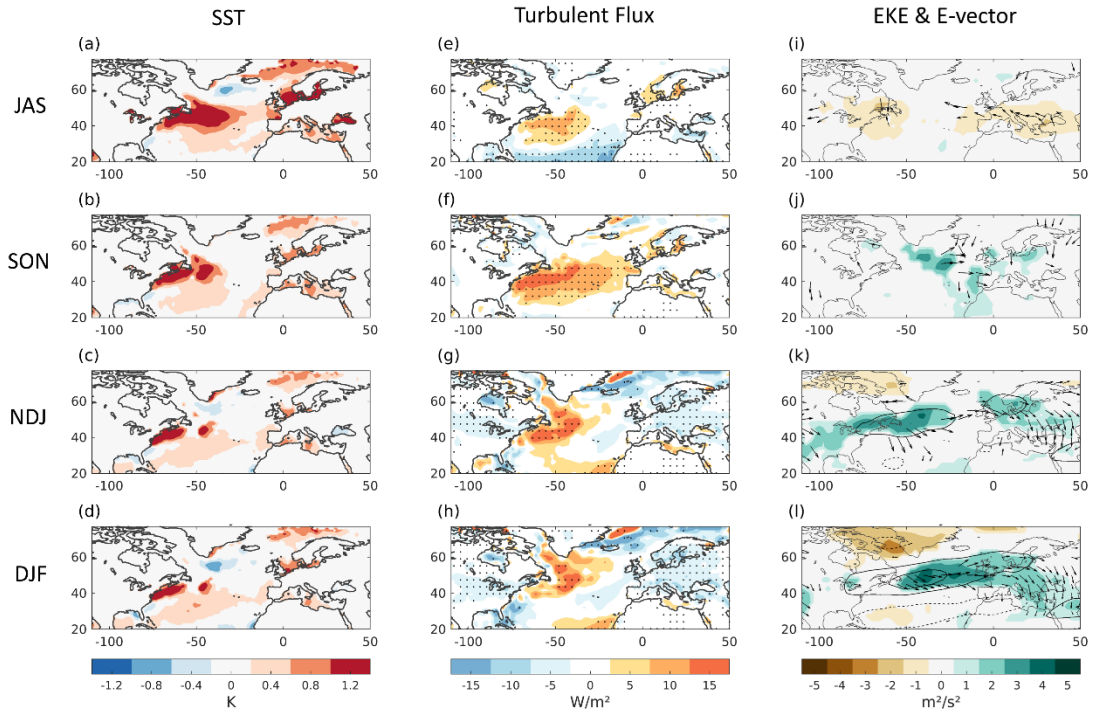

Figure VIII.7 NAH driven interaction between the ocean and atmosphere. Regression maps of different monthly fields at different Lags onto the JAS NAH index. First row shows the regression maps computed with fields during JAS, second during SON, third during NDJ and fourth during NDJ. Fields include (first column) SST (shading, [K]), (second column) turbulent flux (shading, [Wm^{-2}]) and (third column) eddy kinetic energy averaged between 1000-200 hPa (EKE, shading, [m^2s^{-2}]), wind at 200 hPa (contours, [ms^{-1}]) and **E**-vectors at 300 hPa (arrows, [m^2s^{-2}]). Only statistically significant coefficients ($p<0.05$) are displayed in first and third column, and indicated by black dots in second column.

Although the MLR shows that the NAH only impacts on the *Til*, it actually does so on *Int*, *Sh* and *Lat* parameters too. The impact on the latter parameters does not appear in the MLR since other drivers capture this influence, due to the collinearity. Concretely, the AMOC (r=-0.36) captures the influence on the wind speed parameters, and the TNH (r=-0.25) captures its influence on the latitudinal parameters.

Figure VIII.7a-d shows that the SST anomalies present its maximum in late summer and become weaker as the season advances. The SST anomalies weaken due to the release of turbulent flux (Figure VIII.7e-h) which becomes maximum around SON (Figure VIII.7f; Wen et al., 2005). The persistence of the SST and turbulent flux anomalies over months allows an interaction with the atmosphere (Czaja & Frankignoul, 1999; 2002), generating EKE and E anomalies and hence, modifying the baroclinicity. Concretely, the NAH related meridional SST gradient in the western NATL (Figure VIII.7a) modifies the atmospheric baroclinicity (Figure VIII.7j) after two months of turbulent flux release (Figure VIII.7f). The further persistence of the energy release (Figure VIII.7g-h) leads to the maximum atmospheric impact on DJF (Figure VIII.7l).

The baroclinic activity enhancement over the EDJ core region in DJF leads to an intensification of the zonal wind by the modification of the vertical shear (Figure VIII.3f) and the convergence of momentum flux driven by the transient eddies (arrows and green colours in Figure VIII.5f). The impact on *Sh* follows the tripolar pattern of the anomalous baroclinicity generated by the NAH, and the consequent EKE counterpart, leading to a narrower EDJ. Lastly, the EKE anomalies together with the southward propagation of the transient wave packets across the NATL indicate a poleward momentum flux propagation and EDJ displacement.

VIII.4 Remarks

In this Chapter, we have studied the drivers of the NATL EDJ wintertime interannual variability. A total of seven remote large-scale phenomena have been found to impact on the EDJ: PNA, TNH and NPO-ENSO, which are related to ENSO, SPV, AMOC, NAH and SNOW. The multiparametric perspective has allowed us to unravel the relation between the drivers

and the specific EDJ features, providing a very detailed picture of this topic. Concretely, ENSO and SPV appear as major drivers since they impact on most of the EDJ parameters whereas AMOC, NAH and SNOW only impact on a few of them (Figure VIII.8).

Our approach presents several advantages in assessing the drivers' impact on the EDJ in comparison to the traditional ones, which typically study the impacts in terms of the NAO (Brönniman, 2007, Kidston et al., 2015; Gastineau et al., 2016; Czaja & Frankignoul, 2002; Cohen & Entekhabi, 2001). Although most of the major extratropical teleconnection patterns project onto the main modes of variability (Wittman et al., 2005; Monahan & Fyfe, 2006), studying the large-scale drivers impact in these terms is restrictive. For instance, in the case of studying the EDJ impacts based on the NAO, these are limited to *Lat* and *Int*. In addition, although the NAO perspective may be useful, not even these EDJ parameters are fully determined by the NAO but, by combinations of NAO and EA patterns (Madonna et al., 2017; Mellado-Cano et al., 2019; Woollings et al., 2010; Woollings & Blackburn, 2012;). Thus, studying the EDJ impacts through the NAO does not provide a complete picture of the topic.

On the contrary, the multiparametric perspective enables the detection and quantification of the impacts on several EDJ features directly. For instance, the canonical influence of the positive ENSO phase on the late winter NATL circulation is an equatorward shift of the EDJ (Brönnimann, 2007; García-Serrano et al., 2010; Li & Lau, 2012; Zhang et al., 2018). Our results present this signal under the influence of the PNA, TNH and NPO-ENSO positive phases (*Lat* blue colours in Figure VIII.8). Following traditional approaches that consider the impacts on *Lat* alone, these drivers appear sort of equivalent since the three of them are related to ENSO and move the EDJ equatorward. However, under the multiparametric perspective they are not. Whereas TNH reduces the EDJ *Int*, PNA and NPO-ENSO shift the EDJ longitudinally. In addition, PNA modulates the EDJ *Til* but NPO-ENSO does not. Similar conclusions can be derived for the study of the impact of the rest of EDJ drivers. It is well-established that a strong intensification of the SPV can induce a positive NAO phase in the following weeks, strengthening and shifting poleward the EDJ underneath, and the opposite under disrupted conditions (Baldwin & Dunkerton, 2001; Kidston et al., 2015; Maycock et al., 2020; Polvani & Kushner, 2003). We detect that the SPV impact on the NATL circulation resembles the NAO structure (Figure VIII.6d) and affects

Int and *Lat* parameters (Figure VIII.8). However, the multiparametric perspective also points out that these changes are accompanied by a longitudinal elongation over northern Europe.

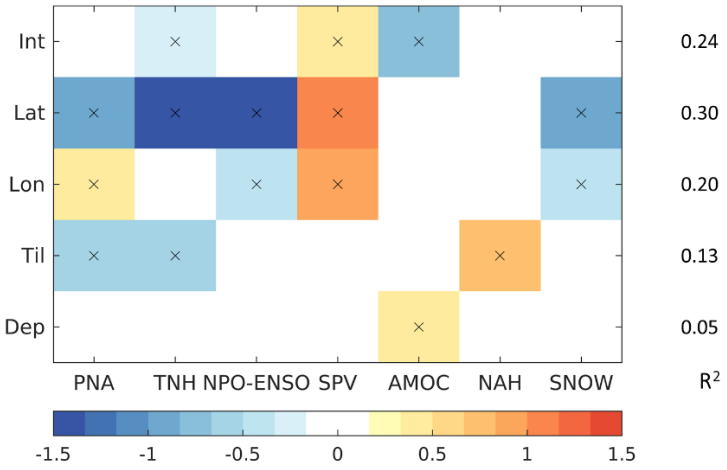

Figure VIII.8 Regression coefficients (*Int* [ms^{-1}]; *Lat* [°N]; *Lon* [°E]; *Til*, *Dep* [°N/60°]) for the predictors of EDJ parameters. As Figure VIII.1 but only for the EDJ parameters representing the parameter categories.

Moving to the North America snow cover, the two cyclonic circulations over eastern North America and western Europe under increased snow cover conditions (Figure VIII.6f) were previously detected by Cohen & Entekhabi, (2001) and Li et al. (2020). However, they considered the entire winter Northern Hemisphere snow cover. Our results show that most of the signal they found come from the North American sector. In addition, although they already showed that the pattern was related to a strengthening of the upper-level jet at its southwestern flank, our approach quantifies the magnitude of the latitudinal and longitudinal shifts. Attending to the AMOC, the relation between its strengthening and negative phase on the NAO has been detected in agreement with previous studies (Figure VIII.6e; Gastineau & Frankignoul, 2012; 2015; Gastineau et al., 2012; 2016). Nevertheless, our approach detects a stronger effect regarding the weakening of the EDJ than its southward shift (Figure VIII.8). In addition, although weak, our approach also detects a significant impact on *Dep*. An accelerated AMOC leads to a double-jet configuration, being the only driver affecting this feature. The upper-level zonal wind response pattern detected by Gastineau et al. (2016) and Gastineau & Frankignoul (2015) under a warm SST forcing at the western subpolar NATL is consistent with our impact pattern on the EDJ frequency (Figure VIII.2e) and *Int* and *Dep* parameters. Similarly, we detect the canonical winter positive NAO following the late summer negative NAH (Figure VIII.6f; Czaja & Franjiknoul,

1999; 2002). However, although the impact on intensity and latitudinal parameters is detected, it is masked when other phenomena are active, particularly, the TNH and AMOC (Table AVIII.1). Besides, NAH is the only driver found to influence *Til*. The latter becomes striking because, as shown in Chapter VII, the parameter *Til* plays a major role in determining the influence of the EDJ on extreme temperature events in the European region.

Further, we have assessed the combined impact of the drivers on the EDJ parameters. These drivers do not explain the different EDJ features equally but, present some diversity. 30% of the variability is explained for the latitudinal parameters, followed by 20% and 24% for the longitudinal and intensity EDJ parameters. In a different way, the parameters related to the EDJ zonal asymmetries are poorly captured, presenting only 13% and 5% of the variance explained.

The mechanisms followed by the drivers to impact on the EDJ have shown a common pathway: the modification of the western NATL baroclinicity. The stationary eddies travel from remote regions until the NATL where they modify the low-level baroclinicity (Inatsu et al., 2003). The latter imprints a direct effect on the EDJ, mainly over the western part of the basin. Further, the modification of the baroclinicity forces downstream development of synoptic eddies, providing a pathway to impact on the EDJ (Takaya & Nakamura, 2001). By positive feedbacks, transient waves would maintain the stationary eddies through the generation of an equivalent barotropic structure (Peng et al., 2003; Deser et al., 2007). Although synoptic eddies have been proposed as the process followed by several drivers like AMOC, NAH or SNOW (Gastineau & Frankignoul, 2015; Soboloski et al., 2007; 2010; Gervais et al., 2019) to impact on the EDJ, it has been only analysed in detail for ENSO (Li & Lau, 2012; Drouard et al., 2013; 2015; Jimenez-Steve & Domeisen, 2018). Here, the dynamical diagnostic of the transient eddies' life cycle, i.e. generation, propagation and decay, has provided the specific patterns of eddy forcing and wave breaking involved in each driver impact. The latter show that, while both types of wave breaking are involved in modifying the EDJ latitude, other variations of the EDJ, such as zonal asymmetries are more strongly mediated by AWB over Europe. Also, impacts on wind related parameters require an intense zonal gradient of G over 50°N, which indicate the acceleration or deceleration of the mean flow induced by the transient eddies.

IX. EDJ Climate Change Projections

Thus far, throughout the PhD thesis, we have characterized the present interannual spatiotemporal variability of the EDJ over the Euro-Atlantic region. Now we explore how the EDJ mean state may change in the future by applying the multiparametric perspective framework to a CMIP6 multimodel ensemble. This Chapter quantifies the projections and intermodel spread of the EDJ parameters by the end of the century. We focus our research on the EDJ changes in winter (NDJF) as a whole season and divided in subseasons, namely, early (ND) and late winter (JF). Our study also provides further insights into the potential influence of remote drivers in the projections of the NATL midlatitude circulation. The results of this Chapter can be found in García-Burgos et al. (2024). The figures that are taken from the latter publication are indicated by †††.

IX.1 Seasonal Analysis

In this Subsection we explore the NATL EDJ winter projections under climate change by comparing the historical and SSP5-8.5 experiments modeled by the CMIP6 multimodel ensemble shown in Table IV.1. Before starting the analysis, the models ability to simulate the NATL low level zonal wind climatology and variability in comparison to ERA5 is examined (Figure IX.1 and 2). Figure IX.1 shows the zonal wind meridional profiles from the models historical simulations in comparison to the ERA5 one. Following the EDJ basic parameters definitions, the profiles are computed over the NATL sector [60°W-0°], the core region of the wintertime EDJ. Overall, all models simulate a realistic climatology with a single westerly maximum between 40°-50°N and easterly winds at subtropical latitudes. Although MIROC-ES2L presents a too southward shifted maximum, southern than 40°N, we do not reject the model since the other two mentioned features are well represented. The models variability is assessed by computing the coefficient of variation, which measures the dispersion of the data relative to the mean ($C_v=\sigma/\mu$ where σ is the standard deviation and μ the mean; Abdi, 2010). Natural and simulated variability (Figure IX.2a and b, respectively) present good agreement in magnitude and spatial structure over the NATL

sector, although models tend to overestimate the variability in the EDJ exit region over western Europe.

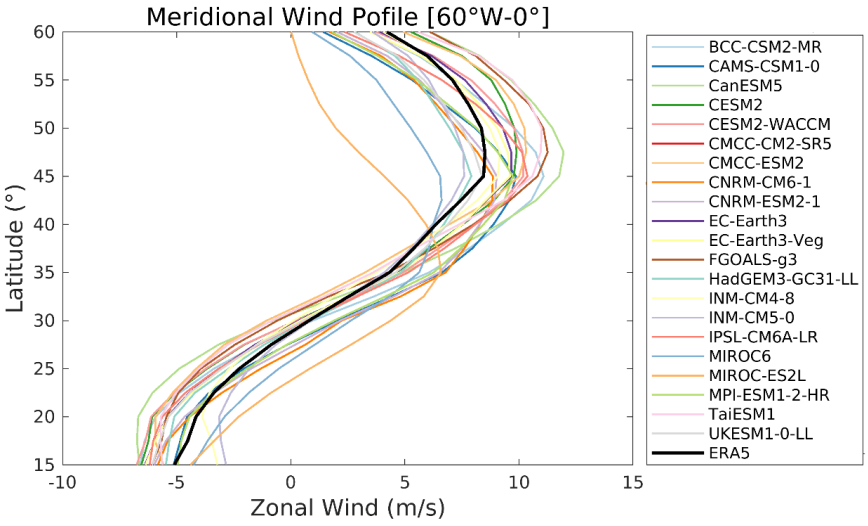

Figure IX.1 Zonal wind meridional profiles ([ms^{-1}]) at 850 hPa averaged over [60°W-0°] with each CGM historical simulation (coloured curves) and ERA5 reanalysis (black curve) during 1979-2009 period.

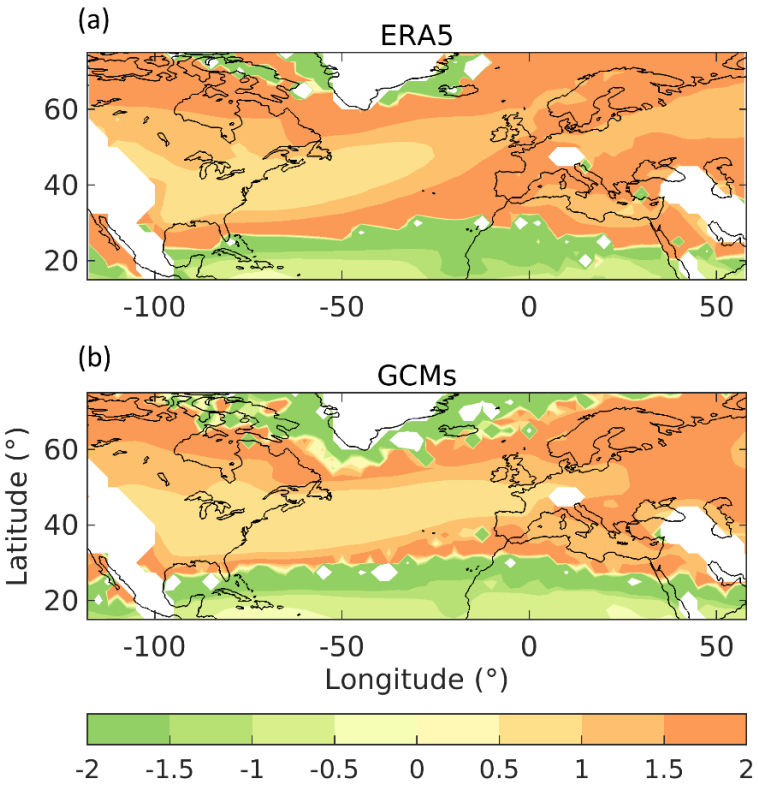

Figure IX.2 Coefficient of variation of monthly zonal wind at 850 hPa over the period 1979-2014, by (a) ERA5 and (b) CMIP6 models historical simulations.

Figure IX.3 shows the multimodel mean of future change in the frequency of occurrence of EDJ during the extended winter, defined from November-to-February (NDJF). The main feature of the spatial pattern is a tripolar structure, which represents a squeezing of the climatological EDJ, depicted by an intensification of its central part and a weakening of the northern and southern flanks (Figure IX.3a). A similar pattern is found for the 850 hPa zonal wind but with noisier characteristics (Figure AIX.1). The tripolar pattern does not imply a clear change in the *Lat* or *Int* of the EDJ in the future, as shown by the distributions of the changes in the corresponding parameters (grey boxplots in Figure IX.3b), which are centred around the zero-line. The similarity of the *Lat* distributions in both future and historical periods confirm the lack of changes in the latitudinal position of the EDJ (Figure IX.4a).

The tripolar pattern influences the EDJ *Dep* parameter, which, as mentioned above, measures the deviation of the EDJ from a structure with a single wind maximum. Large values of this parameter indicate a split-like structure with two or more wind maxima. The models project a robust increase in *Dep* and tendency towards EDJs with a single flow configuration, since the distribution of the change is displaced toward negative values. This is consistent with the increased occurrence of EDJ detections over western Europe (Figure IX.3a). The eastward displacement of the EDJ is also captured by the projected changes in *Lon*, *Lone* and *Lonw* (Figure IX.3b), although the associated spread is large spanning from negative (westward) to positive (eastward) values.

Despite the general consistency of the EDJ future changes reported by EDJ parameters and 2D EDJ frequency analyses, the apparent squeezing shown in the 2D frequency plot (Figure IX.3a) and several works (Peings et al., 2017; 2018; Oudar et al., 2020; Dorrington et al., 2022) is not detected in the multiparametric EDJ approach (Figure IX.3b). This emphasizes the complementary information provided by these two EDJ perspectives and calls for caution when interpreting changes in zonal wind and/or 2D EDJ frequency. In particular, the tripolar pattern of Figure IX.3a allows various interpretations, since changes in different EDJ features can lead to the same pattern. The combined analysis of the 2D EDJ frequency and the EDJ parameters provides a more complete view of the EDJ, making it possible to deepen into its complex structure. In this sense, the parameter *Sh* measures the sharpness of the EDJ and can be taken as an indicator of the squeezing, with a narrowing and widening of the EDJ translating to positive and negative changes in *Sh*,

respectively. The median of the multimodel changes of *Sh* indicates a slight narrowing, in agreement with all above mentioned previous works. However, our parametric approach also reveals a large uncertainty (non-significant narrowing): the distribution of the changes is located around the zero line, ranging from positive to negative values. Thus, our daily-based diagnostics does not reveal a significant narrowing of the EDJ. Alternatively, the apparent squeezing pattern might be understood as sole changes in the latitudinal frequency, involving more frequent central EDJs and less poleward and equatorward excursions, but without changes in the EDJ width. However, as previously mentioned, *Lat* and *Int* parameters do not show clear changes in the future either (Figure. IX.3b and Figure. IX.4). Thus, none of the interpretations of the spatial squeezing depicted by the EDJ 2D frequency pattern is supported by the future changes in EDJ parameters.

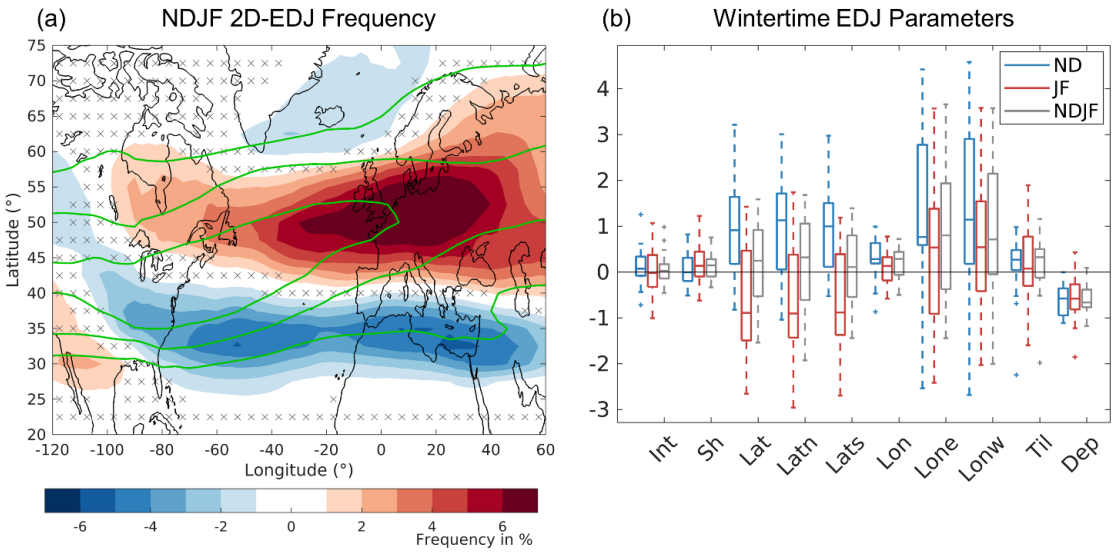

Figure IX.3 Winter projections of the EDJ (a) Multimodel mean climate change signal in the winter (NDJF) 2D EDJ frequency (shading, [%]). The 1979-2009 NDJF climatology is shown with contours (starting at 20% and drawn every 20%). Crosses indicate the grid-points with non- significant differences at the 95% confidence level (after a 1000-trial Monte Carlo test). (b) Boxplots with the changes in the EDJ parameters (*Int*, *Sh* [ms^{-1}]; *Lat*, *Latn*, *Lats* [°N]; *Lon*, *Lone*, *Lonw* [°E]; *Til*, *Dep* [°N/60°]) for NDJF (grey), ND (blue) and (JF) red. The distance between the box limits denotes the interquartile range and the horizontal line corresponds to the median. Whiskers indicate the extremes of the distribution without considering outliers. Outliers, defined as values greater than 1.5 times the interquartile range, are represented with crosses. The climate change signal is defined as the difference between future (2069-99; SSP5-8.5) and present-day (1979-2009; historical) means. †††

Considering the mentioned consensus of previous studies on the squeezing in the EDJ projections (Oudar et al., 2020; Peings et al., 2017; 2018; Dorrington et al., 2022) together with the strong impacts of the EDJ shape on European regional climate and particularly, extreme events (Barriopedro et al., 2023; García-Burgos et al., 2023), the mismatch between the projected changes retrieved from the two EDJ perspectives (2D EDJ frequency pattern and EDJ parameters) needs to be reconciled. One possible explanation for the apparent inconsistency is that the 2D squeezing is the result of including in the same analysis elements that are responding differently to climate change. One of these elements might be the consideration of the NDJF as a whole, given that the signals of certain EDJ drivers such as the SPV or the equatorial Pacific SSTs are not stationary during the winter. The next section presents the EDJ projections for the early (ND) and late (JF) winter separately to address the inconsistency and further dissect the spread in the EDJ projections.

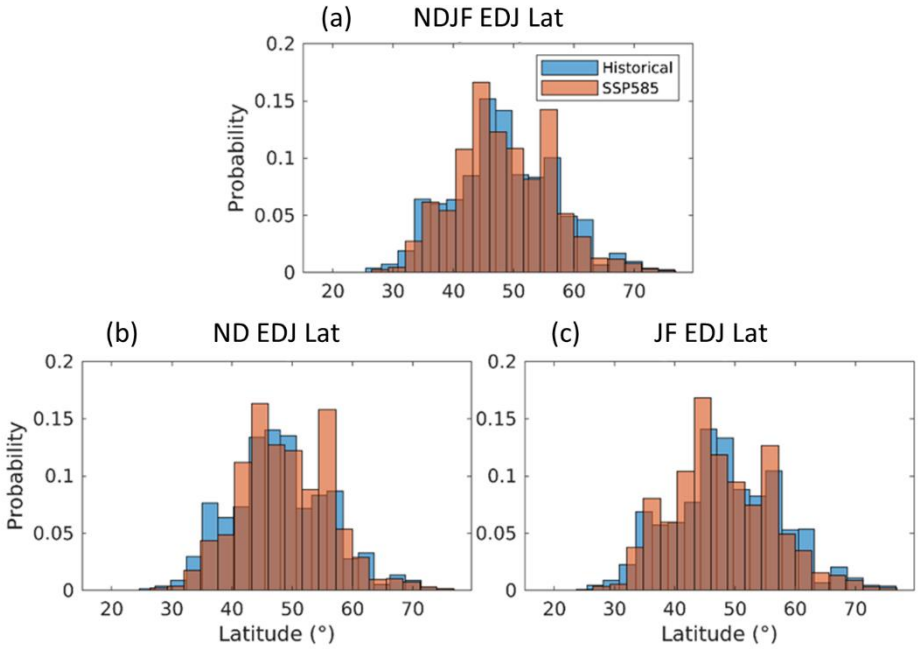

Figure IX.4 Distributions of the EDJ *Lat* simulated by the models in Historical (blue) and SSP5-8.5 (red) experiments, for the whole (a), early (b) and late (c) winter. †††

IX.2 Subseasonal Analysis

The projected changes in the pattern of 2D EDJ frequency (Figure IX.5a and c) and distribution of EDJ parameters (coloured boxplots in Figure IX.1b) show large intraseasonal variations, and notable differences between early (ND) and late (JF) winter. Considering the EDJ width (*Sh* parameter), the corresponding distributions for ND and JF (Figure IX.3b) do not show appreciable changes, similarly to NDJF. However, this is not consistent with the two subseasonal EDJ frequency field maps, neither of which show a squeezing-like pattern (Figure IX.5a and c). Note that the frequency changes in one of the meridional flanks of the EDJ tend to be opposite to those in the other, resulting in meridional shifts rather than changes in the EDJ width over the NATL sector.

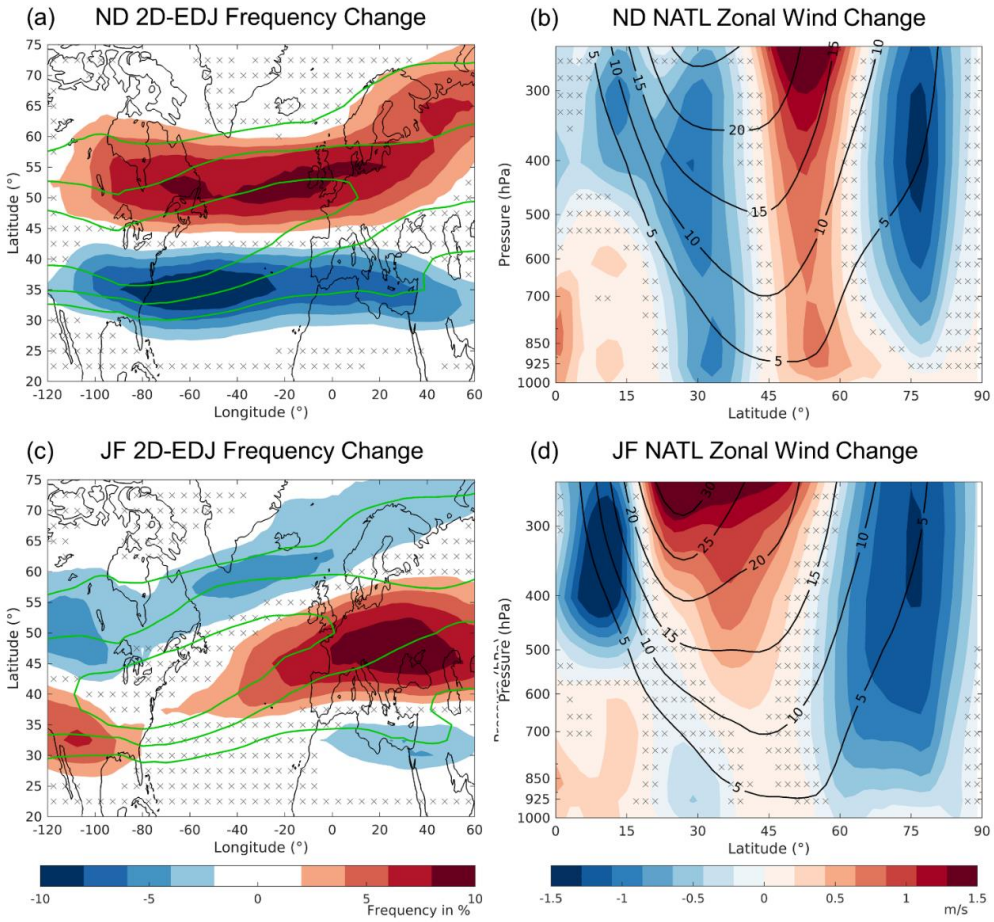

Figure IX.5 Projections of the EDJ for early and late winter. (a) and (c) As Figure IX.3a but for early (ND; a) and late (JF; c) winter. (b) and (d) Multimodel mean of the future (2069-2099) minus present-day (1979-2009) difference in the zonal wind averaged over the NATL. Crosses indicate the grid-points with non-significant differences at the 95% confidence level (after a 1000-trial Monte Carlo test). †††

More interestingly, the early winter EDJ shows a statistically significant displacement to the pole, to the east and toward positive tilts (a higher SW-NE orientation of the EDJ) (Figure IX.5a and blue boxplots in Figure IX.3b; note that the interquartile range for the associated EDJ parameters of *Lat*, *Lon* and *Til* does not include zero). The poleward latitudinal shift can also be clearly seen in the two meridional flanks of the EDJ (*Latn*, *Lats*), confirming the absence of changes in the EDJ width, as well as NATL zonal wind cross section (Figure IX.5b, poleward peak in Figure IX.4b). Differently, the late winter EDJ does not show such changes but, if any, a tendency to be southward displaced (equatorward peaks in Figure IX.4c), although this equatorward shift is not very well captured in the cross section (Figure IX.5d). The reason is that the EDJ is tilted in the NATL, therefore presenting positive and negative frequency changes at the same latitude (Figure IX.5c). As a consequence, the signal weakens when the longitudinal average is computed over the NATL (Figure IX.5d). Like in early winter, the distributions of longitudinal parameters continue to display an eastward EDJ shift in late winter. However, there are marked differences in uncertainty: during ND there is a high model agreement on the EDJ elongation over Europe, whereas the distribution of the JF changes presents a large spread and hence, an uncertain projection.

Out of the ten EDJ parameters, only the latitudinal ones (*Lat*, *Latn* and *Lats*) present significant changes in early and late winter, but of opposite sign (Figure IX.3b). The latitudinal parameters are the most salient features of the NATL EDJ and they explain most of its variability. Indeed, the EDJ latitudinal shift is the primary mode of variability of the NATL zonal wind (Woollings et al., 2010). Besides, the changes in the latitudinal parameters are consistent with those found for the 2D EDJ frequency. Therefore, from now on we will focus on the projections of the EDJ latitude (*Lat*) and the cause of its opposite responses to climate change in early and late winter.

- Projections of wintertime temperature and zonal wind mean state at a subseasonal scale

To understand the intraseasonal change in EDJ latitudes, we assess the future changes in the mean state of NATL zonal mean T, zonal mean U and SSTs (Figure IX.6). The climate

change pattern of T is characterized by a stratospheric cooling and a tropospheric warming, the latter being dominated by the Tropical Amplification (TA) and Arctic Amplification (AA) throughout the entire winter (Figure IX.6a and d). The main intraseasonal difference is that the change in T at upper levels and polar latitudes is not statistically significant in late winter (Figure IX.6d), suggesting that the intensification of the negative meridional temperature gradient at 200 hPa by the TA is stronger in early than in late winter. On the other hand, the SST changes display very similar characteristics in both subseasons too (Figure IX.6b and e). Besides the NATL Warming Hole (WH), longitudinal asymmetric warming is present at the equatorial Pacific, leading to a weakening of the longitudinal SST gradient between the western and eastern edges of the basin.

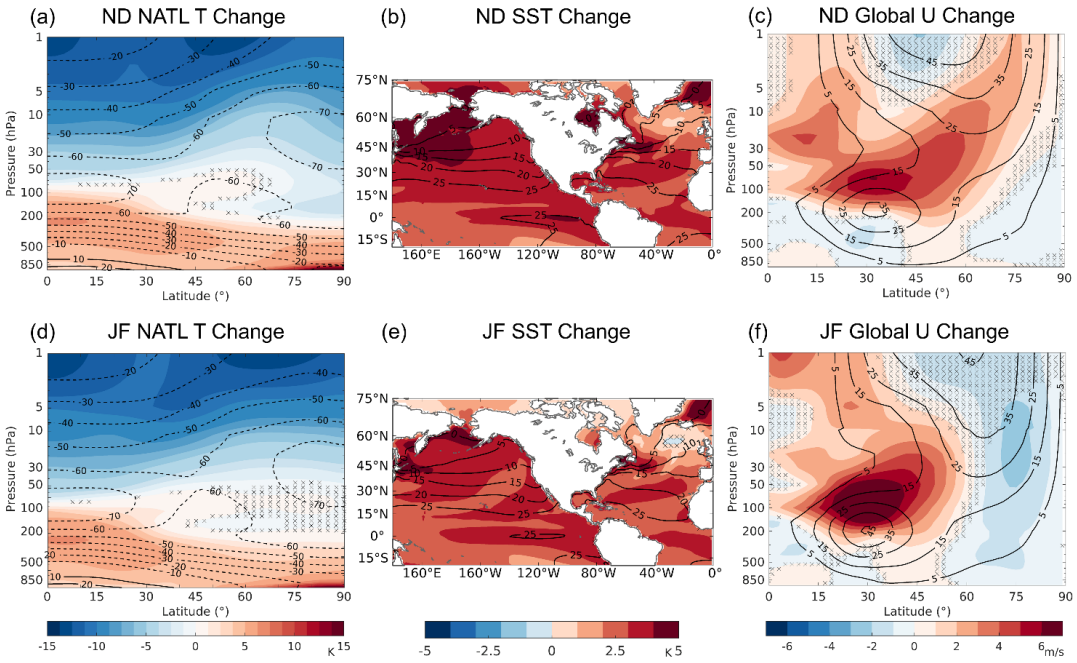

Figure IX.6 Climate change projections of temperature, SST and zonal wind. Multimodel mean future changes (shading) and 1979-2009 climatology (contour) of the zonal mean T over the NATL [K] (a, d), SST [K] (b, e) and hemispheric zonal mean U [ms^{-1}] (c, f). The future (2069-2099; SSP5-8.5) minus present-day (1979-2009) differences are computed for early (upper row) and late (bottom row) winter separately. Crosses indicate the grid-points with non-significant differences at the 95% confidence level (after a 1000-trial Monte Carlo test). †††

Moving to the zonal mean zonal wind changes, a reinforced subtropical jet is observed in both subseasons (Figure IX.6c and f). Moreover, the maximum wind speeds are located

at higher levels than in the historical period, which is consistent with the expansion of the troposphere and the subsequent rise of the tropopause (Lorenz & DeWeaver, 2007; O'Gorman & Singh, 2013). Note that in Figures IX.6c and f, the latitudinal shifts of the NATL EDJ are masked by the zonal mean (the zonal wind is averaged globally). Interestingly, the stratospheric zonal wind response to climate change in extratropical latitudes differs between subseasons. Early winter displays an intensification of the zonal wind at polar latitudes and stratospheric levels, which expands from the subtropical jet (Figure IX.6c). The reinforcement of the zonal wind in the polar stratosphere does not extend to tropospheric levels though, suggesting that the changes in the two atmospheric layers are not coupled in this case. Late winter shows a very different picture (Figure IX.6f). Contrary to the early winter case, the SPV weakens in late winter, and the stratospheric and tropospheric changes are coupled in this sub-season since the zonal wind weakening is vertically continuous along the atmospheric column. Late winter is also the typical timing of the strongest stratosphere-troposphere coupling (Butchart et al., 2022). Therefore, our results indicate a potential influence of the stratospheric future changes on the troposphere (and the EDJ) in late winter only.

Next, we explore the linkages between the projected changes in the EDJ and its drivers (atmospheric and oceanic mean states) in order to explain the intraseasonal differences in the latitudinal shift of the EDJ. We consider some of the drivers of the EDJ climatology reported in the literature, including the ones defined below. Note that the drivers are different from those in Chapter VIII. Whereas the ones below account for the mean state changes, those in Chapter VIII do it for interannual changes. The chosen phenomena are well-established drivers of the EDJ mean state and capture the most relevant signatures of the atmospheric and oceanic changes identified in Figure IX.6. The direction of the relation has been established by several studies showing them as precursors of the EDJ variability but not the opposite (Oudar et al., 2020; Butler et al., 2010; Gervais et al., 2019; Butchart et al., 2022). Additional drivers, such as the subtropical jet location, the global surface temperature or zonal 850 hPa temperature gradient in the NATL, were also analysed. However, they are not included in the following analysis as they were not found independent from other drivers. The considered drivers hereafter are:

- Meridional temperature gradient at 200 hPa (Grad200): difference of the polar ([70°-90°N]) and tropical ([0°-20°N]) averages of the zonal mean temperature computed over the NATL [120°W-60°E] at 200 hPa.
- Meridional temperature gradient at 850 hPa (Grad850): same as Grad200 but at 850 hPa.
- Stratospheric Polar Vortex (SPV): zonal mean zonal wind averaged between 60°-75°N at 10 hPa.
- Warming Hole (WH): sea surface temperature (SST) averaged over [35°-60°N; 40°-10°W]. To capture the impact of the lack of warming the averaged SST is multiplied by -1.
- Zonal asymmetries in the equatorial Pacific SST: SST difference between the NIÑO4 [5°S-5°N; 160°E-150°W] and the NIÑO3 [5°S-5°N; 150°-90°W] region.

One additional consideration will be introduced for the study of relationship between the projected changes of the EDJ and the drivers. We will analyse two different populations of models. The first one is the full multimodel ensemble, which considers the 21 models of Table IV.1. A second group only includes those models that represent the climatological EDJ latitude sufficiently well for the 1979-2009 period. The purpose is to investigate if the projected changes depend or not on the ability of the models to capture the observed EDJ. The model bias is defined as the difference of the climatology of the monthly latitude of the EDJ in each model minus that corresponding to the ERA5 reanalysis for the 1979-2009 period. The significance of the difference is assessed with a 1000-trial Monte Carlo at the 95% confidence level applied to the monthly series of EDJ *Lat* (defined for early or late winter). Monthly time series are computed based on daily data of reanalysis and models. This allows us to construct two sets of models: Neutral-models, which comprise those with non-significant differences in the EDJ latitude with respect to ERA5 (Figure IX.7b and d) and Biased-models, those that present a significantly biased EDJ *Lat* (Figure IX.7a and c). All models of the biased population are characterized by southward displaced EDJs with respect to ERA5.

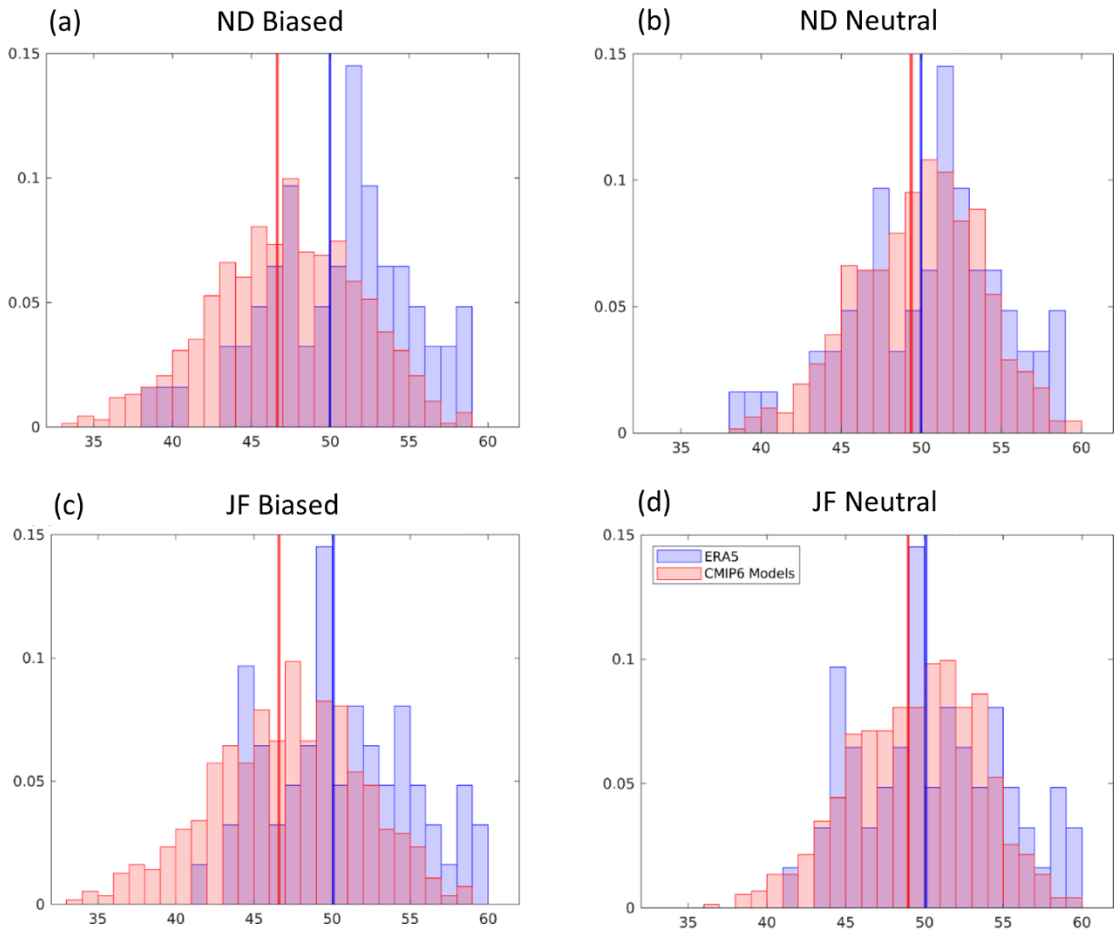

Figure IX.7 Distributions of the daily latitude of the North Atlantic Eddy-Driven Jet during the early (a, b) and late (c, d) winters of the period 1979-2009 for ERA5 (purple) and: (a, c) biased, and; (b, d) unbiased models of the CMIP6 (pink). For each panel, all models are pooled together, and the frequency distributions are normalized to add 1. †††

IX.3 Drivers of the intraseasonal responses in EDJ latitude

As hypothesized above, the detected future changes in the frequency pattern and parameters of the EDJ may be described as a linear combination of the drivers' responses to climate change. To find the leading drivers of the projected changes of the EDJ in the multimodel ensemble, we perform a multiple linear regression similar to Zappa and Shepherd (2017).

A regression framework similar to the one presented in Chapter VIII is applied, but in this case, the predicted variables are the future changes in the EDJ parameters (Equation

VIII.1) and in the 2D EDJ frequency field (Equation VIII.2). In both cases, the predictors correspond to a vector constructed from the simulated responses of that driver to climate change across the multimodel ensemble (each element of the vector represents the driver's response in one model). For instance, for the sample considering all models, the changes in the EDJ latitude and the changes in the drivers' vectors have a length of 21, that is the number of models that forms the sample. Before building the regression models, the predictors and predicted variables have been scaled by the global warming of each model, dividing them by the simulated future change in the global surface temperature. This way, the climate sensitivity signal of each model is removed. The multilinear regression framework is applied to winter averages of the EDJ, as well as to the early and late winter subseasons, separately. The sign of EDJ frequency maps in Figures IX.8 and IX.9 corresponds to that associated with the southward *Lat* EDJ Bias and the projections of the drivers detected in Figure VIII.6, i.e. an intensification of the negative Grad200, the development of the WH and a weakening of SPV. The predictor selection is based on the computation of the p-value to compare the models with and without the potential predictor, following a stepwise procedure with forward selection and backward elimination, as in the previous Chapter.

- Early Winter

The multiple linear regression (MLR) identifies Grad200 and WH as the main large-scale drivers of the future changes in the early winter EDJ latitude ($\boldsymbol{\Delta Lat}$). Model biases of the EDJ *Lat* also have an influence. The three mentioned drivers can explain together 72% of the $\boldsymbol{\Delta Lat}$ variance simulated by the multimodel ensemble (Grad200 explains 18%, WH 33% and the model biases 21% of the $\boldsymbol{\Delta Lat}$ variance). Similar explained variances are obtained for *Latn* and *Lats*, as they are correlated with *Lat*. The influence of the drivers' responses on the projected changes in EDJ frequency are shown in Figure IX.8. For all drivers, their climate change fingerprints induce a meridional dipole in the EDJ extending along the NATL. Grad200 is expected to decrease further, which implies a strengthening of the (negative) meridional temperature gradient. A stronger Grad200 is expected to move the EDJ poleward (Figure IX.8a). The WH directly affects the location of the strongest baroclinicity in the NATL (Gervais et al., 2019). As the WH intensifies, the region of no warming also has a larger extension. In that case, the southern edge of the deep WHs reaches lower

latitudes, shifting the baroclinicity region and the EDJ equatorward (Figure IX.8b). Contrary, shallow WH would indicate a small warming in that area, but still weaker than in the rest of the NATL. This would confine the WH at very high latitudes, which in turn would push the baroclinicity and the EDJ poleward.

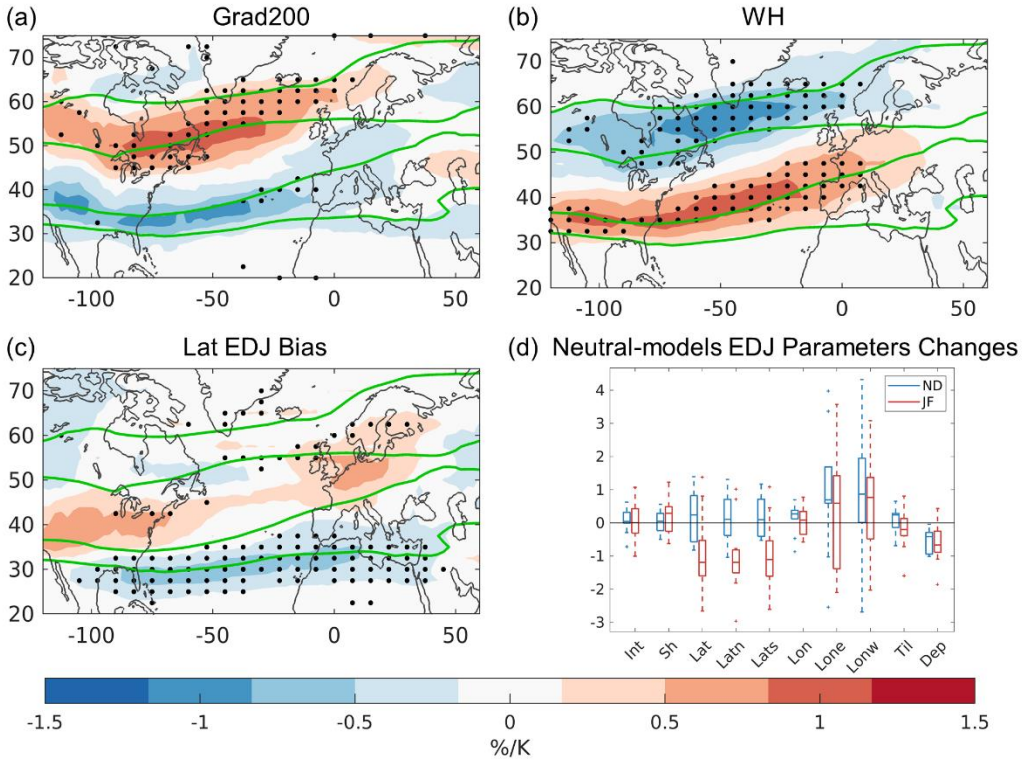

Figure IX.8 Contribution of the EDJ *Lat* drivers future changes to the early winter (ND) EDJ response to climate change and Neutral-models EDJ parameters response to climate change. (a) EDJ frequency response (scaled by global warming) [%/K] to a +1 sigma future change in Grad200. Green contours show the multimodel mean climatology of EDJ frequency for the 1979-2009 period (starting at 20% and drawn every 30%). Stippling indicates significance at the 95% confidence level (i.e. local regression coefficients of the corresponding driver that are significantly different from zero). (b) Same as (a) but for the NATL WH. (c) Same as (a) but for the *Lat* EDJ Bias. (d) Same as Figure IX.3b but for Neutral-models. †††

Finally, the historical biases in the EDJ latitude influence its response to climate change, especially in the southern flank of the EDJ (Figure IX.8c). The dipole pattern indicates that equatorward biased models (i.e. with a negative *Lat* EDJ Bias) display more poleward shifted EDJs in the future (Figure IX.8c) than the unbiased (Neutral-models) ones. There are 11 models with a significant bias in EDJ *Lat* (Biased-models), out of the 21 models of the multimodel ensemble, and all of them present a southward shifted EDJ in the historical period (Figure IX.7a and c). Therefore, the contribution of model biases to the multimodel EDJ response to climate change consists of a poleward shift of the EDJ. In fact, if we analyse

the projected changes in the latitudinal parameters for the Neutral-models sample (blue boxplots in Figure IX.8d), the poleward displacement of the EDJ is no longer present in early winter, and there is no meridional shift in the EDJ projections. These results show that at least part of the detected poleward migration of the EDJ under climate change scenarios can be a consequence of the model biases. For Neutral-models, the biases in the EDJ latitude are small and the other drivers (Grad200 and WH) explain most (~90%) of the spread in ΔLat, with ~27% of the variance corresponding to Grad200 and ~63% to WH. As the climate change responses of Grad200 and WH involve opposite changes in the EDJ latitude, the behaviour of the Neutral-models projections reflect the competing effects of these two drivers. This explains the lack of agreement in the sign of the early winter latitudinal EDJ parameters in Figure IX.8d.

- Late Winter

The picture changes when assessing the drivers of the latitude changes in the EDJ latitude for late winter. In this case, our regression approach indicates that the multimodel spread in ΔLat is largely explained by only one large-scale driver, the SPV. A weakening of the SPV is associated with an equatorward shift of the EDJ (Figure IX.9a), as expected from the stratosphere-troposphere coupling (Butchart, 2022). The projections of SPV and EDJ in late winter show a consistent picture: in the future the SPV weakens (Figure IX.6f) and the EDJ latitude shifts equatorward (see also the red boxplot in Figure IX.3b). For this sub-season, the bias in *Lat* EDJ is again found to influence the ΔLat. The spatial pattern is similar to the ND one, but with the meridional dipole more defined and displaced to the east (Figure IX.9b). Like in early winter, all Biased-models are shifted equatorward, contributing to a poleward shift of the EDJ that opposes the equatorward shift induced by the weakening of the SPV. The SPV together with the *Lat* EDJ Bias explain half of the total variance in ΔLat. For the Neutral-models sub-sample, the SPV is the only driver influencing the EDJ latitudinal response to climate change (~50% of the explained variance). In addition, the consensus on the equatorward shift detected in the multimodel ensemble is stronger in the Neutral-models sample (cf. Figure IX.3b and IX.8d). Therefore, the results for late winter reinforce the fact that the projected poleward migration of the EDJ can be substantially driven by model biases. Note that future changes in the other drivers

(equatorial Pacific SST and Grad850) have negligible influences on EDJ latitude for both early and late winter.

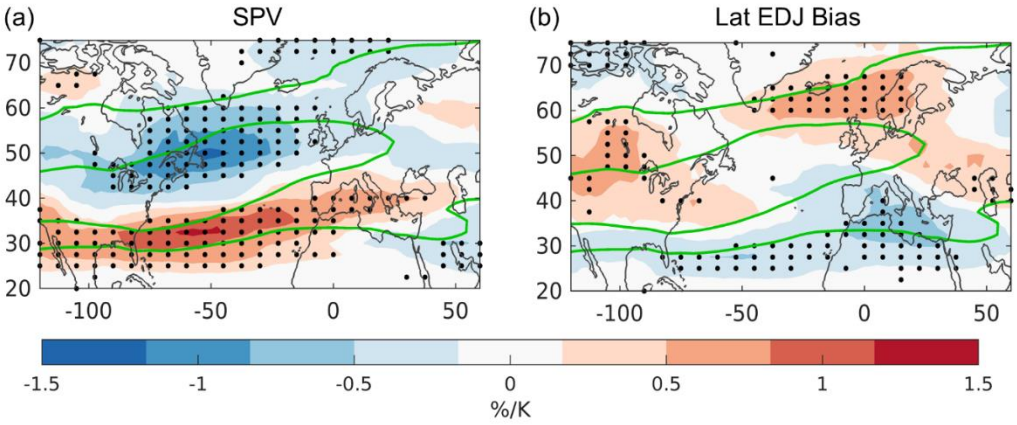

Figure IX.9 Contributions of the EDJ *Lat* drivers future changes to the late winter (JF) EDJ response to climate change. Same as Figure IX.8 but for the drivers of EDJ latitude in late winter (JF). †††

IX.4 Remarks

In this Chapter, we have described the future winter changes in the NATL EDJ in the last generation of models by exploiting our novel description of the EDJ on daily scales.

Although there is a consensus on the future poleward shift of the EDJ at hemispheric scales, several studies did not find clear latitudinal migrations in the NATL. Instead, a large spread in the projections of EDJ latitude has been detected across the models, ranging from poleward to equatorward displacements (Barnes & Polvani, 2015; Oudar et al., 2020). Other studies report that the lack of a robust EDJ response to climate change is due to opposing effects of two drivers of the NATL EDJ, TA and AA, which result in small net changes in latitude, but a pronounced squeezing of the EDJ (Barnes & Polvani, 2015; Oudar et al., 2010). However, our results indicate that the future squeezing pattern of the winter EDJ would be an artefact from mixing different intraseasonal EDJ responses to climate change that involve opposite meridional shifts of the EDJ. By splitting the winter (NDJF) into two subperiods, we find a high model agreement on a poleward EDJ shift in early winter (ND), followed by a slight equatorward shift in late winter (JF). In fact, when we diagnose changes in the EDJ width explicitly, we do not find significant changes towards narrower or wider EDJs in the future, not even in early and late winter. Indeed, the apparent winter

squeezing evidenced in zonal wind and 2D EDJ frequency maps is no longer present when the EDJ changes are computed for early and late winter separately. Therefore, the effect of combining the two winter subseasons is two-fold: it yields a disproportionate increase in the uncertainty of the projections of the EDJ parameters, and a misleading response of the EDJ due to averaging opposite signals that occur at different times of the winter season.

The intraseasonal latitudinal responses of the EDJ to climate change are shown to be promoted by different drivers: Grad200 and NATL WH in early winter, and SPV in late winter. This means that the processes that drive the future changes in the EDJ latitude change throughout the winter from thermodynamic to dynamic processes. In particular, the strong influence of the SPV on the EDJ latitudes in late winter, outweighs the effect of other active drivers of this sub-season (Manzini et al., 2018), such as Grad200 and NATL WH. According to our regression model, SPV, and not the AA, represented herein as the low tropospheric temperature gradient (Grad850), would be the main responsible of the projected equatorward shifts of the EDJ, albeit limited to late winter. Therefore, the drivers of the 'tug-of-war' could be different (or at least should be expanded) from those previously thought. The stratosphere-troposphere coupling is typically stronger in late than in early winter, which could explain why the SPV plays an active role in the JF period but not in ND. Although some authors have linked AA to an equatorward shift of the EDJ (Butler et al., 2010; Barnes & Polvani, 2015; Barnes & Simpson, 2017; Peings et al., 2019), more recent studies such as Zappa and Shepherd (2017) have not found a significant impact of the AA on the zonal wind across NATL region.

Model biases in the EDJ latitude also influence its projections. Models simulating an equatorward shifted EDJ in the historical period project a larger poleward shift of the EDJ in the future than unbiased models. Indeed, when analyzing the sample formed by the models without biases in the EDJ latitude, the projections present no clear shift of the EDJ in early winter and a strong displacement of the EDJ towards the equator in late winter. This indicates that part of the projected poleward shift of the EDJ under climate change could be exacerbated by the model biases. One may speculate about the underlying mechanism for this influence of model biases on the EDJ response to climate change. The answer could be found in the relative location of the EDJ to the tropical warming. Experiments carried out with idealized models have shown that the tropical warming forces a poleward shift of the EDJ through the eddy heat and momentum fluxes (Butler et al.,

2010). More recently, Baker et al. (2017; 2018) have designed a set of experiments to study the sensitivity of the EDJ to different warming locations and intensities. They found that the poleward displacement of the EDJ was driven by warming sources situated at its equatorial flank, with larger tropical warmings inducing larger poleward shifts. Accordingly, the Biased-models, which are equatorward shifted in present-day conditions, would exhibit larger poleward shifts in the future than the Neutral-models since their EDJs are closer to the equator and experience greater warming on their equatorial flank.

In summary, the multiparametric perspective of the EDJ has provided a better understanding of the winter EDJ responses to climate change, allowing us to question some established changes like the EDJ squeezing, disentangle the ambiguous latitudinal EDJ responses and identify the key role of model biases. Furthermore, the use of the EDJ parameters together with the MLR framework has enabled the identification of the major drivers of the future changes in the EDJ latitude, and the quantification of their relative roles and spatial fingerprints, facilitating the interpretation of the mechanisms behind the intraseasonal latitudinal shifts. Although useful, our approach also presents some drawbacks. For instance, the EDJ detection method does not account for multiple EDJs and their associated latitudes. This restriction might affect the latitudinal projections, although the effects should be small because multiple EDJs are relatively uncommon. Unravelling the potential dependences among the drivers and their non-linear effects on the EDJ could further improve the assessment of the uncertainties in regional climate change projection.

X. Conclusions and Outlook

Along this PhD thesis, some open questions in the current literature about the NATL EDJ climate variability have been addressed. To do so, we have developed a multiparametric characterization of the EDJ. Under the new perspective, 1) a description of the 2D EDJ preferred patterns and transitions has been provided. In addition, 2) we have identified the EDJ configurations leading to temperature extreme events over Europe. Then, 3) we have assessed the effect of natural drivers on the EDJ parameters variability with a special focus on the involved dynamical mechanisms. Finally, 4) we have quantified and evaluated the future changes of the EDJ parameters and structure. The main conclusions of each topic are summarized below:

Recurrent Patterns and Transitions of the EDJ

- A combination of several parameters is required to describe the EDJ structures and so, more parameters than the EDJ latitude (*Lat*) are needed. These parameters are intensity (*Int*), sharpness (*Sh*), latitudinal flanks (*Latn*, *Lats*), longitudinal position (*Lon*) and elongations (*Lone*, *Lonw*), tilt (*Til*) and departure (*Dep*).
- The multiparametric perspective enables the detection of four recurrent patterns, corresponding to northern (N4), central (C4), southward-shifted and tilted (St4) and southernmost-shifted and split-like (Sp4) EDJs. The three latitudinal regimes perspective is not able to distinguish between St4 and Sp4 patterns.
- The four preferred patterns show some tendency for a poleward migration of EDJs (Sp4-St4-C4-N4 events), which is further accompanied by an eastward progression, followed by a weakening and increasing asymmetry as the EDJ approaches the northern state. The consideration of the St4 and Sp4 multiparametric EDJ patterns unveil that the well-established abrupt transition between northern and southern latitudes is not that likely.

EDJ configurations leading to extreme temperatures over Europe during winter

- Four distinct European regions were identified based on the EDJ configurations triggering cold and warm extreme temperature events: Scandinavia (SCA), Central (CEU) and Eastern (EEU) Europe and western (WMED).
- The EDJ configurations defining the regions not only differ in *Lat*, but more parameters are required for their obtention. For each region, the cold and warm events EDJ structures are different, but not opposite.

  Cold spells occur under a localized disruption of the westerlies over the region of occurrence, implying different rearrangements of the EDJ depending on the region. SCA events present southward shifted strong zonal EDJs and WMED weak and eastward elongated northern EDJs. CEU and EEU events present NW-SE tilted EDJs but weakened for the former region and westward contracted for the latter. Such disparity is not reported for warm events which present intensified and NE-SW tilted EDJs, albeit with appreciable differences across regions, like zonal asymmetries and elongation.
- For all regions and types of events, the joint action of the selected parameters increases the odds of the extremes several times more than *Int* and *Lat*. The EDJ *Int* is a critical aspect for the occurrence of temperature extremes, being relevant in almost all regions. The *Lat* plays a less important role since the EDJ latitudinal position can often be inferred from other parameters, like the longitude, and because some regional extremes can occur under northward and southward shifted EDJs, such the cold spells in CEU and EEU. The *Til* appears as a relevant parameter in more than half of the regions, and as the leading EDJ parameter in some of them. Changes in the *Til* imply substantial variations in the odds of extreme occurrence, which are comparable to those deduced from the *Lat* or *Int* of the EDJ.

Interannual EDJ driven variability

- The wintertime interannual variability of the EDJ was detected to be influenced by seven drivers: PNA, TNH and NPO-ENSO, which are related to ENSO, SPV, AMOC, NAH and SNOW. The multiparametric perspective reveals a hierarchy among the drivers since their influence on the EDJ parameters is very heterogeneous. Whereas ENSO and SPV appear as major drivers impacting on most of the EDJ parameters, AMOC, NAH and SNOW behave as minor drivers.
- The multiparametric perspective captures the reported impacts of the drivers on the EDJ in terms of the NAO (*Int* and *Lat*), but provides additional ones. Positive phases of PNA, TNH and NPO-ENSO shift the EDJ *Lat* equatorward. In addition, PNA and NPO-ENSO elongate the EDJ westward and PNA and TNH reduce the EDJ *Til*. The intensification of the SPV is associated with strengthened, poleward and eastward elongated EDJs. The reduction in the Northern Hemisphere snow cover modifies the position of the EDJ towards the west and the equator. A reinforced AMOC strongly weakens the EDJ and exerts some influence towards a split structure. The late summer NAH modulates the winter EDJ *Til*.
- The EDJ parameters variability are explained unequally. 30% is explained for latitudinal parameters and a 20% for longitudinal and wind-related parameters. The parameters associated with the EDJ zonal asymmetries are poorly captured.
- The specific patterns of eddy forcing and wave breaking involved in each driver impact were assessed, revealing the forcing patterns that impact on a specific set of EDJ parameters. Drivers impacting on EDJ latitudinal parameters present both types of wave breaking. Those with significant influence on zonal asymmetries show an elongated AWB over Europe, and those on wind speed related parameters present a zonal gradient of G around 50°N.

Evaluation of the EDJ parameters future changes

- Under the radiative forcing scenario SSP5-8.5, the current literature reports a no clear latitudinal shift of the EDJ for the winter season. However, by splitting the winter into two subperiods, our approach finds a high model agreement on a

poleward EDJ shift in early winter (ND), followed by a slight equatorward shift in late winter (JF). Following the latitudinal behaviour, the longitudinal parameters display an eastward EDJ shift but, although there is a high model agreement on the EDJ elongation over Europe during ND, the distribution of the JF changes presents a large spread.

- We do not find the well-stablished future EDJ squeezing of the literature, not even in early and late winter. The multiparametric perspective indicates that the future squeezing pattern of the winter EDJ could be an artefact from mixing different intraseasonal EDJ responses to climate change that involve opposite meridional shifts of the EDJ.
- The intraseasonal latitudinal responses of the EDJ to climate change are shown to be promoted by future changes in other atmospheric/oceanic regions: the upper tropospheric temperature meridional gradient (Grad200) and the NATL sea surface temperature warming hole (WH) in early winter, and the stratospheric polar vortex (SPV) in late winter. Thus, the processes driving the future changes in the EDJ latitude change throughout the winter from thermodynamic to dynamic processes.
- The model biases in the EDJ latitude also influence its projections. We find that the projections of the models without biases in the EDJ latitude present no clear shift in early winter and a strong displacement of the EDJ towards the equator in late winter. Thus, part of the projected poleward shift of the EDJ under climate change could be exacerbated by the model biases.

In summary, the multiparametric perspective improves our previous knowledge about the NATL EDJ climate variability.

➢ Outlook

Although some questions have been addressed in this PhD thesis, further applications of the multiparametric perspective of the EDJ remain for future investigation. For instance, we have only investigated the link between the EDJ dynamics and the winter extreme temperature over European sectors, the analysis may be applied to other extreme fields such summer heatwaves, droughts or extreme rainfalls. In addition, it could be applied to explore the EDJ relation with other less studied variables like the PM_{10} concentrations. The regional distribution over Europe of PM_{10} concentrations was detected to be controlled by the EDJ latitudinal position in recent years (Ordóñez et al., 2019). In this line, the multiparametric perspective has provided additional insights about the influence of the large-scale conditions on air stagnation (Maddison et al., 2023). Considering that air stagnation is associated with air pollutants (Garrido-Perez et al., 2021), the application of the new EDJ diagnostics could help to better understand the relation between the EDJ and the regional European pollution concentrations beyond the EDJ *Lat*. Moving away from the current climate, similar analysis could be explored in the ScenarioMIP experiments. Particularly, the relation between the projections of regional climate and the EDJ parameters could be assessed, as well as the influence of the parameter biases.

With respect to the EDJ parameter projections, the multiparametric perspective could also shed some light on the eastward displacement of the EDJ over Europe and the tendency towards EDJs with a single flow configuration. The occurrence of more zonal and eastward displaced EDJs in the future is consistent with the projected decreases in European blocking (Barnes & Polvani, 2015; Harvey et al., 2023), although feedbacks between the eddies and the mean flow prevent the separation of cause and effect. Also, our approach could in principle be extended to analyse future projections of the EDJ in other seasons, such as summer. EDJ changes in that season have been linked to an unprecedented increase in the frequency of extreme events (Rousi et al., 2022).

Further, in this PhD thesis we have detected the drivers of the EDJ parameters and analysed the model biases in the representation of the EDJ, especially in *Lat*. Future investigation could explore whether models with biases in some drivers derive in deficiencies when simulating the EDJ parameters affected by those biased drivers. Moreover, a storyline approach (Zappa & Shepherd, 2017) could be built to obtain different

climate change scenarios for single EDJ parameters or combinations, based on the different responses of the EDJ drivers detected in Chapter VIII.

The algorithm could also characterize the EDJ in other basins. Very recently, Collazo et al. (2024) has adapted the multiparametric perspective to characterize the summer upper-level jets in South America, uncovering novel properties and aspects of the jet configuration. The latter has allowed the authors to detect the upper-level jet recurrent states and associated synoptic patterns, as well as, to study their influence on the temperature and precipitation patterns in South America. Similar projects could be carried out in the North Pacific basin.

Although we have analysed only the interannual variability and climatological changes along the PhD thesis, the EDJ varies in multiple frequencies (Woollings et al., 2018). It could be noteworthy analyse the EDJ multidecadal variability since, at these timescales, the changes in the EDJ intensity dominates over the meridional shifts, characteristic of the shorter interannual-to-decadal variability (Woollings et al., 2015). By applying our approach, changes in the relative importance of other EDJ parameters could be investigated. Also, the multidecadal variations could be related to some drivers like the Atlantic Multidecadal Oscillation (AMO), which is already known to play an important role driving the EDJ intensity (Gastineau et al., 2012), or the Pacific Decadal Oscillation (PDO), which could also influence the EDJ variability by the downstream signal of the changes in the North Pacific baroclinicity and Pacific jet (Fang & Yang, 2016).

XI. Publications

The results presented in this PhD thesis are included in the following publications:

- Barriopedro, D., Ayarzagüena, B., García-Burgos, M., & García-Herrera, R. (2023). A multi-parametric perspective of the North Atlantic eddy-driven jet. *Climate Dynamics*, *61*(1), 375-397.

- García-Burgos, M., Ayarzagüena, B., Barriopedro, D., & García-Herrera, R. (2023). Jet configurations leading to extreme winter temperatures over Europe. *Journal of Geophysical Research: Atmospheres*, *128*(24), e2023JD039304.

- García-Burgos, M., Ayarzagüena, B., Barriopedro, D., Woollings, T., & García-Herrera, R. (2024). Intraseasonal shift in the wintertime North Atlantic jet structure projected by CMIP6 models. *npj Climate and Atmospheric* Science, 7(1), 1-11.

In addition, the author has led the following publication during the development of the PhD thesis:

- García-Burgos, M., Gómara, I., Rodríguez-Fonseca, B., González-Alemán, J. J., Zurita-Gotor, P., & Ayarzagüena, B. (2023). Abrupt and persistent atmospheric circulation changes in the North Atlantic under La Niña conditions. *Weather and Climate Extremes*, *42*, 100609.

Annex: Additional Information of the Chapter VI

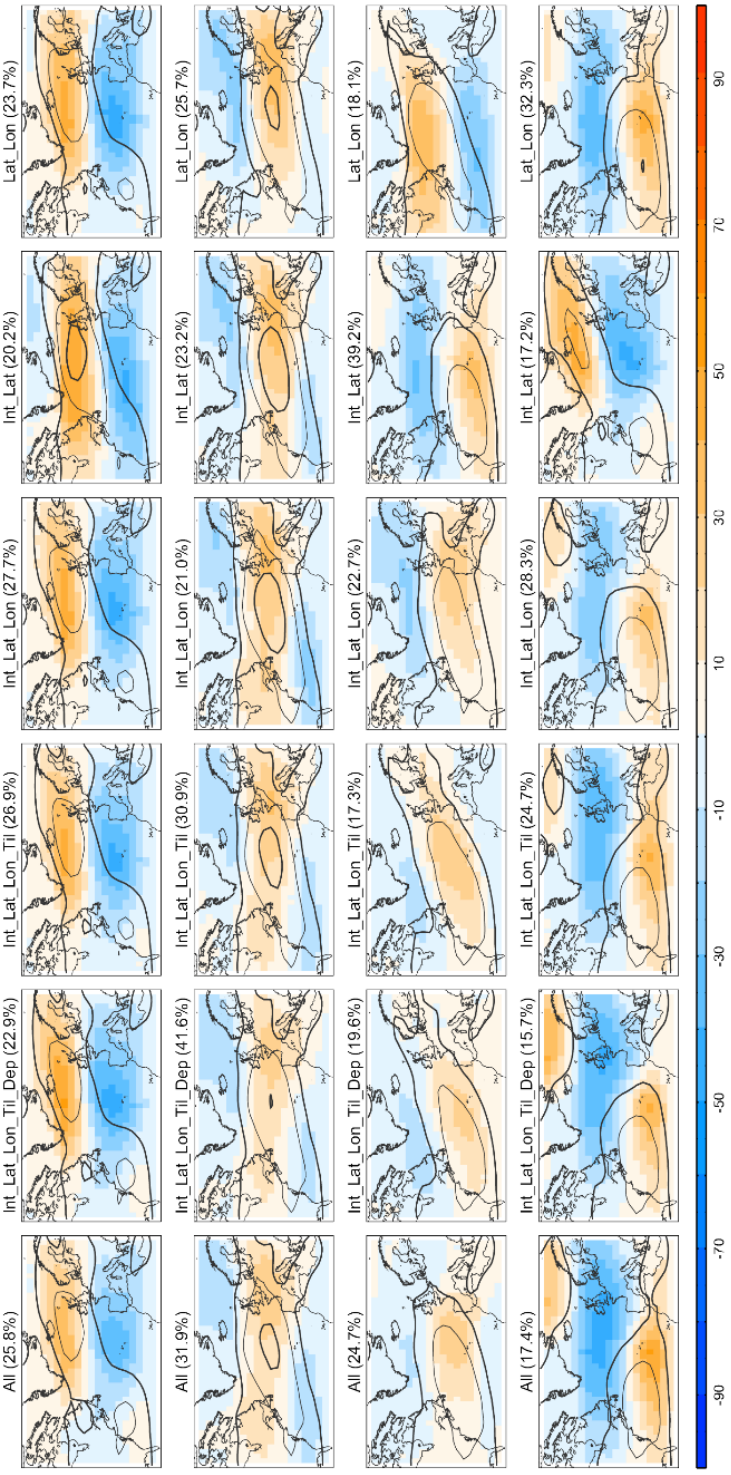

Figure AVI.1 Comparison of the four clusters obtained with different combinations of EDJ parameters: Composites of zonal wind at 925-700 hPa (contours [ms^{-1}], contour interval of 5 ms^{-1} starting at 5 ms^{-1}) and EDJ frequency (shading, in percentage of days) for days assigned to each cluster computed with (first column) all, (second column) *Int*, *Lat*, *Lon*, *Til* and *Dep*, (third column) *Int*, *Lat*, *Lon* and *Til*, (fourth column) *Int*, *Lat* and *Lon*, (fifth column) *Lat* and *Lon* and (sixth column) *Lat* parameters. Clusters correspond to (first row) northern, (second row) central, southern-tilted (third row) and (fourth row) southern-split EDJs.

Annex: Additional Information of the Chapter VII

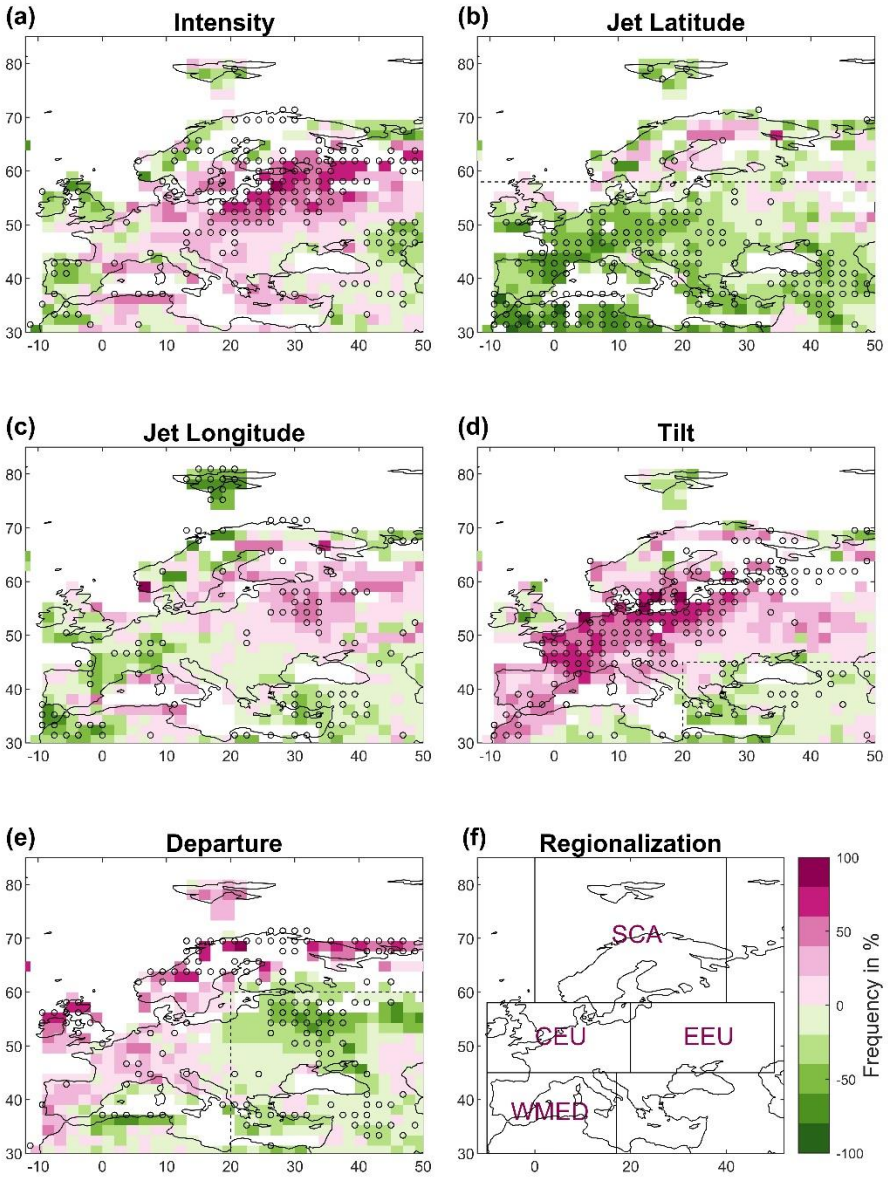

Figure VII.1 Same as Figure VII.1 but based on warm events frequency. ††

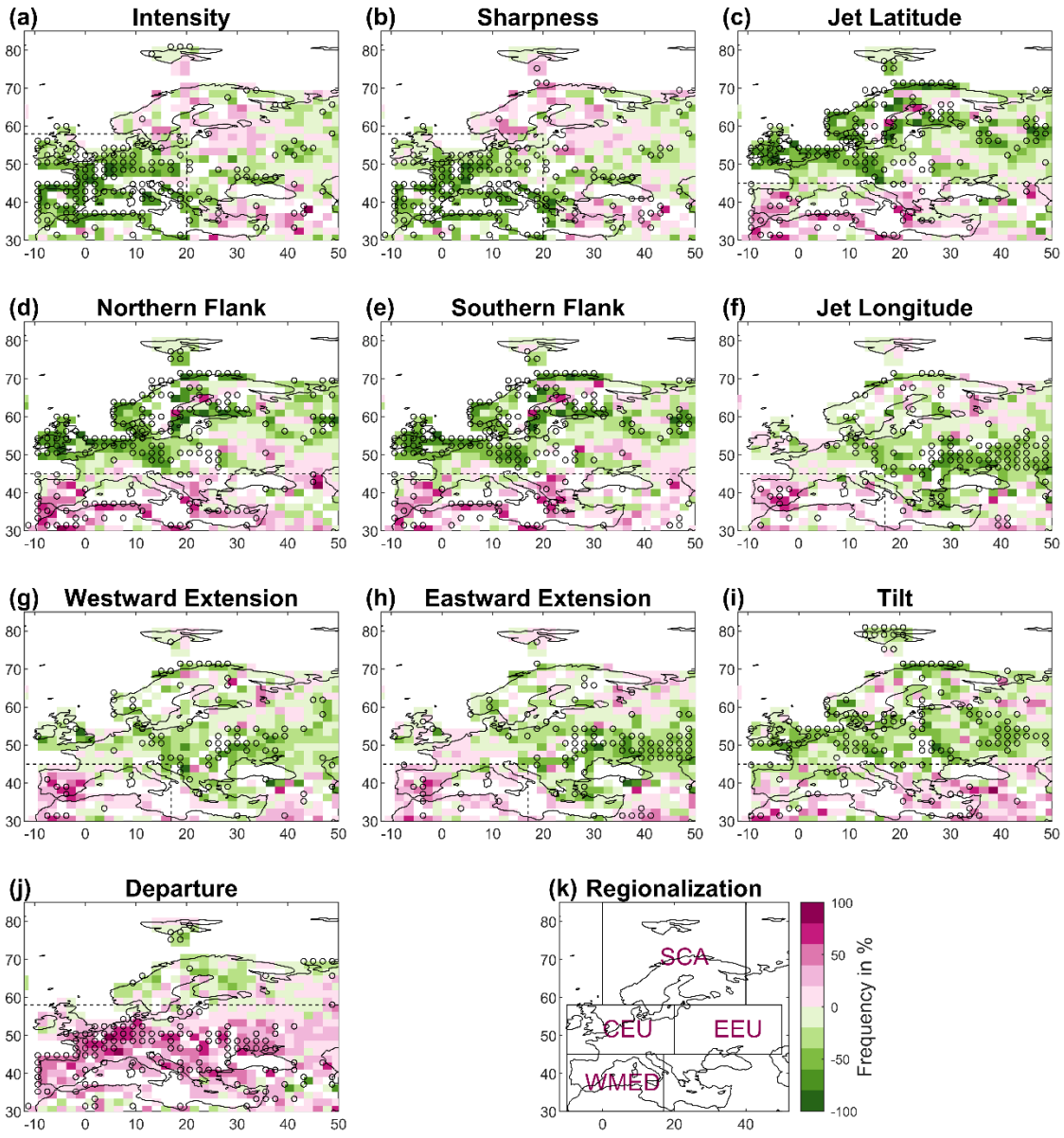

Figure VII.2 Same as Figure VII.1 but for all the EDJ parameters: (a) intensity, (b) sharpness, (c) jet latitude, (d) northern flank, (e) southern flank, (f) jet longitude, (g) westward elongation, (h) eastward elongation, (i) tilt, and (j) departure. (h) European regionalization based on the impacts of the EDJ parameters shown in (a–j).

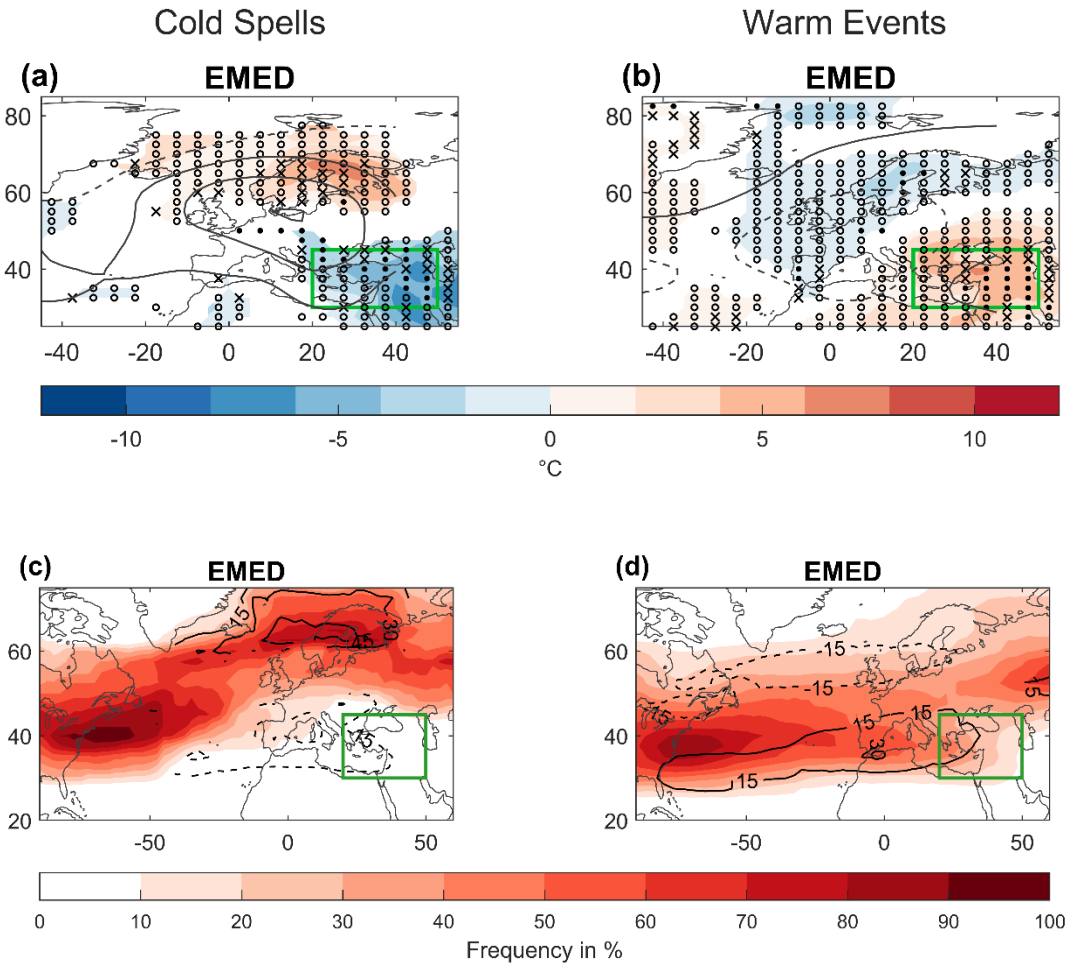

Figure AVII.3 Mechanisms and EDJ configurations for EMED. (first row) Same Figure VII.2 and (second row) same as Figure VII.3 for extreme temperature events occurring over the [30°-45°N; 20°-50°E] region.

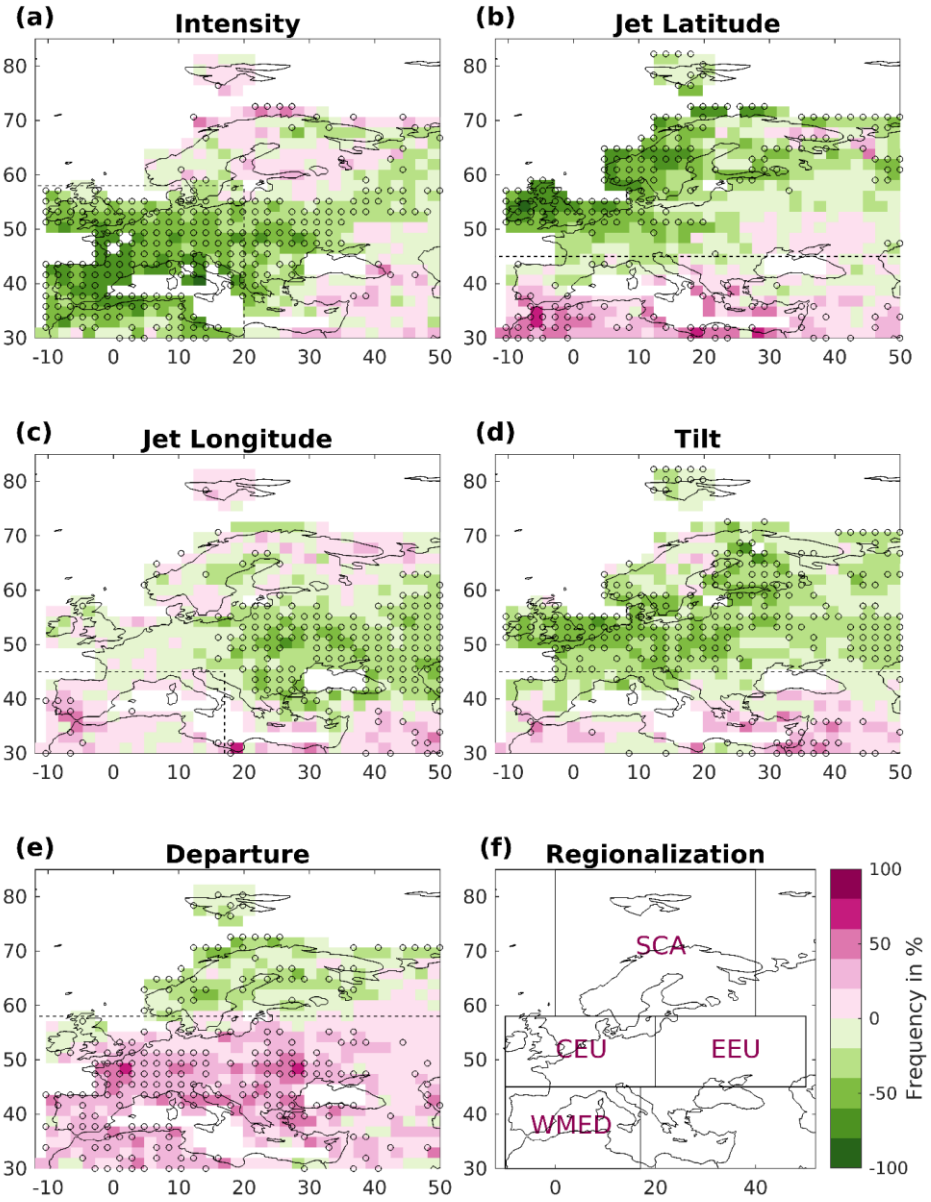

Figure AVII.4 Same as Figure VII.1 but computed with ERA5.

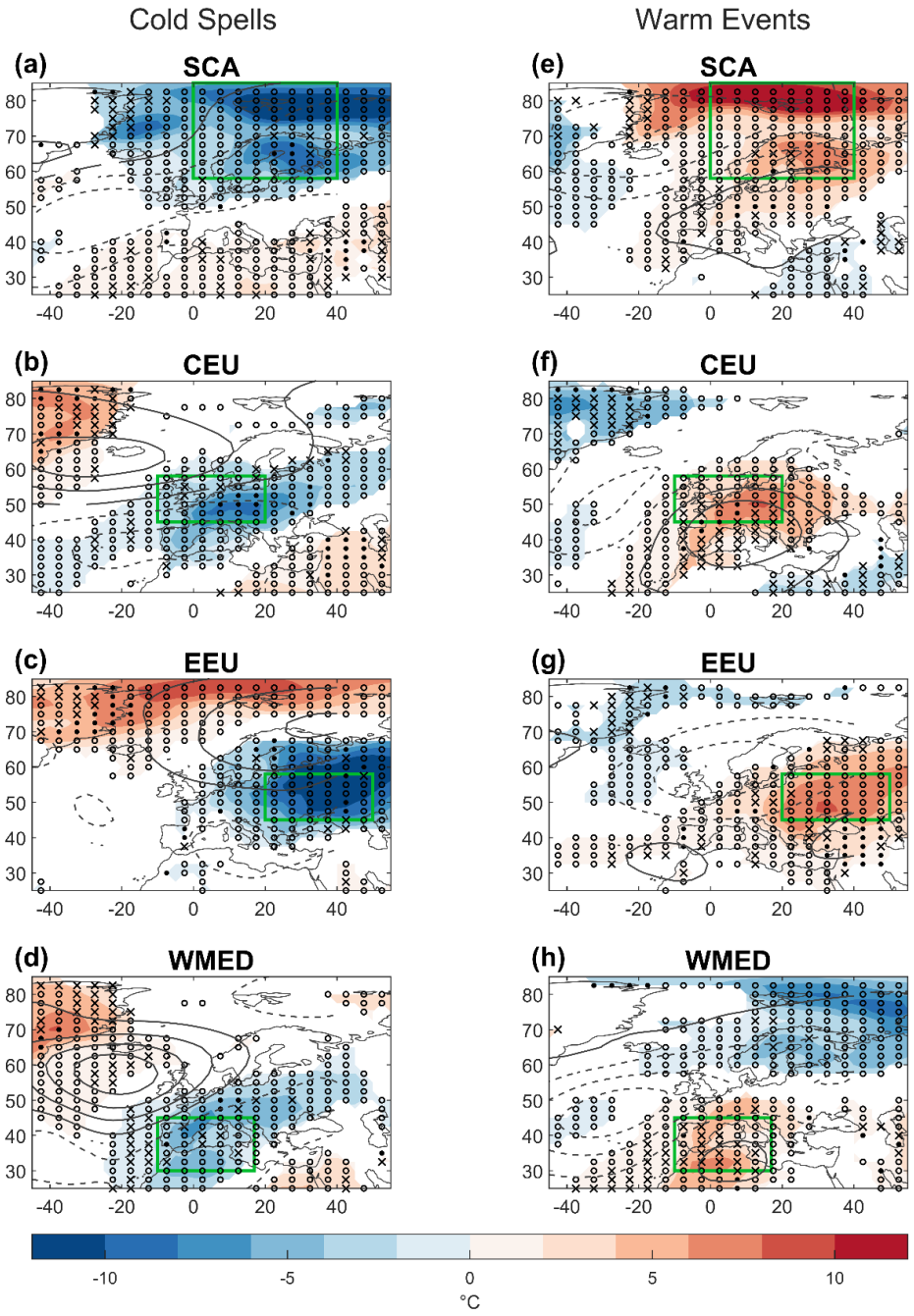

Figure AVII.5 Same as Figure VII.2 but for independent events.

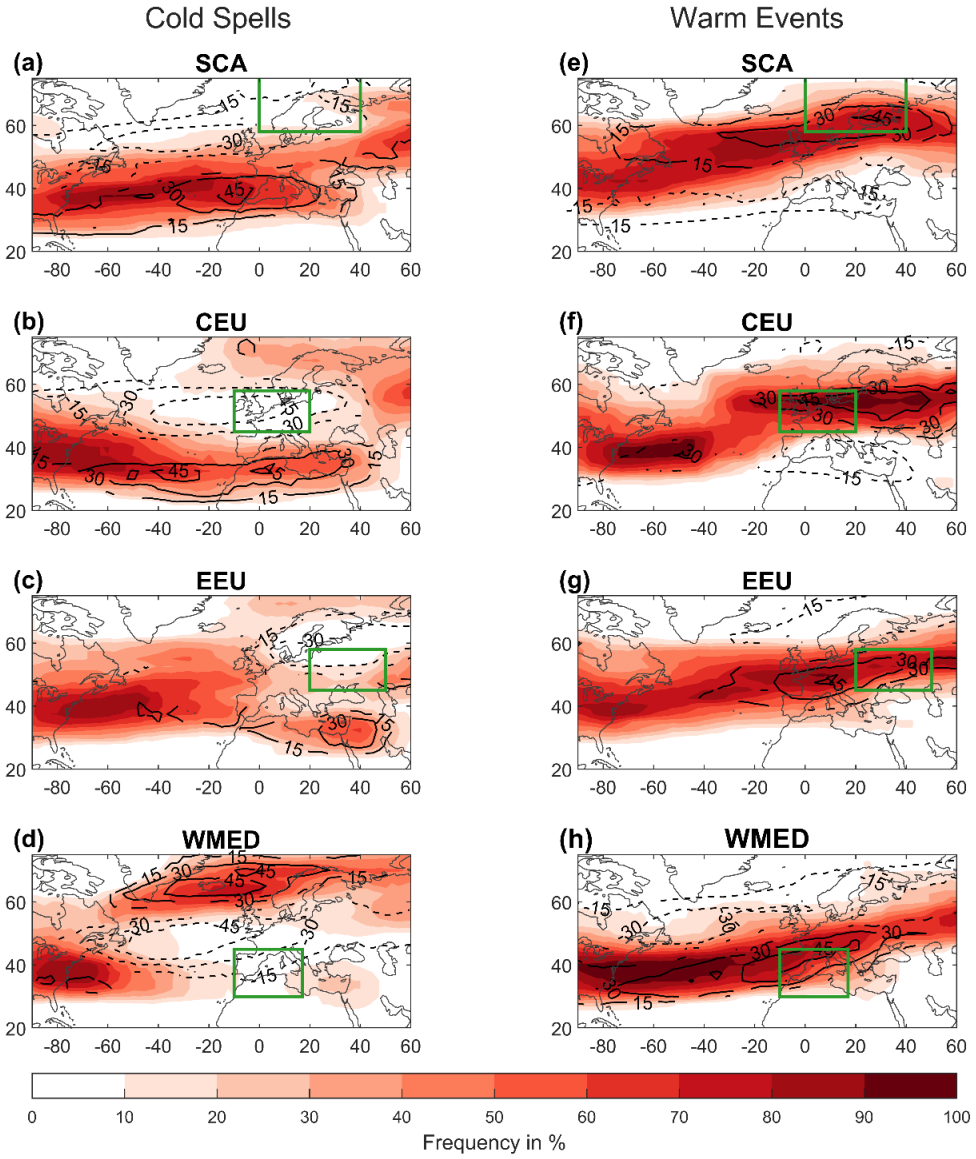

Figure AVII.6 Same as Figure VII.5 but for independent events.

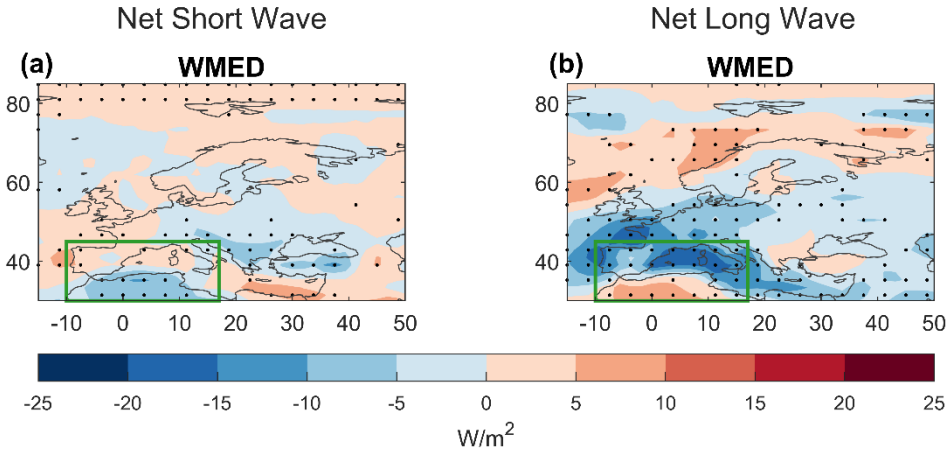

Figure AVII.7 Composites of net short (a) and long (b) wave radiation anomalies for WMED warm events. Colour shadings depict the anomalies of upward radiation fluxes (in Wm^{-2}). Statistically significant anomalies at 95% confidence level are indicated with the stippling.

Table AVII.1 Summary of the selected models based on the goodness of the fit and the exp(b) value of the added predictor in two competing logistic regression models with n+1 and n predictors for each region (rows) and type of event: cold events (central heading column) and warm events (right heading column). The number of predictors is indicated in the second row. The symbol '-' indicates that the model does not pass the second criterion (i.e. the added parameter is excluded because it does not increase the odds of an extreme). Otherwise, the cell values show the result of the log-likelihood ratio test obtained from the comparison of the two logistic regression models. Values shown in italics are not statistically significant at the 95% confidence level, indicating that the n+1 model is not significantly better that the n model. See main text for details.

	COLD SPELLS				WARM EVENTS			
	0→ 1	1→ 2	2→ 3	3→4	0→ 1	1→ 2	2→ 3	3→ 4
SCA	80.9	26.9	12.1	*	20.5	12.4	5.7	*
CEU	83.7	65.3	17.0	-	36.4	20.4	7.4	-
EEU	29.6	13.7	10.4	-	21.9	24.2	7.4	-
WMED	103.7	42.3	*	-	88.4	37.6	9.2	*

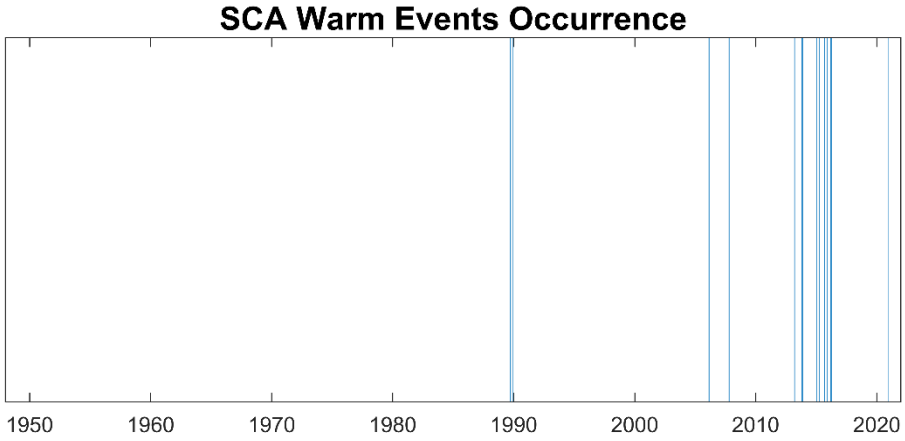

Figure AVII.8 Distribution of the SCA warm events occurrence across the analysed period.

Annex: Additional Information of the Chapter VIII

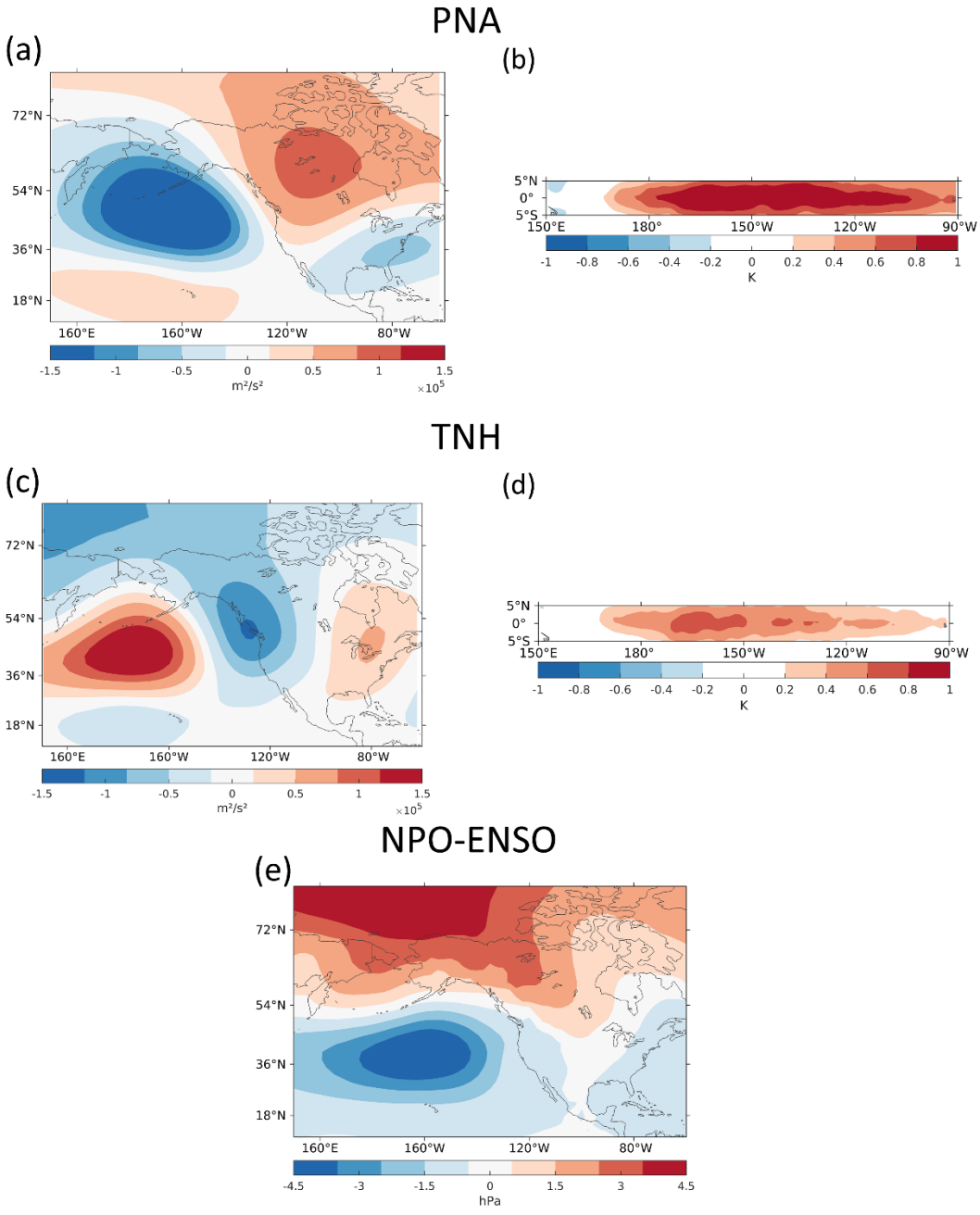

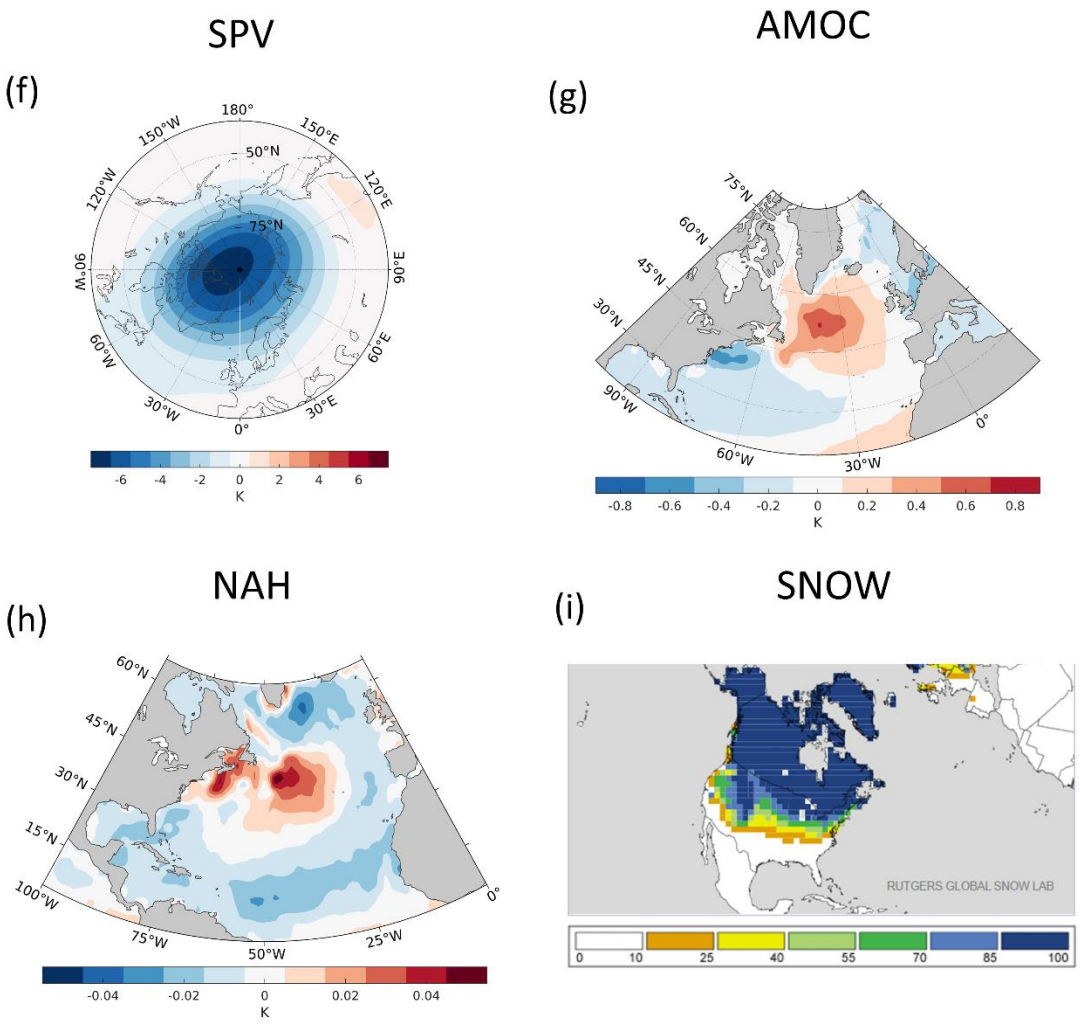

Figure AVIII.1 Spatial patterns of the EDJ drivers. (a, c) Z500 and (b, d) SST patterns associated with PNA and TNH, respectively, computed as the first and second modes of the MCA between DJF [150°E-60°W; 10°-80°N] Z500 anomalies and DJF [160°E-80°W; 5°S-5°N] SST anomalies, (e) SLP pattern associated with NPO-ENSO during El Niño-Low NPO minus La Niña-High NPO months. (f) T10 pattern for SPV, (g) SST pattern for AMOC, (h) SST pattern associated with NAH defined as the first mode of MCA between DJF [100°W-20°E; 20°-80°N] Z500 anomalies and the JAS [100°W-20°E; 0°-65°N] SST anomalies and (g) percentage pattern of snow-covered area for SNOW.

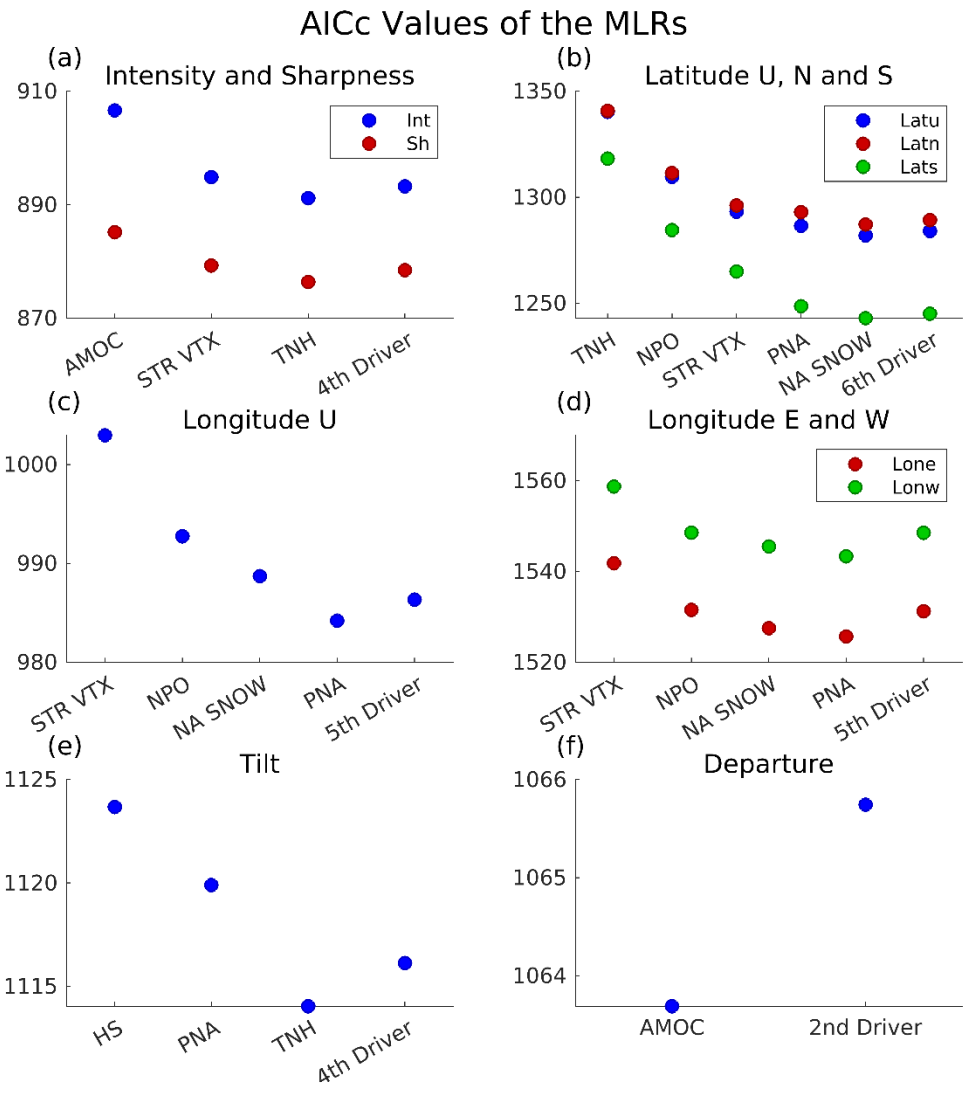

Figure VIII.2 AICc values corresponding to the EDJ parameters MLRs. Dots indicate the AICc value of the MRL when that driver is added to the MLR. Decreasing AIC values indicate that the model improves when considering further predictors.

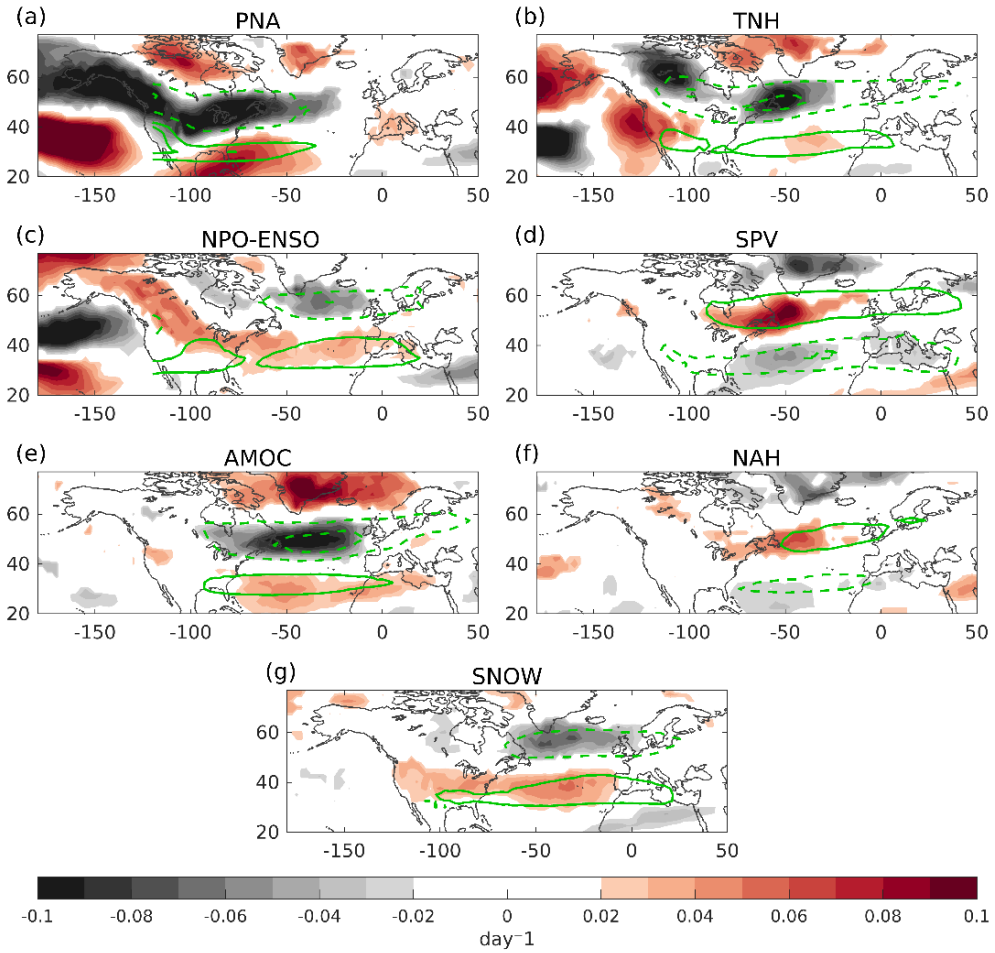

Figure AVIII.3: Same as Figure VIII.3 but including the North Pacific.

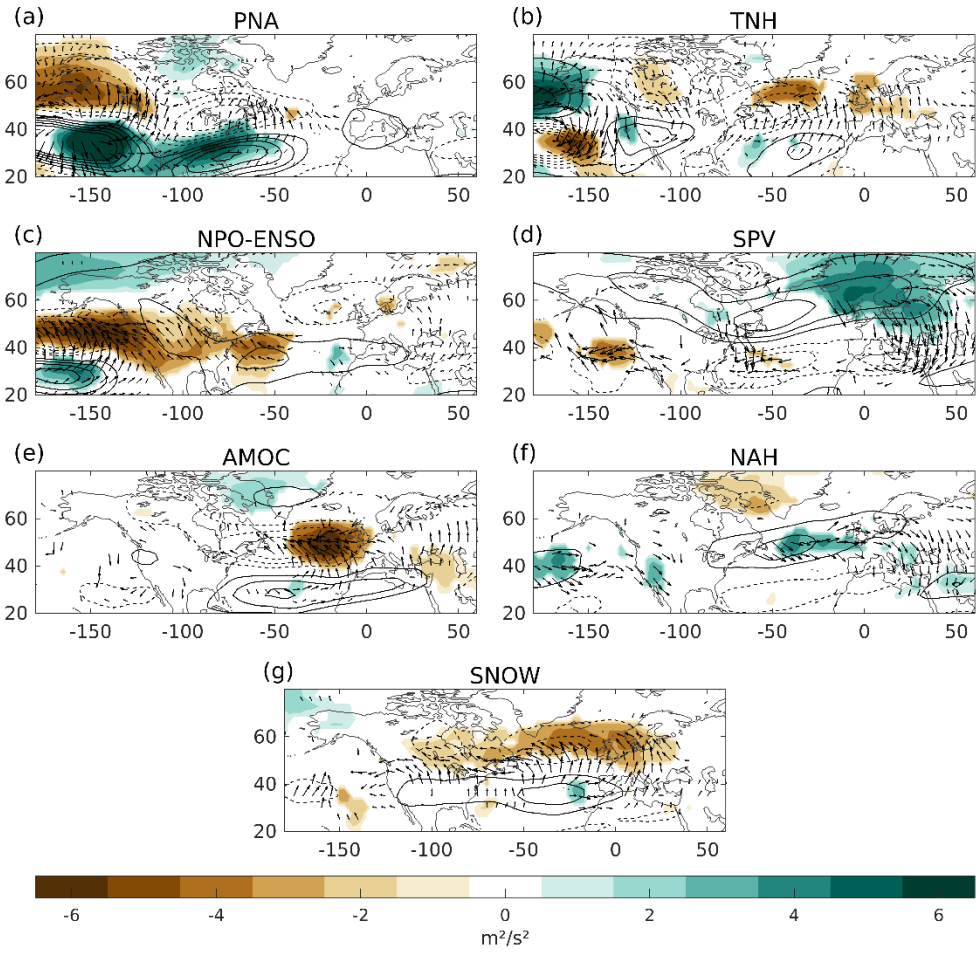

Figure AVIII.4: Same as Figure VIII.4 but including the North Pacific.

Table AVIII.1 Collinearity between the EDJ Drivers. Pearson's correlation coefficient between the different Drivers. Significant correlations are indicated in bold.

	PNA	TNH	NPO-ENSO	SPV	AMOC	NAH	SNOW
PNA							
TNH	**-0.27**						
NPO-ENSO	-0.02	**-0.28**					
SPV	**-0.18**	**-0.15**	-0.12				
AMOC	-0.05	**0.21**	0.05	**-0.15**			
NAH	-0.02	**-0.25**	-0.10	0.02	**-0.36**		
SNOW	-0.09	**0.14**	**0.30**	-0.10	0.08	0.02	

Annex: Additional Information of the Chapter IX

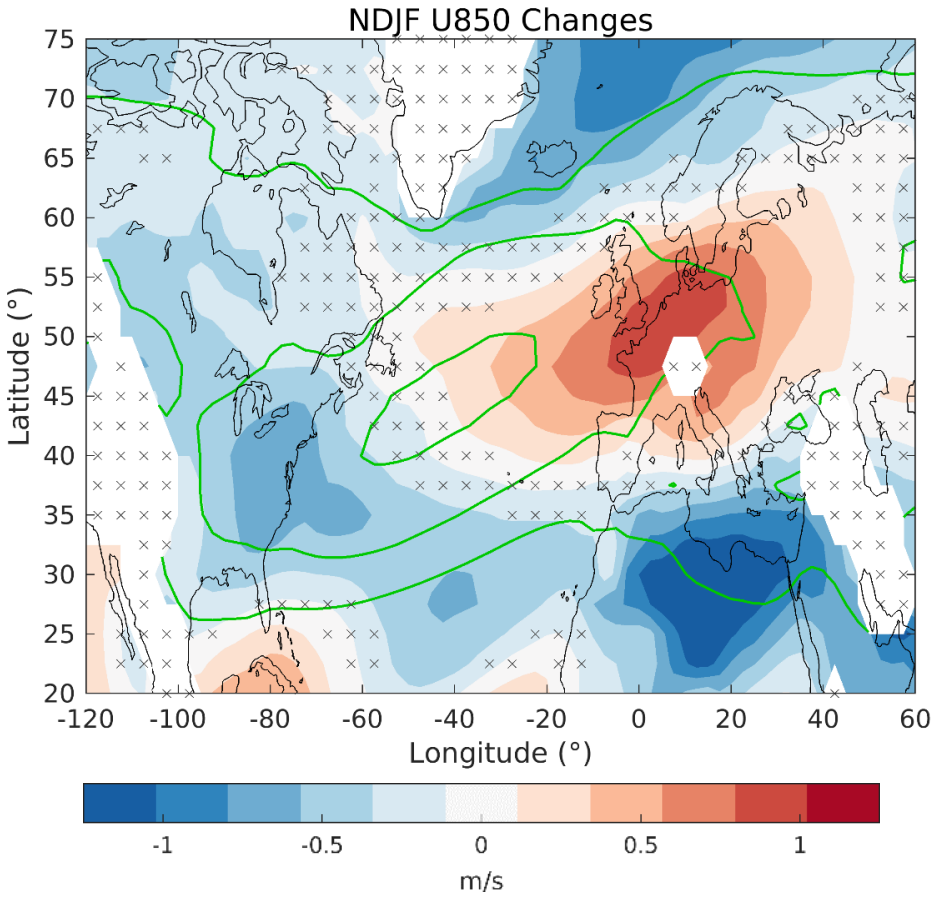

Figure AIX.3 Winter projections of the EDJ. Multimodel mean of the climate change signal in the winter (NDJF) zonal wind at 850 hPa (shading, [ms^{-1}]). The 1979-2009 NDJF climatology is shown with contours (starting at 2 ms^{-1} and drawn every 4 ms^{-1}). Crosses indicate the grid-points with no significant differences at the 95% confidence level (after a 1000-trial Monte Carlo test) and masked grid-points. The mask is constructed as the set of grid-points where the models do not present data at 850 hPa. †††

References

Abdi, H. (2010). Coefficient of Variation. *Encyclopedia of Research Design*, *1(5)*, 169–171. https://doi.org/10.1007/978-3-642-04898-2_177

Abid, M. A., Kucharski, F., Molteni, F., Kang, I. S., Tompkins, A. M., & Almazroui, M. (2021). Separating the indian and pacific ocean impacts on the euro-atlantic response to enso and its transition from early to late winter. *Journal of Climate*, *34*(4), 1531–1548. https://doi.org/10.1175/JCLI-D-20-0075.1

Ambaum, M. H. P., Hoskins, B. J., & Stephenson, D. B. (2001). Arctic Oscillation or North Atlantic Oscillation? *Journal of Climate*, *14*(16), 3495–3507. https://doi.org/10.1175/1520-0442(2001)014<3495:AOONAO>2.0.CO;2

Andrade, C., Leite, S. M., & Santos, J. A. (2012). Temperature extremes in Europe: Overview of their driving atmospheric patterns. *Natural Hazards and Earth System Science*, *12*(5), 1671–1691. https://doi.org/10.5194/nhess-12-1671-2012

Athanasiadis, P. J., Wallace, J. M., & Wettstein, J. J. (2010). Patterns of wintertime jet stream variability and their relation to the storm tracks. *Journal of the Atmospheric Sciences*, *67*(5), 1361–1381. https://doi.org/10.1175/2009JAS3270.1

Ayarzagüena, B., Ineson, S., Dunstone, N. J., Baldwin, M. P., & Scaife, A. A. (2018). Intraseasonal effects of El Niño-Southern Oscillation on North Atlantic climate. *Journal of Climate*, *31*(21), 8861–8873. https://doi.org/10.1175/JCLI-D-18-0097.1

Baker, H. S., Mbengue, C., & Woollings, T. (2018). Seasonal Sensitivity of the Hadley Cell and Cross-Hemispheric Responses to Diabatic Heating in an Idealized GCM. *Geophysical Research Letters*, *45*(5), 2533–2541. https://doi.org/10.1002/2018GL077013

Baker, H. S., Woollings, T., & Mbengue, C. (2017). Eddy-driven jet sensitivity to diabatic heating in an idealized GCM. *Journal of Climate*, *30*(16), 6413–6431. https://doi.org/10.1175/JCLI-D-16-0864.1

Baldwin, M. P., Ayarzagüena, B., Birner, T., Butchart, N., Butler, A. H., Charlton-Perez, A. J., Domeisen, D. I. V., Garfinkel, C. I., Garny, H., Gerber, E. P., Hegglin, M. I., Langematz, U., & Pedatella, N. M. (2021). Sudden Stratospheric Warmings. *Reviews of Geophysics*, *59*(1), 1–37. https://doi.org/10.1029/2020RG000708

Baldwin, M. P., & Dunkerton, T. J. (2001). Stratospheric harbingers of anomalous weather regimes. *Science*, *294*(5542), 581–584. https://doi.org/10.1126/science.1063315

Barnes, E. A. (2013). Revisiting the evidence linking Arctic amplification to extreme weather in

midlatitudes. *Geophysical Research Letters*, *40*(17), 4734–4739. https://doi.org/10.1002/grl.50880

Barnes, E. A., & Hartmann, D. L. (2011). Rossby wave scales, propagation, and the variability of eddy-driven jets. *Journal of the Atmospheric Sciences*, *68*(12), 2893–2908. https://doi.org/10.1175/JAS-D-11-039.1

Barnes, E. A., Hartmann, D. L., Frierson, D. M. W., & Kidston, J. (2010). *Effect of latitude on the persistence of eddy - driven jets*. *37*, 1–5. https://doi.org/10.1029/2010GL043199

Barnes, E. A., & Polvani, L. (2013). Response of the midlatitude jets, and of their variability, to increased greenhouse gases in the CMIP5 models. *Journal of Climate*, *26*(18), 7117–7135. https://doi.org/10.1175/JCLI-D-12-00536.1

Barnes, E. A., & Polvani, L. M. (2015). CMIP5 projections of arctic amplification, of the North American/North Atlantic circulation, and of their relationship. *Journal of Climate*, *28*(13), 5254–5271. https://doi.org/10.1175/JCLI-D-14-00589.1

Barnes, E. A., & Simpson, I. R. (2017). Seasonal sensitivity of the Northern Hemisphere jet streams to Arctic temperatures on subseasonal time scales. *Journal of Climate*, *30*(24), 10117–10137. https://doi.org/10.1175/JCLI-D-17-0299.1

Barnston, A. G., & Livezey, R. E. (1987). Classification, seasonality and persistence of low-frequency atmospheric circulation patterns. *Monthly Weather Review*, *115(6)*, 1083–1126.

Barriopedro, D., Ayarzagüena, B., García-Burgos, M., & García-Herrera, R. (2023). A multi-parametric perspective of the North Atlantic eddy-driven jet. *Climate Dynamics*, *61*(1–2), 375–397. https://doi.org/10.1007/s00382-022-06574-w

Barry, R. G., & Chorley, R. J. (2009). Atmosphere, Weather and Climate. In *Atmosphere, Weather and Climate*. https://doi.org/10.4324/9780203871027

Bellomo, K., Angeloni, M., Corti, S., & von Hardenberg, J. (2021). Future climate change shaped by inter-model differences in Atlantic meridional overturning circulation response. *Nature Communications*, *12*(1). https://doi.org/10.1038/s41467-021-24015-w

Benedict, J. J., Lee, S., & Feldstein, S. B. (2004). Synoptic view of the North Atlantic Oscillation. *Journal of the Atmospheric Sciences*, *61*(2), 121–144. https://doi.org/10.1175/1520-0469(2004)061<0121:SVOTNA>2.0.CO;2

Bjerknes, J. (1969). Monthly Weather Reyiew Atmospheric Teleconnections From the Equatorial Pacific. *Monthly Weather Review*, *97*(3), 163–172.

Blackport, R., & Screen, J. A. (2020). Insignificant effect of Arctic amplification on the amplitude of midlatitude atmospheric waves. *Science Advances*, *6*(8), 1–9. https://doi.org/10.1126/sciadv.aay2880

Blackport, R., Screen, J. A., van der Wiel, K., & Bintanja, R. (2019). Minimal influence of reduced Arctic sea ice on coincident cold winters in mid-latitudes. *Nature Climate Change*, *9*(9), 697–704. https://doi.org/10.1038/s41558-019-0551-4

Boucher, O., Servonnat, J., Albright, A. L., Aumont, O., Balkanski, Y., Bastrikov, V., Bekki, S., Bonnet, R., Bony, S., Bopp, L., Braconnot, P., Brockmann, P., Cadule, P., Caubel, A., Cheruy, F., Codron, F., Cozic, A., Cugnet, D., D'Andrea, F., … Vuichard, N. (2020). Presentation and Evaluation of the IPSL-CM6A-LR Climate Model. *Journal of Advances in Modeling Earth Systems*, *12*(7), 1–52. https://doi.org/10.1029/2019MS002010

Bracegirdle, T. J., Lu, H., & Robson, J. (2022). Early-winter North Atlantic low-level jet latitude biases in climate models: Implications for simulated regional atmosphere-ocean linkages. *Environmental Research Letters*, *17*(1). https://doi.org/10.1088/1748-9326/ac417f

Branstator, G. (2002). Circumglobal teleconnections, the jet stream waveguide, and the North Atlantic Oscillation. *Journal of Climate*, *15*(14), 1893–1910. https://doi.org/10.1175/1520-0442(2002)015<1893:CTTJSW>2.0.CO;2

Brayshaw, D. J., Hoskins, B., & Blackburn, M. (2009). The basic ingredients of the North Atlantic storm track. Part I: Land-Sea contrast and orography. *Journal of the Atmospheric Sciences*, *66*(9), 2539–2558. https://doi.org/10.1175/2009JAS3078.1

Brayshaw, D. J., Hoskins, B., & Blackburn, M. (2011). The basic ingredients of the north atlantic storm track. Part II: Sea surface temperatures. *Journal of the Atmospheric Sciences*, *68*(8), 1784–1805. https://doi.org/10.1175/2011JAS3674.1

Bretherton, C. S., Smith, C., & Wallace, J. M. (1992). An intercomparison of methods for finding coupled patterns in climate data. *Journal of Climate*, *5(6)*, 541–560.

Brönnimann, S. (2007). Impact of El Niño–southern oscillation on European climate. *Reviews of Geophysics*, *45(3)*. https://doi.org/10.1029/2006RG000199.1.INTRODUCTION

Brown, R., Derksen, C., & Wang, L. (2010). A multi-data set analysis of variability and change in Arctic spring snow cover extent, 1967-2008. *Journal of Geophysical Research Atmospheres*, *115*(16), 1–16. https://doi.org/10.1029/2010JD013975

Buehler, T., Raible, C. C., & Stocker, T. F. (2011). The relationship of winter season North Atlantic blocking frequencies to extreme cold or dry spells in the ERA-40. *Tellus, Series A: Dynamic Meteorology and Oceanography*, *63*(2), 212–222. https://doi.org/10.1111/j.1600-0870.2010.00492.x

Butchart, N. (2022). The stratosphere: a review of the dynamics and variability. *Weather and Climate Dynamics*, *3*(4), 1237–1272. https://doi.org/10.5194/wcd-3-1237-2022

Butler, A. H., Thompson, D. W. J., & Heikes, R. (2010). The steady-state atmospheric circulation

response to climate change-like thermal forcings in a simple general circulation model. *Journal of Climate*, *23*(13), 3474–3496. https://doi.org/10.1175/2010JCLI3228.1

Butterworth, S. (1930). On the Theory of Filter Amplifiers. https://www.changpuak.ch/electronics/downloads/On_the_Theory_of_Filter_Amplifiers.pdf . In *Experimental Wireless & The Wireless Engineer* (Issue October, pp. 536–541).

Cagnazzo, C., & Manzini, E. (2009). Impact of the stratosphere on the winter tropospheric teleconnections between ENSO and the North Atlantic and European region. *Journal of Climate*, *22(5)*, 1223–1238. https://doi.org/10.1175/2008JCLI2549.1

Cassou, C. (2008). Intraseasonal interaction between the Madden-Julian Oscillation and the North Atlantic Oscillation. *Nature*, *455*(7212), 523–527. https://doi.org/10.1038/nature07286

Cassou, C., Terray, L., Hurrell, J. W., & Deser, C. (2004). North Atlantic winter climate regimes: Spatial asymmetry, stationarity with time, and oceanic forcing. *Journal of Climate*, *17*(5), 1055–1068. https://doi.org/10.1175/1520-0442(2004)017<1055:NAWCRS>2.0.CO;2

Cattiaux, J., Peings, Y., Saint-Martin, D., Trou-Kechout, N., & Vavrus, S. J. (2016). Sinuosity of midlatitude atmospheric flow in a warming world. *Geophysical Research Letters*, *43*(15), 8259–8268. https://doi.org/10.1002/2016GL070309

Cavanaugh, J. E., & Neath, A. A. (2019). The Akaike information criterion: Background, derivation, properties, application, interpretation, and refinements. *Wiley Interdisciplinary Reviews: Computational Statistics*, *11*(3), 1–11. https://doi.org/10.1002/wics.1460

Chang, E. K. M. (2001). GCM and observational diagnoses of the seasonal and interannual variations of the Pacific storm track during the cool season. *Journal of the Atmospheric Sciences*, *58*(13), 1784–1800. https://doi.org/10.1175/1520-0469(2001)058<1784:GAODOT>2.0.CO;2

Chen, H. W., Zhang, F., & Alley, R. B. (2016). The robustness of midlatitude weather pattern changes due to arctic sea ice loss. *Journal of Climate*, *29*(21), 7831–7849. https://doi.org/10.1175/JCLI-D-16-0167.1

Chen, S., Wu, R., & Chen, W. (2021). Influence of North Atlantic sea surface temperature anomalies on springtime surface air temperature variation over Eurasia in CMIP5 models. *Climate Dynamics*, *57*(9–10), 2669–2686. https://doi.org/10.1007/s00382-021-05826-5

Chen, S., Wu, R., Chen, W., Hu, K., & Yu, B. (2020). Structure and dynamics of a springtime atmospheric wave train over the North Atlantic and Eurasia. *Climate Dynamics*, *54*(11–12), 5111–5126. https://doi.org/10.1007/s00382-020-05274-7

Cherchi, A., Fogli, P. G., Lovato, T., Peano, D., Iovino, D., Gualdi, S., Masina, S., Scoccimarro, E., Materia, S., Bellucci, A., & Navarra, A. (2019). Global Mean Climate and Main Patterns of

Variability in the CMCC-CM2 Coupled Model. *Journal of Advances in Modeling Earth Systems*, *11*(1), 185–209. https://doi.org/10.1029/2018MS001369

Cohen, J., Agel, L., Barlow, M., & Entekhabi, D. (2023). No detectable trend in mid-latitude cold extremes during the recent period of Arctic amplification. *Communications Earth and Environment*, *4*(1), 2–10. https://doi.org/10.1038/s43247-023-01008-9

Cohen, J., & Entekhabi, D. (2001). The influence of snow cover on northern hemisphere climate variability. *Atmosphere - Ocean*, *39*(1), 35–53. https://doi.org/10.1080/07055900.2001.9649665

Cohen, J., Zhang, X., Francis, J., Jung, T., Kwok, R., Overland, J., Ballinger, T. J., Bhatt, U. S., Chen, H. W., Coumou, D., Feldstein, S., Gu, H., Handorf, D., Henderson, G., Ionita, M., Kretschmer, M., Laliberte, F., Lee, S., Linderholm, H. W., … Yoon, J. (2020). Divergent consensuses on Arctic amplification influence on midlatitude severe winter weather. *Nature Climate Change*, *10*(1), 20–29. https://doi.org/10.1038/s41558-019-0662-y

Collazo, S., García-Herrera, R., & Barriopedro, D. (2024). Summer upper-level jets modulate the response of South American climate to ENSO. *Climate Dynamics*, *62*(2), 1031–1054. https://doi.org/10.1007/s00382-023-06955-9

Czaja, A., & Frankignoul, C. (1999). Influence of the North Atlantic SST variability on the atmospheric circulation during the twentieth century. *Geophysical Research Letters*, *26(19)*, 2969–2972. https://doi.org/10.1175/JCLI-D-14-00424.1

Czaja, A., & Frankignoul, C. (2002). Observed impact of Atlantic SST anomalies on the North Atlantic Oscillation. *Journal of Climate*, *15(6)*, 606–623. https://doi.org/10.1175/1520-0442(2002)015<2707:OTRONA>2.0.CO;2

Danabasoglu, G., Lamarque, J. F., Bacmeister, J., Bailey, D. A., DuVivier, A. K., Edwards, J., Emmons, L. K., Fasullo, J., Garcia, R., Gettelman, A., Hannay, C., Holland, M. M., Large, W. G., Lauritzen, P. H., Lawrence, D. M., Lenaerts, J. T. M., Lindsay, K., Lipscomb, W. H., Mills, M. J., … Strand, W. G. (2020). The Community Earth System Model Version 2 (CESM2). *Journal of Advances in Modeling Earth Systems*, *12*(2), 1–35. https://doi.org/10.1029/2019MS001916

Deser, C., Tomas, R. A., & Peng, S. (2007). The transient atmospheric circulation response to North Atlantic SST and sea ice anomalies. *Journal of Climate*, *20*(18), 4751–4767. https://doi.org/10.1175/JCLI4278.1

Deser, C., Tomas, R. A., & Sun, L. (2015). The role of ocean-atmosphere coupling in the zonal-mean atmospheric response to Arctic sea ice loss. *Journal of Climate*, *28*(6), 2168–2186. https://doi.org/10.1175/JCLI-D-14-00325.1

Di Capua, G., & Coumou, D. (2016). Changes in meandering of the Northern Hemisphere

circulation. *Environmental Research Letters*, *11*(9). https://doi.org/10.1088/1748-9326/11/9/094028

Dickson, R. R., & Namias, J. (1979). Atmospheric climatology and its effect on sea surface temperature-1976. *Haynes (Eds.), Ocean Variability in the US Fishery Conservation Zone. NOAA Tech. Rep., Natl. Mar. Fish. Ser. Circ, (427)*, 19–23.

Domeisen, D. I. V., Garfinkel, C. I., & Butler, A. H. (2019). The Teleconnection of El Niño Southern Oscillation to the Stratosphere. *Reviews of Geophysics*, *57*(1), 5–47. https://doi.org/10.1029/2018RG000596

Dorrington, J., Strommen, K., Fabiano, F., & Molteni, F. (2022). CMIP6 Models Trend Toward Less Persistent European Blocking Regimes in a Warming Climate. *Geophysical Research Letters*, *49*(24), 1–12. https://doi.org/10.1029/2022GL100811

Dorrington, J., & Strommen, K. J. (2020). Jet Speed Variability Obscures Euro-Atlantic Regime Structure. *Geophysical Research Letters*, *47*(15). https://doi.org/10.1029/2020GL087907

Döscher, R., Acosta, M., Alessandri, A., Anthoni, P., Arsouze, T., Bergman, T., Bernardello, R., Boussetta, S., Caron, L. P., Carver, G., Castrillo, M., Catalano, F., Cvijanovic, I., Davini, P., Dekker, E., Doblas-Reyes, F. J., Docquier, D., Echevarria, P., Fladrich, U., … Zhang, Q. (2022). The EC-Earth3 Earth system model for the Coupled Model Intercomparison Project 6. *Geoscientific Model Development*, *15*(7), 2973–3020. https://doi.org/10.5194/gmd-15-2973-2022

Drouard, M., Rivière, G., & Arbogast, P. (2015). The link between the north pacific climate variability and the north atlantic oscillation via downstream propagation of synoptic waves. *Journal of Climate*, *28*(10), 3957–3976. https://doi.org/10.1175/JCLI-D-14-00552.1

Drouard, M., Rivière, G., & Arbogast, P. (2013). The north Atlantic oscillation response to large-scale atmospheric anomalies in the northeastern Pacific. *Journal of the Atmospheric Sciences*, *70*(9), 2854–2874. https://doi.org/10.1175/JAS-D-12-0351.1

Eichelberger, S. J., & Hartmann, D. L. (2007). Zonal jet structure and the leading mode of variability. *Journal of Climate*, *20*(20), 5149–5163. https://doi.org/10.1175/JCLI4279.1

Eyring, V., Bony, S., Meehl, G. A., Senior, C. A., Stevens, B., Stouffer, R. J., & Taylor, K. E. (2016). Overview of the Coupled Model Intercomparison Project Phase 6 (CMIP6) experimental design and organization. *Geoscientific Model Development*, *9*(5), 1937–1958. https://doi.org/10.5194/gmd-9-1937-2016

Fang, J., & Yang, X. Q. (2016). Structure and dynamics of decadal anomalies in the wintertime midlatitude North Pacific ocean–atmosphere system. *Climate Dynamics*, *47*(5–6), 1989–2007. https://doi.org/10.1007/s00382-015-2946-x

Feldstein, S. B. (2000). The timescale, power spectra, and climate noise properties of teleconnection patterns. *Journal of Climate*, *13*(24), 4430–4440. https://doi.org/10.1175/1520-0442(2000)013<4430:TTPSAC>2.0.CO;2

Foukal, P. N., & Chafik, L. (2022). The AMOC needs a universally-accepted definition. *ESS Open Archive*, *8.5.2017*, 2003–2005.

Frame, T. H. A., Ambaum, M. H. P., Gray, S. L., & Methven, J. (2011). Ensemble prediction of transitions of the north atlantic eddy-driven jet. *Quarterly Journal of the Royal Meteorological Society*, *137*(658), 1288–1297. https://doi.org/10.1002/qj.829

Frame, T. H. A., Methven, J., Gray, S. L., & Ambaum, M. H. P. (2013). Flow-dependent predictability of the North Atlantic jet. *Geophysical Research Letters*, *40*(10), 2411–2416. https://doi.org/10.1002/grl.50454

Francis, J. A., & Vavrus, S. J. (2012). Evidence linking Arctic amplification to extreme weather in mid-latitudes. *Geophysical Research Letters*, *39*(6), 1–6. https://doi.org/10.1029/2012GL051000

Frankignoul, C., & Kestenare, E. (2005). Observed Atlantic SST anomaly impact on the NAO: An update. *Journal of Climate*, *18*(19), 4089–4094. https://doi.org/10.1175/JCLI3523.1

Franzke, C., Woollings, T., & Martius, O. (2011). Persistent Circulation Regimes and Preferred Regime Transitions in the North Atlantic. *Journal of the Atmospheric Sciences*, *68(12)*, 2809–2825. https://doi.org/10.1175/JAS-D-11-046.1

Franzke, C., Feldstein, S. B., & Lee, S. (2011). Synoptic analysis of the Pacific-North American teleconnection pattern. *Quarterly Journal of the Royal Meteorological Society*, *137*(655), 329–346. https://doi.org/10.1002/qj.768

Franzke, C., Lee, S., & Feldstein, S. B. (2004). Is the North Atlantic Oscillation a breaking wave? *Journal of the Atmospheric Sciences*, *61*(2), 145–160. https://doi.org/10.1175/1520-0469(2004)061<0145:ITNAOA>2.0.CO;2

Galfi, V. M., & Messori, G. (2023). Erratum: Persistent anomalies of the North Atlantic jet stream and associated surface extremes over Europe (Environmental Research Letters (2023) 18 (024017) DOI: 10.1088/1748-9326/acaedf. *Environmental Research Letters*, *18*(3). https://doi.org/10.1088/1748-9326/acbdb3

García-Burgos, M., Ayarzagüena, B., Barriopedro, D., & García-herrera, R. (2023). *Jet Configurations Leading to Extreme Winter Temperatures Over Europe Journal of Geophysical Research : Atmospheres*. https://doi.org/10.1029/2023JD039304

García-Burgos, M., Ayarzagüena, B., Barriopedro, D., Woollings, T., & García-Herrera, R. (2024). Intraseasonal shift in the wintertime North Atlantic jet structure projected by CMIP6 models.

Npj Climate and Atmospheric Science, *7*(1), 1–11. https://doi.org/10.1038/s41612-024-00775-2

García-Serrano, J., Rodríguez-Fonseca, B., Bladé, I., Zurita-Gotor, P., & de la Cámara, A. (2011). Rotational atmospheric circulation during North Atlantic-European winter: The influence of ENSO. *Climate Dynamics*, *37*(9–10), 1727–1743. https://doi.org/10.1007/s00382-010-0968-y

Garrido-Perez, J. M., García-Herrera, R., & Ordóñez, C. (2021). Assessing the value of air stagnation indices to reproduce PM10 variability in Europe. *Atmospheric Research*, *248*(September 2020), 105258. https://doi.org/10.1016/j.atmosres.2020.105258

Gastineau, G., D'Andrea, F., & Frankignoul, C. (2013). Atmospheric response to the North Atlantic Ocean variability on seasonal to decadal time scales. *Climate Dynamics*, *40*(9–10), 2311–2330. https://doi.org/10.1007/s00382-012-1333-0

Gastineau, G., & Frankignoul, C. (2012). Cold-season atmospheric response to the natural variability of the Atlantic meridional overturning circulation. *Climate Dynamics*, *39*(1–2), 37–57. https://doi.org/10.1007/s00382-011-1109-y

Gastineau, G., & Frankignoul, C. (2015). Influence of the North Atlantic SST variability on the atmospheric circulation during the twentieth century. *Journal of Climate*, *28*(4), 1396–1416. https://doi.org/10.1175/JCLI-D-14-00424.1

Gastineau, G., Frankignoul, C., Gao, Y., Liang, Y. C., Kwon, Y. O., Cherchi, A., Ghosh, R., Manzini, E., Matei, D., Mecking, J., Suo, L., Tian, T., Yang, S., & Zhang, Y. (2023). Forcing and impact of the Northern Hemisphere continental snow cover in 1979-2014. *Cryosphere*, *17*(5), 2157–2184. https://doi.org/10.5194/tc-17-2157-2023

Gastineau, G., L'Hévéder, B., Codron, F., & Frankignoul, C. (2016). Mechanisms determining the winter atmospheric response to the Atlantic overturning circulation. *Journal of Climate*, *29*(10), 3767–3785. https://doi.org/10.1175/JCLI-D-15-0326.1

Gerber, E. P., Butler, A., Calvo, N., Charlton-Perez, A., Giorgetta, M., Manzini, E., Perlwitz, J., Polvani, L. M., Sassi, F., Scaife, A. A., Shaw, T. A., Son, S. W., & Watanabe, S. (2012). Assessing and understanding the impact of stratospheric dynamics and variability on the earth system. *Bulletin of the American Meteorological Society*, *93*(6), 845–859. https://doi.org/10.1175/BAMS-D-11-00145.1

Gershunov, A., & Barnett, T. P. (1998). Interdecadal Modulation of ENSO Teleconnections. *Bulletin of the American Meteorological Society*, *79*(12), 2715–2725. https://doi.org/10.1175/1520-0477(1998)079<2715:IMOET>2.0.CO;2

Gervais, M., Shaman, J., & Kushnir, Y. (2019). Impacts of the North Atlantic warming hole in future climate projections: Mean atmospheric circulation and the North Atlantic jet. *Journal of*

Climate, *32*(10), 2673–2689. https://doi.org/10.1175/JCLI-D-18-0647.1

Gill, A. E. (1980). Some simple solutions for heat-induced tropical circulation. In *Quarterly Journal of the Royal Meteorological Society* (Vol. 106, Issue 449, pp. 447–462). https://doi.org/10.1002/qj.49710644905

Gong, G., Entekhabi, D., & Cohen, J. (2002). A large-ensemble model study of the wintertime AO-NAO and the role of interannual snow perturbations. *Journal of Climate*, *15*(23), 3488–3499. https://doi.org/10.1175/1520-0442(2002)015<3488:ALEMSO>2.0.CO;2

Gong, G., Entekhabi, D., & Cohen, J. (2003). Modeled Northern Hemisphere winter climate response to realistic Siberian snow anomalies. *Journal of Climate*, *16*(23), 3917–3931. https://doi.org/10.1175/1520-0442(2003)016<3917:MNHWCR>2.0.CO;2

Hajima, T., Watanabe, M., Yamamoto, A., Tatebe, H., Noguchi, M. A., Abe, M., Ohgaito, R., Ito, A., Yamazaki, D., Okajima, H., Ito, A., Takata, K., Ogochi, K., Watanabe, S., & Kawamiya, M. (2020). Development of the MIROC-ES2L Earth system model and the evaluation of biogeochemical processes and feedbacks. *Geoscientific Model Development*, *13*(5), 2197–2244. https://doi.org/10.5194/gmd-13-2197-2020

Hall, R., Erdélyi, R., Hanna, E., Jones, J. M., & Scaife, A. A. (2015). Drivers of North Atlantic Polar Front jet stream variability. *International Journal of Climatology*, *35*(8), 1697–1720. https://doi.org/10.1002/joc.4121

Hall, R. J., Jones, J. M., Hanna, E., Scaife, A. A., & Erdélyi, R. (2017). Drivers and potential predictability of summer time North Atlantic polar front jet variability. *Climate Dynamics*, *48*(11), 3869–3887. https://doi.org/10.1007/s00382-016-3307-0

Hannachi, A., Woollings, T., & Fraedrich, K. (2012). The North Atlantic jet stream: A look at preferred positions, paths and transitions. *Quarterly Journal of the Royal Meteorological Society*, *138*(665), 862–877. https://doi.org/10.1002/qj.959

Hartmann, D. L. (2007). The atmospheric general circulation and its variability. *Journal of the Meteorological Society of Japan*, *85 B*, 123–143. https://doi.org/10.2151/jmsj.85B.123

Harvey, B., Hawkins, E., & Sutton, R. (2023). Storylines for future changes of the North Atlantic jet and associated impacts on the UK. *International Journal of Climatology*, *December 2022*, 1–18. https://doi.org/10.1002/joc.8095

Harvey, B. J., Cook, P., Shaffrey, L. C., & Schiemann, R. (2020). The Response of the Northern Hemisphere Storm Tracks and Jet Streams to Climate Change in the CMIP3, CMIP5, and CMIP6 Climate Models. *Journal of Geophysical Research: Atmospheres*, *125*(23), 1–10. https://doi.org/10.1029/2020JD032701

Harvey, B. J., Shaffrey, L. C., & Woollings, T. J. (2015). Deconstructing the climate change response

of the Northern Hemisphere wintertime storm tracks. *Climate Dynamics*, *45*(9–10), 2847–2860. https://doi.org/10.1007/s00382-015-2510-8

Hassanzadeh, P., Kuang, Z., & Farrell, B. F. (2014). Responses of midlatitude blocks and wave amplitude to changes in the meridional temperature gradient in an idealized dry GCM. *Geophysical Research Letters*, *41*(14), 5223–5232. https://doi.org/10.1002/2014GL060764

Hay, S., Kushner, P. J., Blackport, R., McCusker, K. E., Oudar, T., Sun, L., England, M., Deser, C., Screen, J. A., & Polvani, L. M. (2022). Separating the Influences of Low-Latitude Warming and Sea Ice Loss on Northern Hemisphere Climate Change. *Journal of Climate*, *35*(8), 2327–2349. https://doi.org/10.1175/JCLI-D-21-0180.1

Held, I. M., & Hou, A. Y. (1980). Nonlinear axially symmetric circulations in a nearly inviscid atmosphere. In *Journal of the Atmospheric Sciences* (Vol. 37, Issue 3, pp. 515–533). https://doi.org/10.1175/1520-0469(1980)037<0515:NASCIA>2.0.CO;2

Herceg-Bulić, I., Ivasić, S., & Popović, M. (2023). Impact of tropical SSTs on the late-winter signal over the North Atlantic-European region and contribution of midlatitude Atlantic. *Npj Climate and Atmospheric Science*, *6*(1). https://doi.org/10.1038/s41612-023-00493-1

Hersbach, H., Bell, B., Berrisford, P., Hirahara, S., Horányi, A., Muñoz-Sabater, J., Nicolas, J., Peubey, C., Radu, R., Schepers, D., Simmons, A., Soci, C., Abdalla, S., Abellan, X., Balsamo, G., Bechtold, P., Biavati, G., Bidlot, J., Bonavita, M., … Thépaut, J. N. (2020). The ERA5 global reanalysis. *Quarterly Journal of the Royal Meteorological Society*, *146*(730), 1999–2049. https://doi.org/10.1002/qj.3803

Holland, M. M., & Bitz, C. M. (2003). Polar amplification of climate change in coupled models. *Climate Dynamics*, *21*(3–4), 221–232. https://doi.org/10.1007/s00382-003-0332-6

Holton, J. . R. (2004). An introduction to Dynamic Meteorology. In *A Sociology of Friendship and Kinship*. https://doi.org/10.4324/9780429345050

Holton, J. R., & Hakim, G. J. (2012). An introduction to dynamic meteorology: Fifth edition. In *An Introduction to Dynamic Meteorology: Fifth Edition* (Vol. 9780123848). https://doi.org/10.1016/C2009-0-63394-8

Hoskins, B. J., & Hodges, K. I. (2002). New Perspectives on the Northern Hemisphere Winter Storm Tracks. *Journal of the Atmospheric Sciences*, *59(6)*, 1041–1061.

Hoskins, B. J., & Karoly, D. J. (1981). The steady linear response of a spherical atmosphere to thermal and orographic forcing. *Journal of the Atmospheric Sciences*, *38(6)*, 1179–1196.

Hoskins, B. J., & Valdes, P. J. (1990). On the existence of storm-tracks. *Universitas Nusantara PGRI Kediri*, *47(15)*, 1854–1864.

Hoskins, B. J., James, I. N., White, G. H. (1983). The shape, propagation and mean-flow interaction

of large-scale weather systems. *Journal of the Atmospheric Sciences*, *40(7)*, 1595–1612.

Hurrell, J. W. (1995). Decadal trends in the North Atlantic oscillation: Regional temperatures and precipitation. *Science*, *269*(5224), 676–679. https://doi.org/10.1126/science.269.5224.676

Hurrell, J. W. (1996). Influence of variations in extratropical wintertime teleconnections on Northern Hemisphere temperature. *Geophysical Research Letters*, *23*(6), 665–668. https://doi.org/10.1029/96GL00459

Hurrell, J. W., & Deser, C. (2010). North Atlantic climate variability: The role of the North Atlantic Oscillation. *Journal of Marine Systems*, *79*(3–4), 231–244. https://doi.org/10.1016/j.jmarsys.2009.11.002

Hurrell, J. W., & Van Loon, H. (1997). Decadal variations in climate associated with the North Atlantic oscillation. *Climatic Change*, *36*(3–4), 301–326. https://doi.org/10.1023/a:1005314315270

Iturbide, M., Gutiérrez, J. M., Alves, L. M., Bedia, J., Cerezo-Mota, R., Cimadevilla, E., Cofiño, A. S., Luca, A. Di, Faria, S. H., Gorodetskaya, I. V., Hauser, M., Herrera, S., Hennessy, K., Hewitt, H. T., Jones, R. G., Krakovska, S., Manzanas, R., Martínez-Castro, D., Narisma, G. T., … Vera, C. S. (2020). An update of IPCC climate reference regions for subcontinental analysis of climate model data: definition and aggregated datasets. *Earth System Science Data*, *12*(4), 2959–2970. https://doi.org/10.5194/essd-12-2959-2020

Ivasić, S., Herceg-Bulić, I., & King, M. P. (2021). Recent weakening in the winter ENSO teleconnection over the North Atlantic-European region. *Climate Dynamics*, *57*(7–8), 1953–1972. https://doi.org/10.1007/s00382-021-05783-z

Johnson, N. C., & Feldstein, S. B. (2010). The continuum of North Pacific sea level pressure patterns: Intraseasonal, interannual, and interdecadal variability. *Journal of Climate*, *23*(4), 851–867. https://doi.org/10.1175/2009JCLI3099.1

Kalnay, E., Collins, W., Deaven, D., Gandin, L., Iredell, M., Jenne, R., & Joseph, D. (1996). The NCEP NCAR 40-year reanalysis project. 1996.pdf. *Bulletin of the American Meteorological Society*, *77*(3), 437–472.

Kautz, L.-A., Martius, O., Pfahl, S., Pinto, J. G., Ramos, A. M., Sousa, P. M., & Woollings, T. (2022). Atmospheric blocking and weather extremes over the Euro-Atlantic sector – a review. *Weather and Climate Dynamics*, *3*(1), 305–336. https://doi.org/10.5194/wcd-3-305-2022

Kidston, J., Scaife, A. A., Hardiman, S. C., Mitchell, D. M., Butchart, N., Baldwin, M. P., & Gray, L. J. (2015). Stratospheric influence on tropospheric jet streams, storm tracks and surface weather. *Nature Geoscience*, *8*(6), 433–440. https://doi.org/10.1038/NGEO2424

Koch, P., Wernli, H., & Davies, H. C. (2006). An event-based jet-stream climatology and typology.

International Journal of Climatology, *26*(3), 283–301. https://doi.org/10.1002/joc.1255

Kodera, K., Chiba, M., Koide, H., Kitoh, A., & Nikaidou, Y. (1996). Interannual variability of the winter stratosphere and troposphere in the Northern Hemisphere. *Journal of the Meteorological Society of Japan. Ser. II*, *74(3)*, 365–382.

Lee, J. Y., Marotzke, J., Bala, G., Cao, L., Corti, S., Dunne, J. P., ... & Zhou, T. (2021). Future Global Climate: Scenario-based Projections and Near-term Information. In *Climate Change 2021 – The Physical Science Basis*. https://doi.org/10.1017/9781009157896.006

Lee, S., & Feldstein, S. (1996). Mechanism of zonal index evolution in a two-layer model. *Journal of the Atmospheric Sciences*, *53(15)*, 2232–2246.

Lee, S., & Kim, H. K. (2003). The dynamical relationship between subtropical and eddy-driven jets. *Journal of the Atmospheric Sciences*, *60*(12), 1490–1503. https://doi.org/10.1175/1520-0469(2003)060<1490:TDRBSA>2.0.CO;2

Li, J., Li, F., He, S., Wang, H., & Orsolini, Y. J. (2020). Influence of December snow cover over North America on January surface air temperature over the midlatitude Asia. *International Journal of Climatology*, *40*(1), 572–584. https://doi.org/10.1002/joc.6235

Li, J., Swinbank, R., Grotjahn, R., & Volkert, H. (2016). Dynamics and predictability of large-scale, high-impact weather and climate events (No. 2). In *Cambridge University Press* (Vol. 94, Issue 12). https://doi.org/10.1175/BAMS-D-12-00213.1

Li, C., & Wettstein, J. J. (2012). Thermally driven and eddy-driven jet variability in reanalysis. *Journal of Climate*, *25*(5), 1587–1596. https://doi.org/10.1175/JCLI-D-11-00145.1

Limbach, S., Schömer, E., & Wernli, H. (2012). Detection, tracking and event localization of jet stream features in 4-D atmospheric data. *Geoscientific Model Development*, *5*(2), 457–470. https://doi.org/10.5194/gmd-5-457-2012

Limpasuvan, V., & Hartmann, D. L. (2000). Wave-maintained annular modes of climate variability. *Journal of Climate*, *13*(24), 4414–4429. https://doi.org/10.1175/1520-0442(2000)013<4414:WMAMOC>2.0.CO;2

Lin, H., & Wu, Z. (2011). Contribution of the autumn Tibetan Plateau snow cover to seasonal prediction of North American winter temperature. *Journal of Climate*, *24*(11), 2801–2813. https://doi.org/10.1175/2010JCLI3889.1

Liu, Q. (1994). On the definition and persistence of blocking. *Tellus*, *46A*, 286–290.

Liu, S., Wu, Q., Yao, Y., Schroeder, S., & Wang, L. (2022). Impacts of Autumn-Winter Tibetan Plateau Snow Anomalies on North Atlantic-Europe and Arctic Climate. *Journal of Geophysical Research: Atmospheres*, *127*(12). https://doi.org/10.1029/2021JD035791

López, J., Belén, P., Fonseca, R., & Terray, L. (2015). A mechanism for the multidecadal modulation

of ENSO teleconnection with Europe. *Climate Dynamics*, 867–880. https://doi.org/10.1007/s00382-014-2319-x

Lorenz, D. J., & DeWeaver, E. T. (2007). Tropopause height and zonal wind response to global warming in the IPCC scenario integrations. *Journal of Geophysical Research Atmospheres*, *112*(10), 1–11. https://doi.org/10.1029/2006JD008087

Lorenz, D. J., & Hartmann, D. L. (2003). Eddy-zonal flow feedback in the Northern Hemisphere winter. *Journal of Climate*, *16*(8), 1212–1227. https://doi.org/10.1175/1520-0442(2003)16<1212:EFFITN>2.0.CO;2

Lorenz, E. N. (1955). Available Potential Energy and the Maintenance of the General Circulation. *Tellus A: Dynamic Meteorology and Oceanography*, *7*(2), 157–167. https://doi.org/10.3402/tellusa.v7i2.8796

Lorenz, E. N. (1956). Empirical Orthogonal Functions and Statistical Weather Prediction. In *Technical report Statistical Forecast Project Report 1 Department of Meteorology MIT 49* (Vol. 1, Issue Scientific Report No. 1, Statistical Forecasting Project, p. 52).

Lorenz, E. N. (1963). Deterministic nonperiodic flow. *Journal of Atmospheric Sciences*, *20(2)*, 130–141.

Ma, L., Woollings, T., Williams, R. G., Smith, D., & Dunstone, N. (2020). How does the winter jet stream affect surface temperature, heat flux, and sea ice in the North Atlantic? *Journal of Climate*, *33*(9), 3711–3730. https://doi.org/10.1175/JCLI-D-19-0247.1

Madden, R. A. (1976). Estimates of the natural variability of time-averaged sea-level pressure. *Monthly Weather Review*, *104(7)*, 942–952.

Maddison, J. W., Ayarzagüena, B., Barriopedro, D., & García-Herrera, R. (2023). Added value of a multiparametric eddy-driven jet diagnostic for understanding European air stagnation. *Environmental Research Letters*, *18*(8). https://doi.org/10.1088/1748-9326/ace72e

Madonna, E., Li, C., Grams, C. M., & Woollings, T. (2017). The link between eddy-driven jet variability and weather regimes in the North Atlantic-European sector. *Quarterly Journal of the Royal Meteorological Society*, *143*(708), 2960–2972. https://doi.org/10.1002/qj.3155

Madonna, E., Li, C., & Wettstein, J. J. (2019). Suppressed eddy driving during southward excursions of the North Atlantic jet on synoptic to seasonal time scales. *Atmospheric Science Letters*, *20*(9), 1–11. https://doi.org/10.1002/asl.937

Mahlstein, I., Martius, O., Chevalier, C., & Ginsbourger, D. (2012). Changes in the odds of extreme events in the Atlantic basin depending on the position of the extratropical jet. *Geophysical Research Letters*, *39*(22), 1–6. https://doi.org/10.1029/2012GL053993

Mak, M., & Cai, M. (1989). Local barotropic instability. *Journal of the Atmospheric Sciences*,

46(21), 3289–3311.

Manzini, E., Giorgetta, M. A., Esch, M., Kornblueh, L., & Roeckner, E. (2006). The influence of sea surface temperatures on the northern winter stratosphere: Ensemble simulations with the MAECHAM5 model. *Journal of Climate*, *19(16)*, 3863–3881.

Manzini, E., Karpechko, A. Y., & Kornblueh, L. (2018). Nonlinear Response of the Stratosphere and the North Atlantic-European Climate to Global Warming. *Geophysical Research Letters*, *45*(9), 4255–4263. https://doi.org/10.1029/2018GL077826

Marshall, J., Kushnir, Y., Battisti, D., Chang, P., Czaja, A., Dickson, R., Hurrell, J., McCartney, M., Saravanan, R., & Visbeck, M. (2001). North Atlantic climate variability: Phenomena, impacts and mechanisms. *International Journal of Climatology*, *21*(15), 1863–1898. https://doi.org/10.1002/joc.693

Martin, J. (2006). Mid-Latitude Atmospheric dynamics: a first course. In *F3.Tiera.Ru*.

Masato, G., Hoskins, B. J., & Woollings, T. (2013). Wave-Breaking Characteristics of Northern Hemisphere Winter Blocking: A Two-Dimensional Approach. *Journal of Climate*, *26*(13), 4535–4549. https://doi.org/10.1175/jcli-d-12-00240.1

Matsuno, T. (1966). Quasi-Geostrophic Motions in the Equatorial Area. *Journal of the Meteorological Society of Japan. Ser. II*, *44*(1), 25–43. https://doi.org/10.2151/jmsj1965.44.1_25

Maycock, A. C., Masukwedza, G. I. T., Hitchcock, P., & Simpson, I. R. (2020). A regime perspective on the north atlantic eddy-driven jet response to sudden stratospheric warmings. *Journal of Climate*, *33*(9), 3901–3917. https://doi.org/10.1175/JCLI-D-19-0702.1

Meehl, G. A., Boer, G. J., Covey, C., Latif, M., & Stouffer, R. J. (1997). Intercomparison makes for a better climate model. *Eos*, *78*(41), 445–451. https://doi.org/10.1029/97eo00276

Mellado-Cano, J., Barriopedro, D., García-Herrera, R., Trigo, R. M., & Hernández, A. (2019). Examining the north atlantic oscillation, east atlantic pattern, and jet variability since 1685. *Journal of Climate*, *32*(19), 6285–6298. https://doi.org/10.1175/JCLI-D-19-0135.1

Messori, G., & Caballero, R. (2015). On double Rossby wave breaking in the North Atlantic. *Journal of Geophysical Research*, *120*, 11129–11150. https://doi.org/10.1038/175238c0

Mo, K. C., & Livezey, R. E. (1986). Tropical-extratropical geopotential height teleconnections during the Northern Hemisphere winter. *Monthly Weather Review*, *114(12)*, 2488–2515.

Monahan, A. H., & Fyfe, J. C. (2006). On the nature of zonal jet EOFs. *Journal of Climate*, *19*(24), 6409–6424. https://doi.org/10.1175/JCLI3960.1

Mote, T. L., & Kutney, E. R. (2012). Regions of autumn Eurasian snow cover and associations with North American winter temperatures. *International Journal of Climatology*, *32*(8), 1164–

1177. https://doi.org/10.1002/joc.2341

Müller, W. A., Jungclaus, J. H., Mauritsen, T., Baehr, J., Bittner, M., Budich, R., Bunzel, F., Esch, M., Ghosh, R., Haak, H., Ilyina, T., Kleine, T., Kornblueh, L., Li, H., Modali, K., Notz, D., Pohlmann, H., Roeckner, E., Stemmler, I., … Marotzke, J. (2018). A Higher-resolution Version of the Max Planck Institute Earth System Model (MPI-ESM1.2-HR). *Journal of Advances in Modeling Earth Systems*, *10*(7), 1383–1413. https://doi.org/10.1029/2017MS001217

Nakamura, H., Sampe, T., Goto, A., Ohfuchi, W., & Xie, S. P. (2008). On the importance of midlatitude oceanic frontal zones for the mean state and dominant variability in the tropospheric circulation. *Geophysical Research Letters*, *35*(15), 1–5. https://doi.org/10.1029/2008GL034010

Nakamura, H., Sampe, T., Tanimoto, Y., & Shimpo, A. (2004). Observed associations among storm tracks, jet streams and midlatitude oceanic fronts. *Geophysical Monograph Series*, *147*, 329–345. https://doi.org/10.1029/147GM18

Nakamura, N., & Huang, C. S. Y. (2018). Atmospheric blocking as a traffic jam in the jet stream. *Science*, *361*(6397), 42–47. https://doi.org/10.1126/science.aat0721

Nie, Y., Ren, H. L., & Zhang, Y. (2019). The role of extratropical air–sea interaction in the autumn subseasonal variability of the North Atlantic Oscillation. *Journal of Climate*, *32*(22), 7697–7712. https://doi.org/10.1175/JCLI-D-19-0060.1

O'Gorman, P. A., & Singh, M. S. (2013). Vertical structure of warming consistent with an upward shift in the middle and upper troposphere. *Geophysical Research Letters*, *40*(9), 1838–1842. https://doi.org/10.1002/grl.50328

O'Neill, B. C., Kriegler, E., Ebi, K. L., Kemp-Benedict, E., Riahi, K., Rothman, D. S., van Ruijven, B. J., van Vuuren, D. P., Birkmann, J., Kok, K., Levy, M., & Solecki, W. (2017). The roads ahead: Narratives for shared socioeconomic pathways describing world futures in the 21st century. *Global Environmental Change*, *42*, 169–180. https://doi.org/10.1016/j.gloenvcha.2015.01.004

O'Neill, B. C., Tebaldi, C., Van Vuuren, D. P., Eyring, V., Friedlingstein, P., Hurtt, G., Knutti, R., Kriegler, E., Lamarque, J. F., Lowe, J., Meehl, G. A., Moss, R., Riahi, K., & Sanderson, B. M. (2016). The Scenario Model Intercomparison Project (ScenarioMIP) for CMIP6. *Geoscientific Model Development*, *9*(9), 3461–3482. https://doi.org/10.5194/gmd-9-3461-2016

Ordóñez, C., Barriopedro, D., & García-Herrera, R. (2019). Role of the position of the North Atlantic jet in the variability and odds of extreme PM10 in Europe. *Atmospheric Environment*, *210*(April), 35–46. https://doi.org/10.1016/j.atmosenv.2019.04.045

Orlanski, I. (2003). Bifurcation in eddy life cycles: Implications for storm track variability. *Journal of*

the Atmospheric Sciences, *60*(8), 993–1023. https://doi.org/10.1175/1520-0469(2003)60<993:BIELCI>2.0.CO;2

Osborn, T. J., Briffa, K. R., Tett, S. F. B., Jones, P. D., & Trigo, R. M. (1999). Evaluation of the North Atlantic Oscillation as simulated by a coupled climate model. *Climate Dynamics*, *15*(9), 685–702. https://doi.org/10.1007/s003820050310

Oudar, T., Cattiaux, J., & Douville, H. (2020). Drivers of the Northern Extratropical Eddy-Driven Jet Change in CMIP5 and CMIP6 Models. *Geophysical Research Letters*, *47*(8), 1–9. https://doi.org/10.1029/2019GL086695

Oudar, T., Cattiaux, J., Douville, H., Geoffroy, O., Saint-Martin, D., & Roehrig, R. (2020). Robustness and drivers of the Northern Hemisphere extratropical atmospheric circulation response to a CO 2 -induced warming in CNRM-CM6-1. *Climate Dynamics*, *54*(3–4), 2267–2285. https://doi.org/10.1007/s00382-019-05113-4

Oudar, T., Sanchez-Gomez, E., Chauvin, F., Cattiaux, J., Terray, L., & Cassou, C. (2017). Respective roles of direct GHG radiative forcing and induced Arctic sea ice loss on the Northern Hemisphere atmospheric circulation. *Climate Dynamics*, *49*(11–12), 3693–3713. https://doi.org/10.1007/s00382-017-3541-0

Panetta, R. L. (1993). Zonal jets in wide baroclinically unstable regions: Persistence and scale selection. *Journal of the Atmospheric Sciences*, *50(14)*, 2073–2106.

Peings, Y., Cattiaux, J., & Magnusdottir, G. (2019). The Polar Stratosphere as an Arbiter of the Projected Tropical Versus Polar Tug of War. *Geophysical Research Letters*, *46*(15), 9261–9270. https://doi.org/10.1029/2019GL082463

Peings, Y., Cattiaux, J., Vavrus, S. J., & Magnusdottir, G. (2018). Projected squeezing of the wintertime North-Atlantic jet. *Environmental Research Letters*, *13*(7). https://doi.org/10.1088/1748-9326/aacc79

Peings, Y., Cattiaux, J., Vavrus, S., & Magnusdottir, G. (2017). Late twenty-first-century changes in the midlatitude atmospheric circulation in the CESM large ensemble. *Journal of Climate*, *30*(15), 5943–5960. https://doi.org/10.1175/JCLI-D-16-0340.1

Peng, S., Robinson, W. A., & Li, S. (2003). Mechanisms for the NAO responses to the North Atlantic SST tripole. *Journal of Climate*, *16*(12), 1987–2004. https://doi.org/10.1175/1520-0442(2003)016<1987:MFTNRT>2.0.CO;2

Pierce W., D. W. (2002). The role of sea surface temperatures in interactions between ENSO and the North Pacific Oscillation. *Journal of Climate*, *15*(11), 1295–1308. https://doi.org/10.1175/1520-0442(2002)015<1295:trosst>2.0.co;2

Pinto, J. G., & Raible, C. C. (2012). Past and recent changes in the North Atlantic oscillation. *Wiley*

Interdisciplinary Reviews: Climate Change, *3*(1), 79–90. https://doi.org/10.1002/wcc.150

Pinto, J. G., Reyers, M., & Ulbrich, U. (2011). The variable link between PNA and NAO in observations and in multi-century CGCM simulations. *Climate Dynamics*, *36*(1), 337–354. https://doi.org/10.1007/s00382-010-0770-x

Polvani, L. M., & Kushner, P. J. (2003). Tropospheric response to stratospheric degradation in a simple global circulation model. *Geophysical Research Letters*, *29(7)*, 18–1. https://doi.org/10.1175/1520-0469(2003)060<1835:TRTSDI>2.0.CO;2

Polvani, L. M., Sun, L., Butler, A. H., Richter, J. H., & Deser, C. (2017). Distinguishing stratospheric sudden warmings from ENSO as key drivers of wintertime climate variability over the North Atlantic and Eurasia. *Journal of Climate*, *30*(6), 1959–1969. https://doi.org/10.1175/JCLI-D-16-0277.1

Qian, Q. F., Jia, X. J., & Wu, R. (2019). Changes in the Impact of the Autumn Tibetan Plateau Snow Cover on the Winter Temperature Over North America in the mid-1990s. *Journal of Geophysical Research: Atmospheres*, *124*(19), 10321–10343. https://doi.org/10.1029/2019JD030245

Rahmstorf, S., Box, J. E., Feulner, G., Mann, M. E., Robinson, A., Rutherford, S., & Schaffernicht, E. J. (2015). Exceptional twentieth-century slowdown in Atlantic Ocean overturning circulation. *Nature Climate Change*, *5(5)*, 475–480.

Raible, C. C., Luksch, U., & Fraedrich, K. (2004). *Precipitation and Northern Hemisphere regimes*. *5*, 43–55. https://doi.org/10.1016/j.atmoscilet.2003.12.001

Rasmusson, E. M., & Carpenter, T. H. (1982). Variations in tropical sea surface temperature and surface wind fields associated with the Southern Oscillation/El Niño. *Monthly Weather Review*, *110(5)*, 354–384.

Rayner, N. A., Parker, D. E., Horton, E. B., Folland, C. K., Alexander, L. V, Rowell, D. P., Kent, E. C., & Kaplan, A. (2003). *Global analyses of sea surface temperature , sea ice , and night marine air temperature since the late nineteenth century*. *108*. https://doi.org/10.1029/2002JD002670

Riahi, K., van Vuuren, D. P., Kriegler, E., Edmonds, J., O'Neill, B. C., Fujimori, S., Bauer, N., Calvin, K., Dellink, R., Fricko, O., Lutz, W., Popp, A., Cuaresma, J. C., KC, S., Leimbach, M., Jiang, L., Kram, T., Rao, S., Emmerling, J., … Tavoni, M. (2017). The Shared Socioeconomic Pathways and their energy, land use, and greenhouse gas emissions implications: An overview. *Global Environmental Change*, *42*, 153–168. https://doi.org/10.1016/j.gloenvcha.2016.05.009

Rivière, G., Hua, B. L., & Klein, P. (2003). Perturbation growth in terms of barotropic alignment properties. *Quarterly Journal of the Royal Meteorological Society*, *129*(593 PART B), 2613–2635. https://doi.org/10.1256/qj.02.106

Rivière, G., & Orlanski, I. (2007). Characteristics of the Atlantic storm-track eddy activity and its relation with North Atlantic Oscillation. *Journal of the Atmospheric Sciences*, *64*(2), 241–266. https://doi.org/10.1175/JAS3850.1

Robinson, D. A., Dewey, K. F., & Heim, R. R. (1993). Global snow cover monitoring: an update. *Bulletin - American Meteorological Society*, *74*(9), 1689–1696. https://doi.org/10.1175/1520-0477(1993)074<1689:GSCMAU>2.0.CO;2

Robinson, W. A. (2000). A baroclinic mechanism for the eddy feedback on the zonal index. *Journal of the Atmospheric Sciences*, *57*(3), 415–422. https://doi.org/10.1175/1520-0469(2000)057<0415:ABMFTE>2.0.CO;2

Robinson, W. A. (2006). On the self-maintenance of midlatitude jets. *Journal of the Atmospheric Sciences*, *63*(8), 2109–2122. https://doi.org/10.1175/JAS3732.1

Rodríguez-Fonseca, B., Suárez-Moreno, R., Ayarzagüena, B., López-Parages, J., Gómara, I., Villamayor, J., Mohino, E., Losada, T., & Castaño-Tierno, A. (2016). A review of ENSO influence on the North Atlantic. A non-stationary signal. *Atmosphere*, *7*(7), 1–19. https://doi.org/10.3390/atmos7070087

Rogers, J. C. (1997). North Atlantic storm track variability and its association to the North Atlantic oscillation and climate variability of Northern Europe. *Journal of Climate*, *10*(7), 1635–1647. https://doi.org/10.1175/1520-0442(1997)010<1635:NASTVA>2.0.CO;2

Ronalds, B., & Barnes, E. A. (2019). A role for barotropic eddy-mean flow feedbacks in the zonal wind response to sea ice loss and arctic amplification. *Journal of Climate*, *32*(21), 7469–7481. https://doi.org/10.1175/JCLI-D-19-0157.1

Röthlisberger, M., Pfahl, S., & Martius, O. (2016). Regional-scale jet waviness modulates the occurrence of midlatitude weather extremes. *Geophysical Research Letters*, *43*(20), 10,989-10,997. https://doi.org/10.1002/2016GL070944

Rousi, E., Kornhuber, K., Beobide-Arsuaga, G., Luo, F., & Coumou, D. (2022). Accelerated western European heatwave trends linked to more-persistent double jets over Eurasia. *Nature Communications*, *13*(1), 1–11. https://doi.org/10.1038/s41467-022-31432-y

Sampe, T., Nakamura, H., Goto, A., & Ohfuchi, W. (2010). Significance of a midlatitude SST frontal zone in the formation of a storm track and an eddy-driven westerly jet. *Journal of Climate*, *23*(7), 1793–1814. https://doi.org/10.1175/2009JCLI3163.1

Santos, J. A., Woollings, T., & Pinto, J. G. (2013). Are the winters 2010 and 2012 archetypes exhibiting extreme opposite behavior of the north atlantic jet stream. *Monthly Weather Review*, *141*(10), 3626–3640. https://doi.org/10.1175/MWR-D-13-00024.1

Saunders, M. A., & Qian, B. (2002). Seasonal predictability of the winter NAO from north Atlantic

sea surface temperatures. *Geophysical Research Letters*, *29*(22), 6-1-6–4. https://doi.org/10.1029/2002GL014952

Scaife, A. A., Arribas, A., Blockley, E., Brookshaw, A., Clark, R. T., Dunstone, N., ... & Williams, A. (2014). Skillful long-range prediction of European and North American winters. *Geophysical Research Letters*, *41(7)*(April), 2514–2519. https://doi.org/10.1002/2014GL059637.Received

Schiemann, R., Athanasiadis, P., Barriopedro, D., Doblas-Reyes, F., Lohmann, K., Roberts, M. J., Sein, D. V., Roberts, C. D., Terray, L., & Vidale, P. L. (2020). Northern Hemisphere blocking simulation in current climate models: evaluating progress from the Climate Model Intercomparison Project Phase 5 to 6 and sensitivity to resolution. *Weather and Climate Dynamics*, *1*(1), 277–292. https://doi.org/10.5194/wcd-1-277-2020

Screen, J. A. (2017). The missing Northern European winter cooling response to Arctic sea ice loss. *Nature Communications*, *8*. https://doi.org/10.1038/ncomms14603

Screen, J. A., Deser, C., Smith, D. M., Zhang, X., Blackport, R., Kushner, P. J., Oudar, T., McCusker, K. E., & Sun, L. (2018). Consistency and discrepancy in the atmospheric response to Arctic sea-ice loss across climate models. *Nature Geoscience*, *11*(3), 155–163. https://doi.org/10.1038/s41561-018-0059-y

Screen, J. A., & Simmonds, I. (2010). The central role of diminishing sea ice in recent Arctic temperature amplification. *Nature*, *464*(7293), 1334–1337. https://doi.org/10.1038/nature09051

Screen, J. A., & Simmonds, I. (2013). Exploring links between Arctic amplification and mid-latitude weather. *Geophysical Research Letters*, *40*(5), 959–964. https://doi.org/10.1002/grl.50174

Séférian, R., Nabat, P., Michou, M., Saint-Martin, D., Voldoire, A., Colin, J., Decharme, B., Delire, C., Berthet, S., Chevallier, M., Sénési, S., Franchisteguy, L., Vial, J., Mallet, M., Joetzjer, E., Geoffroy, O., Guérémy, J. F., Moine, M. P., Msadek, R., … Madec, G. (2019). Evaluation of CNRM Earth System Model, CNRM-ESM2-1: Role of Earth System Processes in Present-Day and Future Climate. *Journal of Advances in Modeling Earth Systems*, *11*(12), 4182–4227. https://doi.org/10.1029/2019MS001791

Seneviratne, S. I., Zhang, X., Adnan, M., Badi, W., Dereczynski, C., Di Luca, A., Ghosh, S., Iskandar, I., Kossin, J., Lewis, S., Otto, F., Pinto, I., Satoh, M., Vicente-Serrano, S. M., Wehner, M., & Zhou, B. (2021). Weather and Climate Extreme Events in a Changing Climate. In *Climate Change 2021: The Physical Science Basis. Contribution of Working Group I to the Sixth Assessment Report of the Intergovernmental Panel on Climate Change*. https://doi.org/10.1017/9781009157896.013

Shaw, T. A. (2019). Mechanisms of Future Predicted Changes in the Zonal Mean Mid-Latitude

Circulation. *Current Climate Change Reports*, *5*(4), 345–357. https://doi.org/10.1007/s40641-019-00145-8

Sillmann, J., Mischa, C. M., Kallache, M., & Katz, R. W. (2011). Extreme cold winter temperatures in Europe under the influence of North Atlantic atmospheric blocking. *Journal of Climate*, *24*(22), 5899–5913. https://doi.org/10.1175/2011JCLI4075.1

Sobolowski, S., Gong, G., & Ting, M. (2007). Northern Hemisphere winter climate variability: Response to North American snow cover anomalies and orography. *Geophysical Research Letters*, *34*(16), 2–6. https://doi.org/10.1029/2007GL030573

Sobolowski, S., Gong, G., & Ting, M. (2010). Modeled climate state and dynamic responses to anomalous north American snow cover. *Journal of Climate*, *23*(3), 785–799. https://doi.org/10.1175/2009JCLI3219.1

Son, S. W., & Lee, S. (2005). The response of westerly jets to thermal driving in a primitive equation model. *Journal of the Atmospheric Sciences*, *62*(10), 3741–3757. https://doi.org/10.1175/JAS3571.1

Soulard, N., Lin, H., & Yu, B. (2019). The changing relationship between ENSO and its extratropical response patterns. *Scientific Reports*, *9*(1), 1–10. https://doi.org/10.1038/s41598-019-42922-3

Strong, C., & Davis, R. E. (2008). Variability in the position and strength of winter jet stream cores related to northern hemisphere teleconnections. *Journal of Climate*, *21*(3), 584–592. https://doi.org/10.1175/2007JCLI1723.1

Stull, R. (2015). Chapter 4: Water Vapor. In *Practical Meteorology - An Algebra-based Survey of Atmospheric Science*.

Sung, M. K., Ham, Y. G., Kug, J. S., & An, S. Il. (2013). An alterative effect by the tropical North Atlantic SST in intraseasonally varying El Niño teleconnection over the North Atlantic. *Tellus, Series A: Dynamic Meteorology and Oceanography*, *65*, 1–13. https://doi.org/10.3402/tellusa.v65i0.19863

Swart, N. C., Cole, J. N. S., Kharin, V. V., Lazare, M., Scinocca, J. F., Gillett, N. P., Anstey, J., Arora, V., Christian, J. R., Hanna, S., Jiao, Y., Lee, W. G., Majaess, F., Saenko, O. A., Seiler, C., Seinen, C., Shao, A., Sigmond, M., Solheim, L., … Winter, B. (2019). The Canadian Earth System Model version 5 (CanESM5.0.3). *Geoscientific Model Development*, *12*(11), 4823–4873. https://doi.org/10.5194/gmd-12-4823-2019

Takaya, K., & Nakamura, H. (2001). A formulation of a phase-independent wave-activity flux for stationary and migratory quasigeostrophic eddies on a zonally varying basic flow. *Journal of the Atmospheric Sciences*, *58*(6), 608–627. https://doi.org/10.1175/1520-

0469(2001)058<0608:AFOAPI>2.0.CO;2

Tatebe, H., Ogura, T., Nitta, T., Komuro, Y., Ogochi, K., Takemura, T., Sudo, K., Sekiguchi, M., Abe, M., Saito, F., Chikira, M., Watanabe, S., Mori, M., Hirota, N., Kawatani, Y., Mochizuki, T., Yoshimura, K., Takata, K., O'Ishi, R., … Kimoto, M. (2019). Description and basic evaluation of simulated mean state, internal variability, and climate sensitivity in MIROC6. *Geoscientific Model Development*, *12*(7), 2727–2765. https://doi.org/10.5194/gmd-12-2727-2019

Taylor, P. C., Boeke, R. C., Boisvert, L. N., Feldl, N., Henry, M., Huang, Y., Langen, P. L., Liu, W., Pithan, F., Sejas, S. A., & Tan, I. (2022). Process Drivers, Inter-Model Spread, and the Path Forward: A Review of Amplified Arctic Warming. *Frontiers in Earth Science*, *9*(February), 1–29. https://doi.org/10.3389/feart.2021.758361

Tedesco, P., Lenkoski, A., Bloomfield, H. C., & Sillmann, J. (2023). Gaussian copula modeling of extreme cold and weak-wind events over Europe conditioned on winter weather regimes. *Environmental Research Letters*, *18*(3), 1–19. https://doi.org/10.1088/1748-9326/acb6aa

Thorncroft, C. D., Hoskins, B. J., & McIntyre, M. E. (1993). Two paradigms of baroclinic-wave life-cycle behaviour. *Quarterly Journal of the Royal Meteorological Society*, *119(509)*, 17–55.

Trenberth, K. E. (1986). An assessment of the impact of transient eddies on the zonal flow during a blocking episode using localized Eliassen-Palm flux diagnostics. *Journal of the Atmospheric Sciences*, *43(19)*, 2070–2087.

Trenberth, K. E. (1997). The Definition of El Nino. *Bulletin of the American Meteorological Society*, *78(12)*, 2771–2778.

Trenberth, K. E., Branstator, G. W., Karoly, D., Kumar, A., Lau, N. C., & Ropelewski, C. (1998). Progress during TOGA in understanding and modeling global teleconnections associated with tropical sea surface temperatures. *Journal of Geophysical Research: Oceans*, *103*(C7), 14291–14324. https://doi.org/10.1029/97jc01444

Trigo, I. F. (2006). Climatology and interannual variability of storm-tracks in the Euro-Atlantic sector: A comparison between ERA-40 and NCEP/NCAR reanalyses. *Climate Dynamics*, *26*(2–3), 127–143. https://doi.org/10.1007/s00382-005-0065-9

Trigo, R. M., Trigo, I. F., DaCamara, C. C., & Osborn, T. J. (2004). Climate impact of the European winter blocking episodes from the NCEP/NCAR reanalyses. *Climate Dynamics*, *23*(1), 17–28. https://doi.org/10.1007/s00382-004-0410-4

Ulbrich, U., Leckebusch, G. C., & Pinto, J. G. (2009). Extra-tropical cyclones in the present and future climate: A review. *Theoretical and Applied Climatology*, *96*(1–2), 117–131. https://doi.org/10.1007/s00704-008-0083-8

Vallis, G. K. (2006). Atmospheric and Oceanic Fluid Dynamics: Funda-mentals and Large-Scale

Circulation. In *Atmospheric and Oceanic Fluid Dynamics*. Cambridge Univ. Press, Cam-bridge, U. K. https://doi.org/10.1017/cbo9780511790447

Vallis, G. K., & Gerber, E. P. (2008). Local and hemispheric dynamics of the North Atlantic Oscillation, annular patterns and the zonal index. *Dynamics of Atmospheres and Oceans*, *44*(3–4), 184–212. https://doi.org/10.1016/j.dynatmoce.2007.04.003

Vavrus, S. (2007). The role of terrestrial snow cover in the climate system. *Climate Dynamics*, *29*(1), 73–88. https://doi.org/10.1007/s00382-007-0226-0

Vihma, T. (2014). Effects of Arctic Sea Ice Decline on Weather and Climate: A Review. In *Surveys in Geophysics* (Vol. 35, Issue 5). https://doi.org/10.1007/s10712-014-9284-0

Visbeck, M. H., Hurrell, J. W., Polvani, L., & Cullen, H. M. (2001). The North Atlantic oscillation: Past, present, and future. *Proceedings of the National Academy of Sciences of the United States of America*, *98*(23), 12876–12877. https://doi.org/10.1073/pnas.231391598

Voldoire, A., Saint-Martin, D., Sénési, S., Decharme, B., Alias, A., Chevallier, M., Colin, J., Guérémy, J. F., Michou, M., Moine, M. P., Nabat, P., Roehrig, R., Salas y Mélia, D., Séférian, R., Valcke, S., Beau, I., Belamari, S., Berthet, S., Cassou, C., … Waldman, R. (2019). Evaluation of CMIP6 DECK Experiments With CNRM-CM6-1. *Journal of Advances in Modeling Earth Systems*, *11*(7), 2177–2213. https://doi.org/10.1029/2019MS001683

Walker, G. T., & Bliss, E. W. (1932). Memoirs of the royal meteorological society. World weather V,. In *Nature* (Vol. 118, Issue 2980, pp. 4, 53–84). https://doi.org/10.2307/3901664

Walker, C. C., & Schneider, T. (2006). Eddy influences on Hadley circulations: Simulations with an idealized GCM. *Journal of the Atmospheric Sciences*, *63*(12), 3333–3350. https://doi.org/10.1175/JAS3821.1

Wallace, J. M., & Gutzler, D. S. (1981). Teleconnections in the geopotential height field during the Northern Hemisphere winter. *Monthly Weather Review*, *109(4)*, 784–812.

Wallace, J. M., Zhang, Y., & Lau, K. H. (1993). Structure and seasonality of interannual and interdecadal variability of the geopotential height and temperature fields in the Northern Hemisphere troposphere. *Journal of Climate*, *6(11)*, 2063–2082.

Walland, D. J., & Simmonds, I. (1996). Modelled atmospheric response to changes in Northern Hemisphere snow cover. *Climate Dynamics*, *13*(1), 25–34. https://doi.org/10.1007/s003820050150

Walsh, J. E., Phillips, A. S., Portis, D. H., & Chapman, W. L. (2001). Extreme cold outbreaks in the United States and Europe, 1948-99. *Journal of Climate*, *14*(12), 2642–2658. https://doi.org/10.1175/1520-0442(2001)014<2642:ECOITU>2.0.CO;2

Wang, W., Anderson, B. T., Kaufmann, R. K., & Myneni, R. B. (2004). The relation between the

North Atlantic Oscillation and SSTs in the North Atlantic Basin. *Journal of Climate*, *17*(24), 4752–4759. https://doi.org/10.1175/JCLI-3186.1

Waugh, D. W., & Polvani, L. M. (2010). *Stratospheric polar vortices.* https://doi.org/10.1029/2011EO500012

Wen, N., Liu, Z., Liu, Q., & Frankignoul, C. (2005). Observations of SST, heat flux and North Atlantic Ocean-atmosphere interaction. *Geophysical Research Letters*, *32*(24), 1–4. https://doi.org/10.1029/2005GL024871

Wilks D.S. (2011). *Statistical Methods in the Atmospheric Sciences.* (3rd ed.). Academic Press, Oxford, UK.

Wilson, C., Sinha, B., & Williams, R. G. (2009). The effect of ocean dynamics and orography on atmospheric storm tracks. *Journal of Climate*, *22*(13), 3689–3702. https://doi.org/10.1175/2009JCLI2651.1

Wirth, V., Riemer, M., Chang, E. K. M., & Martius, O. (2018). Rossby wave packets on the midlatitude waveguide-A review. *Monthly Weather Review*, *146*(7), 1965–2001. https://doi.org/10.1175/MWR-D-16-0483.1

Wittman, M. A. H., Charlton, A. J., & Polvani, L. M. (2005). On the meridional structure of annular modes. *Journal of Climate*, *18*(12), 2119–2122. https://doi.org/10.1175/JCLI3394.1

Woodruff, S. D., Worley, S. J., Lubker, S. J., Ji, Z., Eric Freeman, J., Berry, D. I., Brohan, P., Kent, E. C., Reynolds, R. W., Smith, S. R., & Wilkinson, C. (2011). ICOADS Release 2.5: Extensions and enhancements to the surface marine meteorological archive. *International Journal of Climatology*, *31*(7), 951–967. https://doi.org/10.1002/joc.2103

Woollings, T., Barnes, E., Hoskins, B., Kwon, Y. O., Lee, R. W., Li, C., Madonna, E., McGraw, M., Parker, T., Rodrigues, R., Spensberger, C., & Williams, K. (2018). Daily to decadal modulation of jet variability. *Journal of Climate*, *31*(4), 1297–1314. https://doi.org/10.1175/JCLI-D-17-0286.1

Woollings, T., & Blackburn, M. (2012). The north Atlantic jet stream under climate change and its relation to the NAO and EA patterns. *Journal of Climate*, *25*(3), 886–902. https://doi.org/10.1175/JCLI-D-11-00087.1

Woollings, T., Drouard, M., O'Reilly, C. H., Sexton, D. M. H., & McSweeney, C. (2023). Trends in the atmospheric jet streams are emerging in observations and could be linked to tropical warming. *Communications Earth and Environment*, *4*(1). https://doi.org/10.1038/s43247-023-00792-8

Woollings, T., Franzke, C., Hodson, D. L. R., Dong, B., Barnes, E. A., Raible, C. C., & Pinto, J. G. (2015). Contrasting interannual and multidecadal NAO variability. *Climate Dynamics*, *45*(1–

2), 539–556. https://doi.org/10.1007/s00382-014-2237-y

Woollings, T., Gregory, J. M., Pinto, J. G., Reyers, M., & Brayshaw, D. J. (2012). Response of the North Atlantic storm track to climate change shaped by ocean-atmosphere coupling. *Nature Geoscience*, *5*(5), 313–317. https://doi.org/10.1038/ngeo1438

Woollings, T., Hannachi, A., & Hoskins, B. (2010). Variability of the North Atlantic eddy-driven jet stream. *Quarterly Journal of the Royal Meteorological Society*, *136*(649), 856–868. https://doi.org/https://doi.org/10.1002/qj.625

Wu, T., Lu, Y., Fang, Y., Xin, X., Li, L., Li, W., Jie, W., Zhang, J., Liu, Y., Zhang, L., Zhang, F., Zhang, Y., Wu, F., Li, J., Chu, M., Wang, Z., Shi, X., Liu, X., Wei, M., … Liu, X. (2019). The Beijing Climate Center Climate System Model (BCC-CSM): The main progress from CMIP5 to CMIP6. *Geoscientific Model Development*, *12*(4), 1573–1600. https://doi.org/10.5194/gmd-12-1573-2019

Xie, S. (2020). Ocean Warming Pattern Effect On Global And Regional Climate Change. *AGU Advances*, *1*(1). https://doi.org/10.1029/2019av000130

Yu, B., Zhang, X., Lin, H., & Yu, J. Y. (2015). Comparison of Wintertime North American Climate Impacts Associated with Multiple ENSO Indices. *Atmosphere - Ocean*, *53*(4), 426–445. https://doi.org/10.1080/07055900.2015.1079697

Yu, S., & Sun, J. (2020). Potential factors modulating ENSO's influences on the East Asian trough in boreal winter. *International Journal of Climatology*, *40*(12), 5066–5083. https://doi.org/10.1002/joc.6505

Zappa, G., & Shepherd, T. G. (2017). Storylines of atmospheric circulation change for European regional climate impact assessment. *Journal of Climate*, *30*(16), 6561–6577. https://doi.org/10.1175/JCLI-D-16-0807.1

Zhang, X., Alexander, L., Hegerl, G. C., Jones, P., Tank, A. K., Peterson, T. C., Trewin, B., & Zwiers, F. W. (2011). Indices for monitoring changes in extremes based on daily temperature and precipitation data. *Wiley Interdisciplinary Reviews: Climate Change*, *2*(6), 851–870. https://doi.org/10.1002/wcc.147

Zou, Y., Yu, J. Y., Lee, T., Lu, M. M., & Kim, S. T. (2014). CMIP5 model simulations of the impacts of the two types of El Niño on the US winter temperature. *Journal of Geophysical Research*, *119(6)*, 3076–3092. https://doi.org/10.1002/2013JD021064.Received